Cranfield University

SCHOOL OF INDUSTRIAL
AND MANUFACTURING SCIENCE

PhD THESIS

Academic Year 1993-1994

RAZALI BIN HAMZAH

Erosion-Corrosion Modelling of Materials Used in Petroleum Production

Supervisors:

Dr. J. E. Strutt Dr. D. J. Stephenson

September 1994

CONTENTS

CONTENTS

CONTENTS

ABSTRACT

Experimental erosion/corrosion modelling was performed on C-Mn steels and corrosion resistant alloys commonly used in petroleum production. A graded commercial sand of 50-300 μm size range, similar to sands produced from typical oil/gas fields was used to simulate the erosive medium. The experimental conditions such as the sand flux, particle velocity, pressure and temperature, were chosen based on typical field operating conditions for corrosion, erosion and erosion-corrosion tests imposed on the materials. The corrosion environment was created by feeding in CO_2 gas with atomised water into the test chamber. A centrifugal erosion rig (45) with necessary modifications to suit wet and dry test conditions was used in the experiments. The rig was capable of generating over 150 m/s particle velocity and could operate at high temperatures to generate consistent results.

Results show that (a) there was a soft thin layer of corrosion products formed on the C-Mn specimens even at 20°C which can easily be removed by the impacting particles , (b) the scale growth rate kinetics were found to be parabolic and vary between $8x10^{-3}$ $\mu m^2/h$ to $50x10^{-3}$ $\mu m^2/h$ depending on the material and temperature, (c) the process of metal recession consists of the removal and regrowth of soft corrosion scale at low flux and low velocity, and erosion of substrate at high flux and high velocity, (d) the erosion-corrosion rates were found to vary between 2 - 30 times over the pure erosion rates under the same conditions, depending on the sand flux, particle velocity and temperature.

An existing computer simulation model (46) was used to simulate the conditions observed from the experiments. Some improvements were incorporated into the programme and the final model is capable of predicting the erosion and erosion-corrosion rates applicable to petroleum production.

ACKNOWLEDGEMENTS

I am grateful and wish to thank PETRONAS, The Malaysian National Petroleum Corporation, for being the main sponsor throughout my programme in Cranfield, PETRONAS Research & Scientific Services Sdn. Bhd. for funding the total project, PETRONAS Carigali Sdn. Bhd./Baram Delta Operations for providing resources and allowing access to field and in-house data; without which this thesis will not be in its proper form.

I also wish to thank my supervisors, Dr. J.E. Strutt and Dr. D. J. Stephenson, for providing the supervision and guidance during this programme; Mr. Tim Prior for providing a lot of technical supports in getting the erosion rig working; Dr. S. Impey, Mrs. C. Kimpton and Mr. C. Matthews for assisting me in material specimen examinations and to all other staff for their cooperation that they have given in the course of my work. To all staff of Cranfield, I wish them the best in their future undertakings.

I am grateful to my wife, Khalijah who constantly gave me great care, encouragement and warmth, my children Redza, Nazmi, Arief and Nur Ain who provided me with a lot of inspiration during the course of my work.

FIGURES

FIGURES.

FIGURES.

FIGURES.

FIGURES.

FIGURES.

FIGURES.

TABLES.

TABLES.

NOTATION.

The following is a list of common notation used in this thesis. All notation are also explained in the thesis immediately after their introduction:-

A	An area, e.g. a surface area.
a	Chordal radius after impact or contact radius.
α	Impact angle.
α_p	Critical impact angle to cause gross plastic damage.
α_r	Critical impact angle to initiate microplastic damage.
D	Diameter of particle or pipe.
D_r	Ratio of depth of contact to depth of cut, in metal cutting.
d_1, d_2	Density of particle, Density of substrate.
E_1, E_2	Young's modulus for particle, substrate.
e, e_R, e_f	Strain, Resultant strain and Strain to fracture.
ϵ	Energy required to deform and remove unit mass or volume of material.
ϕ	Energy required to cut and remove unit mass or volume of material.
F_R	Ratio of vertical force to horizontal force components.
B,C,K	Constants as defined in text.
M	Total mass of impinging particles.
m	Mass of particle.
N	Number of impacts.
n	Velocity exponent.
Ω	Secondary energy required to remove unit mass of substrate.
$P_{(CO2)}$, P	Partial Pressure of CO_2 or pressure resisting indentation.
p	Plastic flow stress of material.

Q	Volume of indentation or erosion volume loss.
q_1, q_2	Poisson's ratio of particle, substrate.
R	Radius of particle or sphere.
r	Rate of corrosion.
σ	Stress as defined in text.
ρ	Density of gas or fluid as defined in text.
T	Temperature.
t	Time.
V	Velocity of particle(s).
V_e	Erosional velocity.
$V_{crit.}$	Critical velocity.
V_p	Critical velocity to cause gross plastic damage.
V_y	Critical velocity to initiate microplastic damage.
W	Erosion rate (Mass of substrate/mass of particles).
Y	Yield strength of material.
y	Elastic load limit.
z	Thickness of scale.

CHAPTER 1

Introduction

CHAPTER 1

1. INTRODUCTION.

In the development of oil-field equipment it is essential to consider the internal erosion and corrosion aspects in determining the design life of the equipment for safe operations. This is due to the fact that while producing hydrocarbon from the reservoir, sand may also be produced. Sand when produced, may remove protective corrosion products which form on the surface of the materials of the equipment and thus expose them for further corrosion. This continuous process of metal loss is now known to be a contributory factor to equipment failure in the oil-fields.

It is expected that once sand production occurs, both erosion and corrosion take place and this will severely affect the life performance of the equipment. The problem of erosion is widely recognised in for example, choke valves, which are amongst the least reliable of all downhole components. The control of fluid flow is achieved by reducing the choke size which results in significant pressure drops across the valve with relatively high fluid velocities which may exceed 100 m/s depending on the valve opening. At such high flow velocities, with particles entrained in the fluid, result in extensive erosion depending on the type of materials employed in the valve and the hydrodynamic conditions. For lower velocity regimes, components such as production tubing, especially the blast joint and at the surface, the christmas-tree components and the flowlines such as the tees and the elbows have also been known to have suffered erosion-corrosion failures.

When corrosion occurs with erosion there is a synergic interaction between them and the process is referred to as erosion-corrosion. Erosion-corrosion is a complex process. At the material level, metal loss can occur by a number of mechanisms namely electrochemical, cutting/abrasive wear, fatigue and fracture. The rate controlling process depends on the corrosion behaviour, the mechanical properties of the materials, the flux density/particle loading and the physical properties of the erodent. The location and extent of erosion, on the other hand, is dependent on the hydrodynamic conditions generated by the shape changes and discontinuities in the components. The fluid response to geometric change will determine the velocity and angle of impact of the particles as well as influencing the particle loading.

In oil and gas production activities the corrosion processes that are of particular importance are associated with the presence of wet CO_2 (sweet corrosion) and wet H_2S (sour corrosion). CO_2 is generally present in produced gases. It is found naturally in reservoir formations (normally from carbonate bearing rocks) or it may be deliberately introduced in later production activities, for example, CO_2 flooding / injection for pressure maintenance to enhance hydrocarbon production rate (1). Gas-fields having 10 - 15 % of CO_2 content are common in the carbonate bearing rocks. Records of as high as 71% of CO_2 content have been known to be present naturally, for example the Natuna Gas-field in Indonesia (2). Corrosivity of wet CO_2 will become a concern to the corrosion engineers when its partial pressure approaches 1 bar. H_2S on the other hand is sometimes encountered naturally in reservoir (normally in sulphate bearing rocks) but may be accidentally introduced by the injection of Sulphate Reducing Bacteria through water injection projects into the reservoir. The presence of H_2S above 0.05 psia partial pressure (sour gas) and above 10 psia

partial pressure (sour crude / condensates) are considered detrimental to the downhole tubular goods and may lead to failure by Sulphide Stress Corrosion Cracking (3).

A significant amount of research has been conducted in the areas of sweet and sour corrosion in general (4,5). Continuation of this area of research is still required to understand the process further. However, surprisingly there has been little research attention on the problem of erosion-corrosion of the downhole tubular goods and the surface facilities. The lack of tools in predicting the service life of the material components in oil and gas production activities under these circumstances, may lead to premature failure and replacement of facilities. On the other hand any delay in performing those activities may result in significant loss in production and also expose the installation to operational and environmental risks. The precise knowledge of erosion-corrosion is therefore essential in the determination of optimum production throughput capacity and in the prediction of the safe life of the material components. In both cases the operators have considerable economic interest in ensuring that all the activities are performed prudently.

It is obvious that erosion corrosion being a complex process causes major difficulties in the ability to predict the rate of material loss. The process is believed to be dependent on the erosive particles (sand) parameters such as size, shape, velocity at impact, impingement angle and the flux rate; the material parameters such as microstructure, hardness and the strength of adherence of the passivating layer of corrosion products (e.g. scales layer); and the environment parameters such as temperature, pressure, hydrodynamic condition and the corrosion mechanisms. The effects of these parameters when applied to oil and gas production activities have not been fully understood. These

are due to, (a) Uncertainty in determining the environmental parameters at design stage such as the particles impact velocity, the flux rate, the size distribution and the nature of oxides formed after material interaction with the environment, and (b) Uncertainty in determining the relationship between the environmental parameters with the erosion-corrosion rates.

Therefore this project was undertaken to chart out the erosion-corrosion behaviour of materials used in petroleum production using typical fields data obtained from Malaysian oil/gas fields.

This thesis describes a research programme on erosion-corrosion behaviour of a range of candidate materials including Carbon-Manganese steels and corrosion resistant alloys which have been exposed to environment simulating wet and dry CO_2 conditions. Erosion was introduced by injecting dry sand (50-300μm) into the centrifugal erosion rig which was modified to operate in dry and wet conditions. The results obtained were used to develop a computer simulation package by which erosion-corrosion rates could be determined by using known materials (metal and corrosion scales), environmental (temperature, pressure and corrosivity) and sand (size, flux density, shapes and angles of impact) parameters.

CHAPTER 2

Background

CHAPTER 2

2. BACKGROUND.

The movement of naturally occurring sand particles into the wellbore along with the production of reservoir fluids is a primary source of petroleum production problems in an unconsolidated or poorly cemented petroleum-bearing-sand. As the majority of petroleum production comes from sandstone reservoirs, the control of sand production is of particular importance. Typical problems which arise directly from sand production are formation damage; plugging of tubing, flowlines and separators, and erosion of production facilities. It is therefore desirable to address these problems early such as during the design, development of equipment specifications, material selection and the manufacture of equipment. It is also advisable to adopt a sound operating procedure in order to minimise the consequence of these problems if they cannot be totally eliminated.

2.1 Sand Production.

Sand production is more likely to occur from the younger Tertiary sediments (6). As a result of local earth stresses, a poor well completion and an unsound production practice may create unstable conditions that lead to sand production from old Tertiary sediments as well.

The compression exerted as a result of overburden on the sand particles in a formation are stabilised by the inter-particle stresses, the shear stresses of cementation between the particles, and the pore/capillary pressure of

fluid occupying the inter-particle spaces. Once production takes place, hydrodynamic stresses due to fluid flowing through the sand and liquid drawdown especially at high rate of production, overcome the cohesive strength of the sand material; the aggregate then collapses and sand particles are let loose to be carried away by the fluid into the wellbore. This process can occur for example when gas wells are made to flow at high rates for 'peaking' purposes. This practice may induce sand production from previously stable reservoir. In doing so, excessive stresses develop across a small region of the formation near to the perforation, due to exposure to high pressure gradient.

In some cases, the onset of sand production occurs late in the life of the producing field when reservoir pressure has declined to the extent that the overburden is supported mainly by the vertical components of the inter-particle stresses rather than the capillary/pore pressure. This may cause the shearing of cementing material allowing sand particles to move and flow into the wellbore or at certain critical pore pressure, the point stresses between the sand particles exceed their fracture strength and the sand particles themselves are crushed causing the instability and resulting in sand production. Figure 1 shows these phenomena schematically.

Some field experiences have shown that sand production may occur both before and after water-cut (6,7). Reservoirs that were producing without sand may suddenly begin to produce sand after water-cut. Alternatively, the rate of sand production may also increase after water-cut. The initiation of sand production or the increase in sand production after water-cut may be due to the following reasons: (a) the capillary pressure holding sand particles may be lost after water-cut, (b) the flow friction may significantly increase because the water saturation

significantly lowers the hydrocarbon relative permeability, (c) the reservoir pressure is generally reduced when water-cut commences, (d) to maintain hydrocarbon flow rate, the tendency is to produce with higher total flow rate, which causes low well pressure and high pressure gradient at the pore spaces and (e) dissolution of cementing material by water.

Figure 1. Mechanisms of Sand Production.

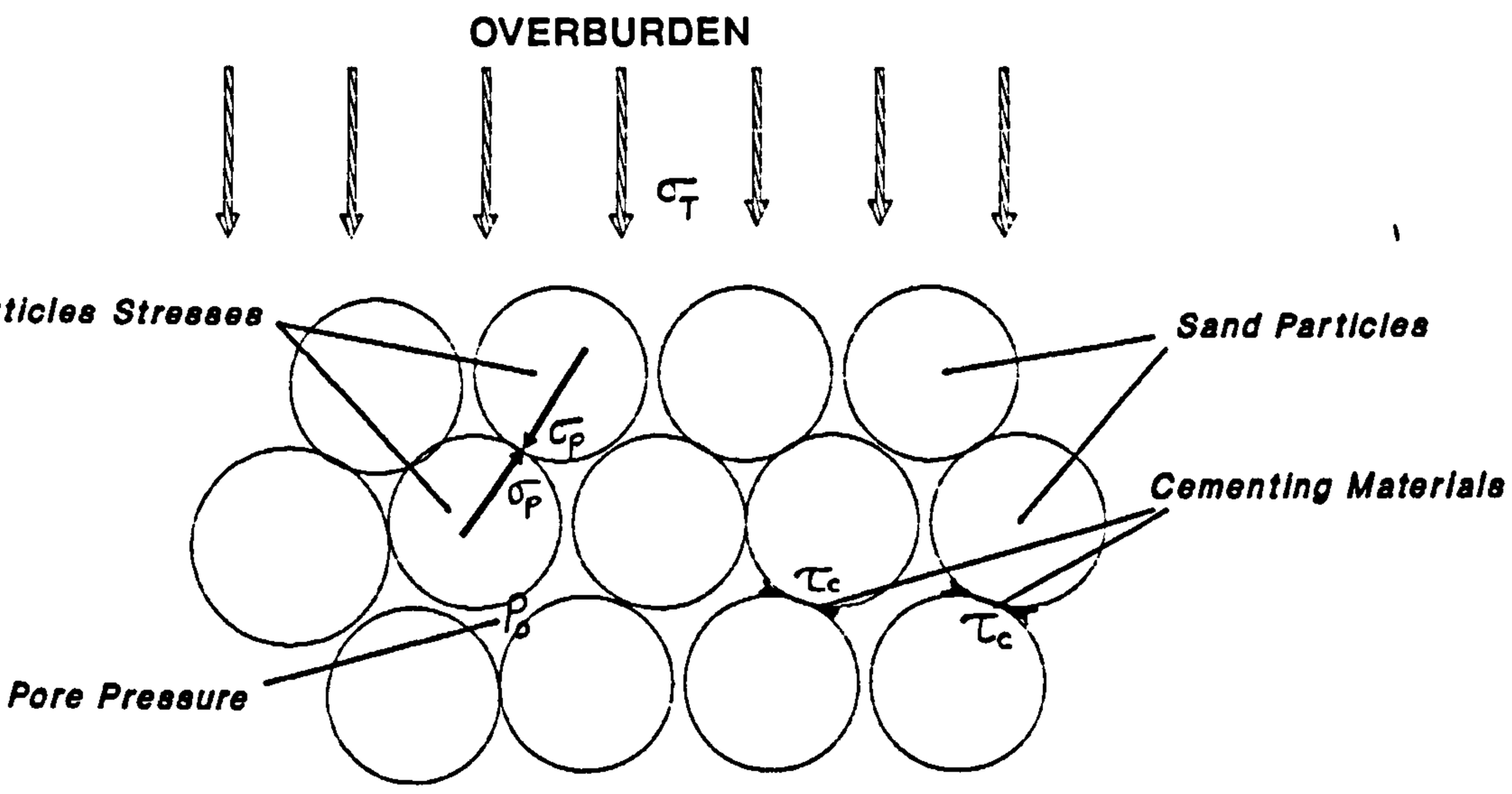

$$\sigma_T = \sigma_p + P_o + \tau_c$$

Where σ_T = total stress due to overburden,

σ_p = inter-particle stresses,

P_o = pore pressure, and

τ_c = shear stresses in cementing materials.

When P_o decreases, τ_c and σ_p increase.

As $\tau_c > \tau_{c\ fracture}$, Cementing failed and sand particles let loose.

$\sigma_p > \sigma_{p\ fracture}$, Sand particles crushed and let loose.

2.2 Problems due to Sand Production.

The production of sand and movement of sand particles are known to be detrimental to the producing processes and has a negative effect throughout the production system from the formation to surface facilities.

2.2.1 Formation.

The movement of crushed sand particles and finally lodging in voids and pore throat spaces will cause the passages/spaces to be plugged and consequently reducing permeability. The migration of sand particles into the wellbore may cause the well to be plugged and in the extreme cases production may cease altogether.

2.2.2 Casing and Liners.

Compaction due to formation collapse, can transmit compressive forces to casing and liners which are sufficient to cause it to buckle and/or balloon. If ballooning occurs in the case of slotted liners, the slots will open up resulting in the loss of gravel if the completion is gravel-packed. Sand production may then take place and the liners erode. The effect of buckling may mean that it becomes impossible to pull or run packers through the deformed section and if liner is subsequently eroded, it may not be possible to remove it out when attempting to work-over the well.

2.2.3 Sub-Surface Equipment.

Sand particles carried by fluids moving at high velocity are very erosive and capable of eroding through, and even parting, tubing and tubing accessories. At low velocity, sand may settle out causing tubing to become plugged.

2.2.4 Surface Facilities.

Christmas trees, flowlines and separators may be eroded and possibly plugged. Large quantity of sand settling out in the separators will cause them to become inefficient, because of reduction in volume available for liquid/vapour phase for separation and reducing the retention time. In some severe cases, production has to be stopped altogether to allow sand, which has settled out, to be removed.

The erosion capability of sand laden fluid flowing at high rates (velocity) is more readily appreciated knowing the fact that it can cut out permanent choke in a matter of minutes.

2.3 Methods of Sand Production Controls.

A number of techniques have been used to exclude sand production from oil and gas wells with some degree of success. The most common techniques are those using gravel-packing well completion, sand consolidation and control of production rate.

2.3.1 Gravel Packing.

The objective of gravel packing is to prevent migration of sand particles from the formation to the wellbore, acting as a sand screen. This is done by placement of specially selected gravel between the formation sand and the wellbore. At the wellbore a wire-wrapped screen or slotted liner is placed in order to retain the gravel.

There are two basic types of gravel-packing completion techniques exist; the open hole or external gravel-packing (EGP) and the inside casing or internal gravel-packing (IGP). Figure 2 shows schematically the two types of gravel-packing completions. The installation of IGP gravel-packing is the most widely used method of sand exclusion in the sand prone wells in Malaysian oil fields, for example. In Malaysian oil fields the gravel-packing depths may range from about 3 metres, for thin reservoir in single zone completion, to almost 200 metres for thick reservoirs or in multiple zone gravel-packing completion (7).

Experiences from some 290 gravel-packing completions from sand prone reservoirs in Malaysia show that complete exclusion of sand production is not possible (7). This is because it is difficult to achieve 100% compaction of the gravel. It is likely that voids in the gravel pack may be present and sometimes the slotted liners become damaged and

allow gravel to migrate along with the sand. However, more than 90% of the IGP completions have managed to reduce sand production down to a value as low as 2 to 5 PPTB (pounds per thousand barrels) (7), which the operators generally assumed to be non-detrimental to the producing process and production facilities.

However, there is a price to pay for employing gravel-packing sand production control. While there is incomplete exclusion of sand production, it also results in a significant reduction in well production rate. This reduction may reach as high as 70% to 90% of the open hole completion. In other words, with a gravel-packing completion, in place, the production rate of the well can be reduced to 30% or even up to 10% of those typical open-holed completions (7).

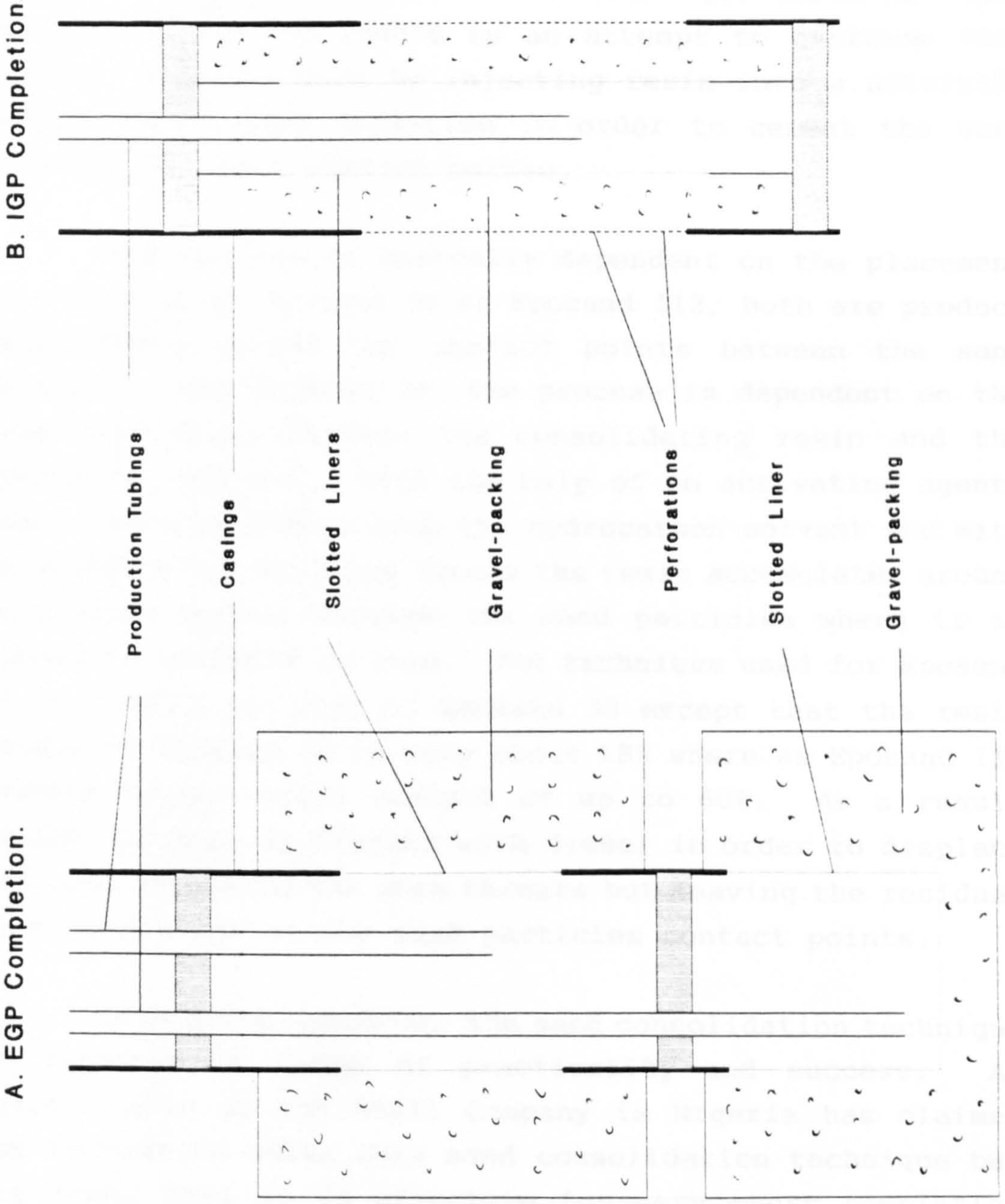

Figure 2. Gravel-packing Well Completions.

2.3.2 Sand Consolidation (6).

Sand production is a result of the absence or inadequacy of cementing material holding the sand particles together. The sand consolidation technique which has been available since the 1940's is an attempt to overcome this problem. This is done by injecting resin into a naturally unconsolidated sand formation in order to cement the sand particles at their contact points.

The process is basically dependent on the placement of a resin (e.g. Eposand 30 or Eposand 112, both are product trade names) around the contact points between the sand particles. For Eposand 30, the process is dependent on the phase separation between the consolidating resin and the hydrocarbon solvent. With the help of an activating agent, liquid resin separates from the hydrocarbon solvent and with the presence of capillary forces the resin accumulates around the contact points between the sand particles where it is allowed to solidify or cure. The technique used for Eposand 112 is similar to that of Eposand 30 except that the resin content of Eposand 30 is only about 18% where as Eposand 112 contains higher resin content of up to 60%. As a result Eposand 112 must be flushed with diesel in order to displace all resin occupying the pore throats but leaving the residual resin saturation at the sand particles contact points.

Like gravel-packing, the sand consolidation technique has problems in terms of practicality and success. An operator such as the Shell Company in Nigeria has claimed some success in using this sand consolidation technique but only found that it is effective for very short completion intervals of 2 to 3 metres only (8). But even then they have only had 4 success and 7 failures in their attempt to use this type of sand consolidation technique.

The problems associated with resin sand consolidation technique are threefold:-

(a). Over-flushing of resin is sometimes difficult to avoid leading to poor sand consolidation. On the other hand because of the high viscosity of certain type of resin used, e.g. Eposand 112, the treatment may leave excessive resin in place which is detrimental to formation permeability, and hence lead to poor well productivity.

(b). The resin may have poor wettability to the sand particle surface which does not provide good bonding between the sand particles. This may lead to the consolidated sand losing strength and resulting sand production soon after production has taken place.

(c). At high resin injection rates and unfavourable viscosity and density ratios between the injected resin and formation fluid, the displacement front will not be stable and uniform. Uneven spreading of resin may occur, in which the injected resin tends to channel out resulting in a poorly consolidated sand volume around the wellbore. A low viscosity resin will also suffer from extensive setting (i.e. high accumulation of the resin in certain area) due to the effects of gravity after pumping has stopped.

2.3.3 Controlled Production.

Another method which is very commonly used to prevent the well from producing sand is simply by controlled production in which the well is produced at a much lower rate such that it reduces the hydrodynamic forces imposed on the sand particles around the wellbore. From field experience, it has been observed that in some sand formations a certain critical flowrate exists above which significant sand

production occurs but below this critical flowrate little or no sand production may take place. Some laboratory tests(6) also show that structural sand arches may form in a small region around perforation, preventing migration of sand. Provided that the flow remain stable, the structural sand arches remain in place and hence retain the formation sand. However, any sudden change in the production rate (either an increase or a decrease) is likely to disturb the structural sand arches and causing them to collapse, thus causing sand being produced with the fluid until new stable arches could form under new stable flow condition.

Sand bridging may also provide a form of sand control in poorly sorted sand formation (i.e. sand formation with a broad size distribution). Larger sand particles may wedge between the openings in a slotted liner or wire-wrapped screen preventing migration of finer sand particles to the wellbore. Likewise as in the structural sand arches, any sudden variation in flow conditions may disturb the sand bridges and allows sand production. Thus, both of these phenomena can only help to minimise sand production under stable flow conditions and at subcritical flowrate. It is therefore impossible to stop sand being produced altogether especially in a very poorly consolidated sand formation.

2.4 Erosion-Corrosion Problems.

It has been mentioned earlier that the well fluid is erosive when it is sand laden. When it contains water and other corrosive gasses such as CO_2/H_2S then corrosion also takes place. Erosion and corrosion are well known to oil field engineers as they often encounter with failures of tubing blast joints, sub-surface safety valves (SSSV), permanent chokes, impact flanges, T-connections and elbows of

flowlines and separators. At the same time, there is very little knowledge currently available in order to fully understand the mechanisms of erosion-corrosion.

When such components fail, through erosion-corrosion, the production system's integrity is affected and may become unsafe for continuation of operations. If left unchecked they may become a threat to the overall safety of the operations and also detrimental to the environment. In most cases, operators have to launch a sand production monitoring programme to assess the severity of sand production. For example, they may adopt some basic practices, such as using a rule of thumb sand production threshold limit in which they like to believe that erosion will not take place, etc. At the same time they may continue monitoring the effects on material failures under such forms of production practices. This will take them a long time before sufficient data and experience can be gathered and become useful. In reality they are lacking tools to assist them in determining the rate of material loss and to formulate the life expectancy of affected production equipment, under an erosion-corrosion condition.

As a result, when an operator adopts a threshold limit which is too stringent they will lose production opportunity, and at the same time, waste away part of the potential of the installed production capacity. On the other hand, they do not want to adopt too relax sand production threshold limit and to cause early failure of those critical components. It is therefore pertinent to understand properly the mechanisms of sand erosion under corrosive environments so that life prediction of critical components can be estimated reliably.

CHAPTER 3

Literature Review

CHAPTER 3

3. LITERATURE REVIEW.

3.1 Theoretical Background.

Corrosion causing the failure of oilfield equipment consists of various types of mechanisms; from common oxidation by oxygen in the presence of water (rusting of iron), galvanic corrosion due to the inhomogeneity of metallurgical properties (be it of the same or of different metals) generating different electrical potentials in the presence of an electrolyte brought in contact, chloride attack resulting in pitted surfaces, aqueous CO_2 corrosion, aqueous H_2S causing sulphide stress corrosion cracking and hydrogen induced cracking, crevice corrosion due to the presence of regions deficient in oxygen thus producing areas of preferred metal deterioration and bacterial (SRB) corrosion. The list may continue when the combinations of the above situations coexist, resulting in a complex corrosion phenomenon.

The type of corrosion being considered in this thesis is that of the aqueous CO_2 corrosion or sweet corrosion. This form of corrosion is known to be a very common form of corrosion encountered in hydrocarbon production scenarios. As mentioned earlier, CO_2 may be present naturally or may be deliberately introduced into the hydrocarbon reservoirs for enhanced hydrocarbon recovery.

Erosion on the other hand, takes place when the flow dynamics of the fluid cause the transfer of sufficient kinetic energy from the fluid and/or the solid particles it

carries by direct and repeated impingement onto the surface of the material causing it to fail. The type of erosion considered in this thesis is that of the erosion of equipment materials due to sand entrained in the hydrocarbons as they are produced.

The combined effects of erosion-corrosion by sand particles in the presence of wet CO_2 and their implication in the life time of equipment component was carefully studied in this thesis.

3.1.1 CO_2 Corrosion Theory.

Newton and Hausler (4), classified CO_2 corrosion into two groups; namely, (a) uniform corrosion of bare steel surfaces, which applies mainly to high fluid flow rate situations, and (b) localised corrosion which occurs, when a scale layer was formed and uniform corrosion rate diminished. In the presence of other corrosive agents such as H_2S or breaks in the passivating scale layer, localised attack can be profound.

Corrosion literature in this area indicates that uniform corrosion rates are extremely high at high partial pressures of CO_2. De Waard and Milliams (9,10), for example, have developed experimental data which predicts the rate of uniform corrosion in aqueous CO_2 of the form :

$$\log r = 0.5\, B \log P_{(CO2)} + C \qquad \text{.....(1)}$$

They demonstrated that the rate of corrosion increases with CO_2 partial pressure and temperature, and presented an overall rate expression for the prediction of film-free corrosion rates for grit-blasted X-52 steel as in equation

(2) below; where r is the corrosion rate in mm/year, T is temperature in °C and $P_{(CO2)}$ is the CO_2 partial pressure in bar.

$$\log r = 7.96 - \frac{2.32\times10^3}{273 + T} - 5.55\times10^{-3}T + 0.67 \log P_{(CO2)} \quad ..(2)$$

Their results can also be represented in the form of a nomograph as shown in Figure 3.

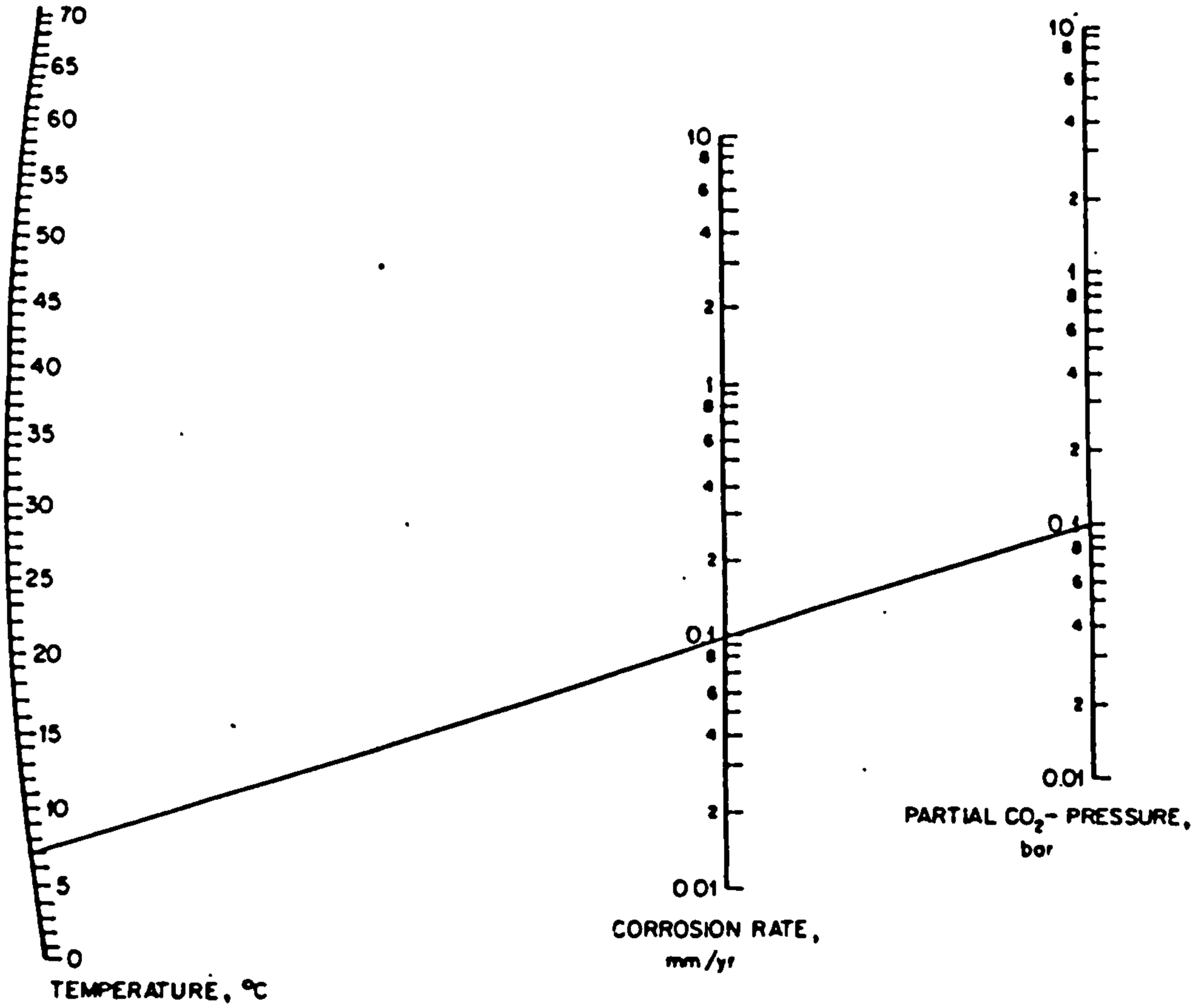

Figure 3. Nomograph for calculation of corrosion rates (mm/y) as a function of CO_2 partial pressure and temperature. (Example shown: At 0.1 bar $P_{(CO2)}$ and 7°C, corrosion rate is 0.1 mm/y) (9).

Dry CO_2 gas is non-corrosive to most engineering metals at temperatures of interest to offshore engineers. Aqueous CO_2 solutions on the other hand are more corrosive than completely disassociated (strong) acids of the same concentration (4,9). It is known that steel (iron) may react with aqueous CO_2 in the following basic chemical reactions;

At anodic sites,

$$Fe \rightarrow Fe^{2+} + 2e^- \quad \text{.....(3)}$$

CO_2 dissolves in water to produce carbonic acid,

$$CO_2 + H_2O \rightarrow H_2CO_3 \quad \text{.....(4)}$$

Carbonic acid is a weakly dissociated acid,

$$H_2CO_3 \rightleftharpoons H^+ + HCO_3^- \rightleftharpoons CO_3^{2-} + 2H^+ \quad \text{.....(5)}$$

The cathodic reaction involves the reduction of carbonic acid (9),

$$H_2CO_3 + e^- \rightleftharpoons HCO_3^- + H^\circ \quad \text{.....(6)}$$

and to a lesser extent, because of the weak acid dissociation in equation (5),

$$H^+ + e^- \rightarrow 1/2\ H_2 \quad \text{.....(7)}$$

and

$$2H^+ + 2e^- \rightarrow H_2 \quad \text{.....(8)}$$

The overall reaction is therefore,

$$Fe + H_2CO_3 \rightarrow FeCO_3 + H_2 \quad \text{.....(9)}$$

Bokris, Drazic and Despic (11, 12), proposed that the corrosion of iron in oxygen free acid solutions is governed by reactions (7) and (8) above and the anodic dissolution of iron is according to the following expressions:

$$Fe + OH^- \rightleftharpoons FeOH + e^- \quad \text{.....(10)}$$

$$Fe(OH) \rightarrow FeOH^+ + e^- \quad (R.D.S.) \quad \text{.....(11)}$$

$$FeOH^+ \rightleftharpoons Fe^{2+} + OH^- \quad \text{.....(12)}$$

Rogers and Rowe (13), proposed that the dissolution of iron in carbonic acid may form two ferrous compounds namely, ferrous bicarbonate and ferrous carbonate according to the following reactions:

$$Fe + 2H_2CO_3 \rightarrow Fe(HCO_3)_2 + H_2 \quad \text{.....(13)}$$

$$Fe(HCO_3)_2 \rightarrow Fe^{2+} + 2HCO_3^- \quad \text{.....(14)}$$

$$HCO_3^- \rightarrow H^+ + CO_3^{2-} \quad \text{.....(15)}$$

$$Fe^{2+} + CO_3^{2+} \rightleftharpoons FeCO_3 \quad \text{.....(16)}$$

However, ferrous bicarbonate is relatively more soluble than ferrous carbonate.

Xia et. al (14), also found in their experiments that at pH values between 5-8, of deaerated CO_2-containing NaCl solution, the pipe steel corroded and ferrous bicarbonate initially forms. After prolonged exposure (e.g. 48 h) both ferrous bicarbonate and ferrous carbonate were found clinging to the pipe wall.

Ferrous carbonate, $FeCO_3$, is usually formed at temperatures below 100°C, but at higher temperatures, magnetite Fe_3O_4 may form (15,16,17,18), probably in accordance with the following reactions,

$$3Fe + 2H_2CO_3 \rightleftharpoons Fe_3O_4 + 2CO + 2H_2 \quad \text{.....(17)}$$

$$2CO + 2H_2O \rightarrow 2CO_2 + 2H_2 \quad \text{.....(18)}$$

Davies and Burstein (19), conducted an experiment and found that the dissolution of iron in the active and prepassive regions is greatly accelerated by the presence of bicarbonate, causing the metal surface to be severely pitted. They believed that a stable complex anion, $Fe(CO_3)_2^{2-}$ forms according to the following reaction;

$$FeCO_3 + HCO_3^- \rightleftharpoons Fe(CO_3)_2^{2-} + H^+ \quad \text{.....(19)}$$

This idea was supported by McIntire et. al (20), who proposed that the the ability to generate a stable complex anion,

$Fe(CO_3)_2^{2-}$ is enhanced even in the presence of low concentration of bicarbonate in solution, but relatively high concentration of bicarbonate ion is always maintained near the metal (iron) surface.

Jasinski (21), conducted corrosion experiments on N80-Type steel in CO_2/water mixtures at 26°C and 95°C at 0.83 MPa CO_2 partial pressure. He found that at 26°C, the corrosion rates after 2 hours were lower than that predicted under film-free surface (5 mm/y) as determined by equation (2), and the corrosion rates started to fall after 24 hours. He found that the corrosion rates at 95°C continued to fall with time. He believed that there were two products resulted on the steel surfaces on both occasions, the properties of which were a function of temperature. In both occasions, iron carbonate ($FeCO_3$) must have formed on the steel surfaces, but at 26°C the corrosion process preferably etched out the metallic iron leaving the iron carbide on the surface of the quenched and tempered steels samples which originally made up of an α-phase iron and iron carbide. All of the deposits were loosely held to the surfaces of the specimen but were sufficiently adherent to physically restrict access of the corrodent species to the metal surface. It is believed that when iron carbonate forms on the surface, ferrous ions concentrations will soon reach a saturation level beneath the scale, effectively polarising the anodic dissolution process.

It is therefore evident that in aqueous CO_2 corrosion of carbon steels, that film-free corrosion probably never actually happens at temperatures as low as 20°C. At some stage after the corrosion takes place, the scale forms on the steel surface becomes protective enough that it has sufficient physical thickness to cause polarisation of the anodic dissolution process, resulting in reduced corrosion rates.

3.1.2 Erosion Theory.

Erosion is a process in which material is removed from a solid surface by the action of impinging solid or liquid particles. The theory of erosion of metal (ductile material) really started in the 1960s when Finnie et. al. (22,23), described the mechanism of material removal by solid particles erosion as similar to that of the micro-machining process. In general, they proposed that the rate of volume of material removal from a surface as a result of particle impingement can be expressed as an equation of the form:-

$$Q = \frac{\Phi M}{p} f(\alpha) V^n \qquad \text{.....(20)}$$

where Q = Rate of volume of material being removed,

Φ = the fraction of particles which cut in idealised manner,

M = Total mass of particles impinging,

$f(\alpha)$ = function of impact angles, α,

V = velocity of particles,

n = velocity exponent (assuming a value between 2-3), and

p = the flow stress of the material (similar to that measured in tension and compression tests).

Finnie (22), proposed that the volume of material removed, Q, by a single abrasive particle of mass, m, having a velocity, V, on striking the surface at and angle of impact α, may simply be calculated by using the following expressions:

$$Q_1 = \frac{mV^2}{pD_rF_R}\left(\sin 2\alpha - \frac{6}{F_R}\sin^2 \alpha\right) \quad if \ \tan \alpha \leq \frac{F_R}{6} \quad ....(21)$$

and

$$Q_2 = \frac{mV^2}{pD_rF_R}\left(\frac{F_R \cos^2 \alpha}{6}\right) \quad if \ \tan \alpha \geq \frac{F_R}{6} \quad .....(22)$$

where F_R= ratio of vertical force to horizontal force components. (F_R = 2 for angular abrasive particle).

D_r= ratio of depth of contact to depth of cut, and

p = plastic flow stress of substrate.

Equations (21) and (22) relate the material loss by erosion to the kinetic energy of the particle and the flow stress of the target material. Q_1 and Q_2 are equal when tan $2\alpha = F_R/6$. The expression for Q_1, at low angles, represents the case where the particle possesses a horizontal velocity component after striking, cutting and leaving the target surface and Q_2 represents the case where the particle completely loses its horizontal velocity component while cutting. When $\alpha = 90°$, the model predicts that the erosion rate is zero (see equation (22)). This model was demonstrated to be good at predicting erosion, of steel and copper, at low angles (15° to 20°) of impacting particles. However, it greatly underestimated erosion for angles above 40° and, as mentioned above, predicted zero erosion at a normal angle of incidence. This model is inaccurate since, practical erosion measurements have shown that significant erosion can and does take place at normal impact angle.

Approximately two years later, Bitter (26,27), extended Finnie's model by considering both ductile and brittle failures, for which removal of material by impacting particles, behaved in distinctly different behaviour. He considered two types of material removal mechanisms, depending on the impact angle of the impinging particle. One is that material surface is initially damaged by repeated deformation during particle collision which eventually results in 'breaking' loose a piece of material. The other is caused by the cutting action of the leading edge of the free-moving particles. He then proposed the following equations to calculate the material volume loss due to particles erosion:

$$Q_D = \left(\frac{0.5M}{\epsilon}\right)(V\sin\alpha - V_y)^2 \qquad \text{.....(23)}$$

$$Q_{C1} = \frac{2MC(V\sin\alpha - V_y)^2}{\sqrt{V\sin\alpha}}\left(V\cos\alpha - \frac{C(V\sin\alpha - V_y)^2}{\sqrt{V\sin\alpha}}\phi\right), \quad \alpha \le \alpha_0 \qquad \text{..(24)}$$

$$Q_{C2} = \frac{0.5M}{\phi}\left[V^2\cos^2\alpha - K(V\sin\alpha - V_y)^{3/2}\right], \quad \alpha \ge \alpha_0 \qquad \text{.....(25)}$$

and therefore, the total erosion of material at any instant equals;

$$Q_T = Q_D + Q_{C1} \qquad \text{.....(26)}$$

or

$$Q_T = Q_D + Q_{C2} \qquad \text{.....(27)}$$

where Q = material volume loss (Q_D is deformation wear and Q_{c1}, Q_{c2} are cutting wear),

M = total mass of impinging particles,

V = particles velocity,

α = impact angle,

V_y = maximum particle velocity at which the collision is purely elastic, given by

$$V_y = \frac{\pi^2}{2\sqrt{10}} \cdot y^{5/2} \cdot \left(\frac{1}{d_1}\right)^{1/2} \cdot \left[\frac{1 - q_1^2}{E_1} + \frac{1 - q_2^2}{E_2}\right]^2 \qquad \ldots\ldots\ldots(28)$$

ϵ = the energy needed to remove a unit volume of material from the body by deformation wear (deformation wear factor),

ϕ = the energy needed to scratch out a unit volume from the surface of the material (assuming the particle is not destroyed).

The equations are valid if V sin $\alpha \geq V_y$. If $\alpha \leq \alpha_0$, equation (24) must be used and if $\alpha \geq \alpha_0$ then equation (25) is used, α_0 being the impact angle at which the horizontal velocity component has just become zero when the particle leaves the body. The values of the constants C and K are given in the following equations:

$$C = \frac{0.288}{y} \sqrt[4]{\frac{d_1}{y}} \qquad \ldots\ldots\ldots\ldots\ldots\ldots(29)$$

$$K = 0.82\ y^2 \cdot \sqrt[4]{\frac{y}{d_1}} \left(\frac{1 - q_1^2}{E_1} + \frac{1 - q_2^2}{E_2}\right) \qquad \ldots\ldots\ldots(30)$$

where d_1, y, q and E are the density, elastic load limit, Poisson's ratio and the Young's Modulus respectively, with subscript 1 for the particle and 2 for the substrate.

Neilson and Gilchrist (28), carried out erosion experiments on aluminium and confirmed that there are two erosion mechanisms acting simultaneously in a given specimen under the impact of particles. The normal component of the force causes deformation wear in which the surface of the specimen is first work-hardened and then cracks develop and ultimately resulting in material removal. The cutting wear mechanism is associated with the force parallel to the surface during the impact. They generalised these mechanisms of erosive wear using the following expressions based on Bitter (26,27):

$$W = \underbrace{\frac{1/2\,(V^2\cos^2\alpha - v_p)}{\phi}}_{(A)} + \underbrace{\frac{1/2\,(V\sin\alpha - V_y)^2}{\epsilon}}_{(B)}, \qquad \alpha<\alpha_0 \quad \ldots(31)$$

and

$$W = \underbrace{\frac{1/2\;V^2\cos^2\alpha}{\phi}}_{(C)} + \underbrace{\frac{1/2\,(V\sin\alpha - V_y)^2}{\epsilon}}_{(B)}, \qquad \alpha>\alpha_0 \quad \ldots\ldots(32)$$

Where W = Erosion rate (kg. of material/kg. of particles),
V = Velocity of particle (m/s),
v_p= Residual parallel component of particle velocity (m/s),
V_y = Particle velocity component normal to surface below which there is no erosion (m/s),
ϕ = Energy required to cut and remove unit mass of material (J/kg.),
ϵ = Energy required to deform and remove unit mass of material (J/kg.),
α = angle of attack, and
α_0= angle of attack when v_p=0.

Parts (A) and (C) account for the cutting wear and part (B) accounts for deformation wear.

Tilly (31), collected photographic and metallographic evidence that erosion in a ductile material involves two stages. The first stage occurs when a particle strikes a surface and produces indentation and possibly removes a chip of metal. The second stage occurs when particles break up during impact; fragments are projected radially from the indentation which can then produce secondary damage. He suggested that the first stage erosion obeys the following expression,

$$W_1 = \frac{V^2}{\phi}\left[1 - \left(\frac{D_c}{D}\right)^{3/2} \frac{V_c}{V}\right]^2 \qquad \text{.....(33)}$$

and the second stage erosion as,

$$W_2 = \frac{V^2}{\Omega} F \qquad \text{.....(34)}$$

where W_1 and W_2 are the primary and secondary erosion rates (mass of material removed per unit mass of particles), ϕ is the energy required to remove unit mass of material by the primary erosion process and Ω is the secondary erosion factor, V is the particle velocity, D is the particle diameter, and D_c and V_c are the threshold particle diameter and velocity to cause any erosion, respectively. F is the degree of fragmentation which is given by the following formula,

$$F = \frac{W_0 - W}{W_0} \qquad \text{.....(35)}$$

where W_0 is the proportion of the particle sample mass within specified range before testing and W is the proportion after. If all of the particles are broken into smaller sizes then F=1.

It is worth noting that the concept of a two-stage erosion process seems to be applicable for erosion at high velocity and relatively large particle sizes. In his experiments Tilly conducted tests on particles size ranges of 350-500 μm and 500-850 μm at a velocity of ≈200 m/s.

Oblique Particle Impact.

Hutchings (33,35,36,38), described three types of ductile erosion mechanism by which material could be removed when erosive particles stroke the surface of a metal at a low angle of impact. The mechanisms are illustrated in Figure 4 below:-

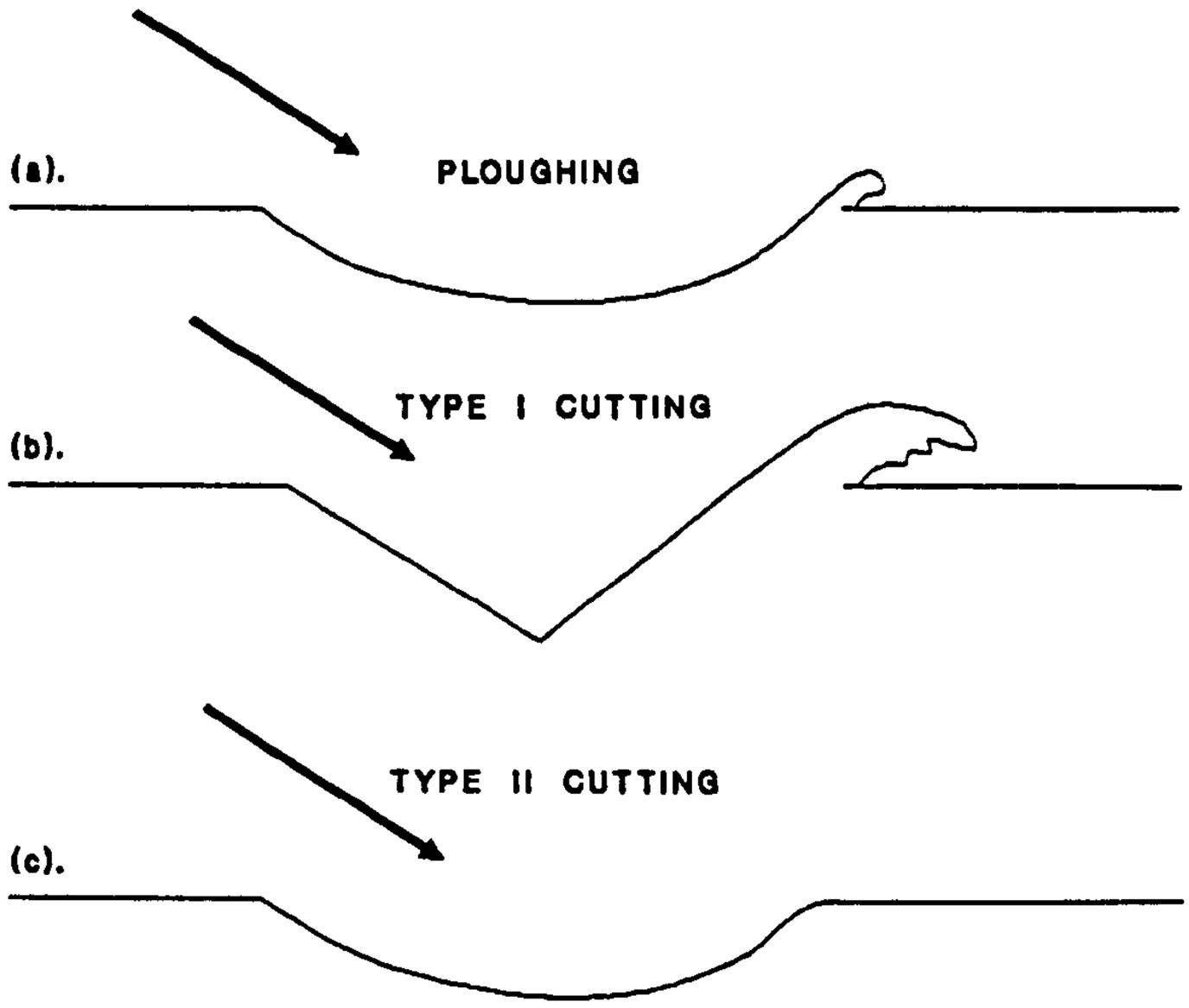

Figure 4. The three types of ductile erosion mechanism by erosive particles.

Ploughing deformation is usually caused by spherical particles or rounded surfaces of irregular particles. Figure 4(a) shows a sectional view of ploughing deformation in which, effectively, no material has been removed. The lip of material formed at the exit of the crater results from material being pushed up in the front of the particle and folded over onto the undisturbed surface of the metal. Material removal may take place after subsequent impact on the lip or particle impacting at high velocity or at lower impact angle.

In Type I cutting deformation, characterised by erosion of angular particles striking at an angle with high rake angle. As the sharp edge strike the surface, the particle rebounds with an appreciable rotational velocity in forward direction, thus generating a deformation as shown in Figure 4(b), while forming a significant lip. Material removal may then take place after subsequent impact on the lip.

Type II cutting deformation is also characterised by erosion of angular particles striking at an angle with low rake angle. After striking the surface, the particle rebounds with rotational velocity in a backward direction, thus effectively grazing the surface of the metal. In this type of cutting there is a greater chance of metal being removed on every strike by the particle. The result of type II cutting is shown in Figure 4(c).

Levy (42), attempted to explain the mechanisms of erosion by particles impacting at an oblique angle by the process of micro-extrusion and forging rather than micro-machining as originally proposed by Finnie (22). He used the concept of micro-extrusion and forging to describe the formation of platelets on eroding surfaces as a means of material failure and removal. It was proposed that in the

beginning, platelets are formed without any loss of material. Adiabatic shear heating (37) of the immediate surface region takes place. Immediately beneath the surface where particles impact, a work-hardened zone will form if sufficient kinetic energy of the impacting particle is transferred to the metal over and above that required for the formation of platelets at the surface. When the surface has completely been converted to platelets and craters, and the work-hardened zone reaches its stable hardness and thickness, a steady state erosion begins. Levy believes that the steady state erosion rate is at its highest when the subsequent cold-worked zone acts as an anvil to increase efficiency for the impacting particle to hammer and extrude-forged platelets in the now fully heated and most deformed region. As more particles impact, the anvil becomes fully developed, the platelets are fully formed and heated, maximum material removal will take place. This cross-section of material conditions will move down through the metal as erosion and loss of metal occur, see Figure 5.

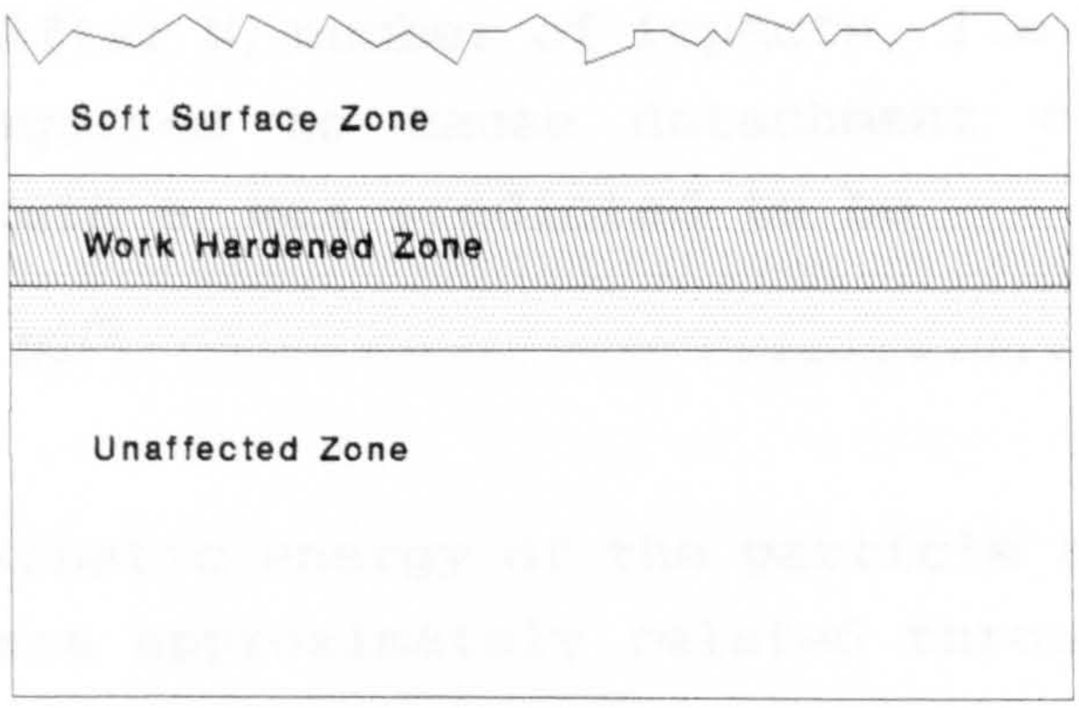

Figure 5. Schematic of a cross-section of an erosion of ductile material (42).

Levy believes that the formation of platelet chips, flakes, and lips as described by other investigators are similar to his platelet mechanisms. However, he did not suggest any mathematical model for predicting erosion.

Normal Particle Impact.

Hutchings (44) conducted model experiments and presents the mechanism of material removal due to impact of spheres at normal incidence. The model employs a criterion of 'critical plastic strain', e_c, which is the maximum plastic strain developed within the fragment or platelet. When plastic strain reaches a critical value, only then does material removal occur. The erosion process involves the accumulation of plastic deformation in the surface layer of the target.

e_c is a property of the material and may be thought of as a measure of its ductility under erosion conditions. It was assumed that, for each impacting sphere, a plastic strain increment of δe_p is developed within circular symmetry about the line of impact on the surface of the target material. After N_f number of impacts, i.e. the mean number of impact required to cause detachment of material, the resultant strain e_f was predicted to be

$$e_f = \delta e_p \, . \, N_f^{1/2} \qquad \ldots\ldots\ldots\ldots\ldots\ldots\ldots\ldots (36)$$

The kinetic energy of the particle and the volume of indentation are approximately related through the following equation,

$$Q = \frac{mV^2}{2P} \qquad \ldots\ldots\ldots\ldots\ldots\ldots\ldots\ldots\ldots\ldots (37)$$

where, Q = volume of indentation,
m = mass of particle,
V = velocity of particle, and
P = the pressure resisting indentation, equivalent to the quasi-static indentation hardness.

There is only a fraction f, of the volume of the indentation in which the material is plastically deformed. Therefore, the plastically deformed volume of the material around the indentation is given by,

$$Q_p = \frac{f\, m\, V^2}{2P} \qquad \text{.....(38)}$$

Therefore, the erosion rate W, defined as the mass loss from the target per unit mass of impinging particles is given by,

$$W = \frac{f\, d_2\, V^2}{2P\, N_f} \qquad \text{.....(39)}$$

Tabor (34), has shown empirically that for quasi-static indentation by a rigid sphere of radius R, the average strain introduced into a metal is given by,

$$e \approx \frac{0.2\, a}{R} \qquad \text{.....(40)}$$

where 'a' is the final chordal radius of the indentation and 'e' is the strain in an equivalent uniaxial compression test. By equating the initial kinetic energy of the impinging sphere with the work done in forming the indentation, it may be shown that,

$$a = 2^{1/2} R\, V^{1/2} \left(\frac{2\, d_1}{3P}\right)^{1/4} \qquad \text{.....(41)}$$

and, combining equations (36), (39), (40) and (41), the erosion rate equation (39) becomes,

$$W = 0.033 \frac{f\, d_1^{1/2}\, d_2\, V^3}{e_c^2\, P^{3/2}} \qquad \text{.....(42)}$$

where d_1 and d_2 are the densities of the impacting particle and the substrate, respectively.

The Incubation Period.

At high angles of incidence, and particularly for normal impacts, the undeformed specimen would not be expected to erode immediately on exposure to a flux of erodent. Plastic strain would have to accumulate in the initial undeformed material before wear fragments could be detached. Incubation periods, i.e. the time for accumulation of plastic strain preceding the establishment of steady state erosion are commonly observed (44,28). Hutchings derived the equation for calculating the mass of particles needed for incubation M_i, on a target surface of an area A as,

$$M_1 \approx \frac{12.5\, e_c^2\, P\, A\, R}{V^2} \qquad \text{.....(43)}$$

Therefore, if the rate of flux hitting the surface is M_r, then the incubation period t_i, can be approximately expressed as,

$$t_i \approx \frac{12.5\, e_c^2\, P\, A\, R}{V^2\, M_r} \qquad \text{.....(44)}$$

Concept of $V_{crit.}$ in Ductile Erosion Mechanisms.

Mamoun (39), attempted to derive expressions to predict $V_{crit.}$. He considered the conditions which result in the initiation of yielding and full plastic deformation of the target surface by an impacting particle.

It is known that when a particle impacts a target surface, below a certain critical velocity, the collision is purely elastic. Above this velocity, V_y, localised yielding of the target surface occurs, and at some point beneath the surface (at approximately 0.5a, 'a' is the contact radius), there is a maximum shear stress occurs, according to simple Hertzian contact conditions. As the impact velocity increases, the plastically deformed region below the impact contact area will grow into a finite volume of full plasticity, and this will occur at a critical velocity of V_p.

Using Tresca and Von Mises yield criterion, Mamoun (39), derived the equation for a particle velocity to initiate localise yielding, V_y,

$$V_y = 5.155 \left[\frac{1-q_1^2}{E_1} + \frac{1-q_2^2}{E_2} \right]^2 d_1^{-1/2} Y^{5/2} \qquad \text{.....(45)}$$

According to Tabor (34), the material under the indentation becomes fully plastic when normal load is about 150 times to that load required to initiate yielding. Since, P_y is directly proportional to $V_y^{6/5}$ and P_p is directly proportional to $V_p^{6/5}$, where P_y and P_p are the loads to initiate yielding and for the onset of full plasticity, then

$$V_p = (150)^{5/6} V_y \qquad \text{.....(46)}$$

Hence, from equations (45) and (46) the values of V_y and V_p may be estimated accordingly.

Estimation of Crater Volume by an Impinging Particle.

The volume of displaced material resulting from each impact event is a parameter often used in the modelling of a ductile erosion phenomenon (45). Normally, it can be assumed that the volume of displaced material is equivalent to the volume of strained material. Therefore, in a model which is based on an accumulated strain criterion, a knowledge of how the volume of strained material varies with the impact dynamics is essential. Such information can be obtained from the analysis of single impact tests (45).

Mamoun (39), had derived an expression for estimating the volume of material experiencing full plasticity by using the original analysis by Tabor (34), for quasi-static contact conditions when applied to dynamic conditions, for a perfectly plastic material and ignoring any elastic recovery; and that

$$Q_p = \frac{1}{2}\,\frac{m\,V^2}{p_d} \qquad \text{.....(47)}$$

where Q_p = Volume of material experiencing full plasticity,

m = mass of particle,

V = velocity of particle,

p_d = dynamic flow stress ≈ 8% permanent strain.

If the effect of work-hardening is taken into account, then the true stress - true strain behaviour of the material can be assumed to follow;

$$Y = K e^{n} \qquad \text{.....(48)}$$

where Y = yield stress,
e = strain,
n = work-hardening exponent, and
K = a constant stress that corresponds to 100% strain.

According to Tabor(34), the strain at the edge of an indentation is given by

$$e = 0.2\left(\frac{a}{R}\right) \qquad \text{.....(49)}$$

where a = contact radius,
R = radius of particle.
Thus,

$$Y = K\left[0.2\left(\frac{a}{R}\right)\right]^{n} \qquad \text{.....(50)}$$

If it is assumed that the average flow stress, $P_f = 3Y$, then

$$P_f = 3K\left[0.2\left(\frac{a}{R}\right)\right]^{n} \qquad \text{.....(51)}$$

On these bases, Mamoun (39), derived an expression for a maximum depth of penetration, L_{max}, from the equation of motion of a spherical particle impacting a flat plate as,

$$L_{max} = \left(\frac{1}{2}mV^2\right)\left[\frac{4+n}{(3\pi K\, 0.2^{n})\; 2^{\frac{4+n}{2}} \cdot R^{\frac{2-n}{2}}}\right]^{\frac{2}{4+n}} \qquad \text{.....(52)}$$

and the volume of strained material, Q_s,

$$Q_s \approx \pi R L_{max}^2 \quad \ldots\ldots(53)$$

and therefore,

$$Q_s = \left[\frac{10^{\frac{4n}{4+N}} . (4+n)^{\frac{4}{4+n}}}{2^{\frac{8+6n}{4+n}}}\right] . \left[\pi^{\frac{n}{4+n}} . R^{\frac{3n}{4+n}}\right] . \left[\frac{1}{2} \frac{mV^2}{3P_d}\right]^{\left(\frac{4}{4+n}\right)} \quad \ldots\ldots(54)$$

where n = work-hardening exponent,
m = mass of particle,
V = velocity of particle,
R = radius of particle and
P_d= dynamic flow stress ≈ 8% permanent strain.

For fully work-hardened material, n=0, therefore equation (54) reduces to equation (47).

Modelling the Effect of Impact Angles.

One of the variables that is considered in erosion modelling is the effect of impact has in the metal removal process. In most earlier models (22,23,26,27), the process of erosion was simply idealised into a ductile or brittle erosion process. In real life, this is not the case, and a good erosion model should be able to predict the combination of both ductile and brittle erosion processes. This could be done by considering the behaviour of material failure processes as a function of impact angles.

Nicholls et. al. (45), suggested that, for a normally impacting particle, the erosional damage volume, Q_v, is of the form,

$$Q_v = \frac{1}{2}\frac{m(V - V_y)^2}{3Y} \qquad \text{.....(55)}$$

where m = mass of particle,

V = particle velocity,

Y = yield stress of substrate and

V_y= critical normal velocity of particle to initiate plastic damage in the surface.

For impacts at angles other than normal, an equation of similar form applies, however, V has to be replaced by the normal component of the velocity, V sin α, where α is the impact angle. Therefore, the general form of the equation becomes

$$Q_v = \frac{1}{2}\frac{m(V \sin \alpha - V_y)^2}{3Y} \qquad \text{.....(56)}$$

Further, by considering that the average flow stress at $\alpha = 90°$, $Y_t = 3Y$ as proposed by Tabor(34), and at $\alpha = 0°$, $Y_t = Y$ as in simple tensile tests, it can be assumed that the flow stress behaves in the form $Y_t = (3 - 2\cos\alpha)Y$ with impact angle, α. Therefore, equation (56) can be re-written as

$$Q_v = \frac{1}{2}\frac{m(V \sin\alpha - V_y)^2}{(3 - 2\cos\alpha)Y} \qquad \text{.....(57)}$$

Nicholls et. al. (45), proposed that, for an impacting particle, there exists a critical impact angle, α_y or α_p, below which the normal velocity component is less than V_y or V_p, such that

$$\alpha_y = \sin^{-1}\left(\frac{V_y}{V}\right) \quad , \quad \alpha_p = \sin^{-1}\left(\frac{V_p}{V}\right) \qquad \text{.....(58)}$$

and $\alpha_y < \alpha_p$. They then suggested the following boundary conditions and erosion scenarios to take place;

(a). $\alpha < \alpha_y$,
Only elastic collision takes place and there is no erosional damage to target material.

(b). $\alpha_y < \alpha < \alpha_p$,
Erosion will take place and the volume of material may be removed according to equation (57), and

(c). $\alpha > \alpha_p$,
Erosion will take place and the volume of material may be removed according to the following equation,

$$Q_v = \frac{1}{2}\frac{m}{Y}\left[\frac{(V\sin\alpha - V_y)^2}{(3 - 2\cos\alpha)} + V^2\cos^2\alpha\right] \quad \ldots.(59)$$

Where the term, $1/2\ m(V\cos\alpha)^2/Y$, appears as the tangential contributory component to cause shearing of the plastically strained surface material and causing its removal.

3.1.3 Erosion-Corrosion Theory.

It is usually found that the rate of metal loss in most corroding systems normally falls with time due to the formation of protective scales. The scales either physically hinder the migration of the active environment from the bulk solution to the metal surface or they prevent the migration of cations to the bulk solution i.e. anodic polarisation takes place. In either case, the rate of corrosion is reduced by the protective scales.

When the protective scales are removed continuously by the impingement of liquid droplets or sand particles, the scales break away allowing the active environment to react with bare metal surface, depolarising the anodic sites. If the scale break away is localised, severe corrosion may take place, accelerated by the galvanic interactions between scaled and scale-free sites. If the break away is more general, then a uniform metal loss will be observed depending on the spacial distribution of impacting particles. It is expected that the combination of chemical (corrosion) and mechanical (erosion) processes acting conjointly will produce far more damage (faster metal loss rates) than if each process acts separately (47).

Evans (47) described the process of scale growth and localised fracture in a more simplistic way, as shown in Figure 6(a), (b) and (c) below:

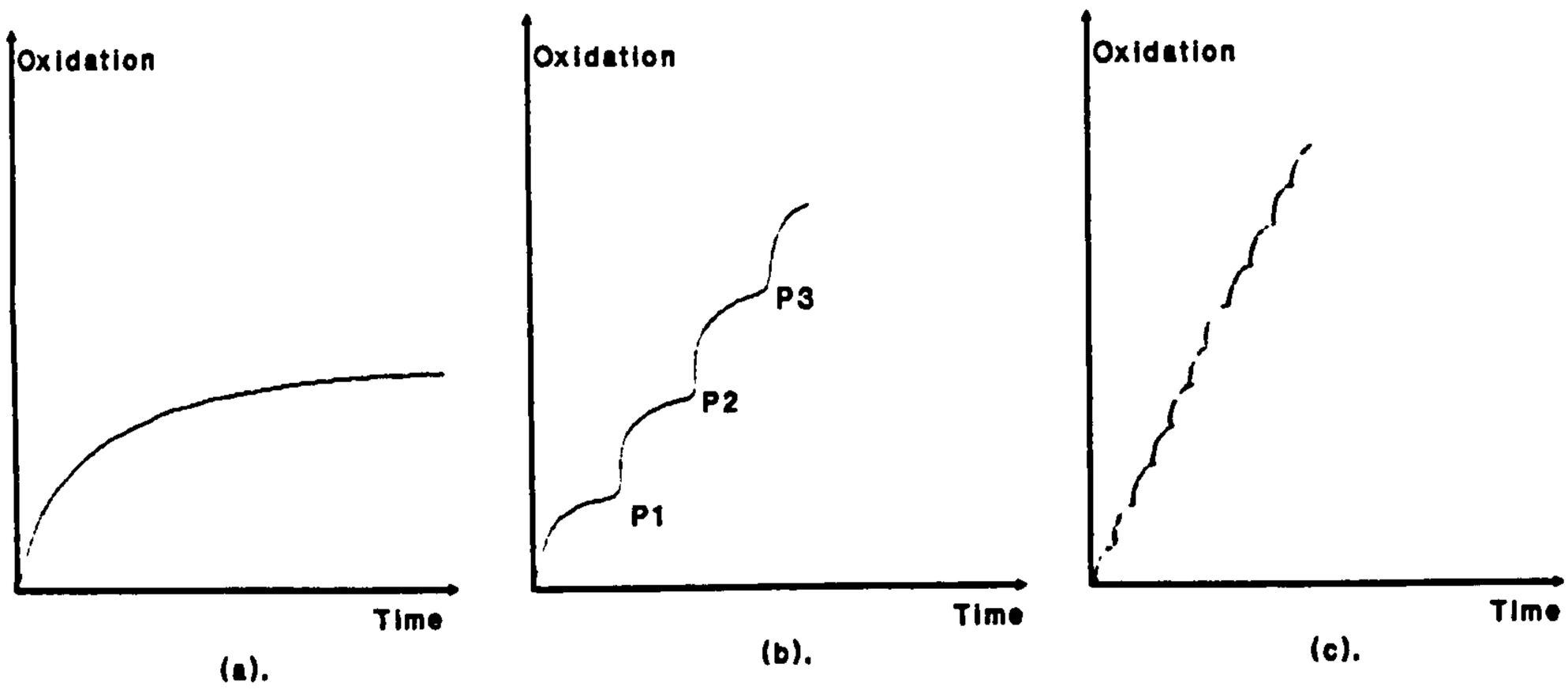

Figure 6. Concept of erosion-corrosion interactions (47).

For corrosion process forming a continuous scale, the rate versus time will be of the form as shown in Figure 6(a). If a series of particles impact on the scale, causing it to fracture and hence expose the metal surface, then corrosion resumed quickly following the initial rate at points P_1, P_2 and P_3 etc.. The metal loss rate will then follow the behaviour suggested in Figure 6(b). When the probability of impact is increased, such as when high particles flux rates are considered and each particle causes damage to the scale, the situation shown in Figure 6(c) may take place. In this case the rate of metal loss versus time approaches a linear rate with a slope approaching to the initial rate in the curve in Figure 6(a).

This argument is general and independent of the nature of the scale. That is, whatever the exact chemical composition of the scale may be, where scale can be removed or rendered non-protective by mechanical means, the resulting erosion-corrosion action will be more rapid and cause greater damage to the metal.

3.2 Erosion-Corrosion Studies.

As pointed out by Evans (47), erosion by solid particles can accelerate the rate of material loss. A number of researchers have performed experiments to investigate the conjoint effects of erosion and corrosion/oxidation in practical applications, with the aim of establishing a predictive tool for use in design and plant performance monitoring purposes(45). Much of these works have focused on high temperature oxidation and erosion from particles derived from coal combustion for coal conversion system (45), chloride shedding in gas turbine operating in a marine environment (49,52), sand ingestion causing erosion of helicopter rotors and turbines operating in sandy desert conditions.

Brijes Vyas (48), conducted a major review of previous erosion-corrosion work and concluded that those studies involve a considerable number of interdependent variables which are peculiar to the types of erosion-corrosion environment in question. The conjoint action of erosion and corrosion may involve such processes as; stress corrosion cracking, corrosion fatigue, fretting as well as the electrochemical processes. The combination of mechanical and chemical modes of attack on the material however, may have some common criteria, such as:

(a). Surface scales: The structure and morphology of surface scales, the kinetics of scale growth, and the mechanical properties of the scales have a large effect on the rate of erosion-corrosion,

(b). Fluid mechanics: The type of flow, (laminar or turbulent) not only controls the rate of mass transport of corrosive and erosive species towards and away from the metal surface, but, at high velocities can generate surface shear

stresses large enough to disrupt the protective scale exposing bare metal to the aggressive environment, and

(c). Particle impact events: The impact of an erosive agent (liquid drop, jet, cavity collapse or solid particles) not only deforms the surface and leads to eventual material loss, but can easily crack and cause the breakaway of soft or brittle surface scale which results in accelerated corrosion at the local exposed areas.

In the modelling of erosion-corrosion processes, some workers have tried to simplify their models by defining erosion-corrosion regimes using either physical, mechanical or thermal properties of the material and scales or by mapping the behaviour of weight loss over temperature of operations. As a result, a number of generic terms such as Substrate Dominated, Scale Modified, Scale Dominated, Erosion Dominated, Erosion-corrosion Dominated, Corrosion Dominated, etc. which describe the regimes have been devised to explain the process taking place in the material/scale/erodent interactions (45,46,53,54,55).

The boundary conditions on erosion-corrosion regimes have been suggested by Stephenson et.al. (53). They are; the Substrate Dominated, Scale Modified and Scale Dominated regimes. In the 'substrate dominated' regime, material degradation is greatly influenced by the erodent/material interaction and the oxidation/corrosion process is found to be insignificant. This regime normally applies when particle loading and velocity are high, and/or the rate of surface scale growth is exceptionally low. In the 'scale modified' regime, there is a gradual increase in the interaction between the erodent and the surface scale. The degree of interaction depends on the physical and mechanical properties of the scale which in themselves depend on the temperature, compositions and thickness, and hence the kinetics of scale

growth. The particle loading also has an effect on the onset of this regime. At a relatively low particle loading, the probability of a particle impacting a given site is low. This allows sufficient time for scale regrowth and removal. When the rate of scale removal is lower than scale regrowth, because of a low probability of particle impact and/or a high scale growth rate, the inception of 'scale dominated' regime is in place. In this situation the erosion rate is determined by the rate of scale erosion rather than the material itself. However, the synergy between the scale growth rate and its removal by erosion may have an overall impact on the total rate of material loss. The boundary between each regime is determined by the 'z/a' ratio, where z is the scale thickness and 'a' is the contact radius of the indentation after impact, which can be predicted assuming Hertzian contact conditions.

Stack et. al. (54), suggested that for high temperature erosion-corrosion, the weight loss regimes could be visualised as shown in Figure 7. They are the Erosion Dominated, Erosion-corrosion Dominated, Corrosion Dominated (Stage I) and Corrosion Dominated (Stage II) regimes. These regimes are said to be established depending on the behaviour of weight loss versus temperature in which the test is carried out. Below T_a, the rate of corrosion may be exceptionally low and thus weight loss due to erosion is predominant and an 'erosion dominated' regime ensues. This is equivalent to the 'substrate dominated' regime as mentioned earlier. As temperature is increased between T_a and T_b, the weight loss rate increases to a maximum value, then the rate of scale growth begin to influence the rate of material loss, then the 'erosion-corrosion dominated' regime is taking place. This could be similar to that of the 'scale modified' regime as mentioned earlier. Between temperature T_b and T_c, the rate of material loss begin to slow down to a much lower value, but the rate of scale growth is increasing

such that the weight loss is influence by the rate of corrosion. Thus this regime is called 'corrosion dominated (Stage I)'. Above T_c, there is no more apparent weight loss, but the rate of scale growth is at its maximum and the properties of the scale are resilient to particle erosion thus, the 'corrosion dominated (Stage II)' regime is taking place. These last two regimes may be similar to the 'scale dominated' regime as mentioned earlier.

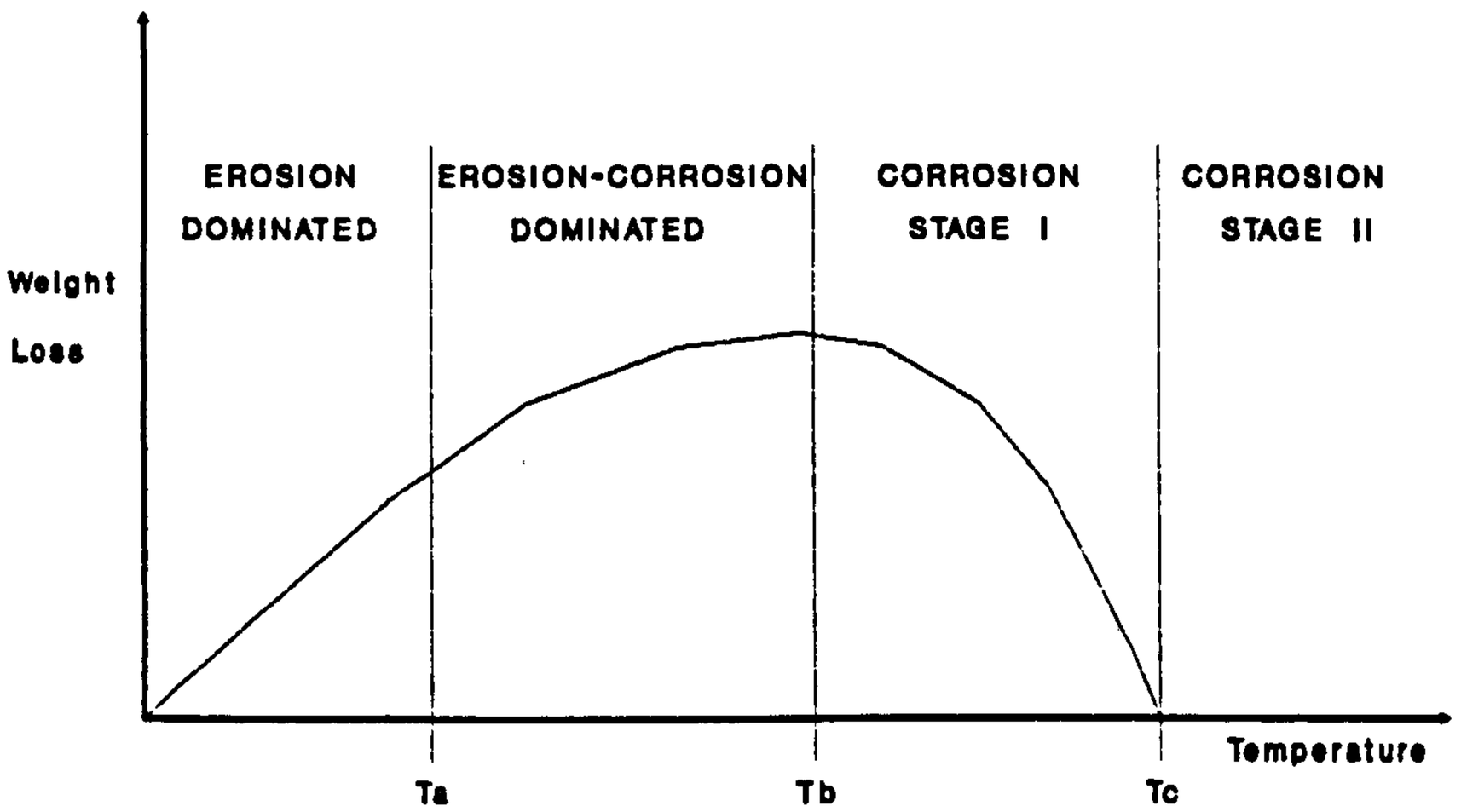

Figure 7. A concept of erosion-corrosion regimes (54).

3.3 Erosion-Corrosion Considerations in Petroleum Production.

In the design of a two-phase flowline, the API RP14E (56) and BS 8010: Part 3 (57), recommend that for sizing criteria in order to avoid erosion problems, the erosional fluid velocity, V_e m/s, may be calculated using the following empirical equation:-

$$V_e = \frac{C}{\sqrt{\rho}} \qquad \ldots\ldots\ldots\ldots\ldots\ldots\ldots\ldots\ldots\ldots (60)$$

where C = the empirical constant,
= 122, for continuous service,
= 152.5, for non-continuous service and
ρ = density of the gas/liquid mixture at operating pressure and temperature, kg/m^3.

These practices generally suggested that if sand production is anticipated the value of empirical constant C should be reduced accordingly.

Engineers have raised concerns over the relevance of the empirical constant C, which many believe to be over conservative. Using the suggested values of empirical constant C in designs may result in over sizing of flowlines and incurring unnecessary costs. Therefore, some researchers have carried out tests to determine the appropriate values of the empirical constant C.

Salama et. al. (58), in the evaluation of API RP14E's erosional velocity limitation for offshore gas wells have suggested that a value of C = 122 is rather inappropriate and over conservative.

They found that material removal by erosion applicable to oil/gas production is due to the combination of the following processes:-

i). Cavitation (formation and collapsing of bubbles),
ii). Liquid particle impingement and
iii). Solid particle impingement, eg. sand.

Material removal is due to the following mechanisms:-

i). Fatigue failure due to repeated loads induced by bubble collapse or particle impingement,
ii). Abrasion/cutting processes due to repeated impingement of hard particles at an angle on the surface of a ductile material, and
iii). Corrosion assisted erosion (erosion-corrosion) due to breakage of the protective surface scale either by fatigue or abrasion.

In their examination, they calculated the empirical constant C to vary from 365 to 40,000 based on pressure drop calculations and the limiting velocity before any surface inhibitor film could be stripped off, respectively. These values are applicable for liquid impingement only (i.e. sand -free situation). Based on most offshore process piping design criteria, the limiting velocity of 30 m/s, is not commonly encountered in the field, but erosion is still apparent and does take place. The most likely cause of this is erosion by sand particles entrained in produced fluid. API RP14E does not explicitly cater for sand particle erosion.

In order to consider the effects due to sand particle erosion, Salama et. al. offer a quick velocity limitation calculation for a design erosion rate of 0.254 mm/y at 90° bends and T-Connections as follows:-

$$V_e = 630 \times 10^{-3} \frac{D}{\sqrt{M}} \quad \text{.....(61)}$$

or alternatively, for a maximum allowable sand production rate of M kg/s, at a design erosion rate of 0.254 mm/y, the equation can be rewritten as,

$$M \approx 0.4 \frac{D^2}{V_e^2} \quad \text{.....(62)}$$

where V_e = Fluid and particles average erosional velocity, (m/s),
D = Diameter of pipe, (m) and
M = Mass of sand produced, (kg/s).

They developed the above equation (61) by using Robinowicz's model (63) that states,

$$Q = \frac{K\,(C\,W)\;V^2\,\beta}{P} \quad \text{.....(63)}$$

where Q = volume of metal eroded, m^3/s,
M = mass of sand produced, kg/s,
C = a fraction of mass of sand produced that is effectively striking the surface and causing erosion (values between 0.4 for oil well and 0.7 for gas well were suggested). In their calculation to arrive at equation (61), C=0.65 was used for a two phase flow,
V = velocity of the fluid flow,
β = a coefficient dependent on impact angle. A value of 0.75 was used in the calculation for a fully developed flow around a short-radius 90° bend,

K = a dimensionless erosive coefficient. A value of 0.71 was used for a producing well system,

P = Penetration hardness of target materials, a value of 1069 MPa was used for steels.

Following a similar approach but treating the velocity exponent n=2.5, Oudeman (59), proposed a slightly modified expression to calculate the allowable fluid velocity as,

$$V = 2.\left(\frac{D^2}{M}\right)^{0.4} \qquad \text{.....(64)}$$

or alternatively the limit of sand production should satisfy the following equation,

$$M = 2.\left(\frac{D^2}{V^{2.5}}\right) \qquad \text{.....(65)}$$

All symbols used in equations (64) and (65) have similar meaning as those in equations (61) and (62).

From here there are many other reports considering the effect of the presence of sand in the petroleum production and the design consideration towards a safe design velocity of the petroleum fluid in pipes (60,61,62). In most of these reports the authors were basically using criteria such as individual field experience and suggestions made from limited laboratory data, and with the idea to devise a guideline for quick decision making in the design of pipelines. In most cases the engineers are still strongly guided by the guidelines as stated in the API RP14E/BS8010 Part 3, with some degree of factor of safety added for sand bearing fluid conditions in their design.

To-date there has been no real effort made to study and understand the mechanisms of erosion-corrosion interactions that are applicable to petroleum production. It is believed that only with the proper understanding of these mechanisms then any predictive model will be as good as the any other, until they are proven otherwise. Therefore, it was hoped that with this work the gaps that still exists can be bridged and that a sound life prediction tool and design basis could be derived.

CHAPTER 4

Experimental Details

CHAPTER 4

4. EXPERIMENTAL DETAILS.

Two types of experiments were conducted, firstly to establish the baseline corrosion behaviour of the materials exposed to wet CO_2 gaseous environment and secondly to study the erosion and erosion-corrosion behaviour of the materials under dry (erosion only) and wet CO_2 environment (erosion-corrosion). The erodent used was a graded commercial sand.

4.1 The Materials.

Two groups of materials were used throughout the experiments. They were the carbon-manganese steels and the corrosion resistant alloys, typically used in the oil and gas field operations. Selection of the materials was based on (a) ease of availability, and (b) cost. A total of seven materials were used in the experiments, and a summary of the composition of each material is shown in Table 1.

Table 1. Materials specification.

Materials	Class	Compositions (%) (NB. The balance is Fe)										
		C	Mn	Cr	Nb	Mo	S	Ni	Cu	Ti	Al	P
1.X52	C-Mn	.3	1.3	-	-	-	.05	-	-	-	-	.04
2.X65	C-Mn	.26	1.4	-	-	-	.05	-	-	-	-	.04
3.L80	C-Mn	.4	1.9	-	-	-	.06	.25	.35	-	-	.04
4.N80	C-Mn	.42	1.66	-	-	.02	.014	.02	.001	.001	-	.01
5.L80/13Cr	CRA	.2	.5	13	-	-	.01	-	-	-	-	.02
6.In625	CRA	.05	-	21.5	3.6	9	-	61	-	.2	.2	-
7.Ferr255	CRA	.01	1.16	25.4	-	3.1	.01	5.8	-	-	-	.02

The physical properties of the materials are summarised in Table 2. The average hardness of each material was determined using a Vickers hardness machine under a 30 Kg. load.

Table 2. Physical properties of the materials.

Materials	σTensile (MPa)	(Ksi)	σYield (MPa)	(Ksi)	El %	W/harden-ing exp (n).	Vicker's Hardness, (Hv).	Density (g/cc).
1. X52	455	66	359	52	24	0.05	162	7.80
2. X65	531	77	488	65	22	0.04	180	7.80
3. L80	689	100	552	80	20	0.037	240	7.64
4. N80	655	95	552	80	20	0.048	298	7.80
5. L80/13Cr	655	95	552	80	20	0.037	246	7.66
6. In 625	855	124	490	71	50	0.10	286	8.39
7. Ferr255	769	112	494	72	37	0.09	263	7.73

The materials were cut into trapezoidal shaped specimens of 6 mm. x 8 mm. x 10 mm. standard size to suite the specimen holder for the centrifugal erosion rig.

4.2 Baseline Corrosion Experiments.

Each specimen was carefully marked with an engraver, spark-eroded to make a hole of approximately 1 mm diameter using a 1 mm copper wire electrode across one end. One side of the specimen was carefully abraded using emery paper and successively polished down to 6 μ surface finish using 6 μ diamond paste on cloth. The polished surface formed the baseline for corrosion measurements. Each specimen was ultrasonically cleansed in a gramosol bath and rinsed with propanol to remove any grease and blow-dried. The initial weight of each specimen was taken carefully using a

microbalance and its thickness was measured at random at 12 locations across the surface using a digital micrometer.

Each specimen was attached to a specially constructed holder made of 316 SS by 0.6 mm diameter nylon fishing line, to avoid any metal-to-metal contact between specimens and the holder. The specimens were arranged such that each type of material was present at each level. There were six levels (see Figure 8) altogether in order to accommodate six different exposure times for a series of experiments. This arrangement was adopted in order to make the process of removal of each set of experimental exposure easier as discussed later. The whole assembly of specimens was lowered carefully into an autoclave whose temperature profile was previously determined to ensure that the specimens were at approximately the same temperature for any set of experiments.

The specimens were placed in the autoclave as shown in Figure 8, and then heated to a selected temperature using the autoclave furnace. CO_2 gas was fed in through the atomizer gas inlet until the autoclave pressure reached approximately 0.5 bar(g). Water, which was obtained from the water mains, was fed in simultaneously with the atomizer power switched on. The required temperature for the experiment was achieved by striking a balance between the temperature of the autoclave furnace, the rate of flow of water through the atomizer and the rate at which water was drained from the bottom of the autoclave. The pressure of the autoclave required for the experiment was achieved by adjusting the CO_2 gas feed pressure regulating valve, the water inlet pressure valve and the outlet pressure valve manually.

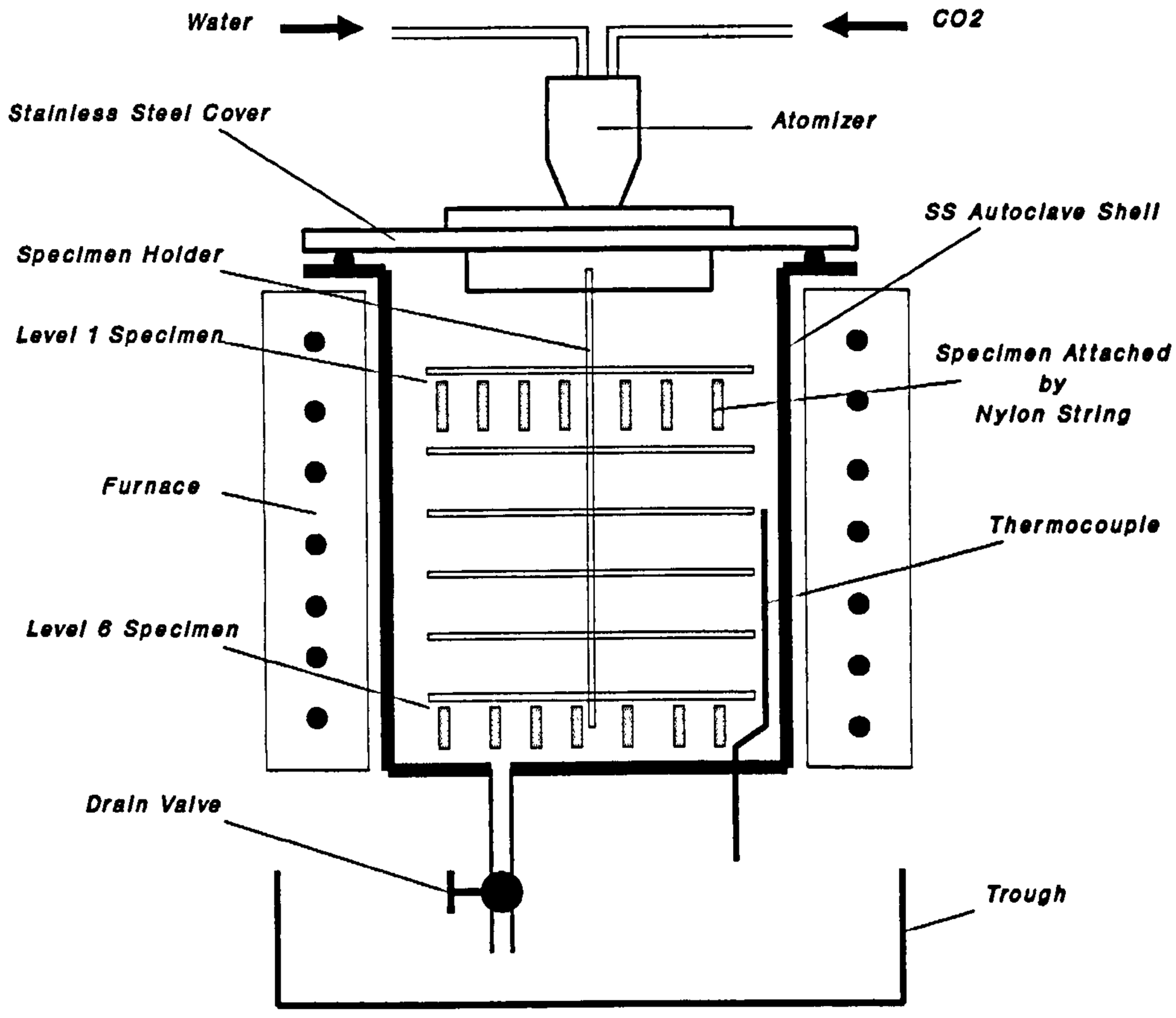

Figure 8. The Autoclave for corrosion experiments.

Experiments were performed at 80°C for the complete set of specimens, and then repeated for a few specimen only at 100°C and at 20°C. The experiments were performed simultaneously for 20 hours (level 1 specimens), 60 hours (level 2 specimens), 100 hours (level 3 specimens), 200 hours (level 4 specimens), 300 hours (level 5 specimens) and 500 hours (level 6 specimens) exposures. The specimens were taken out stage by stage after each exposure time had been

reached, oven-dried and weighed. Then the thickness at 12 locations chosen at random were measured and the average value was determined. Any change in weight and thickness after each experimental exposure was recorded.

Each specimen was spliced into approximately two equal halves along its length and one half was mounted in a conductive bakelite and polished carefully. They were then examined using an optical microscope and/or SEM for any scale that might have been formed, and an estimate made of its thickness. Photo-micrographs of the surface and cross-sections were taken as necessary.

4.3 Sand Selection for Erosion Modelling.

Some 15 sand samples were collected from 15 different oil and condensate wells of 4 different fields typical of producing sand from Baram Delta Operations, an area jointly operated by PETRONAS Carigali Sdn. Bhd. and Sarawak Shell Berhad, offshore Malaysia. The sand samples were examined to assess their size distribution using Malvern Particle Sizer 2600 Series; density and hardness were measured, and their shapes were examined using an optical microscope. The hardness was measured using a Vicker's microhardness machine.

In order to generate erosion results comparable to those in the field, it was considered important to use a graded commercial sand with similar characteristics to those found in the field. The properties of a commercially available sand were therefore studied carefully and compared with the field produced sand. To confirm that the commercially available sand would give similar erosion and impact damage on the materials as that of the sand obtained from the wells, a series of single impact experiments was

carried out using both sands and their results, such as the shape and crater volume distribution, were compared.

4.4 Single Impact Experiments.

A single impact gas gun, set up such as shown in Figure 9 was used in this experiment. A series of characteristic curves as shown in Figure A1 of Appendix A, was established for selected sand sizes to help estimate the average particles velocity before impact at a specific gas pressure. Nitrogen gas was used to accelerate the sand particles along a 66 cm length of 2.5 mm diameter barrel throughout the experiments. Details of the procedure for generating the characteristic curves are given in Appendix A.

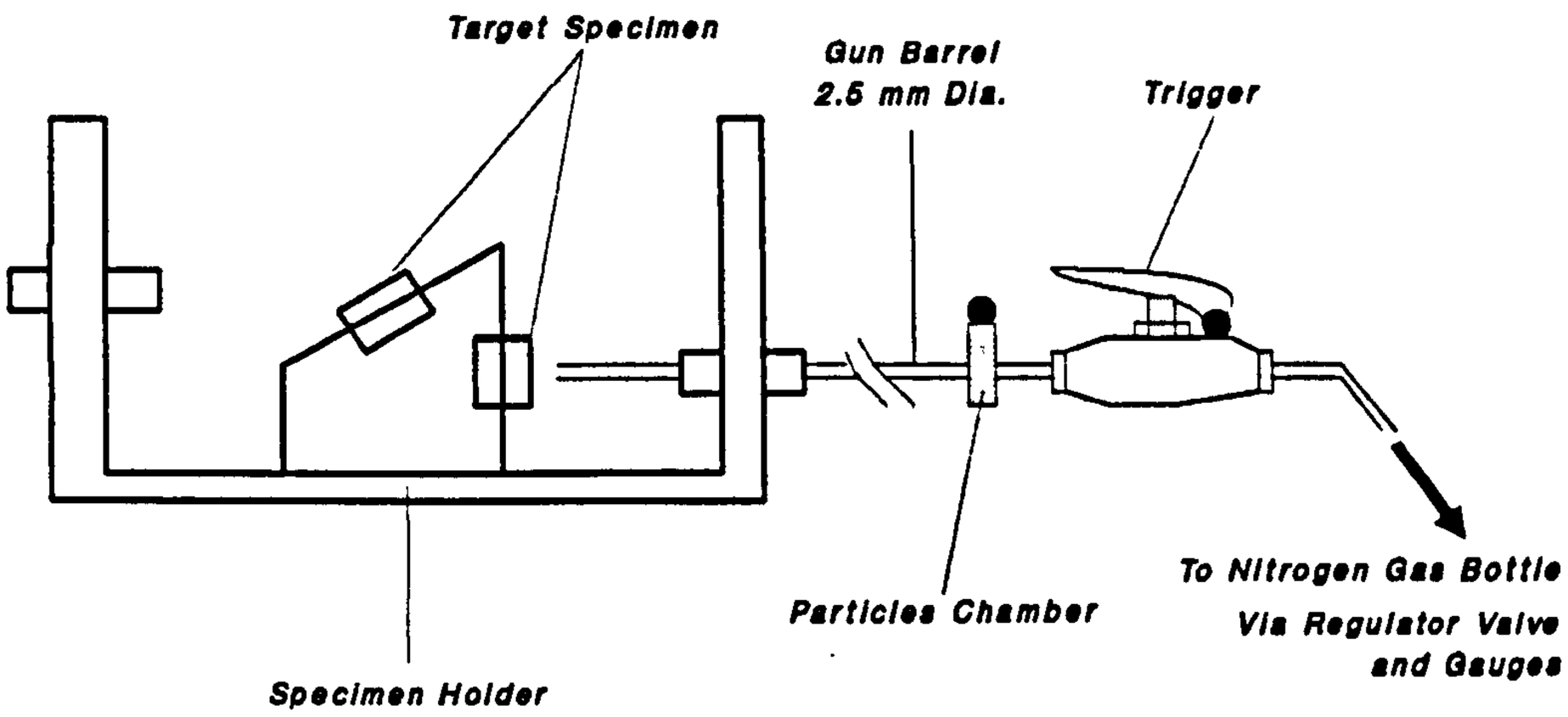

Figure 9. Single impact Gas-gun.

Using the values obtained from the characteristic curves in Figure A1 of Appendix A, the regulator valve setting corresponding to a given nitrogen gas velocity was selected by allowing the gas to flow under stable conditions, across a pitot tube connected to the end of the gas gun barrel. The gas gun trigger was depressed and held in position by a wire ring. A mercury manometer was used to determine the difference between the static and the dynamic pressure across the pitot tube created by the flowing nitrogen gas. Hence the average particle velocities were quickly obtained in this manner. Approximately 50 - 100 sand particles were placed in the chamber and the key was secured tightly in place. A specimen, which had been carefully prepared and weighed was securely placed on the holder, one at a time for each single impact experiment. The trigger was depressed sharply and held in position for 3 - 4 seconds allowing the nitrogen gas to accelerate the sand particles along the barrel hence causing the sand particles to impact on the specimen surface at the required velocity. To ensure consistency in the experimental conditions for all specimen materials, all of the experiments for different materials were performed at the same pressure-regulating-valve setting, which thus gave the same average particle velocity.

All of the seven types of material specimens were tested at average particle velocities of 50 m/s, 80 m/s, 100 m/s and 150 m/s. The specimen holder was designed to hold the specimen at two impact angles of 90° and 30°. All experiments were performed at a room temperature of 20±2°C.

Following the experiment, each specimen was re-weighed carefully using a microbalance and its value recorded to determine the metal loss due to the impact. As craters were formed as a result of the particle impacts, some 24 crater volumes were randomly estimated using the Joyce Loeble's

Particle Image Analyzer. The procedure for estimating the crater volumes is described in Appendix B.

4.5 Erosion and Erosion-Corrosion Experiments.

4.5.1 Baseline Erosion Experiments.

Erosion experiments were performed in a Centrifugal Erosion-Corrosion Rig as shown in Figure 10. Initially, a series of erosion experiments were conducted, (a) to establish the baseline erosion rates of the materials under non-corrosive environment, i.e. under dry environment, and (b) to study the repeatability of results produced by the centrifugal erosion rig. In these experiments, 4 sets of material specimen could be placed on a specimen holder at 5 different impact angles, namely; 15°, 30°, 45°, 60° and 90°. Thus, during any one experiment a total of 20 specimens could be tested.

The hopper was first calibrated to determine the feed rate corresponding to various extruder rotational speed setting. Details of the calibration procedure are described in Appendix C. A range of sand flux rates was chosen throughout these experiments. They were at 0.5, 0.1, 0.05 and 0.01 g/mm^2/h. These flux rates were chosen as the likely rates of sand produced in petroleum production practices. Details are described in Appendix D.

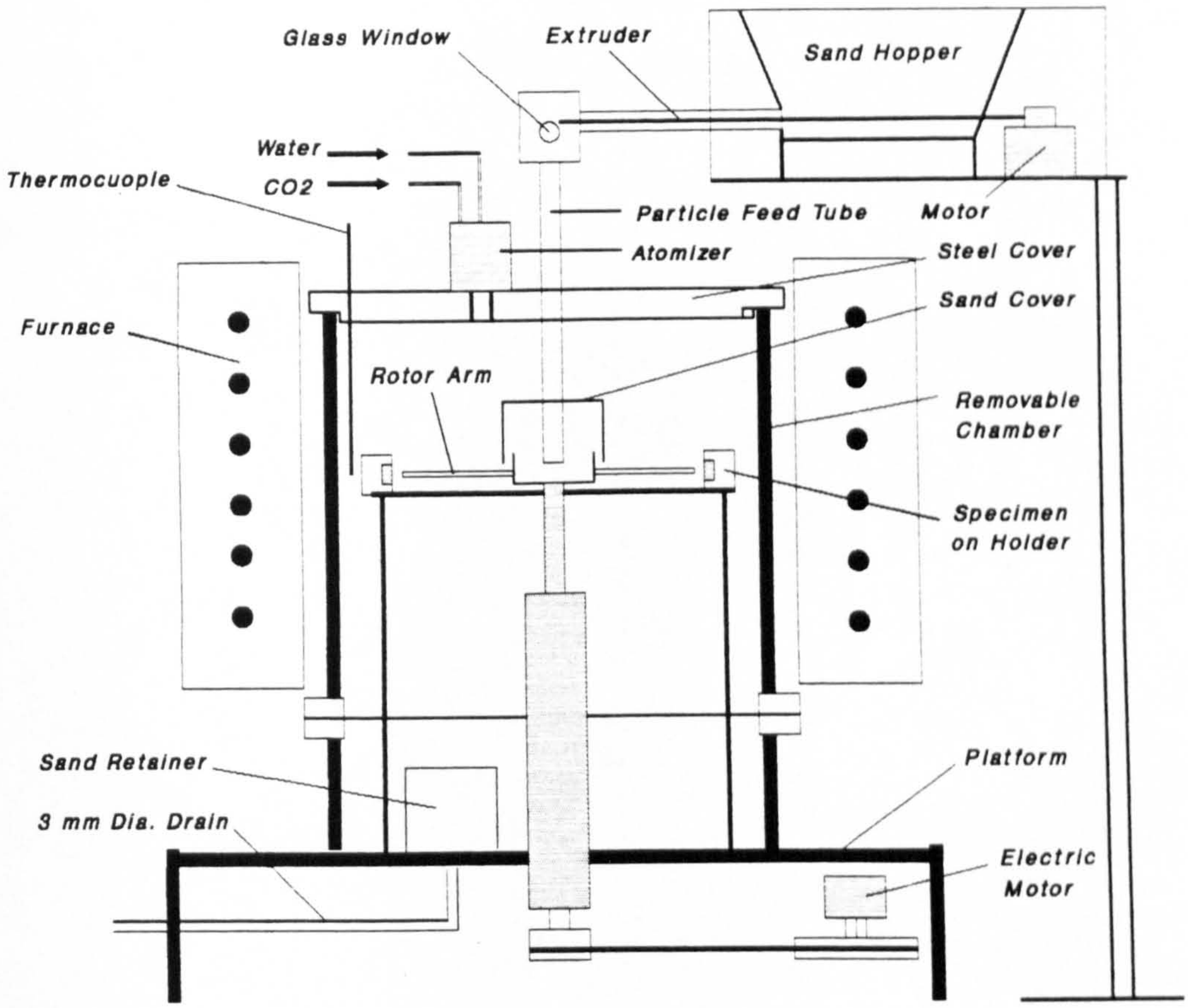

Figure 10. Centrifugal Erosion-Corrosion Rig.

Sample Tagging System.

All specimens were first carefully marked to show the material type and numbered in series by using an engraver. The same set of specimens were used for the same sand flux chosen for the experiments at the same impact angles. For example, specimens of X52 material Nos. 1 - 5 were used for the experiments at sand flux of 0.5 g/mm^2/h; of which specimen No.1 for 15° angle, No. 2 for 30° angle, No. 3 for 45° angle, No. 4 for 60° angle and No. 5 for 90° angle. Subsequently, specimens Nos. 6 - 10 were used for the experiments at sand flux of 0.1 g/mm^2/h at angles of impact of 15° - 90° respectively; similarly for specimens Nos. 11 - 15 were for sand flux of 0.05 g/mm^2/h and specimens Nos. 16 - 20 were sand flux of 0.01 g/mm^2/h at the respective angles of impact. A similar numbering system was used for all of the other materials in these experiments. It is important to mention here that the same set of specimens were used repeatedly for different velocities of impact as well as for erosion-corrosion experiments in order to save the manufacturing time and cost. Experiments were carried out at average particle velocities of 50 m/s for all of the sand fluxes and for sand flux of 0.05 g/mm^2/h erosion and erosion-corrosion experiments were also carried out at average particle velocities of 20 m/s, 80 m/s and 150 m/s. Two test temperatures were chosen for the experiments, namely 20°C and 80°C.

Sample Cleaning.

Prior to the starting up of each experiment, all specimens were degreased in iso-propanol and blow-dried. They were carefully weighed using a microbalance and their weights recorded in a log book. The specimens were then carefully placed on the specimen ring holder making sure that

the correct numbering sequence for the correct impact angle as marked on the ring holder. There were a maximum of 4 sets of material specimens that could be placed on the ring holder for any one experimental run. The ring holder with the specimens on was then mounted into the erosion test rig and secured by using steel pins. The lid of the erosion test rig was then placed with the particle feed tube attached to the outlet of the hopper carefully aligned with the receiver cup of the rotor. It was important to make sure that the hopper switch box properly set for the correct sand flux rate, the hopper and its extruder were filled with dry sand such that when the motor was switched on the sand was immediately fed into the rotor cup and test could start immediately. The test exposure time varied, depending on the sand flux rates; normally about 5 hours for 0.5 flux, 15 to 20 hours for 0.1 flux, 20 - 30 hours for the 0.05 and 0.01 fluxes.

After the experiment was completed all specimens were taken out, ultrasonically cleaned to remove loose debris for about 30 - 40 seconds, rinsed with iso-propanol and blow-dried. Each specimen was weighed again and any weight change was noted in a log book. The rate of metal loss (erosion) was then calculated. Details of the erosion rate calculations are described in Appendix E.

4.5.2 Erosion-Corrosion Experiments.

The erosion rig was modified to enable it to operate in a wet operating environment. The same rig was used as in the erosion experiments, as schematically shown in Figure 10, incorporating all of the modifications to suite for wet operating conditions. The following modifications were carried out on the erosion rig:- (a) An atomizer was placed on top of the chamber securely screwed onto a steel cover

plate, (b) A sand cover made of steel cup was snugly fitted at the end of the particle feed tube to prevent water droplets from wetting the sand in the rotor, (c) A 3 mm. diameter drain tapping was fitted at the base of the chamber, to drain water collected in the chamber during wet tests, and (d) A sand retainer was placed over the drain outlet, to prevent sand particles from blocking the drain. This sand retainer was made up of a 50 mm. diameter steel tube, closed at the top and grooved at base to allow water to pass through. With all of these modifications in place, the erosion rig could operate either in wet or dry environments.

The same sets of specimens were used again in these erosion-corrosion experiments. Experiments were again performed at average particle velocities of 50 m/s at two test temperatures of 20°C and 80°C for all of the sand fluxes. For sand flux of 0.05 g/mm^2/h, experiments were also performed at average particle velocities of 20 m/s, 80 m/s, and 150 m/s and at a temperature of 20°C. The same sand flux ranges (0.5, 0.1, 0.05 and 0.01 g/mm^2/h) were chosen so that the effects of erosion and corrosion could be compared directly with those of pure erosion experiments.

To start an experiment, the specimens were placed on the ring holder, in a proper order of impact angles, which was then placed on its support in the erosion rig. The metal cover was placed on top and clamped securely. The furnace was put in place and switched on. The top portion of the test chamber above the lid was lagged both to prevent heat loss and to protect the atomizer. The atomizer was switched on, the water supply valve was slowly opened and the CO_2 gas pressure regulator valve was opened such that it created a positive pressure above the atmosphere. As the erosion rig was only designed to operate at atmospheric pressure, the CO_2 gas regulator valve was opened such that the outlet pressure indicator was limited to no more than about 0.5

bar(g) pressure. It also helps to ensure that the rate of CO_2 gas utilisation was optimised. The rig control unit was switched on, the erosion rig rotor was gradually regulated to reach the required speed of rotation (RPM) and a time was allowed to enable the temperature for the test to establish. This process normally took approximately one hour. Once the rig had reached thermal stability, the hopper switch box set at the appropriate setting for the correct sand flux rate, the sand was fed into the test rig by switching on the hopper motor switch and the time of exposure started at this point. As before, the exposure times varied according to the sand flux rates.

Once a test exposure completed, the rig was switched off and allowed to cool down for up to two hours and then the specimens were removed, cleaned and dried before each individual piece was weighed and any weight loss recorded in the log book. The rate of metal loss due to erosion and corrosion was then calculated. Details of the calculation of the erosion-corrosion rates are described in Appendix E.

A summary of the erosion and erosion-corrosion experiments performed is shown in Table 3.

Table 3. Summary of erosion and erosion-corrosion experiments performed.

	Sand Flux, g/mm²/h.			
Vp, m/s.	0.5	0.1	0.05	0.01
20	None	None	. Dry Atm. @ 20°C. . Wet CO_2 @ 20°C.	None
50	. Dry & Wet Atm. @ 20°C. . Dry CO_2 @ 20° & 80°C. . Wet CO_2 @ 20° & 80°C	. Dry Atm. @ 20°C. . Wet CO_2 @ 20° & 80°C.	. Dry Atm. @ 20°C. . Wet CO_2 @ 20°& 80°C.	. Dry Atm. @ 20°C & 80°C. . Wet CO_2 @ 20°C & 80°C.
80	None	None	. Dry Atm. @ 20°C. . Wet CO_2 @ 20°C	None
150	None	None	. Dry Atm. @ 20°C. . Wet CO_2 @ 20°C.	None

4.6 Surface Morphology Studies by SEM.

The morphology of the surfaces of the specimens after the erosion and erosion-corrosion experiments were examined using an ABT-55 Scanning Electron Microscope. Any variations observed due to different angles of impact were also noted.

4.7 Identification of Corrosion Scales.

The corrosion scales formed on the specimens, following the corrosion and erosion-corrosion experiments, were examined using, (a) X-ray Diffraction and (b) Auger X-Ray Photo Electron Spectrometer (XPS) Techniques.

The X-Ray Diffraction studies were only performed on scales produced in the corrosion experiments, as only the specimens from the corrosion experiments had generated sufficient scales for XRD examination. The Auger surface analysis was performed on the specimens from the corrosion and the erosion-corrosion experiments.

CHAPTER 5

Results

CHAPTER 5

5. RESULTS.

5.1 Corrosion Experiments.

Typical weight loss/gain obtained from the corrosion experiments are shown in Table 4.

Table 4. Typical results obtained from corrosion experiments.

X52	20h	60h	100h	200h	300h	500h
Orig. Wt.(g)	3.41851	3.38941	3.42407	3.41735	3.39912	3.42732
Wt.After.(g)	3.41848	3.38961	3.42446	3.41719	3.39712	3.42721
Wt.Change(g)	-0.00002	0.00020	0.00039	-0.00016	-0.00200	-0.00011
% Change	-0.00059	0.0059	0.0114	-0.0047	-0.0588	-0.00321
IN625	20h	60h	100h	200h	300h	500h
Orig. Wt.(g)	3.66359	3.71300	3.68010	3.68754	3.60546	3.59409
Wt.After.(g)	3.66358	3.71299	3.68009	3.68753	3.60545	3.59399
Wt.Change(g)	0	0	0	0	0	0
% Change	0	0	0	0	0	0

Other samples of C-Mn steels show a similar trend to X52 steel, and the results of other corrosion resistant alloys, exhibit similar trends to that of the IN625.

There was no significant change in the overall thickness measured before and after the corrosion tests using the micrometer, for each of the specimen. The same was found for the weights of all of the specimens. Sample records of thickness measurements made before and after the tests are shown in Appendix G, Item G1, (a)-X52 and (b)-IN625.

However, by using the SEM, the following scale thickness were estimated to have been formed at 80°C on the surfaces of the specimens, see Table 5.

Table 5. Scale thickness variations with time at 80°C.

Material	t, Hours.	$t^{1/2}$, $(Hours)^{1/2}$	Scale Thickness, µm
1. X52	0	0	0
	60	7.7	1.5
	100	10	2.5
	500	22.4	5.0
2. X65	0	0	0
	60	7.7	1
	100	10	1.5
	500	22.4	3
3. L80	0	0	0
	60	7.7	1
	100	10	1.5
	500	22.4	3
4. N80	0	0	0
	60	7.7	1
	100	10	1.5
	500	22.4	3

The scales were found to grow with time, with a scale thickness variation being directly proportional to $t^{1/2}$ for X52, X65, L80 and N80, as shown in Figure 11. These confirm that the Scale Growth Kinetics are parabolic and for X52, the parabolic growth rate constant, $K_p \approx 50 \times 10^{-3}$ µm²/h, and those of the X65, L80 and N80 $K_p \approx 18 \times 10^{-3}$ µm²/h formed at a temperature of 80°C. No scale thickness could be estimated from the IN625, L80/13Cr and Ferrulium 255 specimens because they were so thin.

Figures 12(a) and (b), show photo-micrographs of the scale formed on X52 steel after 20h and 100h exposure; and Figures 12(c) and (d) are the cross-sections showing the scale thickness formed on the surface of X52 specimen after 100h and 500h exposure, respectively.

The wet scales formed on the surface of the specimens were soft and could easily be removed by scraping them with a soft material such as a piece of cloth or wooden spatula.

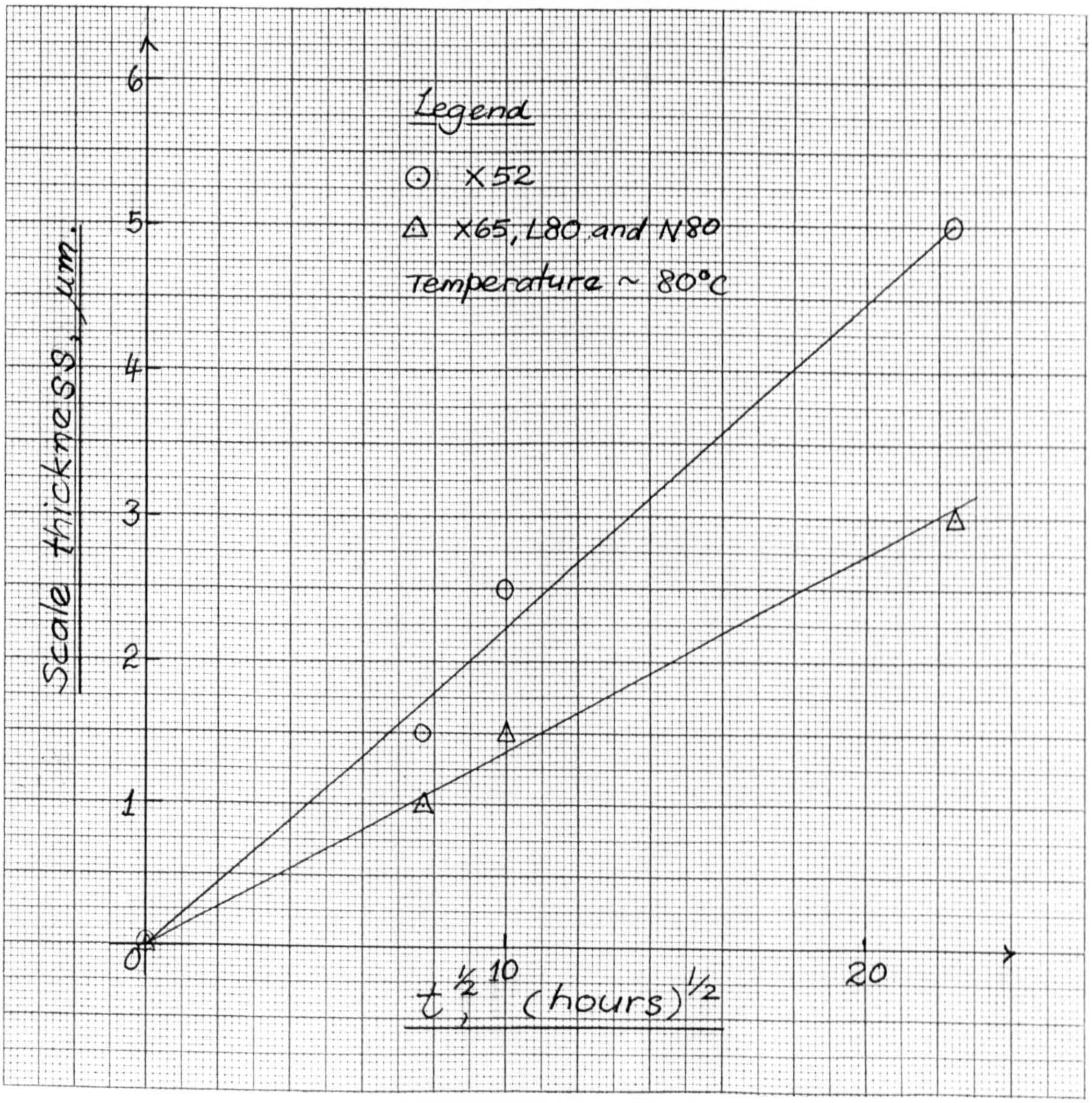

Figure 11. Scale thickness variations with $t^{1/2}$.

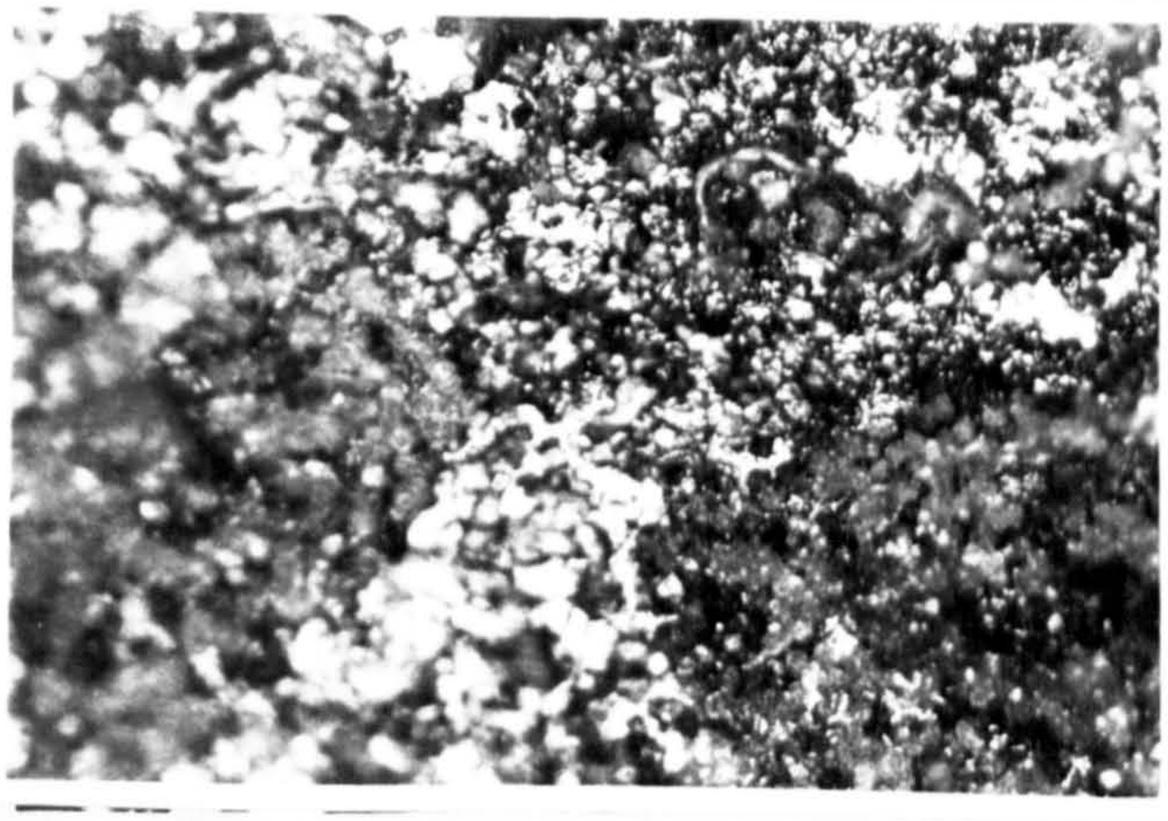

Figure 12(a). Scale formed on a C-Mn steel after 20h exposure (30x).

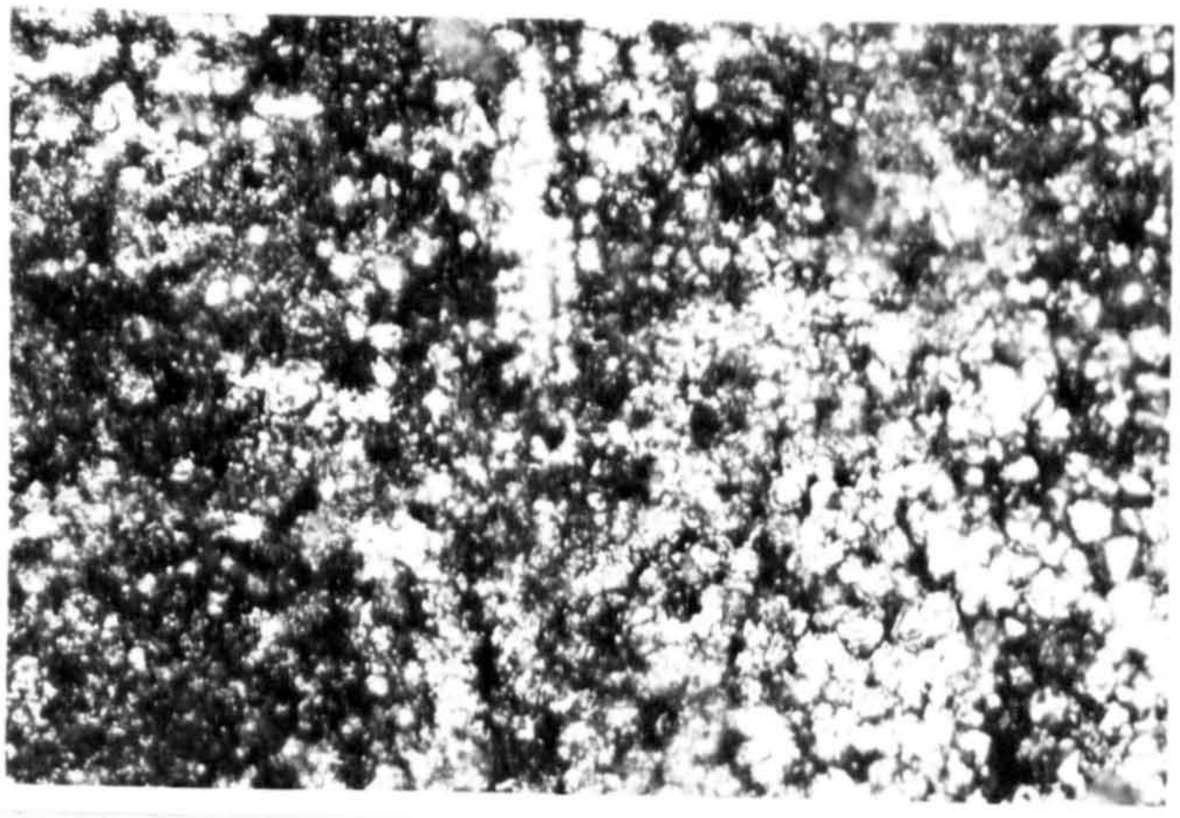

Figure 12(b). Scale formed on a C-Mn steel after 100h exposure (30x).

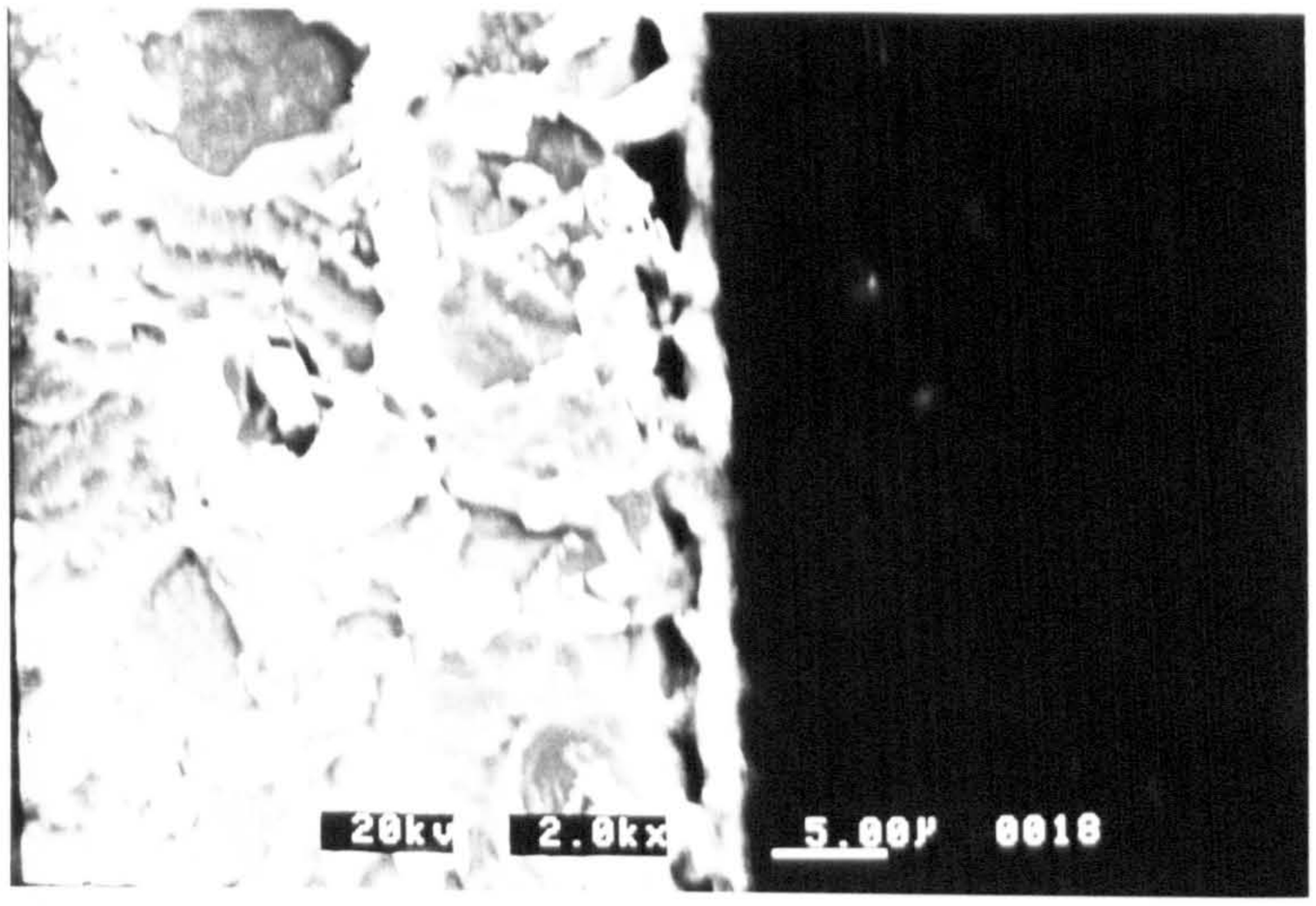

Figure 12(c). Scale thickness formed on a C-Mn steel after 100h exposure (etched for 4 min. in 10 Nital).

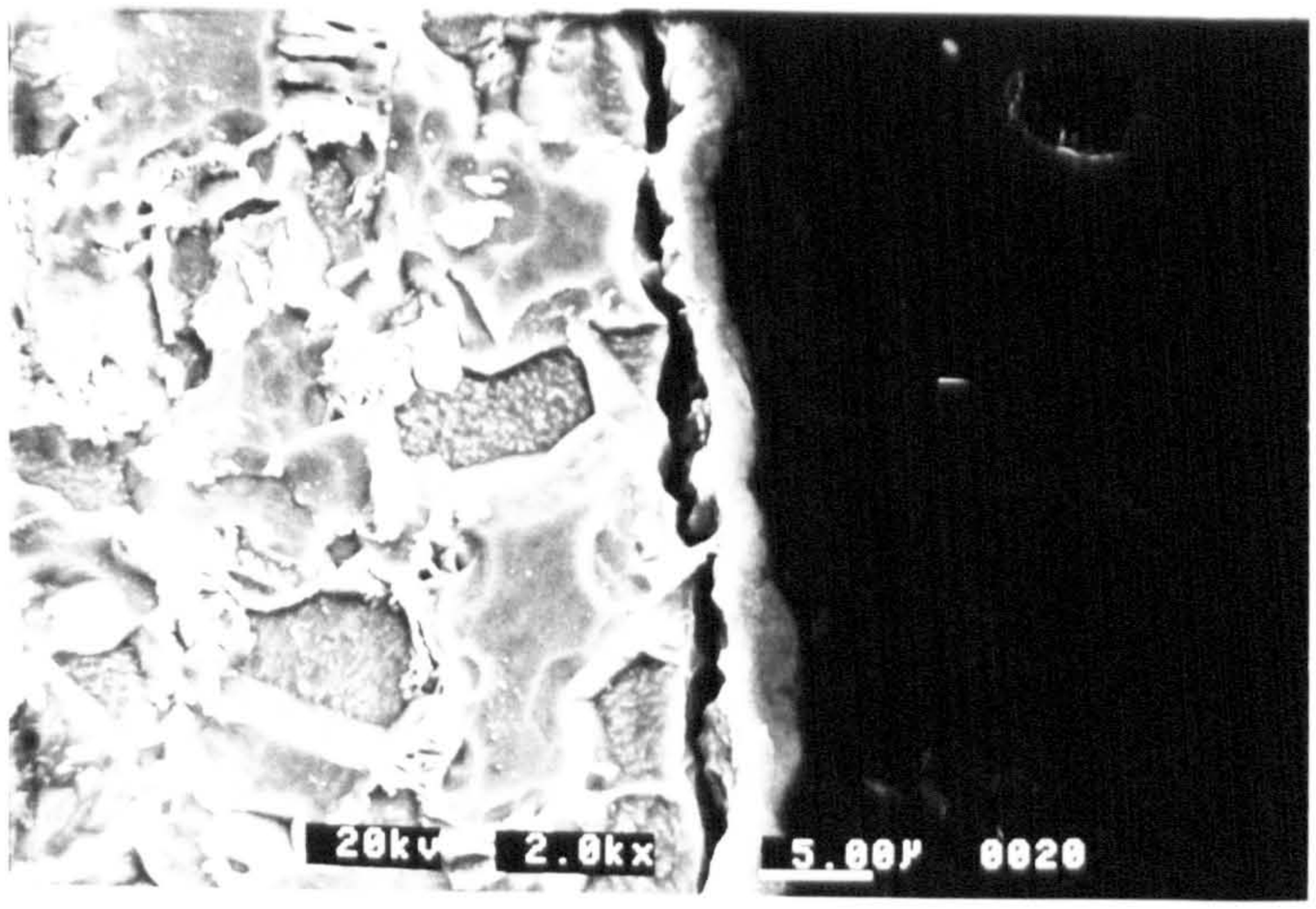

Figure 12(d). Scale thickness formed on a C-Mn steel after 500h exposure (etched for 4 min. in 10 Nital).

5.2 Properties of Field Sands.

Some 15 sand samples were collected from different wells in the area and typical size distributions of two of the samples are shown in Figure 13. A typical field sand has size ranging from 50 to 300μm with a mean size of 200μm and a standard deviation of 80μm. They can be grouped into two main shapes as shown in Figures 14(a) and (b). For the purpose of this modelling they were assigned a shape factor of 0.6; see Appendix G, Item G2, for details of calculation for shape factor. Their densities were found to have an average value of 2.63 g/cc. The micro-hardness of the sand grains was found to be in the region of 9.0 GPa(Hv).

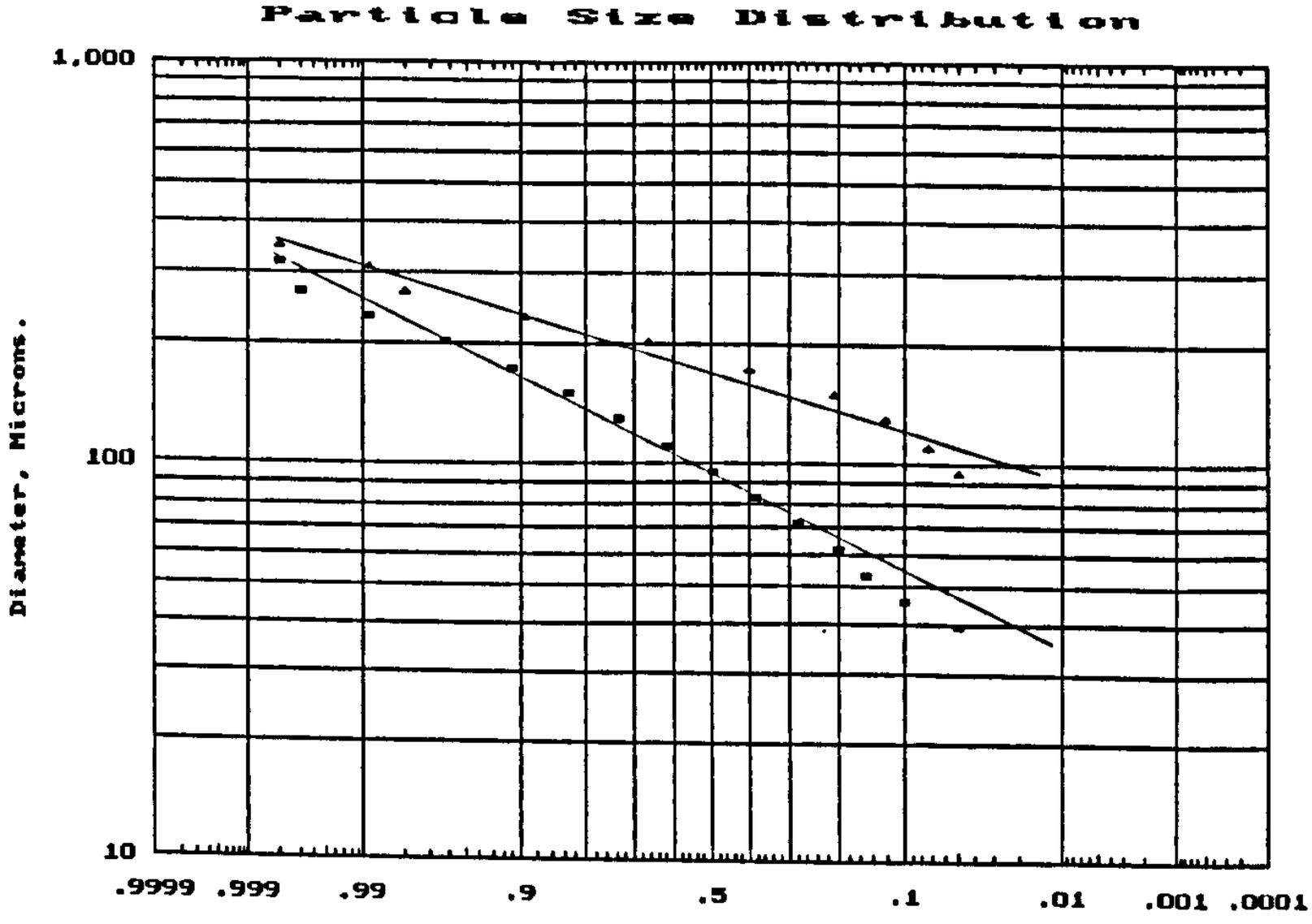

Figure 13. Typical field sands size distribution (Only 2 samples are shown).

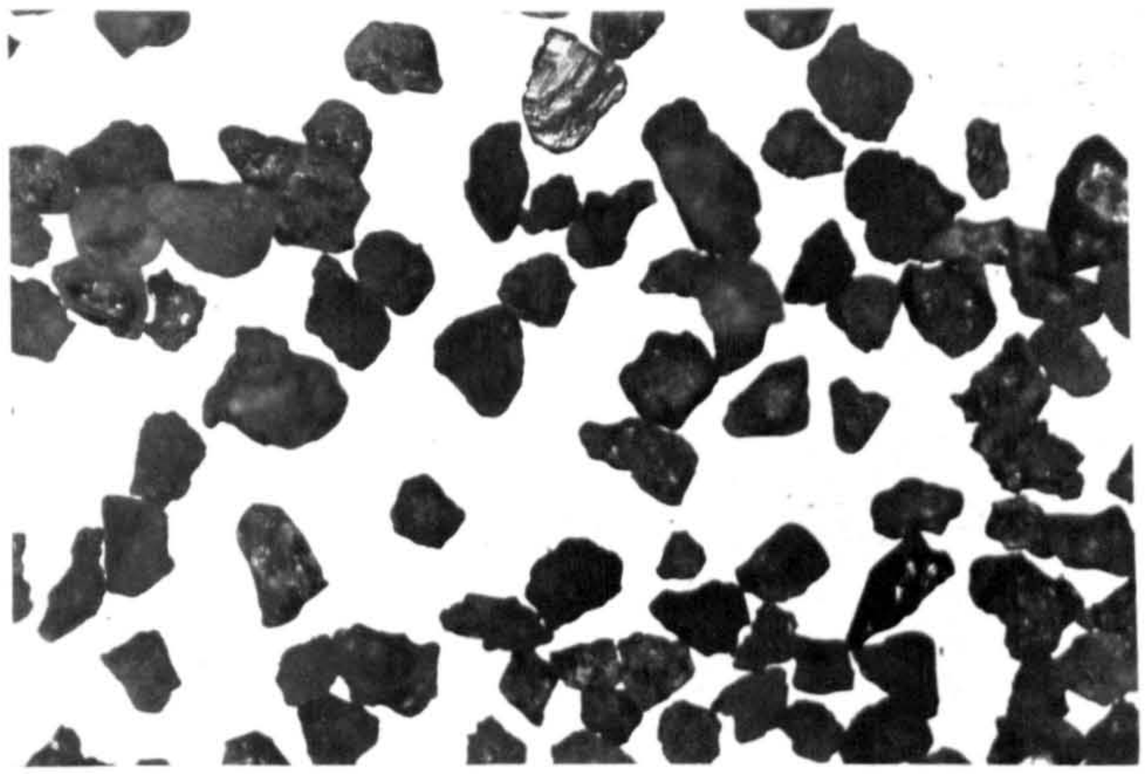

(a) BN37S sand (30x).

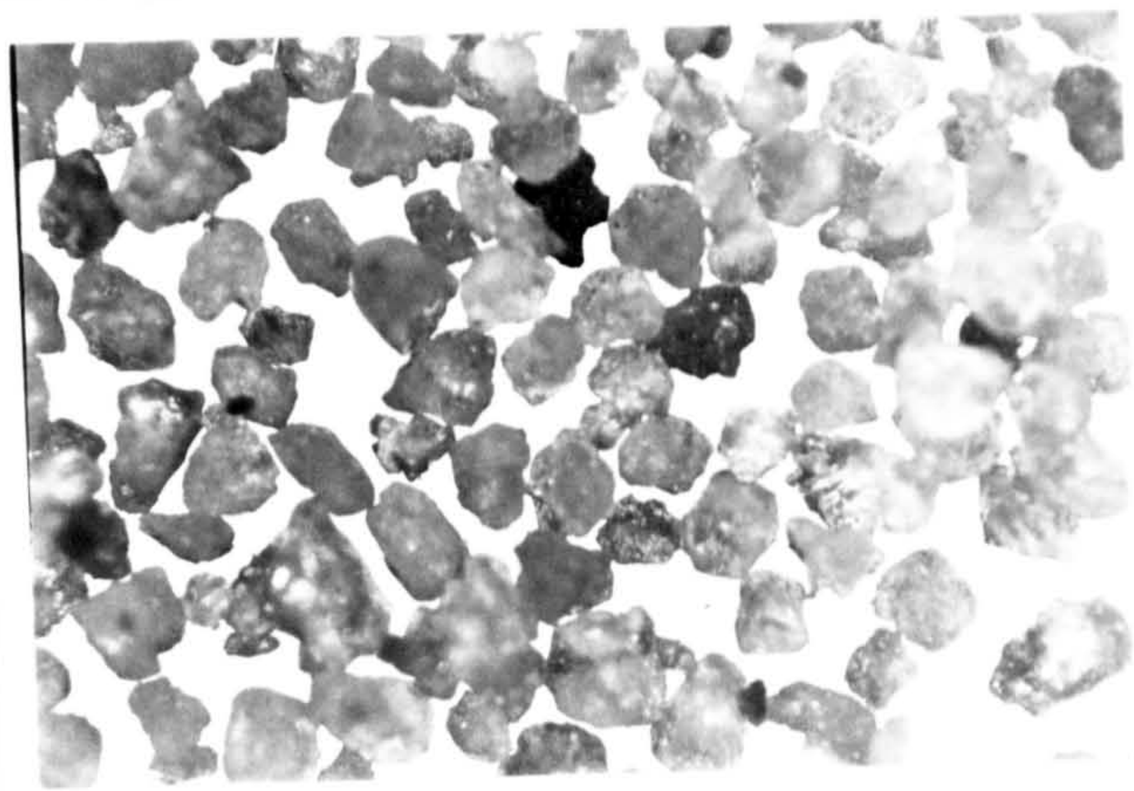

(b). BA27L sand (30x).

Figure 14. Typical shapes of the field sands.

A graded commercial sand supplied, by Arnold Sand Company of Leighton Buzzard, was studied and this was found to meet the general specification of the produced sand from the Baram Delta fields. Arnold obtained the sand by cutting a sand hill in the area nearby, washed, dried and screened to the required size range. The specification of the commercial sand is shown in Table 6. The size distribution and the shape of the commercial sand chosen for the modelling are shown in Figure 15(a) and (b).

Table 6(a). Sieve analysis of a graded commercial sand.

Microns	% Passing	Microns	% Passing
355	Trace	125	22.3
300	0.3	90	15.0
250	6.4	63	0.7
180	29.3	<63	0.1
150	25.9		

Table 6(b). Chemical analysis of a graded commercial sand.

Grade: DA 81 Dry Fine Type: Lower Greensand Location: Leighton Buzzard		Typical Colour: Light Cream Processed:Washing,Drying, Screening	
COMPOSITION	% Wt.	COMPOSITION	% Wt.
SiO_2	97.2	MgO	0.10
Al_2O_3	0.79	ZrO_2	0.06
K_2O	0.46	Na_2O	< 0.05
Fe_2O_3	0.40	CaO	0.03
TiO_2	0.21	BaO	0.01

Grain shape: Medium spherity/ Sub-rounded.

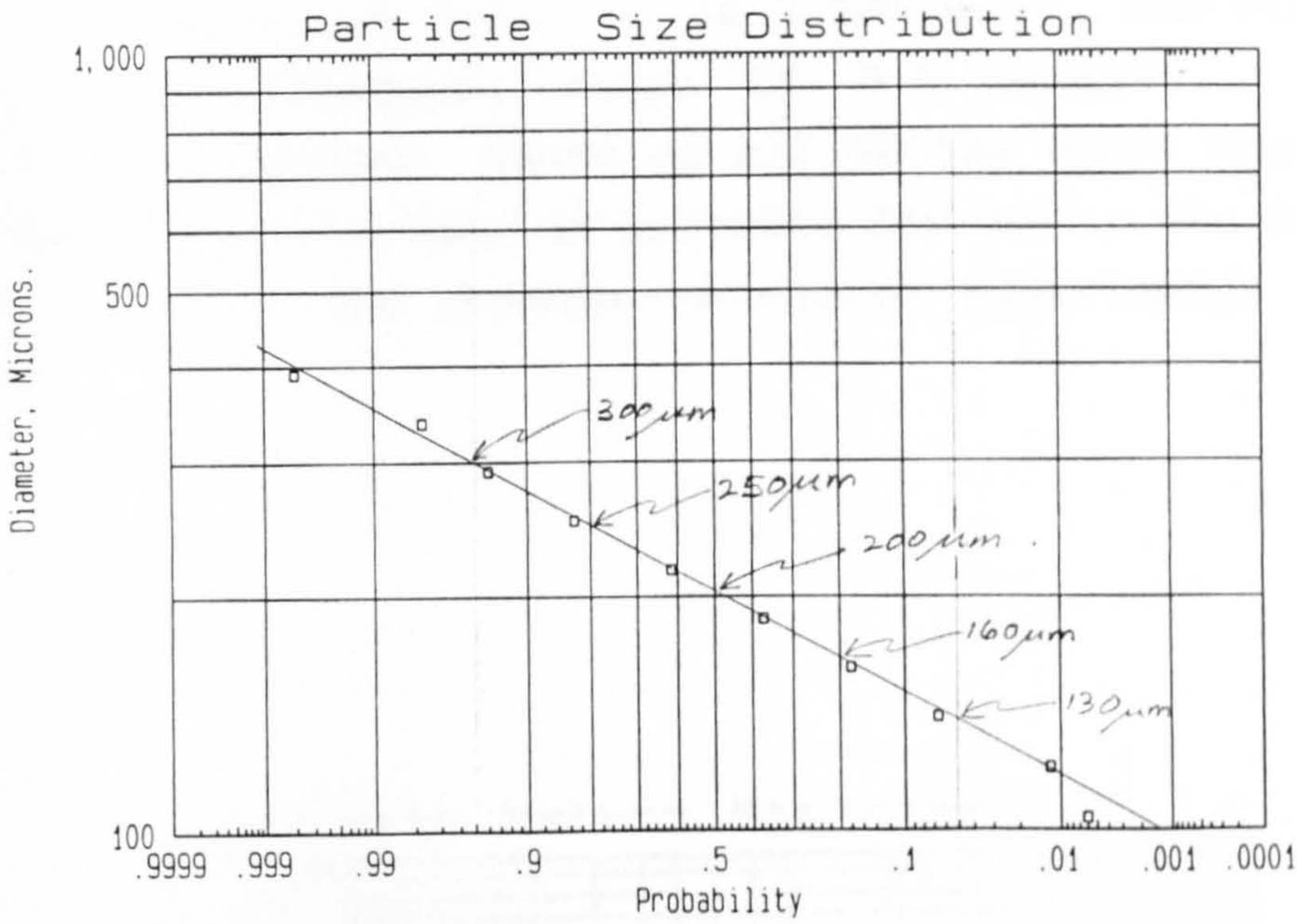

(a). Size distribution of sand.

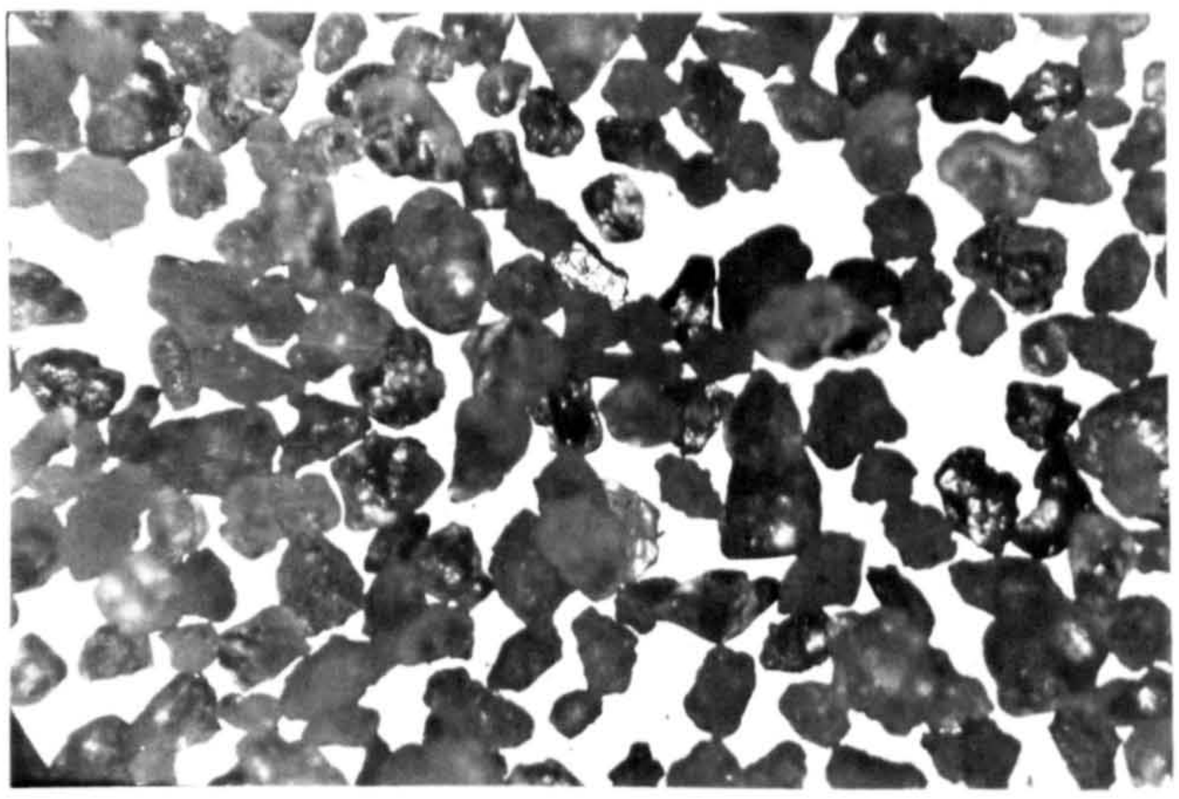

(b). General shape of sand (30x).

Figure 15. Graded commercial sand chosen for modelling.

Figure 16 shows the comparison of the crater volume distributions resulting from the impact by the field sand and the graded commercial sand. The average density of the commercial sand was found to be 2.635 g/cc. and its has an average micro-hardness value of 8.6 GPa(Hv). It can therefore be deduced, based on all of the above comparisons that the commercial sand is suitable for use in the modelling of the erosion and erosion-corrosion experiments in this project.

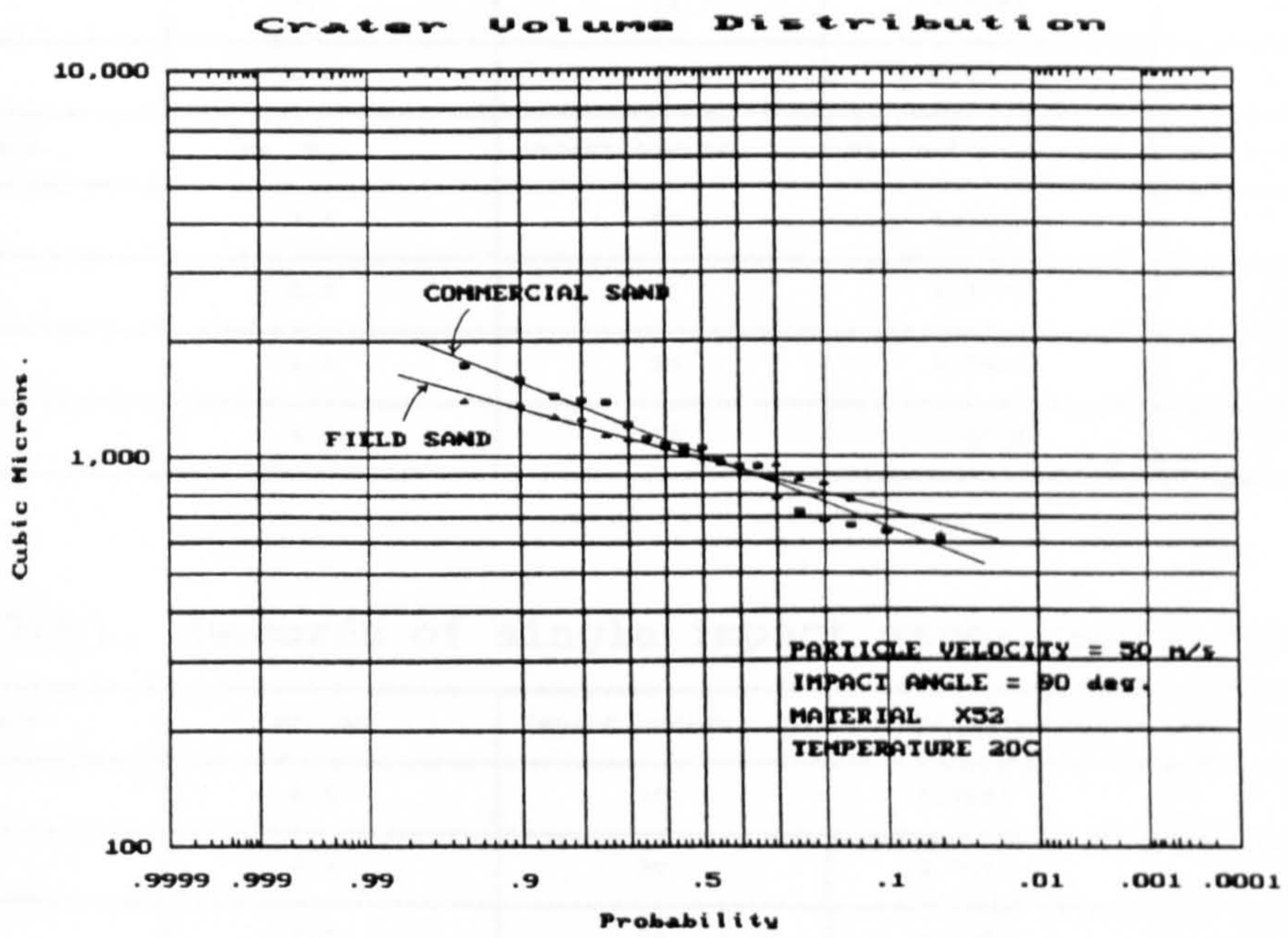

Figure 16. The crater volume distribution of field sand v.s. commercial sand.

5.3 Single Impact Experiments.

Typical records of the results obtained from the single impact experiments are shown in Table 7(a) for X52 and Table 7(b) for IN625; both results for 30° and 90° impact angles are shown. Similar records were made for the rest of the material specimens tested and they are also shown in Appendix G, Item G3, (a)-X65, (b)-N80, (c)-L80, (d)-L80/13Cr and (e)-Ferrulium 255.

Table 7(a). Records of single impact experiments for X52.

Vp, m/s.	Wp, mg.	Impact Angles, °	Wt, B/Impact (g)	Wt, A/Impact (g)
50	5.9	30	3.4526	3.4525
80	6.6	30	3.4356	3.4356
100	7.1	30	3.4289	3.4289
150	8.0	30	3.4020	3.4016
Vp, m/s.	Wp, mg.	Impact Angles, °	Wt, B/Impact (g)	Wt, A/Impact (g)
50	9.4	90	3.4177	3.4179
80	8.0	90	3.3776	3.3777
100	6.0	90	3.4413	3.4415
150	9.2	90	3.4550	3.4549

Table 7(b). Records of single impact experiments for IN625.

Vp, m/s	Wp, mg.	Impact Angles, °	Wt, B/Impact (g)	Wt, A/Impact (g)
50	6.6	30	3.7693	3.7692
80	8.1	30	3.7141	3.7139
100	7.1	30	3.7412	3.7412
150	8.9	30	3.6614	3.6612
Vp, m/s	Wp, mg.	Impact Angles, °	Wt, B/Impact (g)	Wt, A/Impact (g)
50	7.9	90	3.5840	3.5839
80	7.6	90	3.7345	3.7344
100	8.3	90	3.7259	3.7259
150	9.7	90	3.8044	3.8045

The corresponding crater volume distributions are shown in Figure 17 for X52, and Figure 18 for IN625. Similar plots were also constructed for the remaining of the material specimens tested as shown in Appendix G, Item G4, (a)-X65, (b)-N80, (c)-L80, (d)-L80/13Cr and (e)-Ferrulium 255.

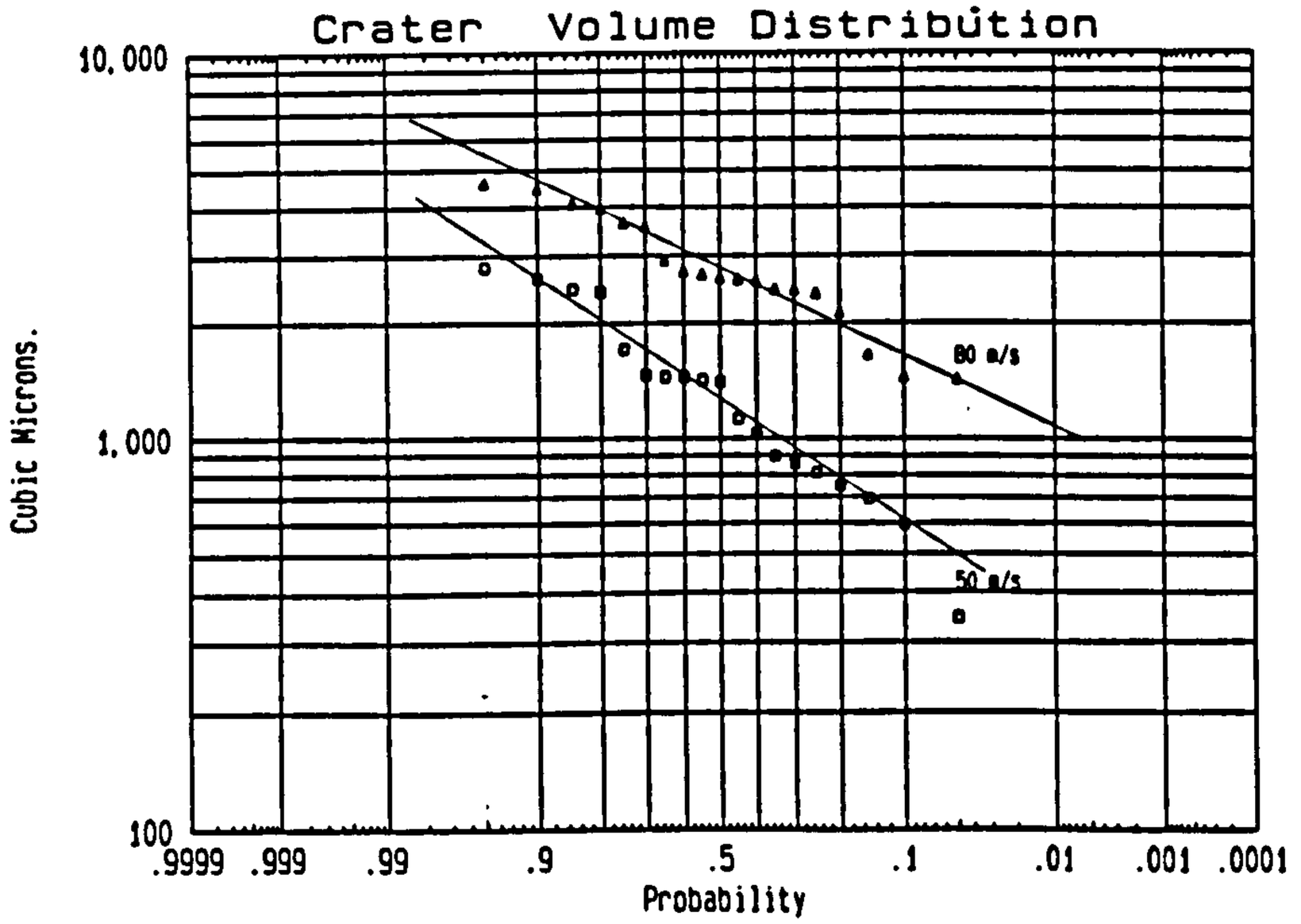

Figure 17(a). Crater volume distribution for X52 at 30°.

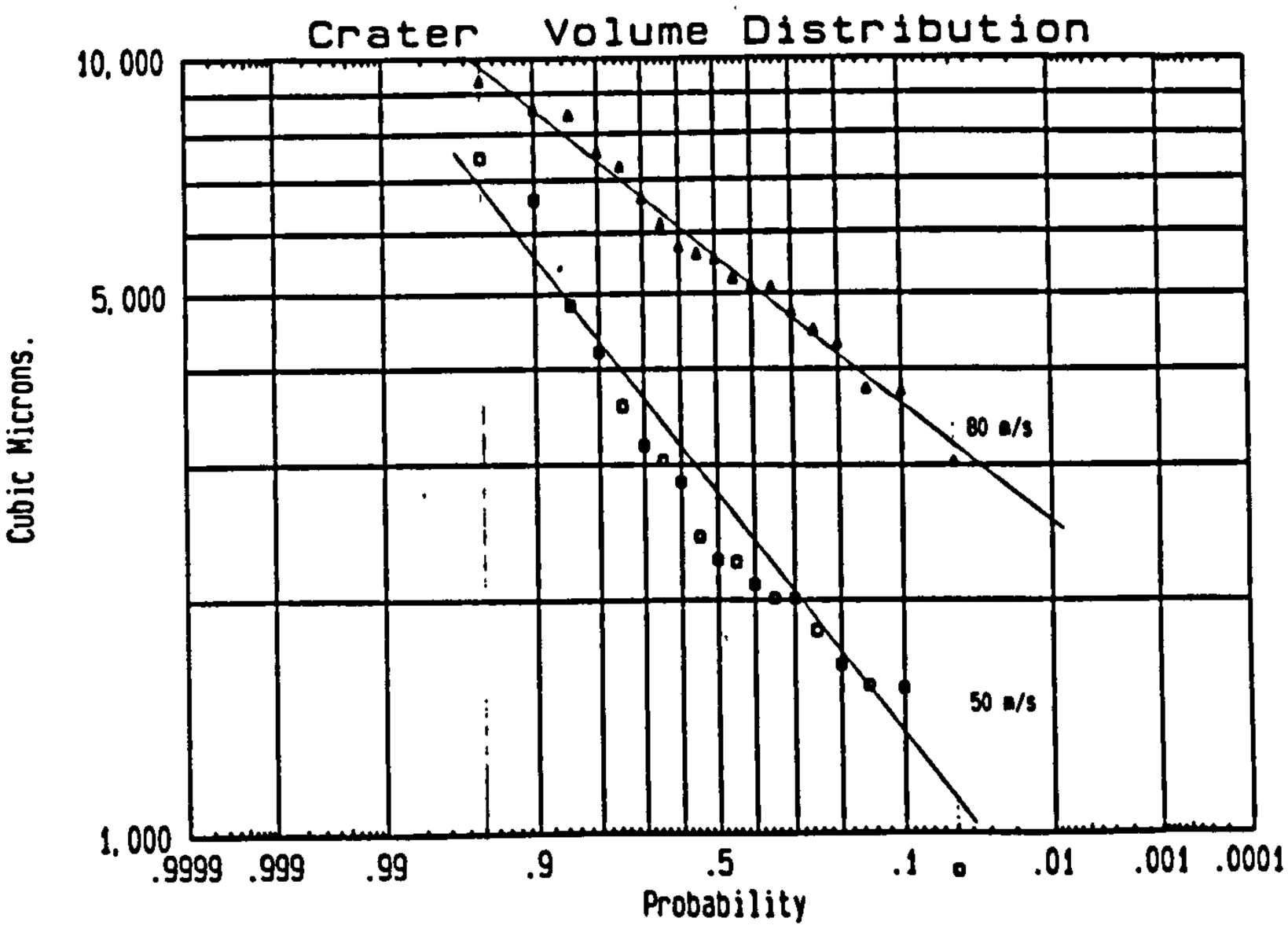

Figure 17(b). Crater volume distribution for X52 at 90°.

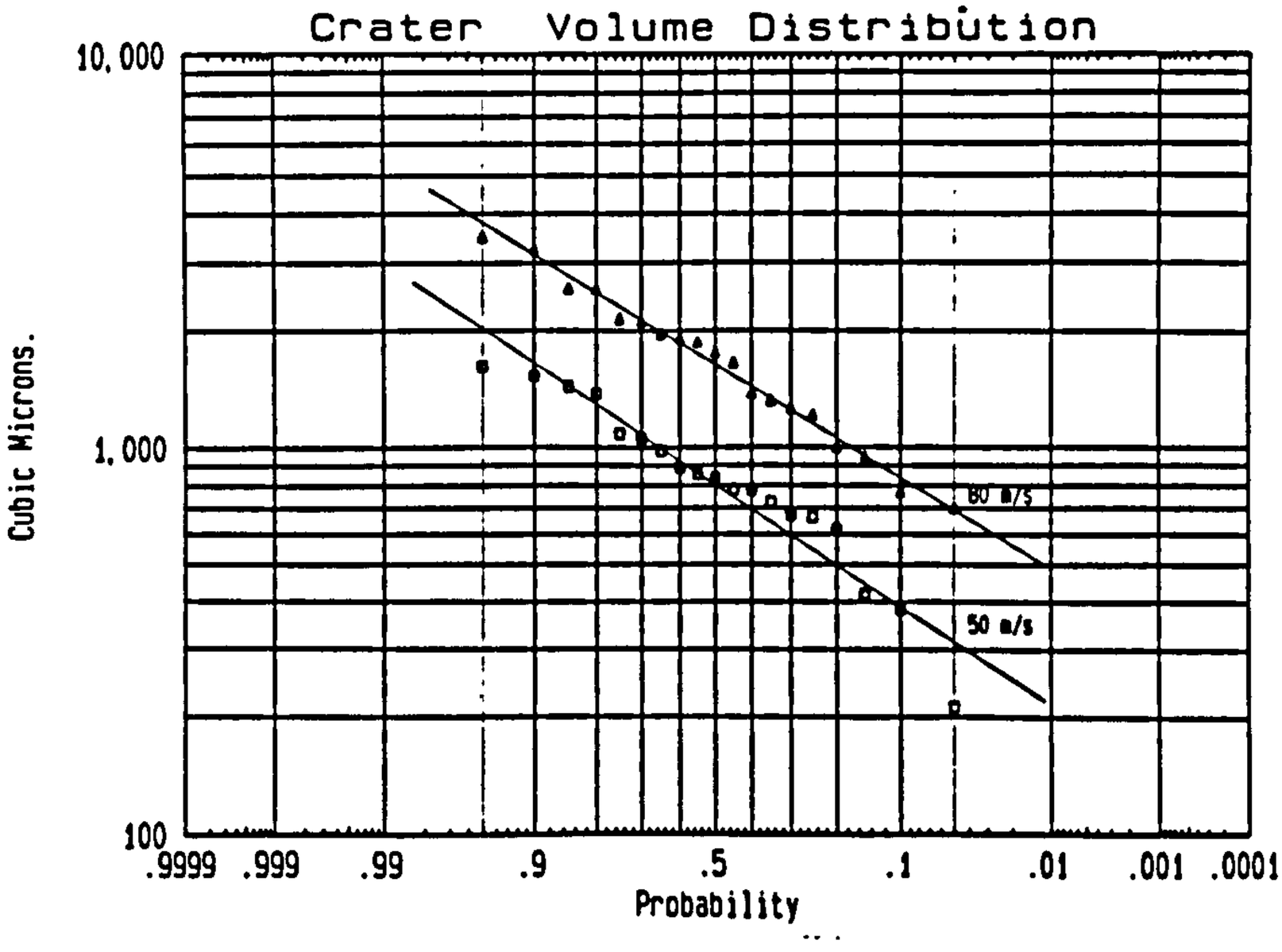

Figure 18(a). Crater volume distribution for IN625 at 30°.

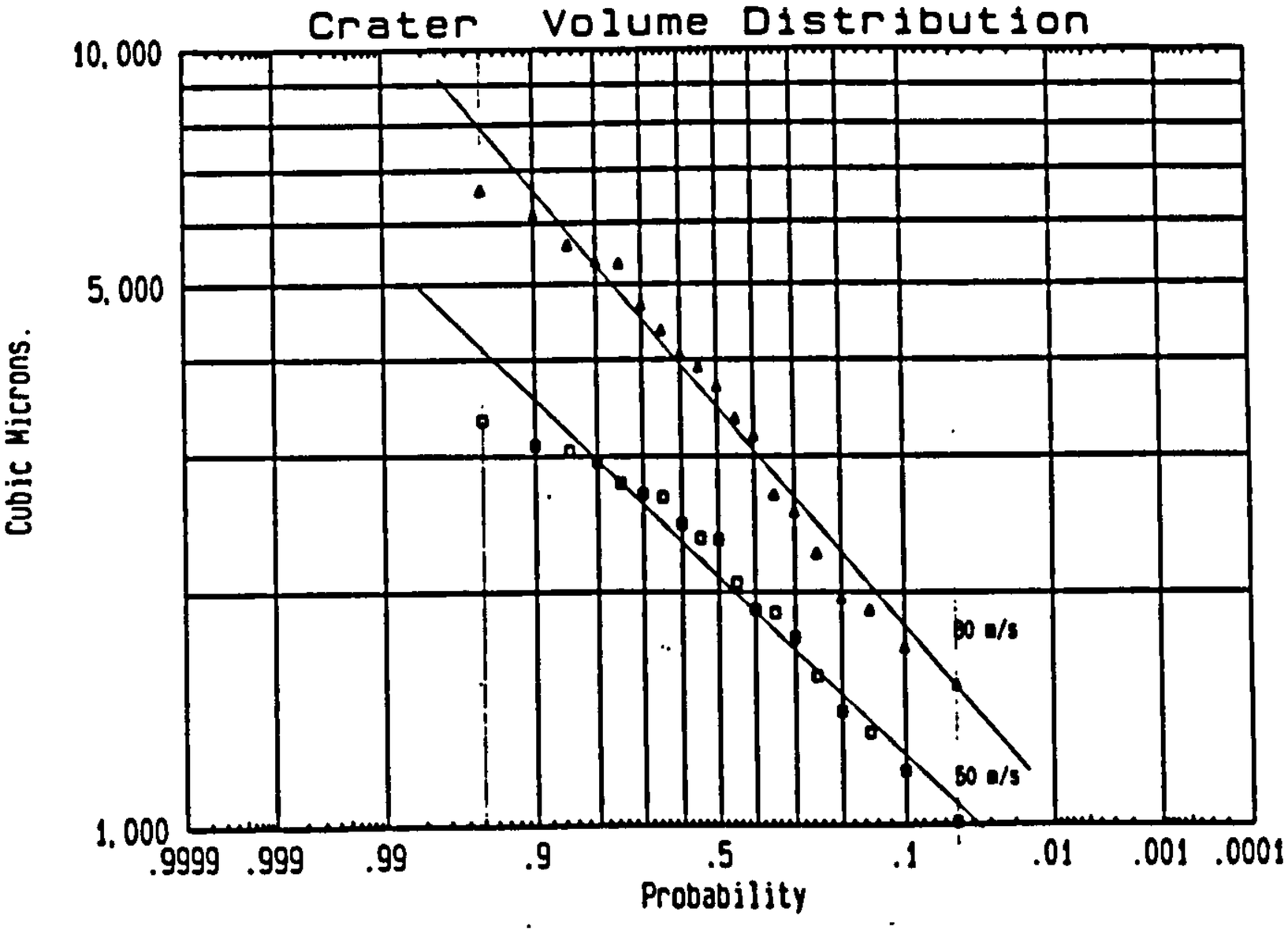

Figure 18(b). Crater volume distribution for IN625 at 90°.

Figures 19(a),(b),(c) and (d) show the band of crater volumes measured at 5%, 20%, 50%, 80% and 95% Probability, plotted against velocity for X52 at 30° and 90°, and for IN625 at 30° and 90° impact angles to demonstrate the change in crater volume distribution with velocity.

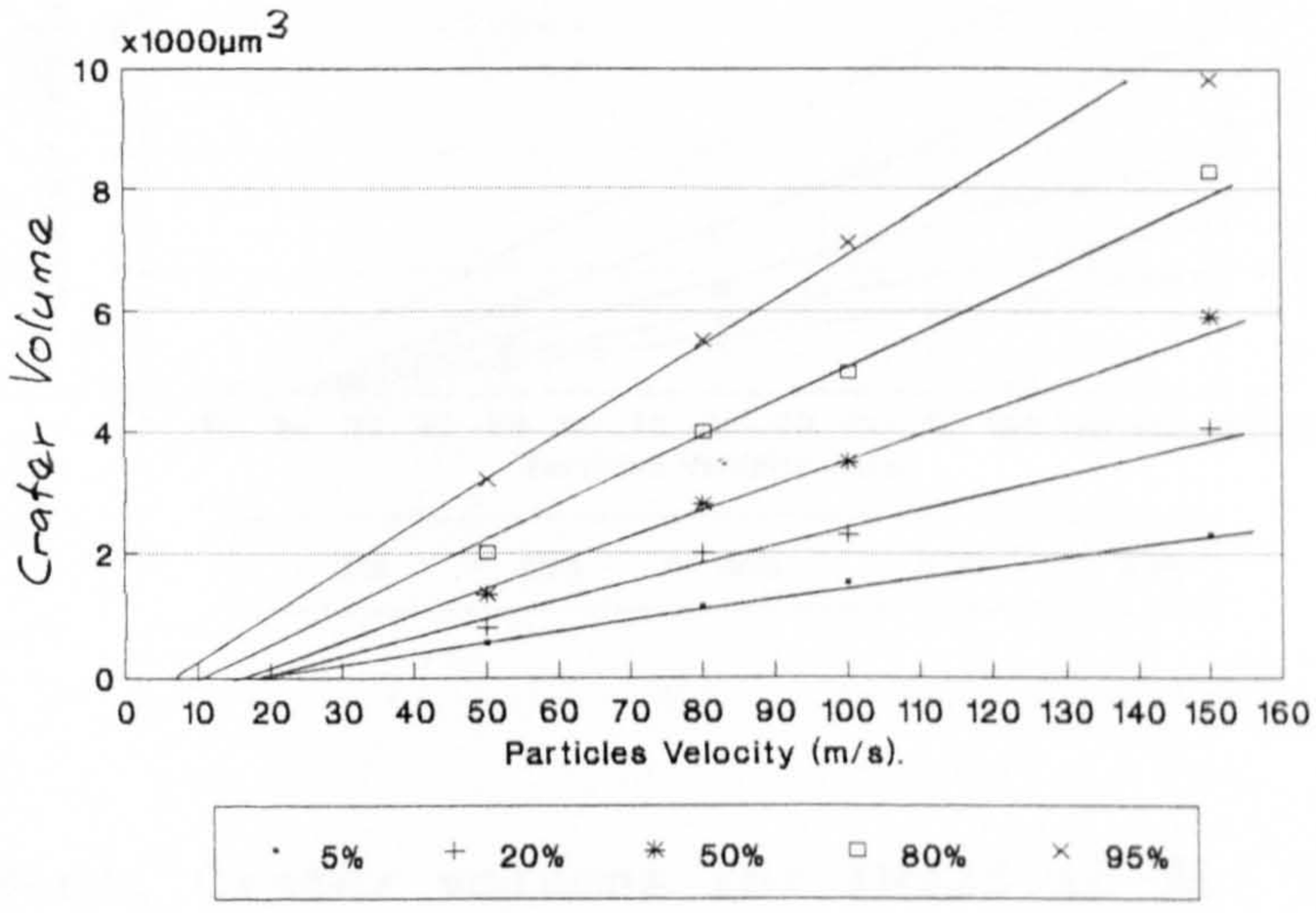

Figure 19(a). Crater volumes for X52 at 30° Impact angle.

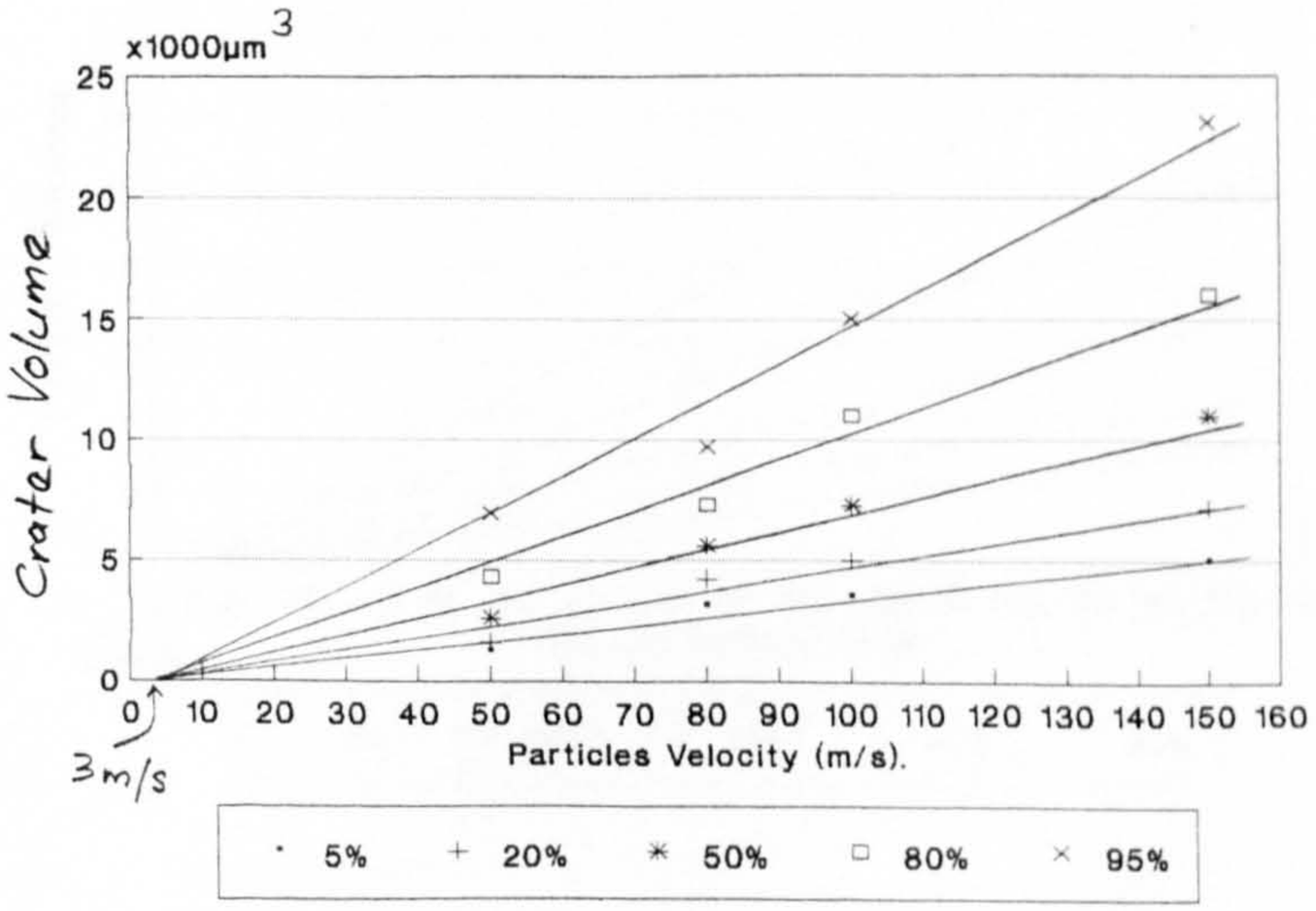

Figure 19(b). Crater volumes for X52 at 90° Impact angle.

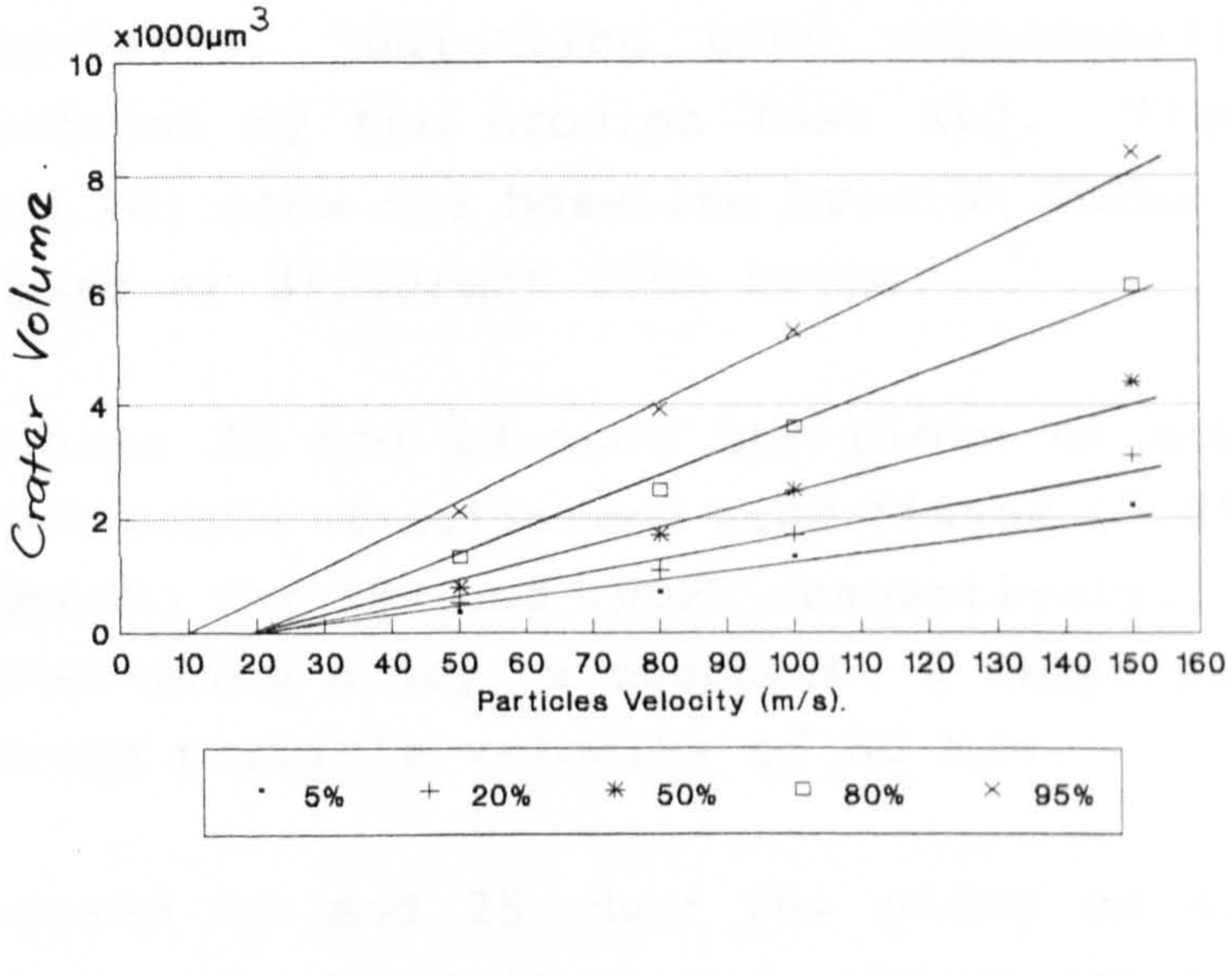

Figure 19(c). Crater volumes for IN625 at 30° Impact angle.

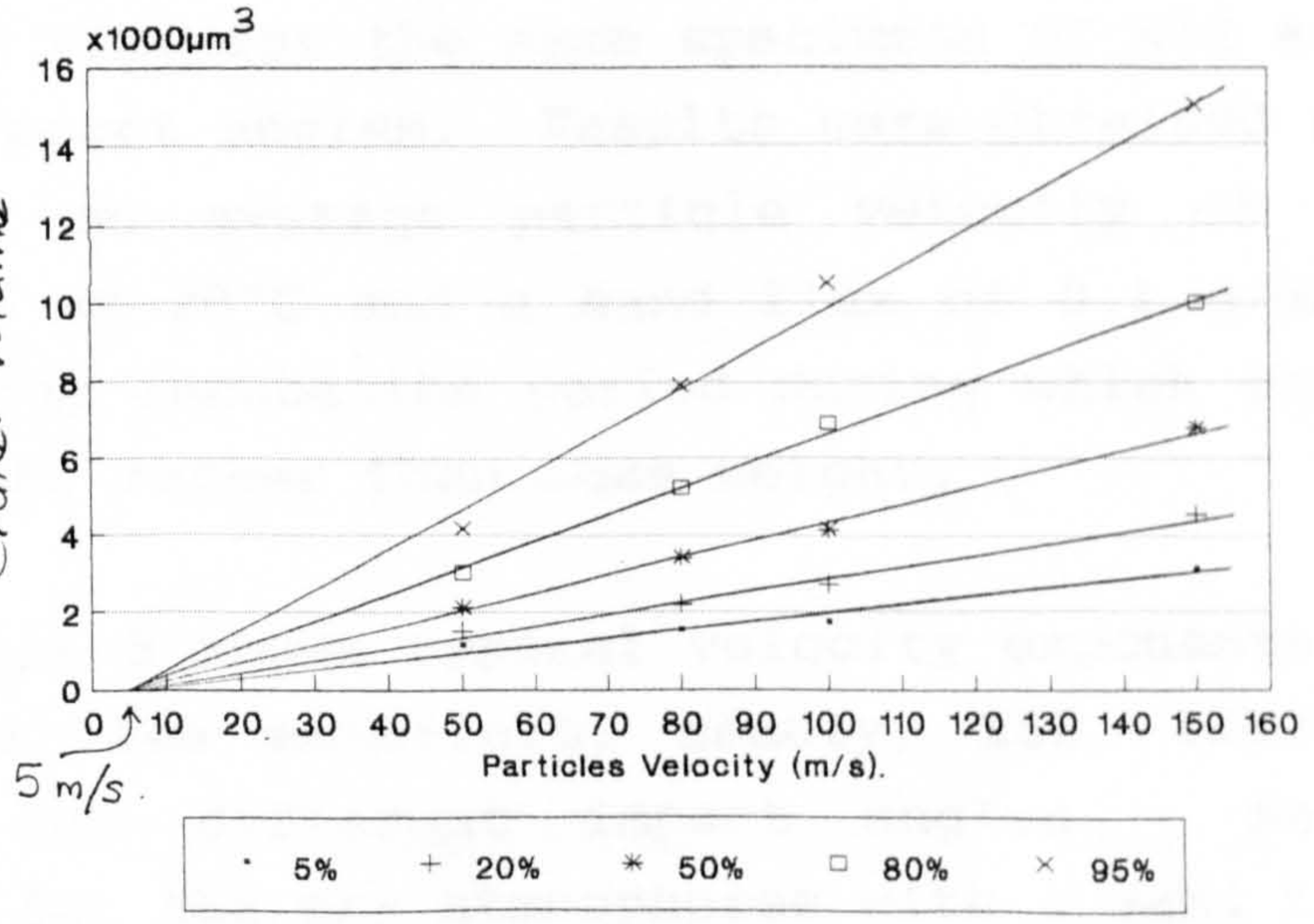

Figure 19(d). Crater volumes for IN625 at 90° Impact angle.

5.4 Baseline Erosion Experiments.

Figures 20(a), (b), (c) and (d) show the plots of erosion rate versus impact angle for X52, L80, 13Cr and IN625 in the dry-tests, indicating good repeatability of the results produced by the Erosion Test Rig. Figures 21(a), (b), (c) and (d) show the baseline Erosion Rates for all the materials used at different flux rates.

Figures 22 and 23 show the plots of erosion rate versus impact angle at different sand fluxes (0.01, 0.05, 0.1 and 0.5 g/mm^2/h) for X52 and IN625 respectively. The results were obtained using a dry atmosphere, a temperature of 20°C and an average particle velocity of 50 m/s.

Figures 24 and 25 show the plots of erosion rate versus impact angle for different average particle velocities of 20 m/s, 50 m/s, 80 m/s and 150 m/s for X52 and IN625 respectively. Results were obtained using a dry atmosphere, a sand flux of 0.05 g/mm^2/h and a temperature of 20°C.

Figures 26 and 27 show the plots of weight loss as a function of time for the same specimens of X52 and IN625 at different impact angles. Results were obtained using a dry atmosphere, an average particle velocity of 50 m/s, a temperature of 20°C and a sand flux of 0.1 g/mm^2/h. They also show the incubation period during which the materials gained weight rather than lose weight.

Table 8 shows typical velocity exponents calculated for four of the materials, namely, X52, IN625, L80 and L80/13Cr, for different impact angles. Results were calculated for the dry atmospheres with a sand flux of 0.05 g/mm^2/h and a temperature of 20°C.

Table 8. Velocity exponents, n, for four different materials.

Materials	15°	30°	60°	90°
X52	2.6	2.7	2.5	2.5
IN625	3.0	2.9	4.0	4.0
L80	2.6	2.8	2.9	2.9
L80/13Cr	3.0	3.1	3.1	3.1

5.5 Erosion-Corrosion Experiments.

Figures 28 to 34 show the plots of erosion-corrosion rate versus impact angle for different sand fluxes for all of the materials used in the experiments. The results for pure erosion were also plotted together for ease of comparison. The results were obtained from experiments at a temperature of 20°C and an average particle velocity of 50 m/s.

Figure 35 shows the influence of temperature on erosion-corrosion rates, for X52. The dry atmospheric experimental results were plotted again for ease of comparison.

Figures 36 and 37 show the plots of erosion-corrosion rates on X52 and L80, respectively, versus impact angles for different velocities of 20 m/s, 50 m/s, 80 m/s and 150 m/s. The sand flux was at 0.05 g/mm^2/h and temperature of 20°C.

Appendix F shows the summary of the results obtained from all of the erosion and erosion-corrosion experiments. The rest of the graphs plotted for the erosion and erosion-corrosion rates obtained are also shown in Appendix G, Item G5.

5.6 Surface Morphology by SEM.

Figures 38(a), (b), (c) and (d) show the surface morphology of X52 surfaces due to erosion at different impact angles. Figures 39(a), (b), (c) and (d) are those of IN625. They were taken after 5h exposure in a dry atmosphere at a flux rate of 0.5 g/mm^2/h and a temperature of 20°C.

Figures 40(a), (b), (c) and (d) show the surface micrographs of X52 following erosion-corrosion at different impact angles. Figure 41(a) and (b) are micrographs for those of IN625 at impact angles of 15° and 90°, respectively. They were taken after 5 hours exposure in wet CO_2 at a flux rate of 0.5 g/mm^2/h and a temperature of 20°C.

Figures 42(a), (b), (c) and (d) show the micrographs of cross-sections of the erosion-corrosion surfaces for X52 material taken at different impact angles. They show the development of work-hardening layer of the grains formed immediately below the impacted surfaces as the impact angle increases.

Figure 43(a) and (b) show the exploded view of two of the previous cross-sections illustrating the results of two distinct erosion mechanisms:

(a). showing material failure and removal by cutting mechanism, where a cutting trough is clearly shown, and

(b). showing material failure and removal by fatigue fracture. The micrograph also shows lateral cracks formed below the impacted surface and a platelet about to be detached.

5.7 Identification of Corrosion Scales.

Table 9(a) lists the 'd' spacings and relative intensities determined by an X-ray diffraction technique. Tables 9(b) and 9(c) are the 'd' spacings and relative intensities expected for Ferrous Carbonate ($FeCO_3$) and Magnetite (Fe_3O_4), respectively (66). By comparing values from Table 9(a) and Table 9(c) it can be said that the corrosion scales contain some magnetite. However, magnetite was believed to have been formed during cooling down of the rig, when specimens were heated up to a temperature above 80°C as the water supply was switched off. It normally took about two hours for the rig to cool down before specimens could be taken out for examination.

Figures 44(a) and (b) are the XPS-Spectra detected from surfaces of as received X52 specimen (before test), an X52 specimen after 5h exposure in erosion-corrosion test at a temperature of 80°C, and magnetite cultured in a separate test when an X52 specimen was exposed to superheated steam containing CO_2 gas for 72 hours at a temperature of 500°C. This test did not conclude that the scales formed at 80°C in wet CO_2 erosion-corrosion consist of magnetite but may contain some Ferric (Fe3+) ions.

Table 9(a). X-Ray Diffraction of scales formed on X52 Surface.

2θ	d	I/I_o, %
15°	2.9789	40
33°	2.7146	50
35.5°	2.5290	100
43°	2.1037	60
57°	1.6158	80
62.5°	1.4862	80

Table 9(b). Characteristics X-Ray Diffraction for $FeCO_3$ (66).

d	2.79	1.73	3.59	3.59	1.963	2.35	1.426
I/I_o	100	80	60	60	60	50	50

Table 9(c). Characteristics X-Ray Diffraction for Fe_3O_4 (66).

d	2.53	1.614	1.48	4.85	2.096	1.0922	1.048
I/I_o	100	85	85	40	70	60	40

5.8 Data From the Field.

Figures 45(a), (b) and (c) show the sand production history of some of the fields in Baram Delta Operations area in Malaysia. They are known to have produced sand, and therefore most of the wells were completed by using Inside-casing Gravel Packing, as labelled with (IGP). Those wells which were not completed with any gravel-packing are labelled with (NGP). The minimum value of sand production, whose maximum in the region of 10 PPTB, is used as a threshold limit for sand production monitoring purposes before petroleum production would be curtailed in order to lower sand production rates. The maximum values are the maxima recorded for each well in their sand monitoring programme. All values were gathered from the respective wells' log book. Because the sand sampling was normally done once every two weeks for all sand producing wells, the value of the maxima should be treated carefully as they may not reflect the true maximum sand production rates as sand could have accumulated prior to samples being taken. However, these high sand rates may sometimes occur due to production disturbances, which again do not necessarily reflect a true steady state sand production rates.

Figures 46(a), (b), (c) and (d) are typical examples of sand erosion of production tubings and a permanent choke commonly experience in the area. They represent the erosion of downhole and wellhead equipment.

Figures 47(a) and (b) are examples of erosion of flanges downstream of the wing valves of a christmas tree obtained from one of the gas platforms. This is typical of medium velocity erosion which takes place in the direction of the flowstream.

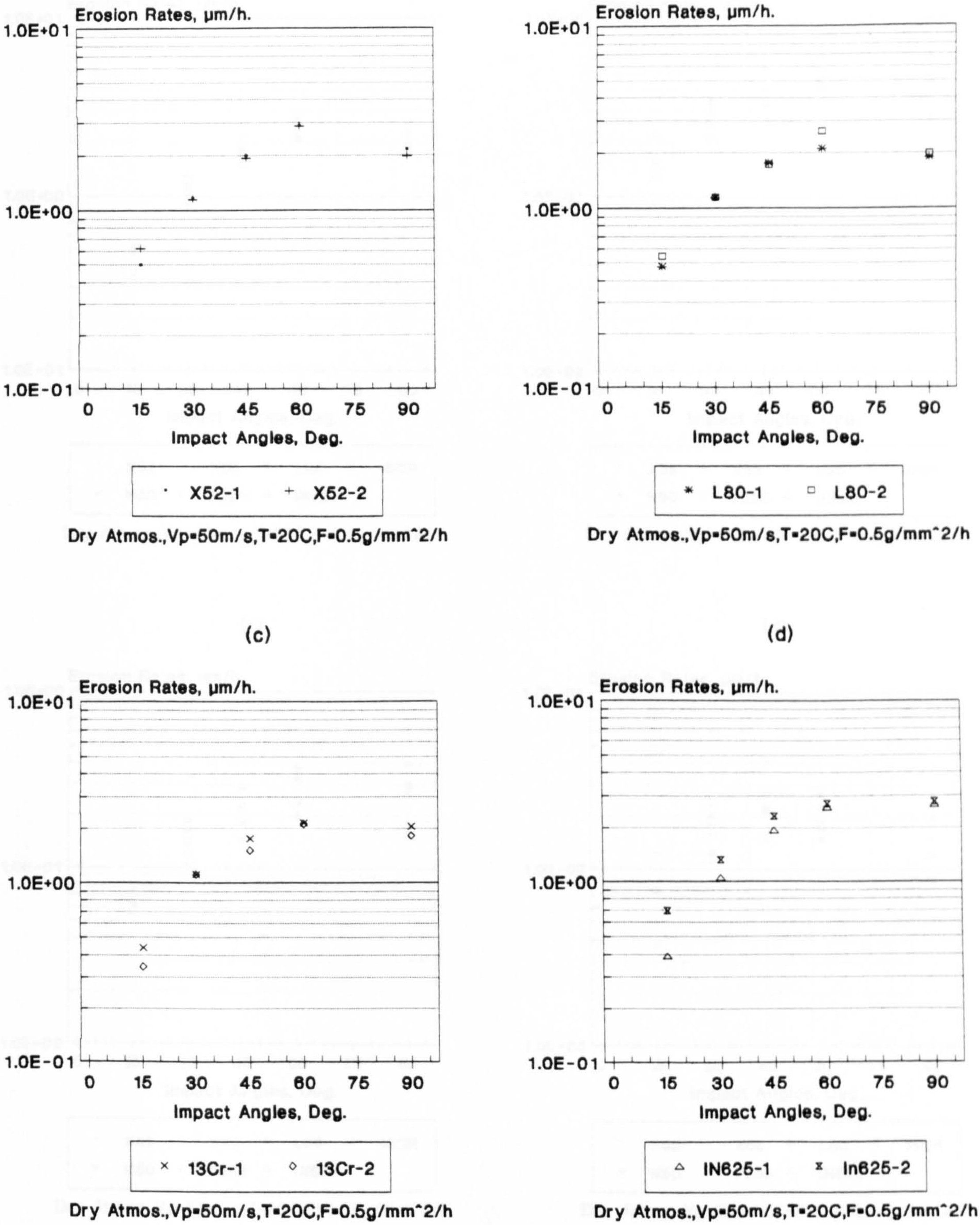

Figure 20. Repeatability of the erosion tests results (Duplicate tests).

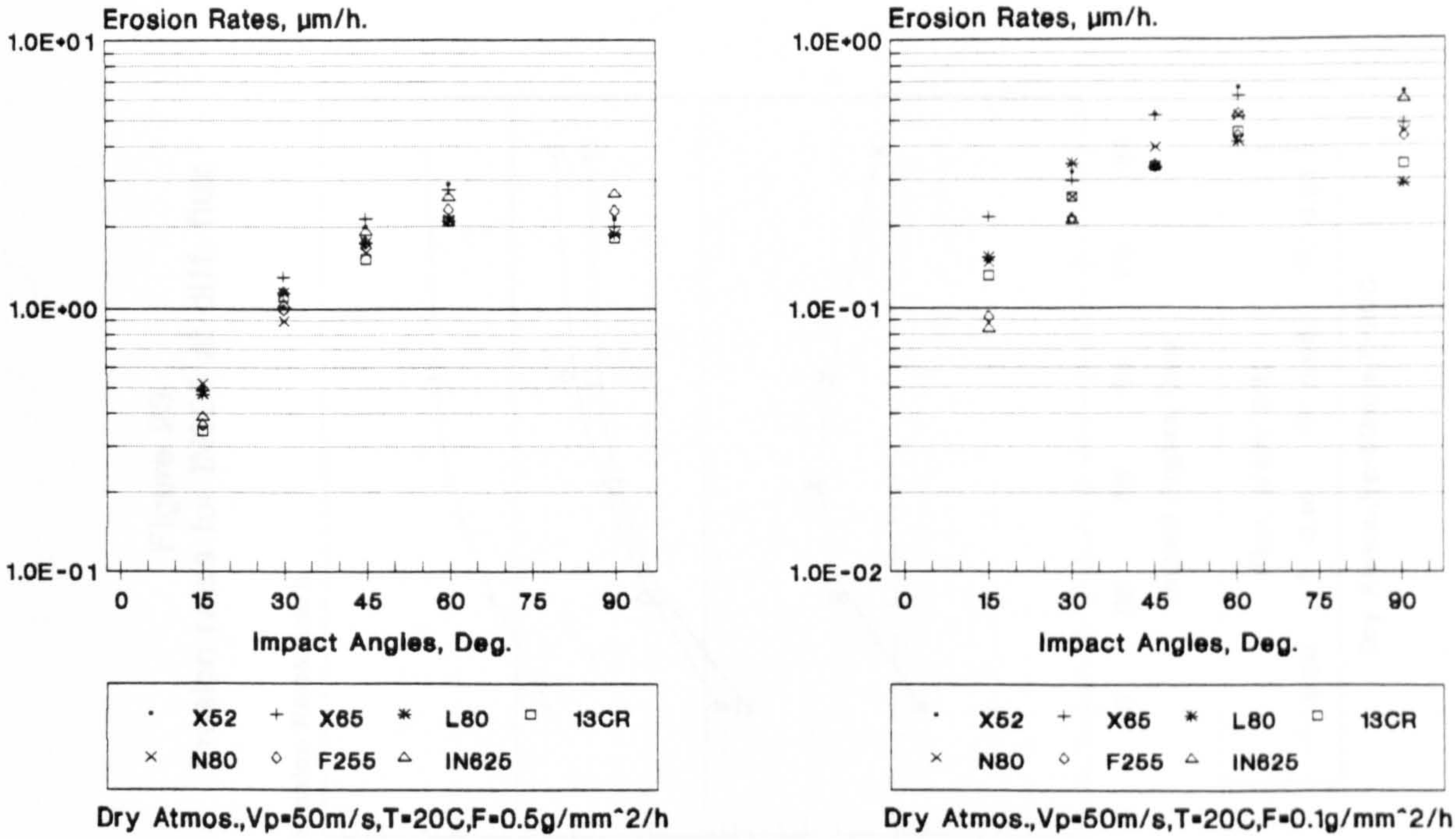

Figure 21. Baseline erosion rates for different materials.

Figure 23
Erosion rates for IN625 at different flux

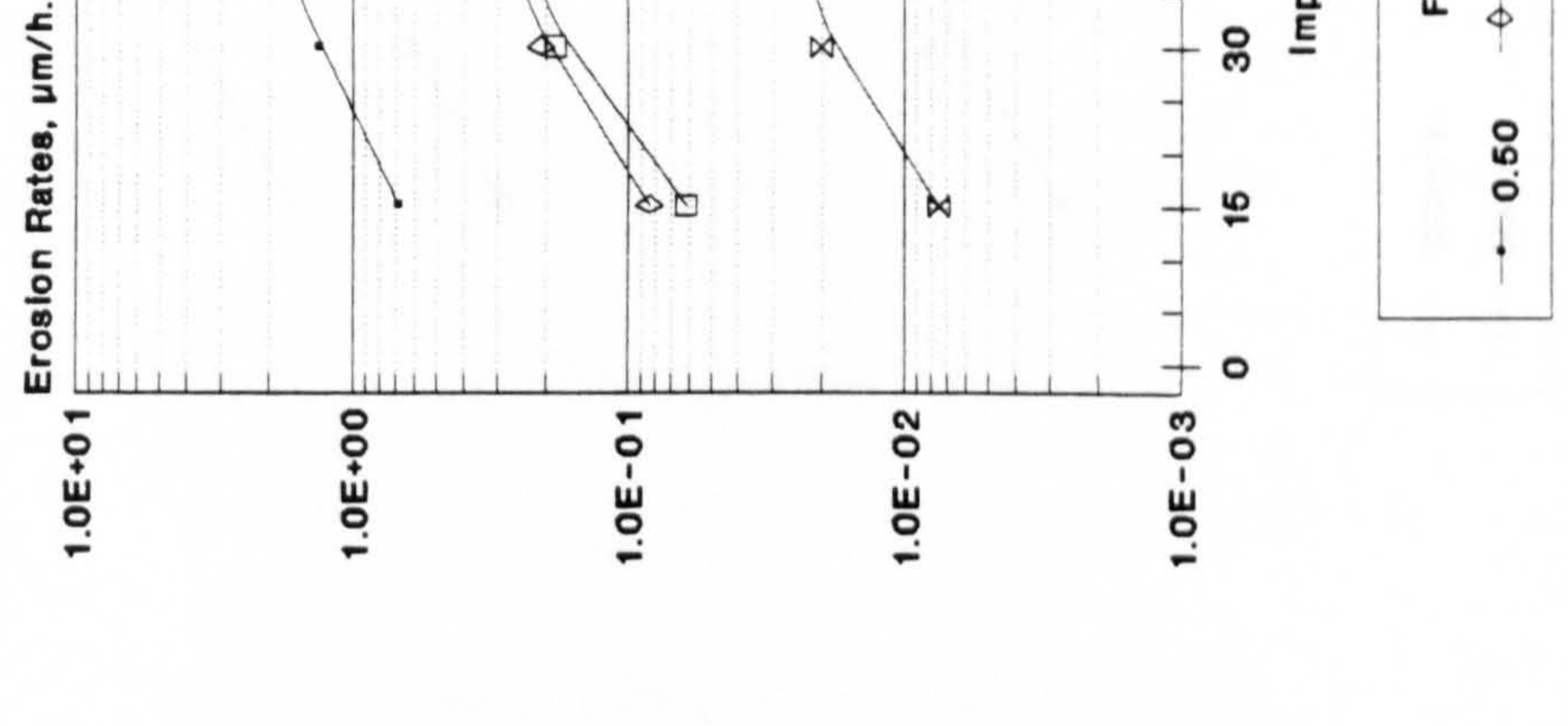

Figure 22
Erosion rates for X52 at different flux

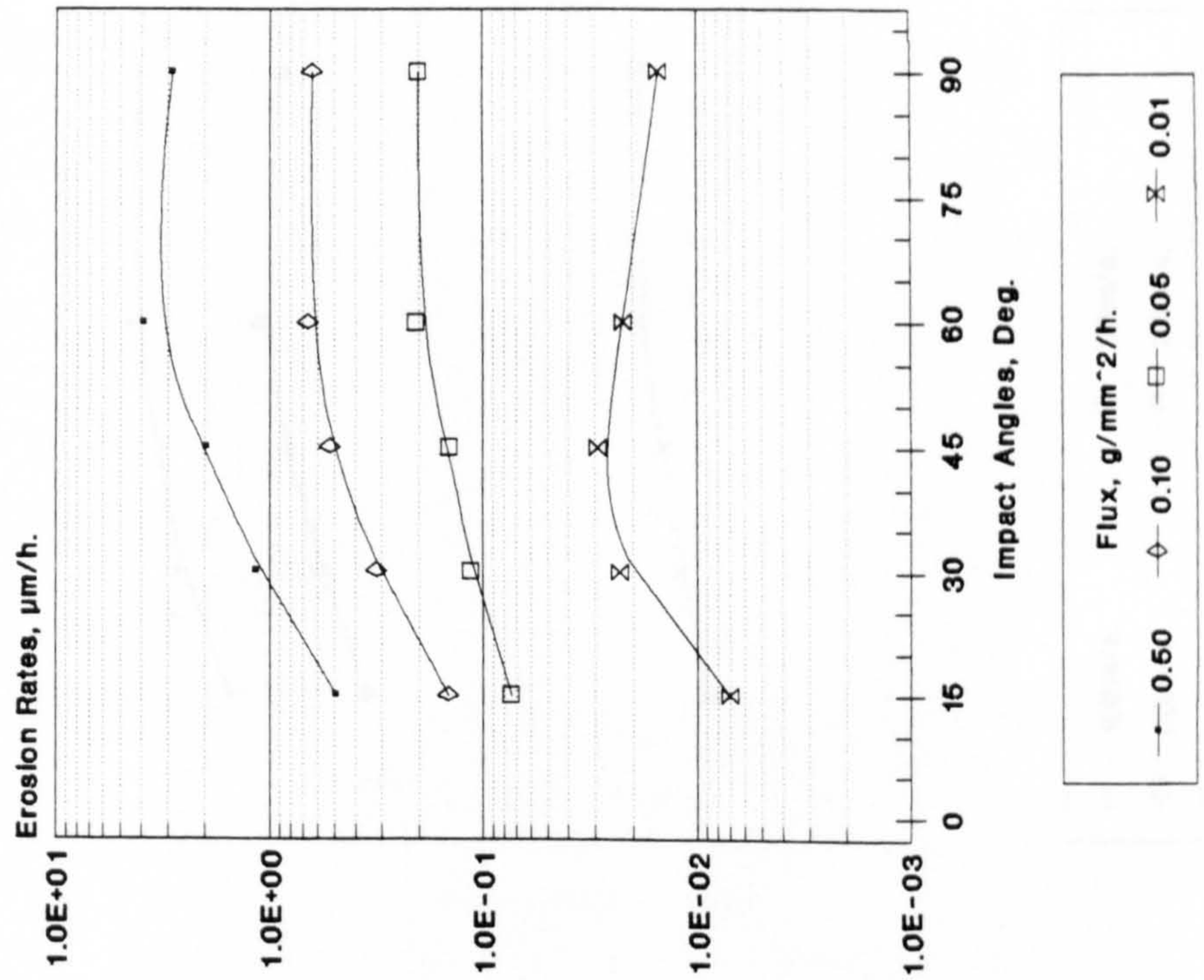

Figure 25
Erosion rates for IN625 at diff.velocity

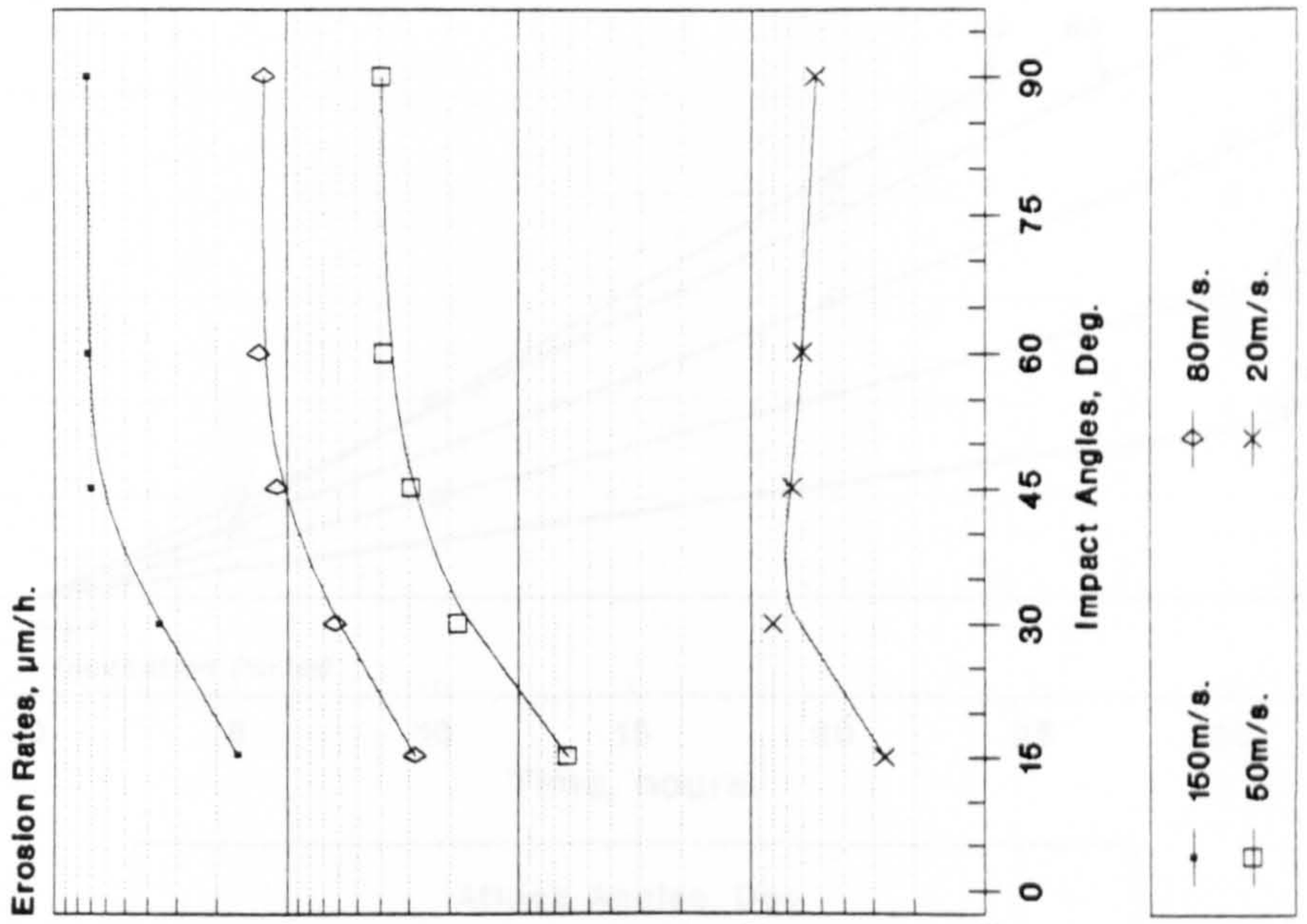

Figure 24
Erosion rates for X52 at diff. velocity

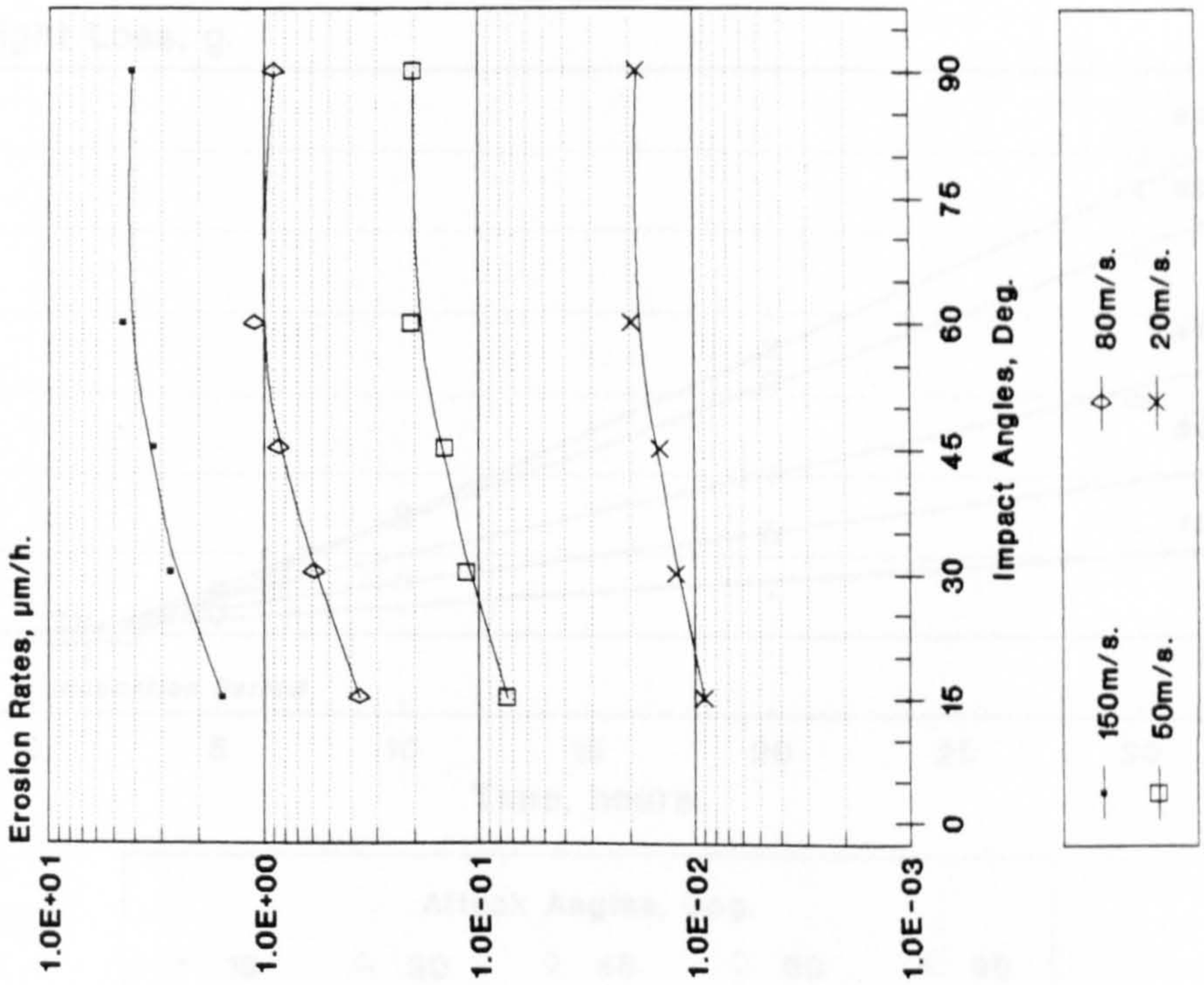

Fig.26. Weight loss versus time for X52

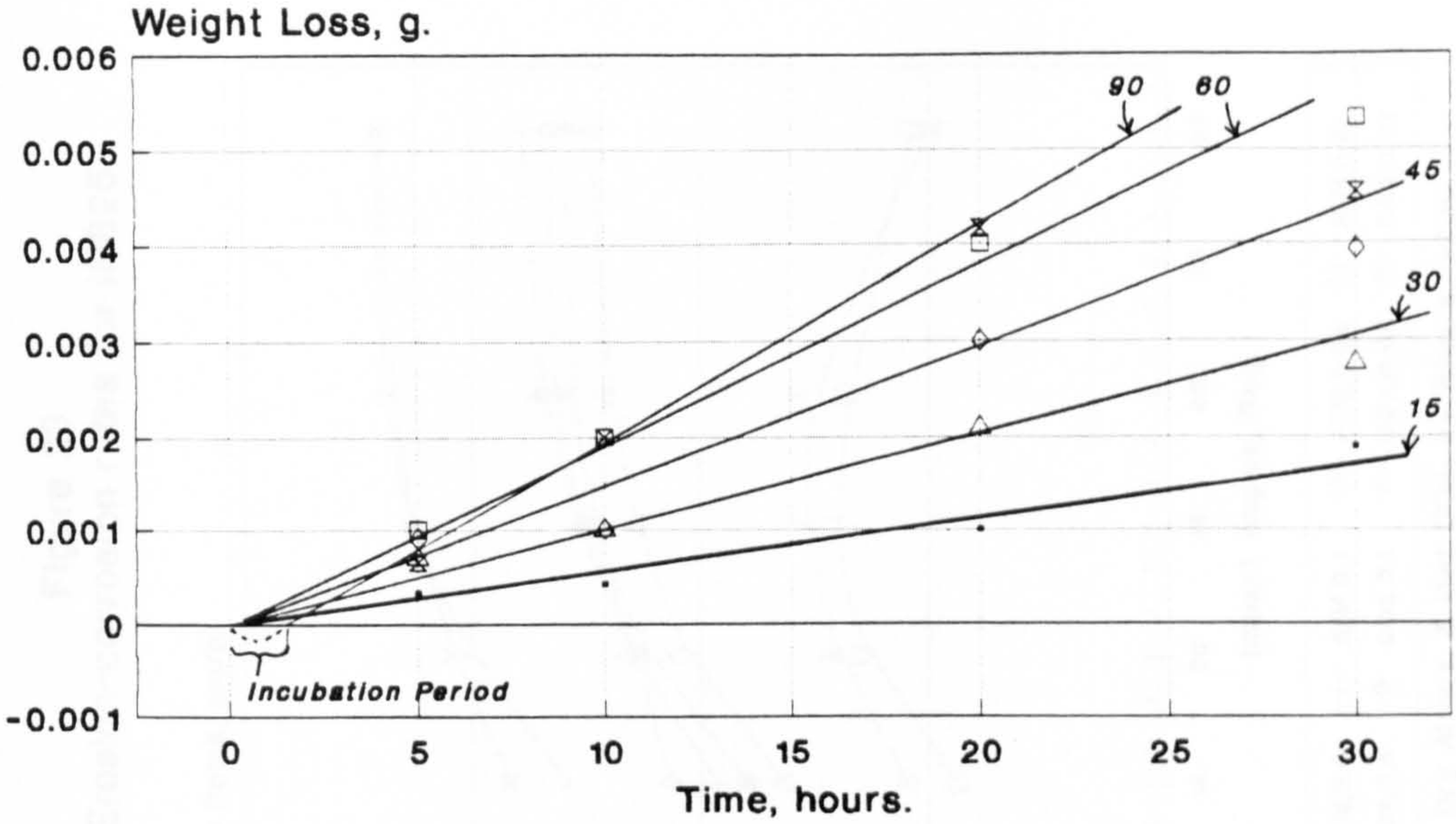

Fig.27.Weight loss versus time for IN625

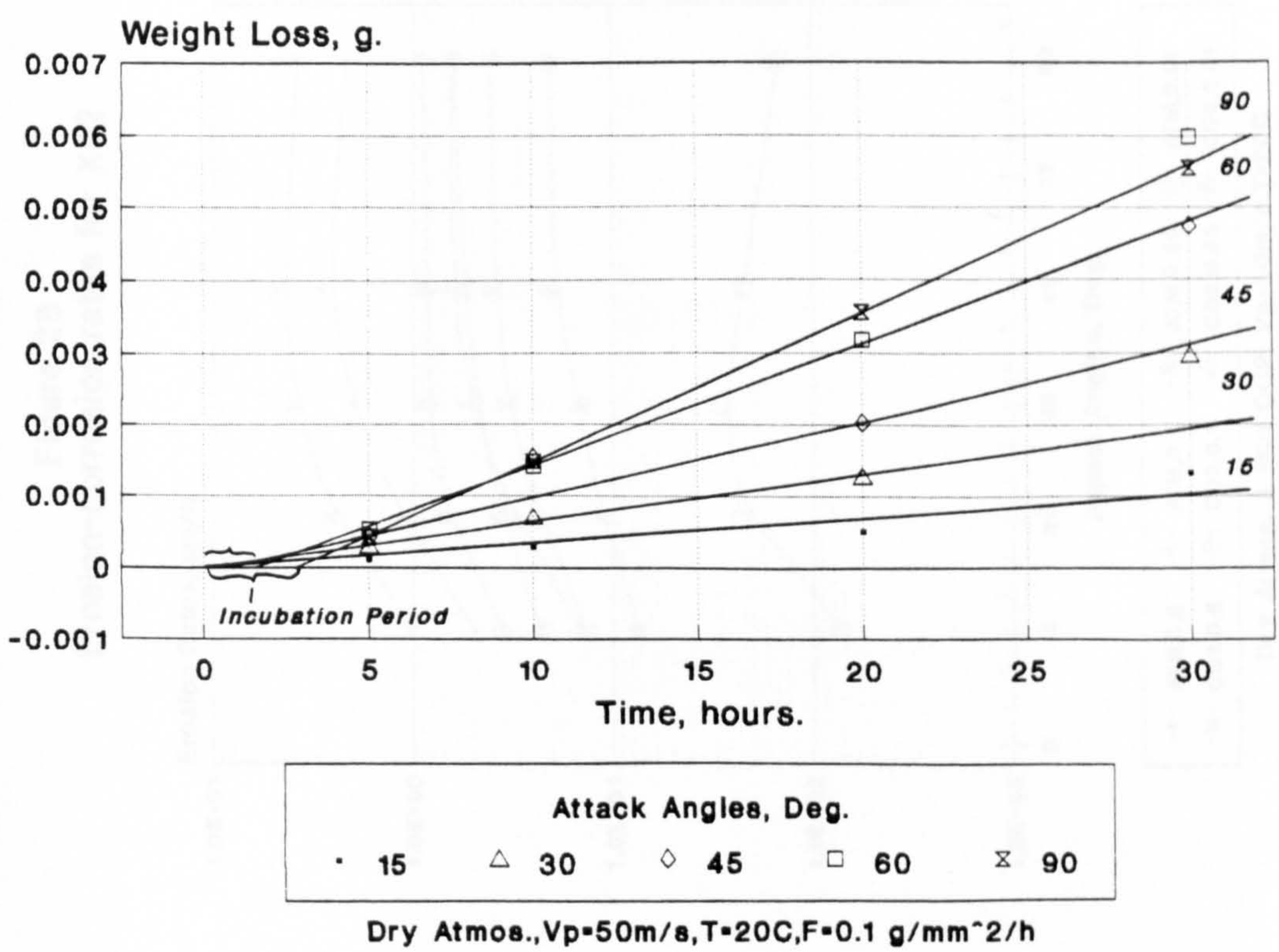

Figure 28
Erosion-corrosion rates for X52

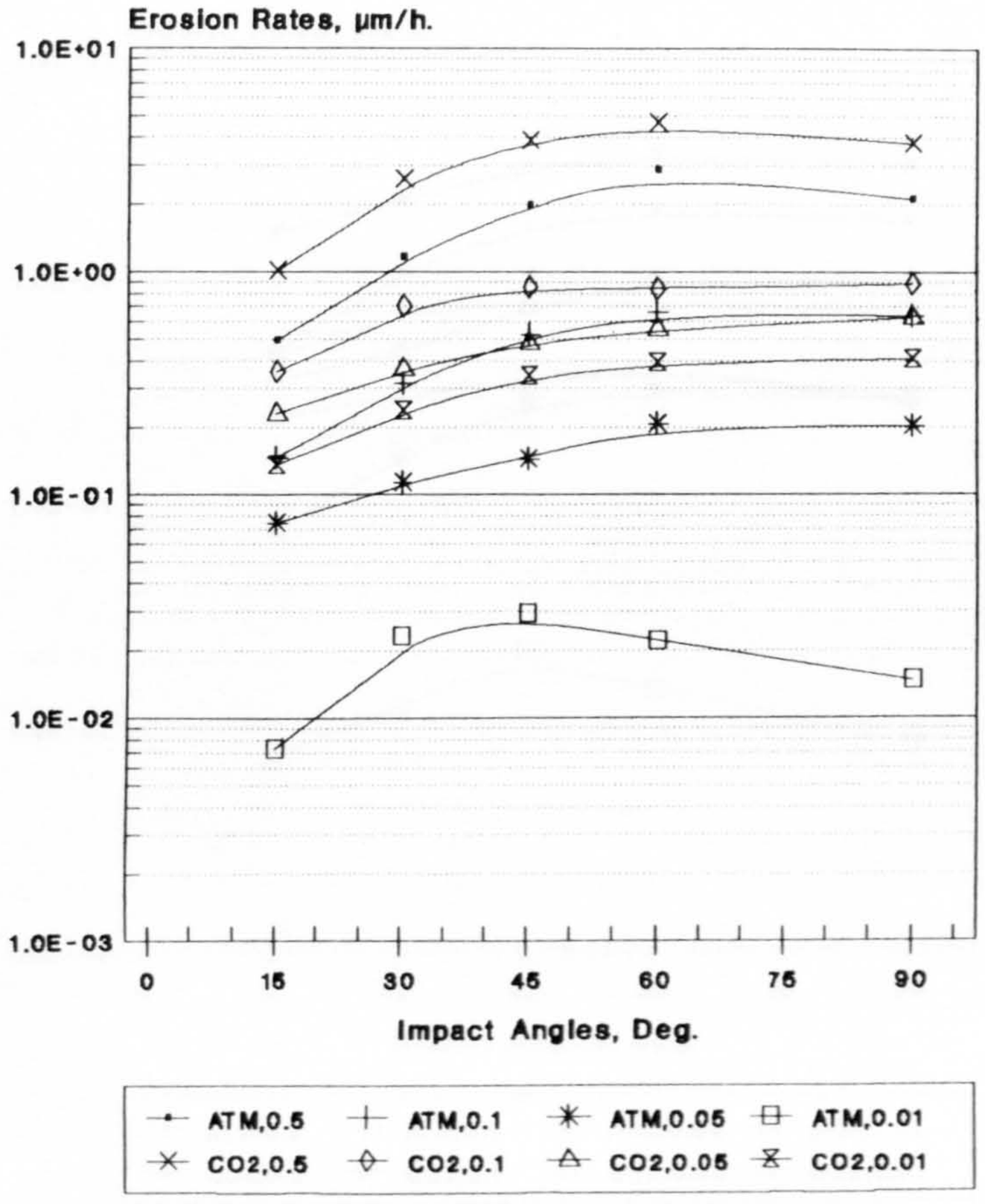

Figure 29
Erosion-corrosion rates for IN625

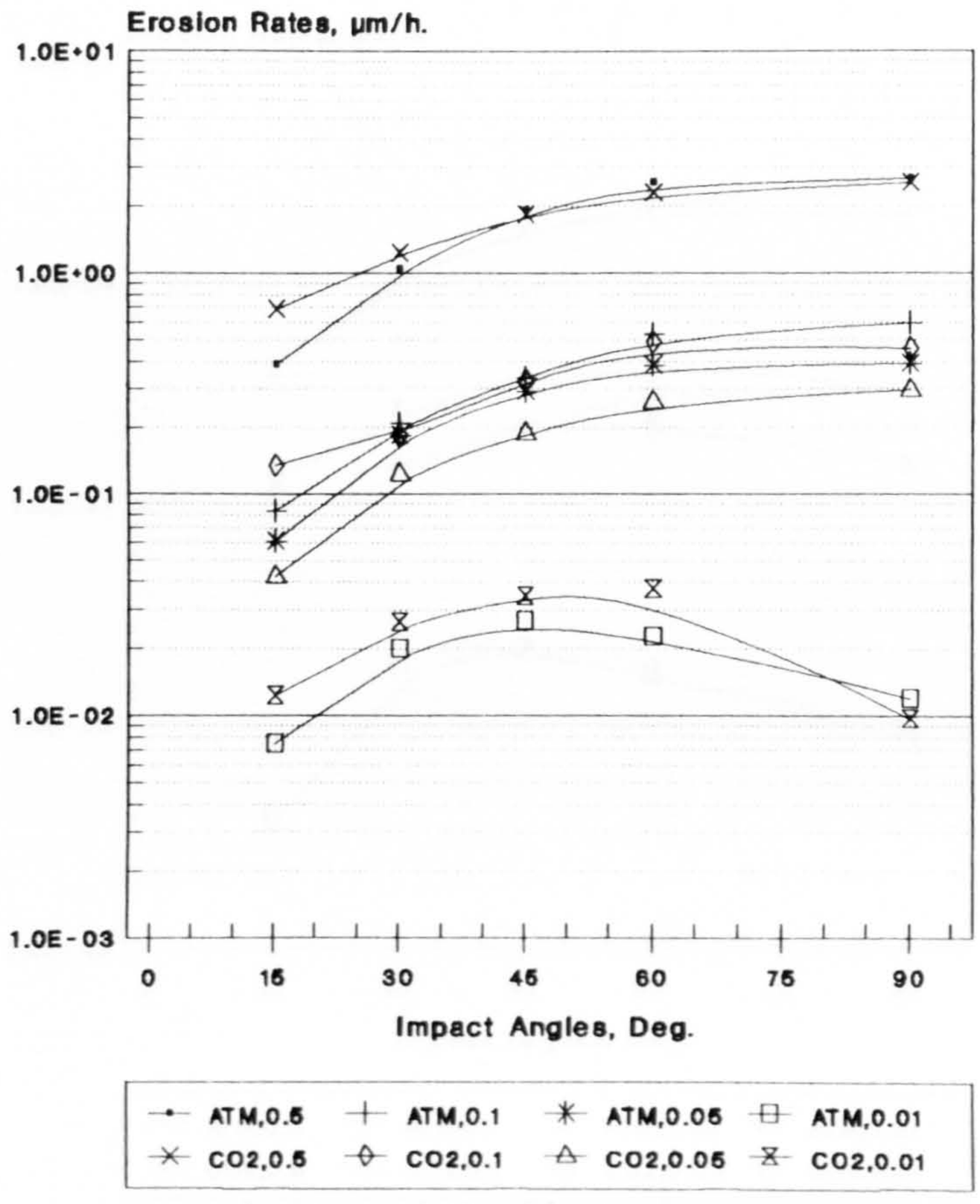

Figure 30
Erosion-corrosion rates for L80

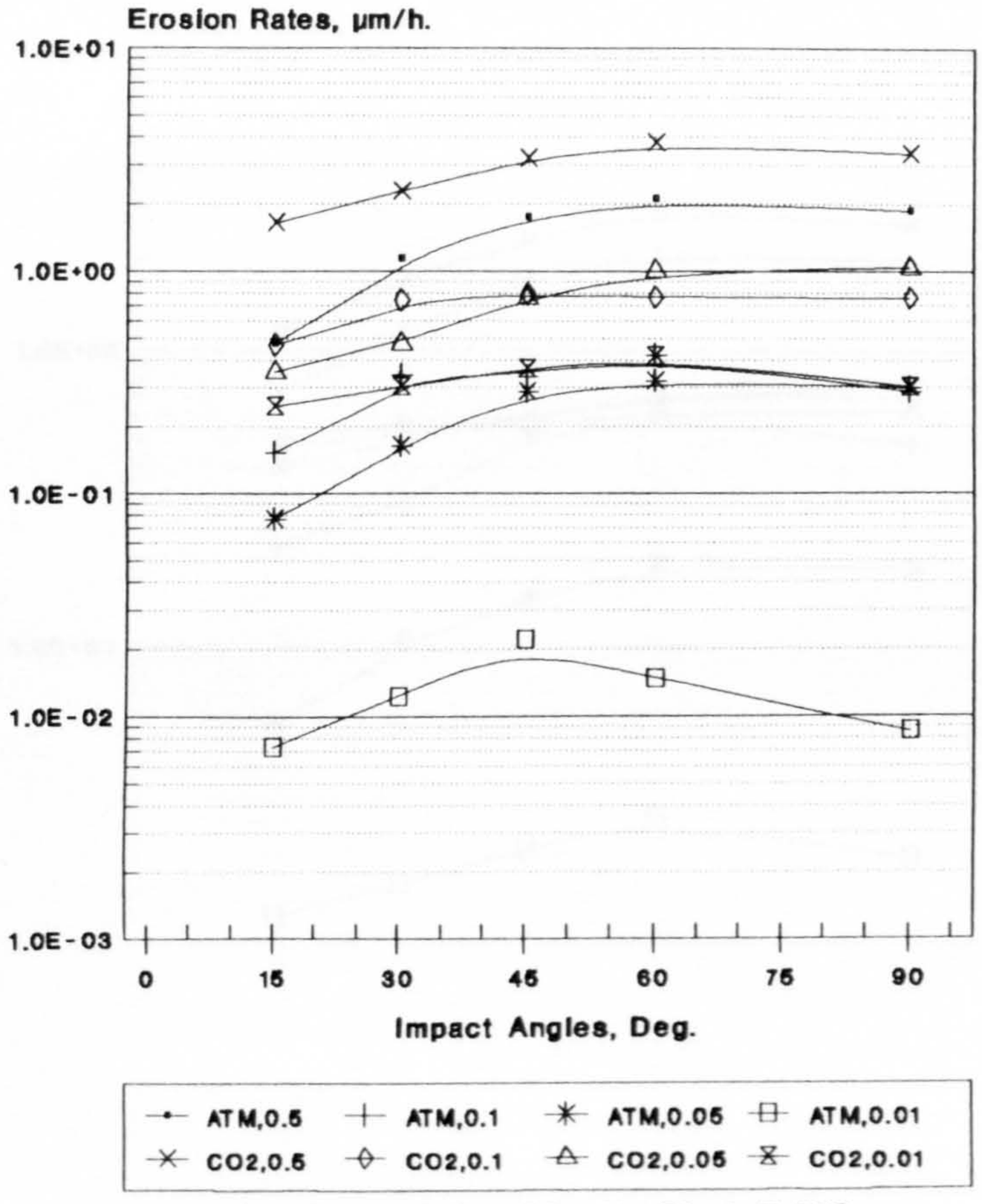

Figure 31
Erosion-corrosion rates for L80/13Cr

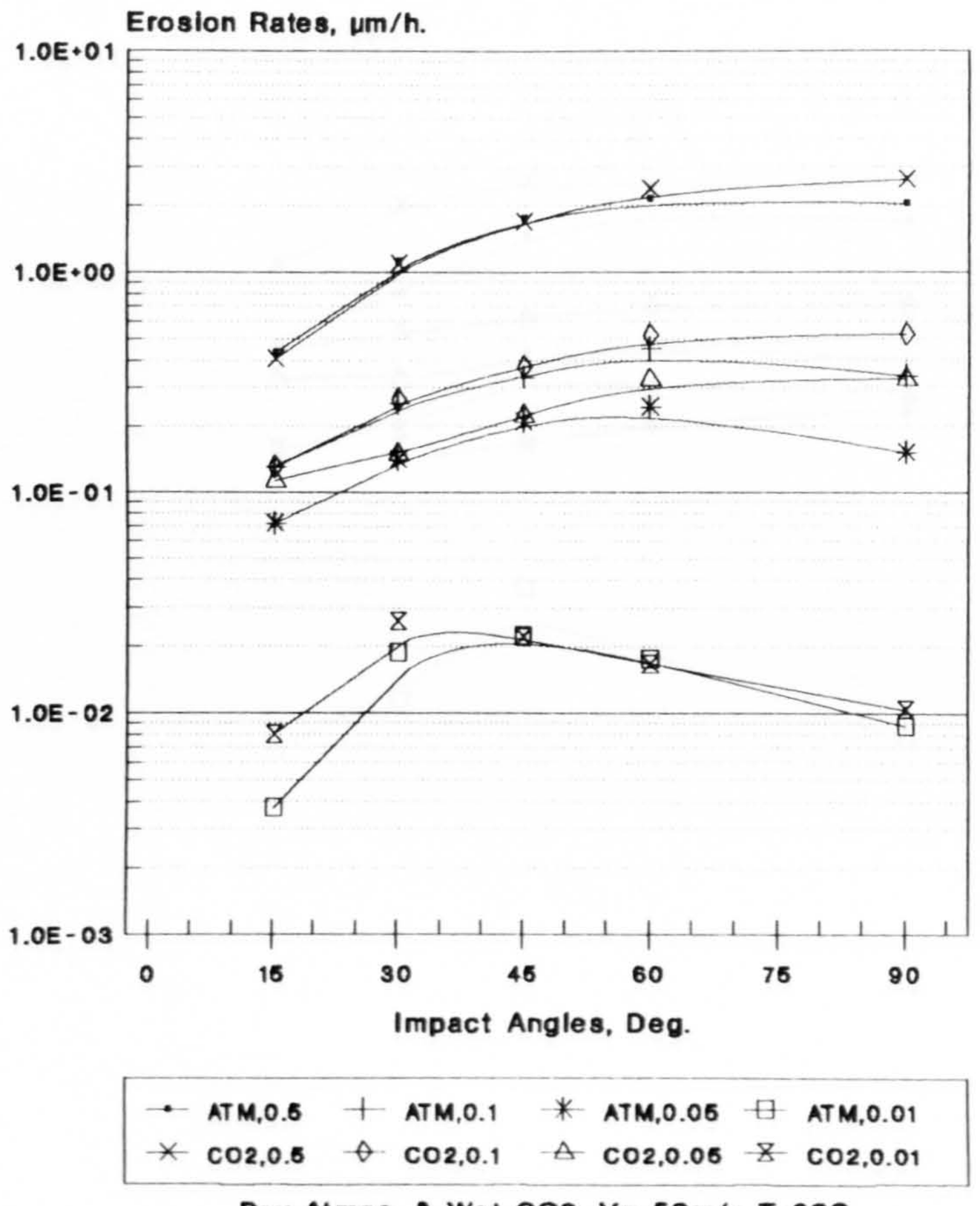

Figure 32
Erosion-corrosion rates for X65

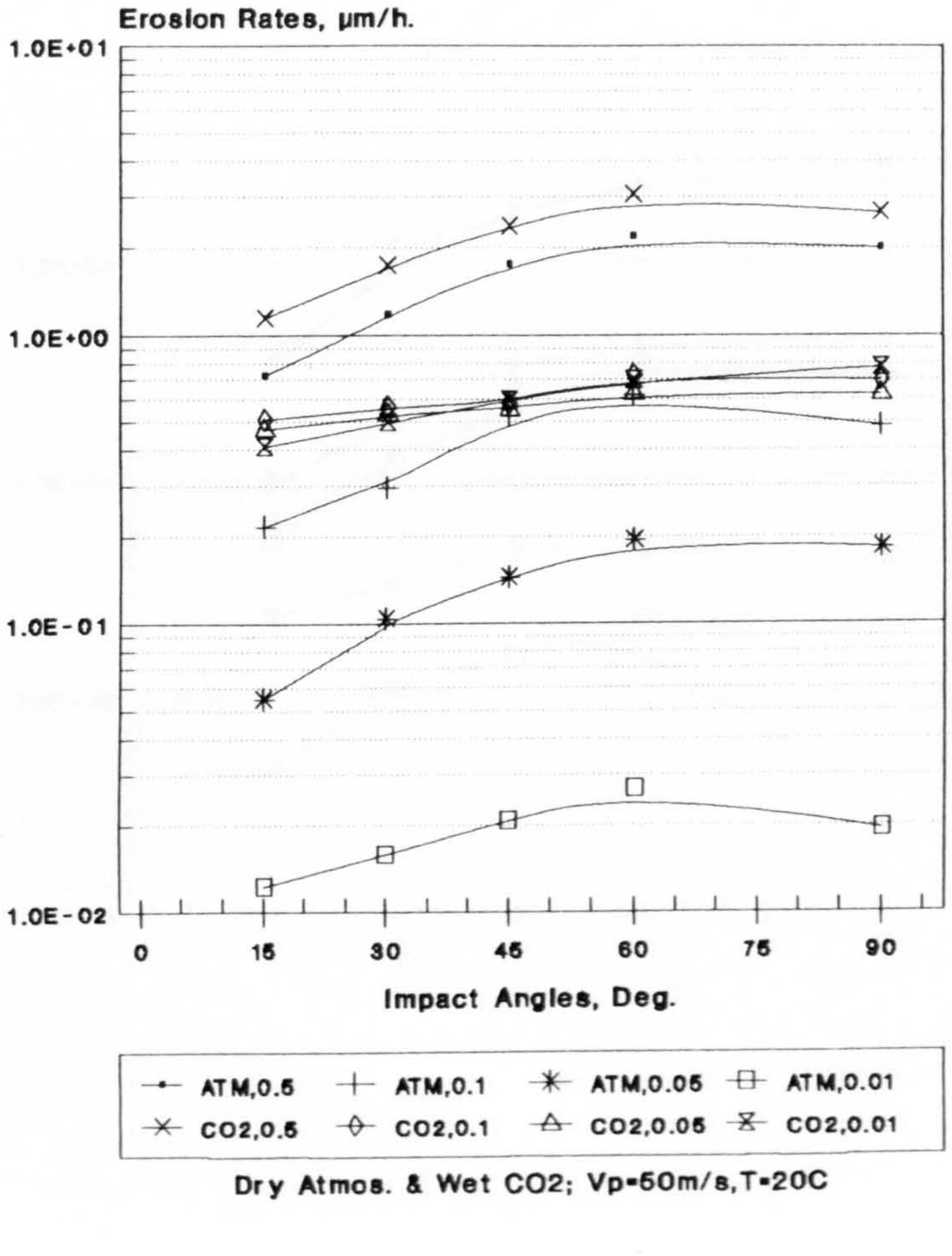

Dry Atmos. & Wet CO2; Vp=50m/s,T=20C

Figure 33
Erosion-corrosion rates for N80

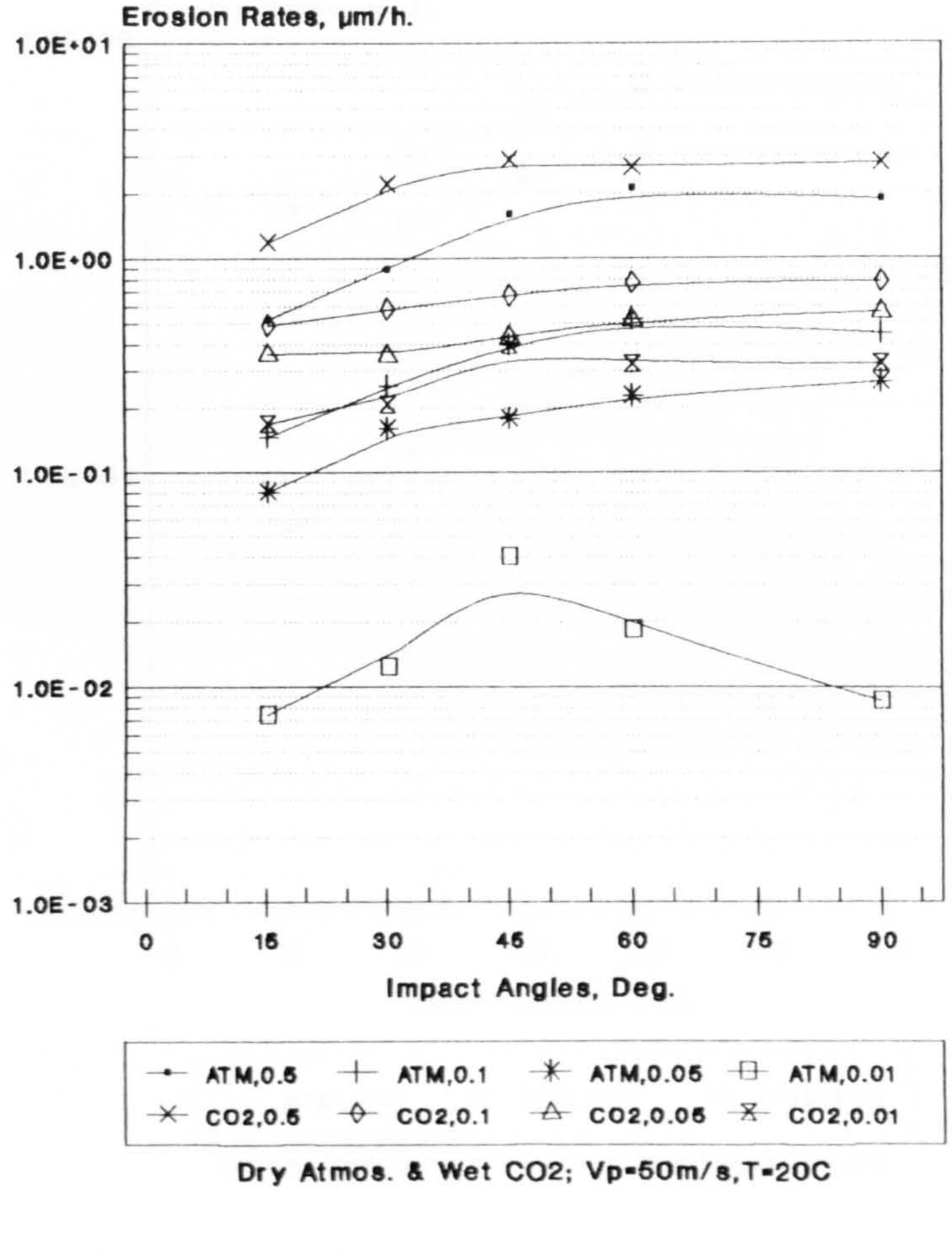

Dry Atmos. & Wet CO2; Vp=50m/s,T=20C

Figure 34
Erosion-corrosion rates for FERR255

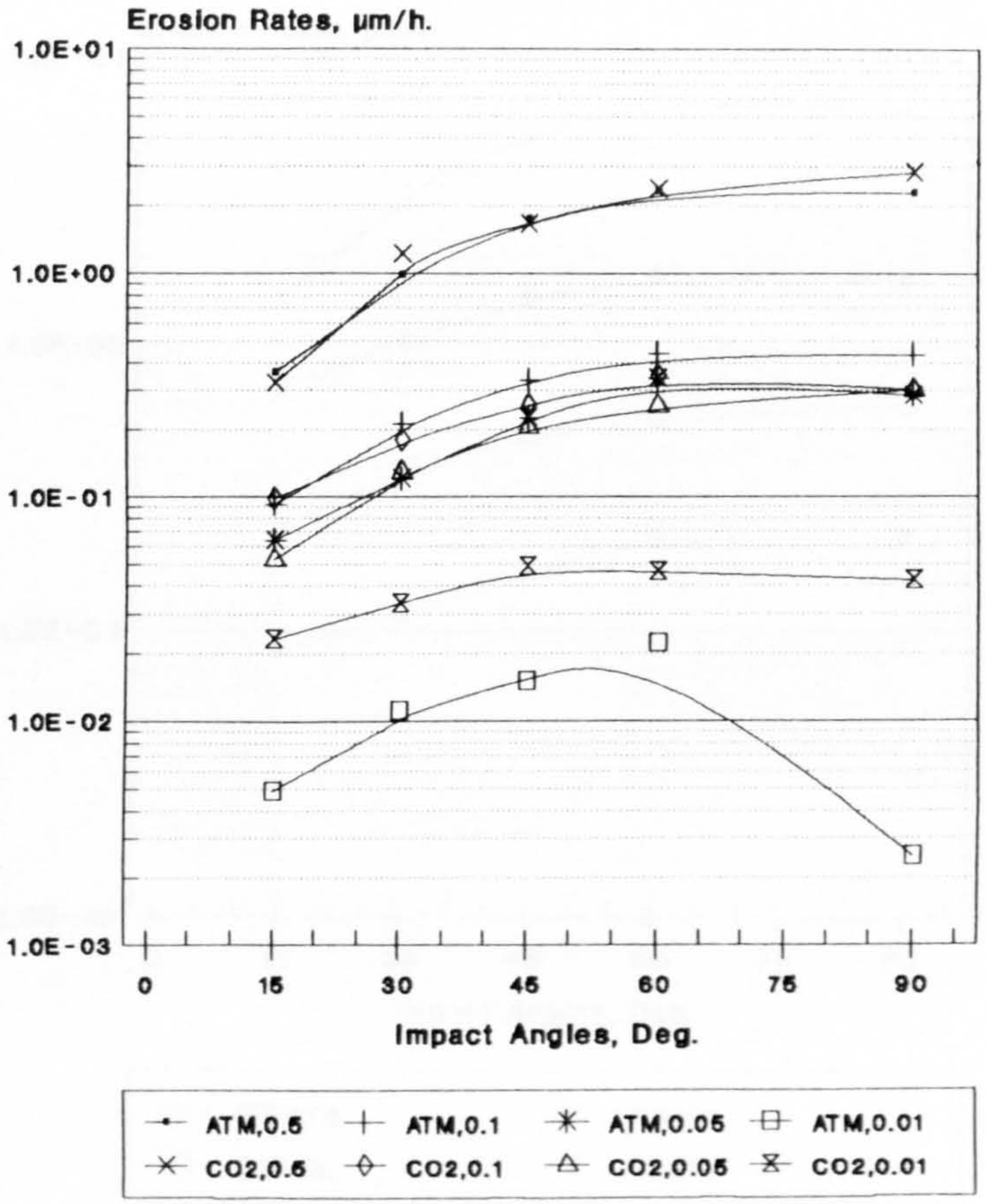

Dry Atmos. & Wet CO2; Vp=50m/s,T=20C

Figure 35
E/C rates for X52 at diff. temperature

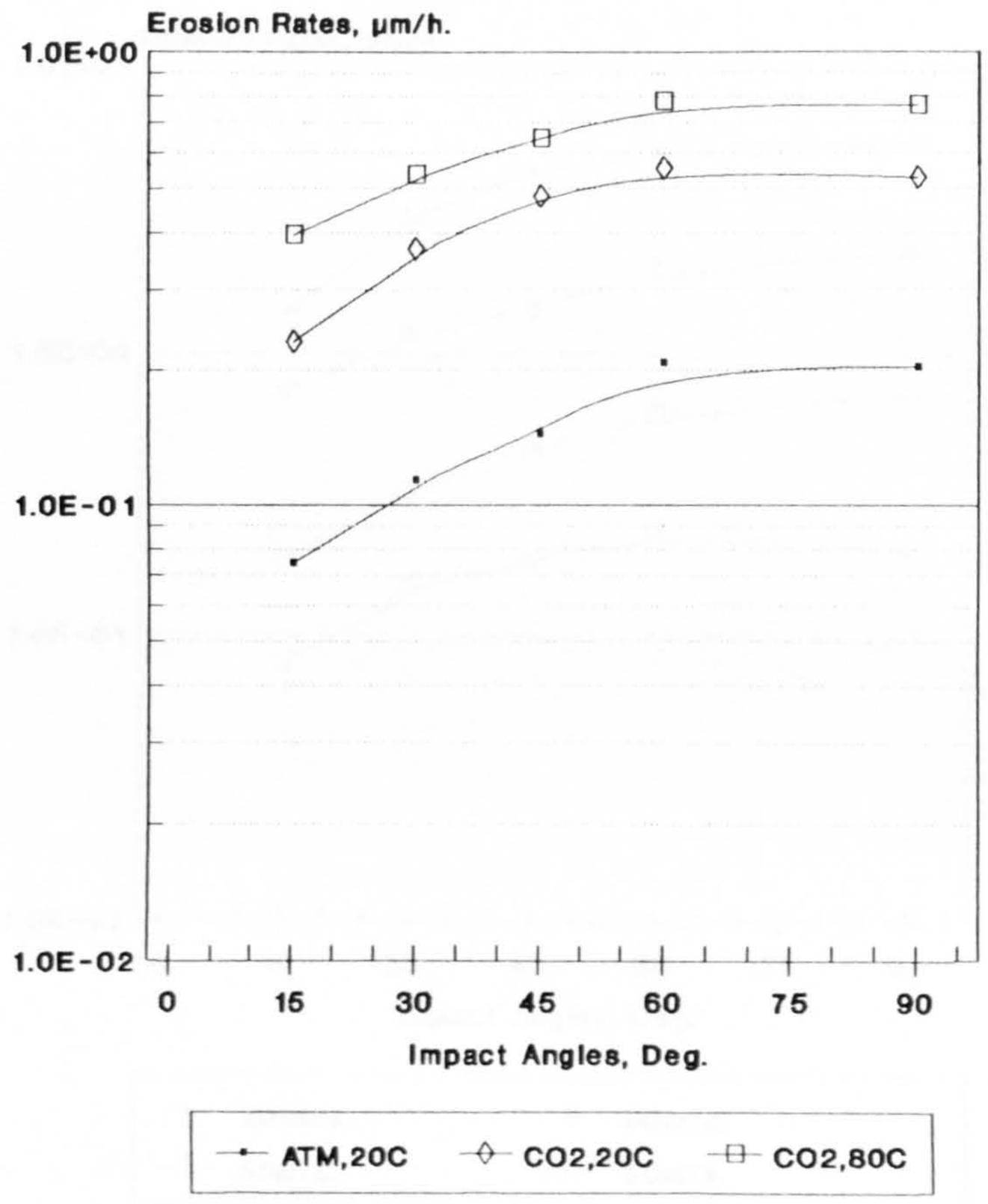

D/Atm.,Wet CO2 @ 20C/80C,Vp=50m/s,F=0.05

Figure 36
E/C rates for X52 at different velocity

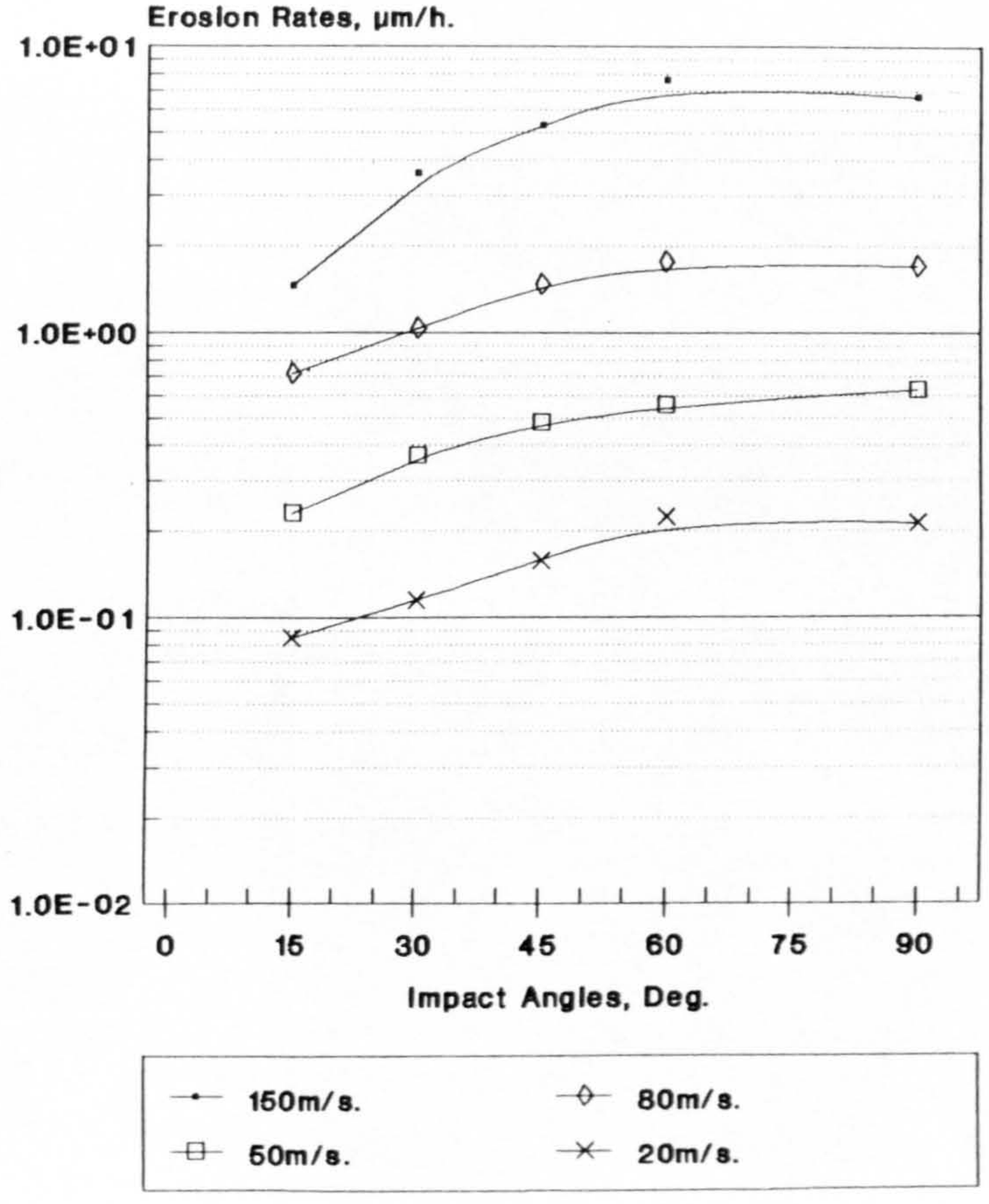

Figure 37
E/C rates for L80 at different velocity

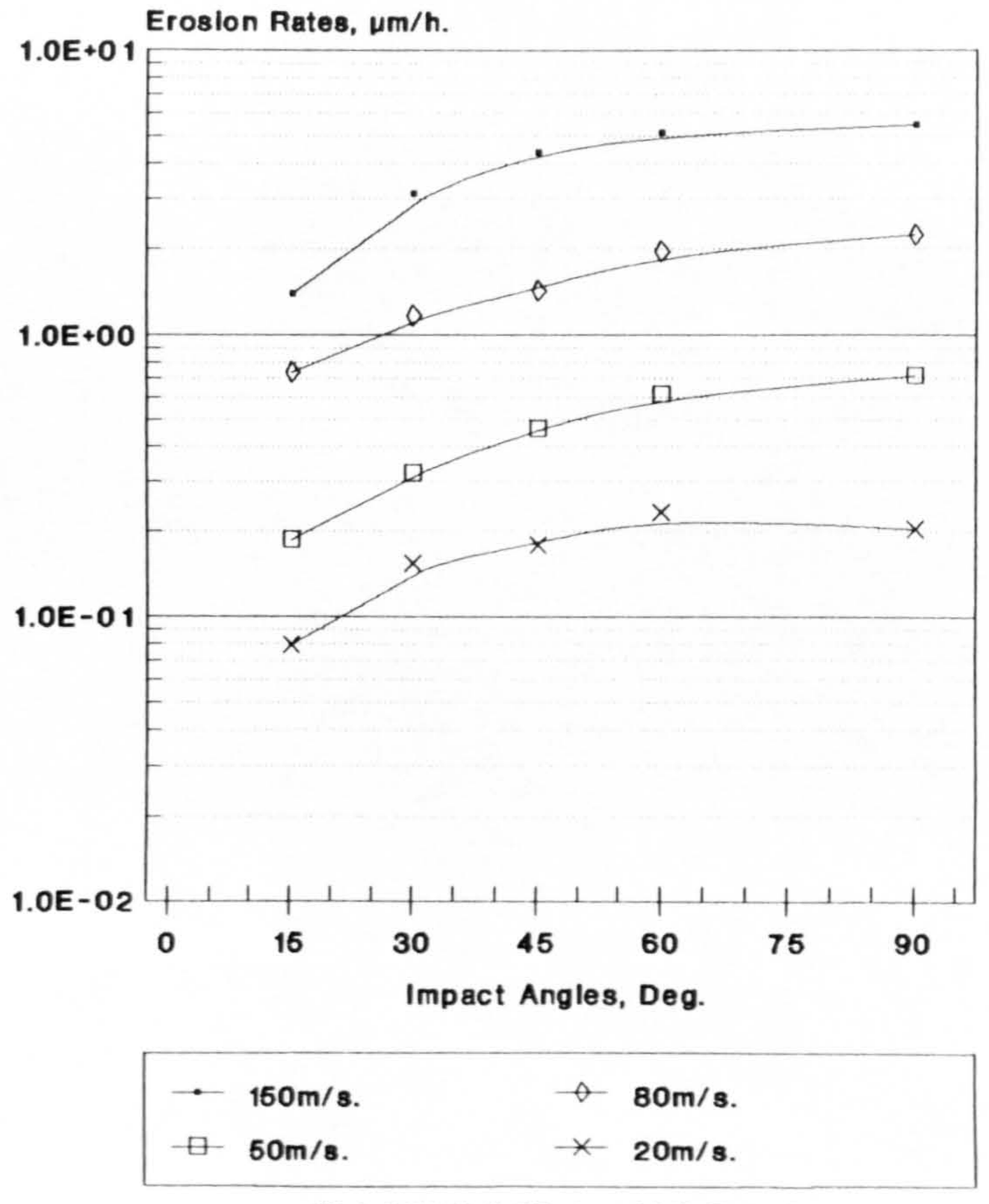

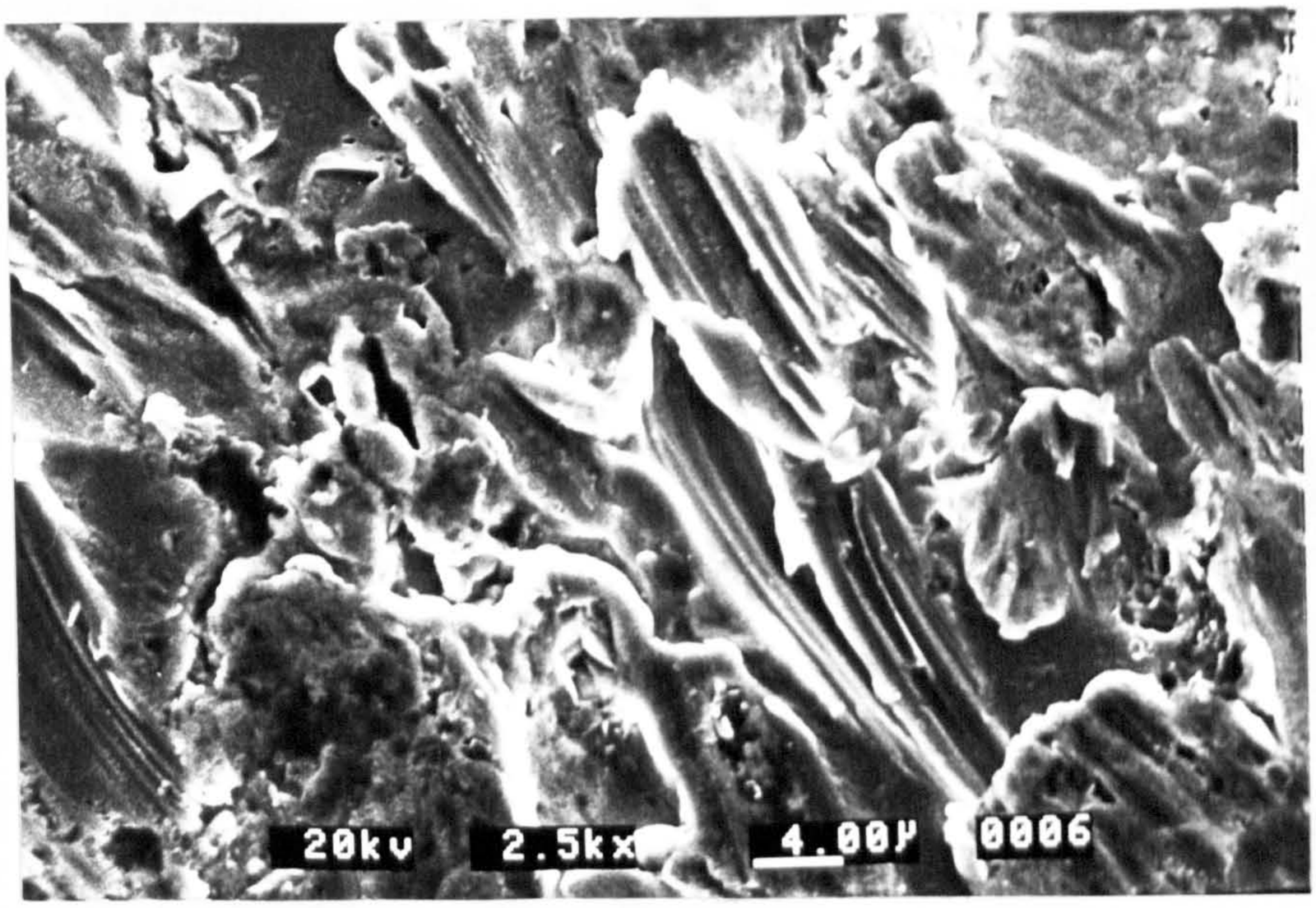

(a). 15° Impact angle.

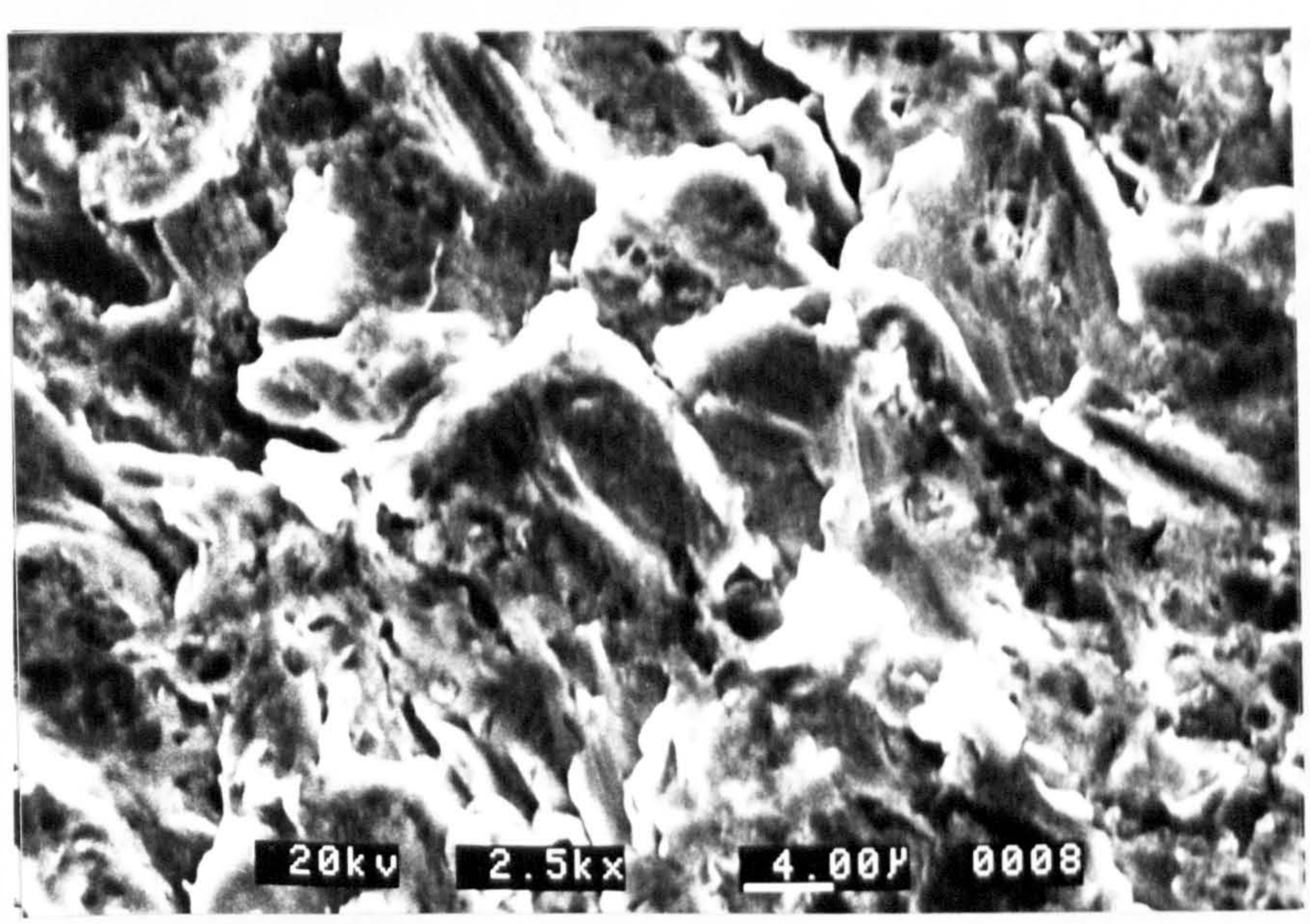

(b). 30° Impact angle.

Figure 38. Surface morphology of a C-Mn steel due to erosion by sand after 5h exposure.

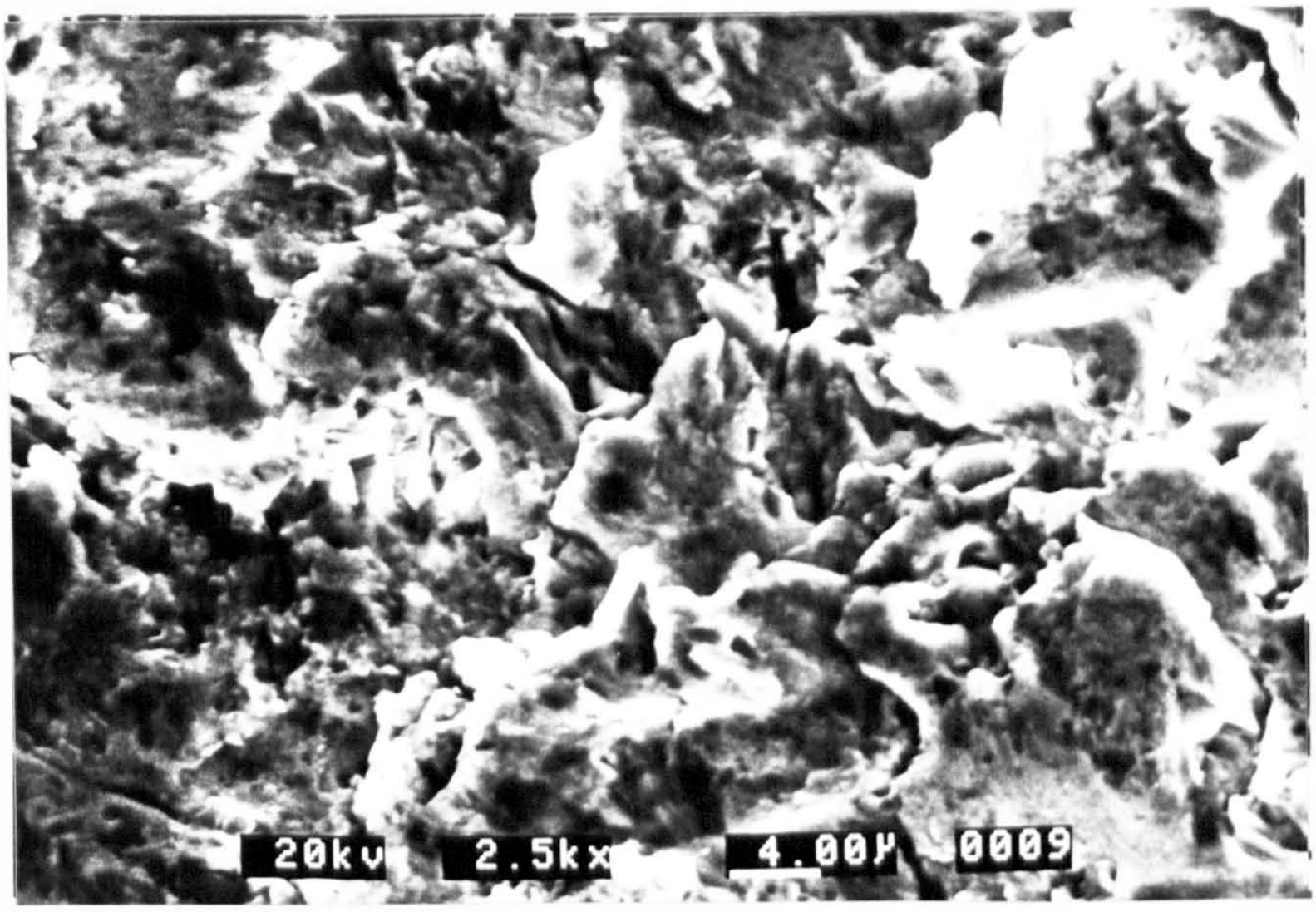

(c). 45° Impact angle.

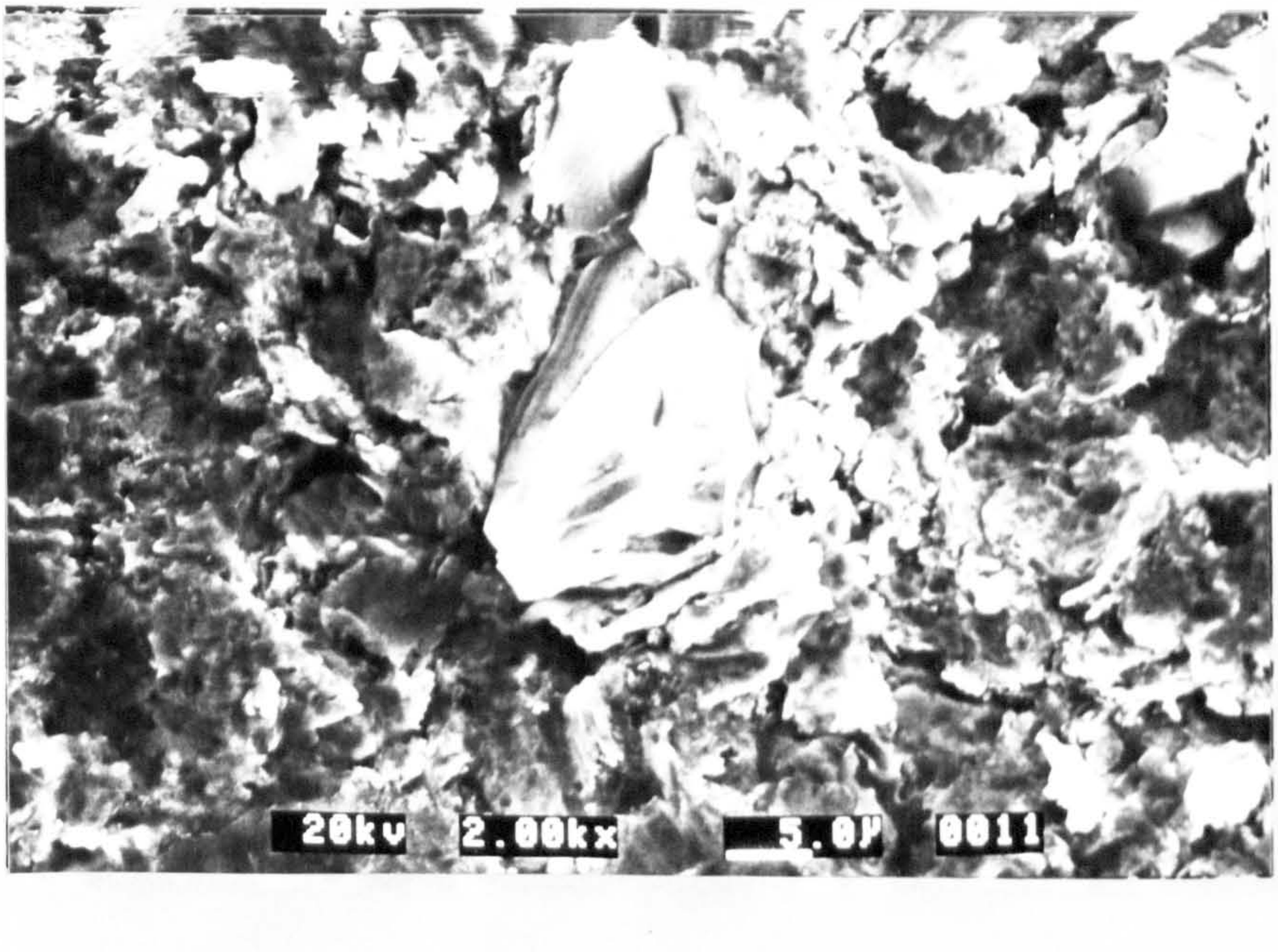

(d). 90° Impact angle.

Figure 38. Surface morphology of a C-Mn steel due to erosion by sand after 5h exposure.

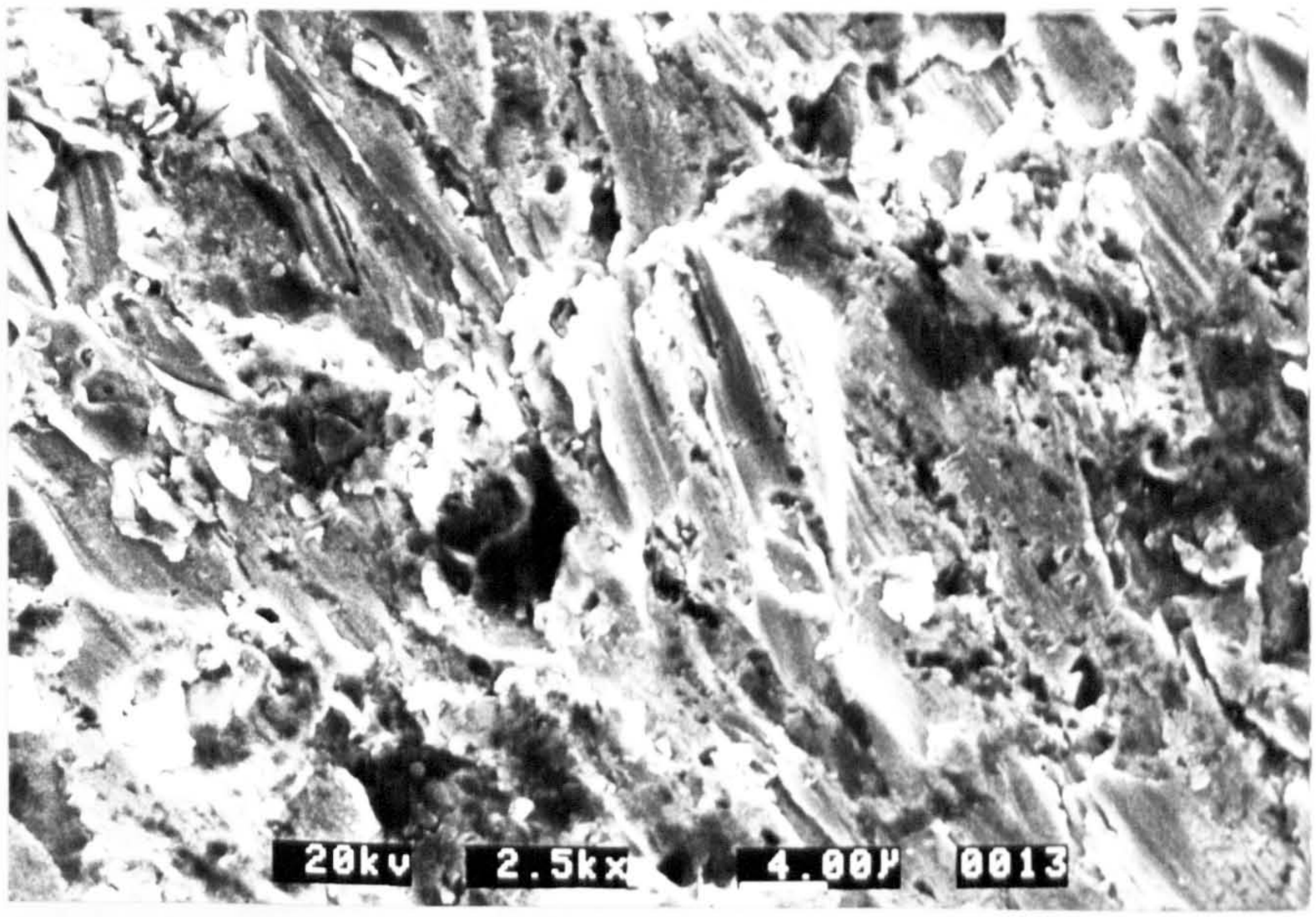

(a). 15° Impact angle.

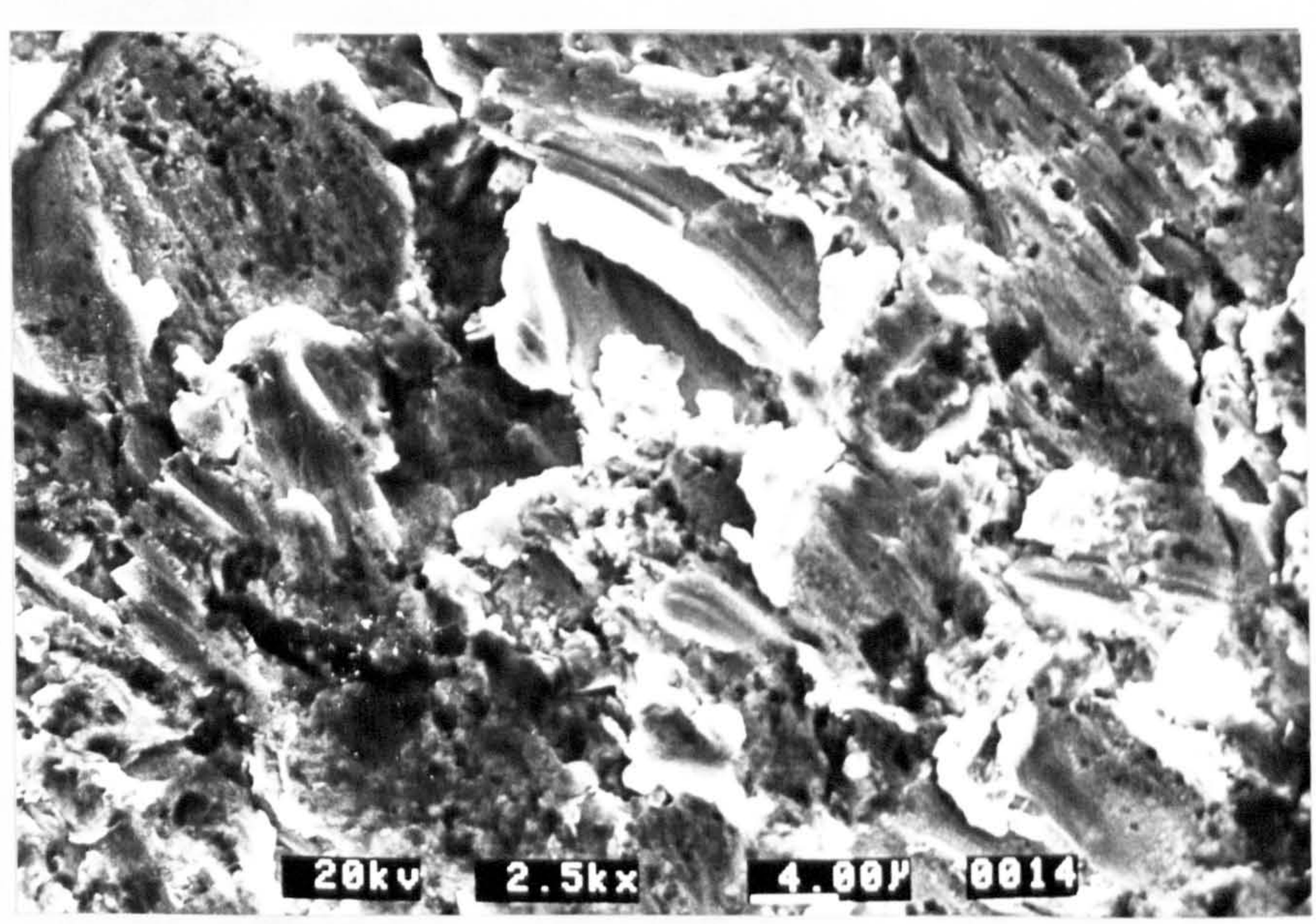

(b). 30° Impact angle.

Figure 39. Surface morphology of IN625 due to erosion by sand after 5h exposure.

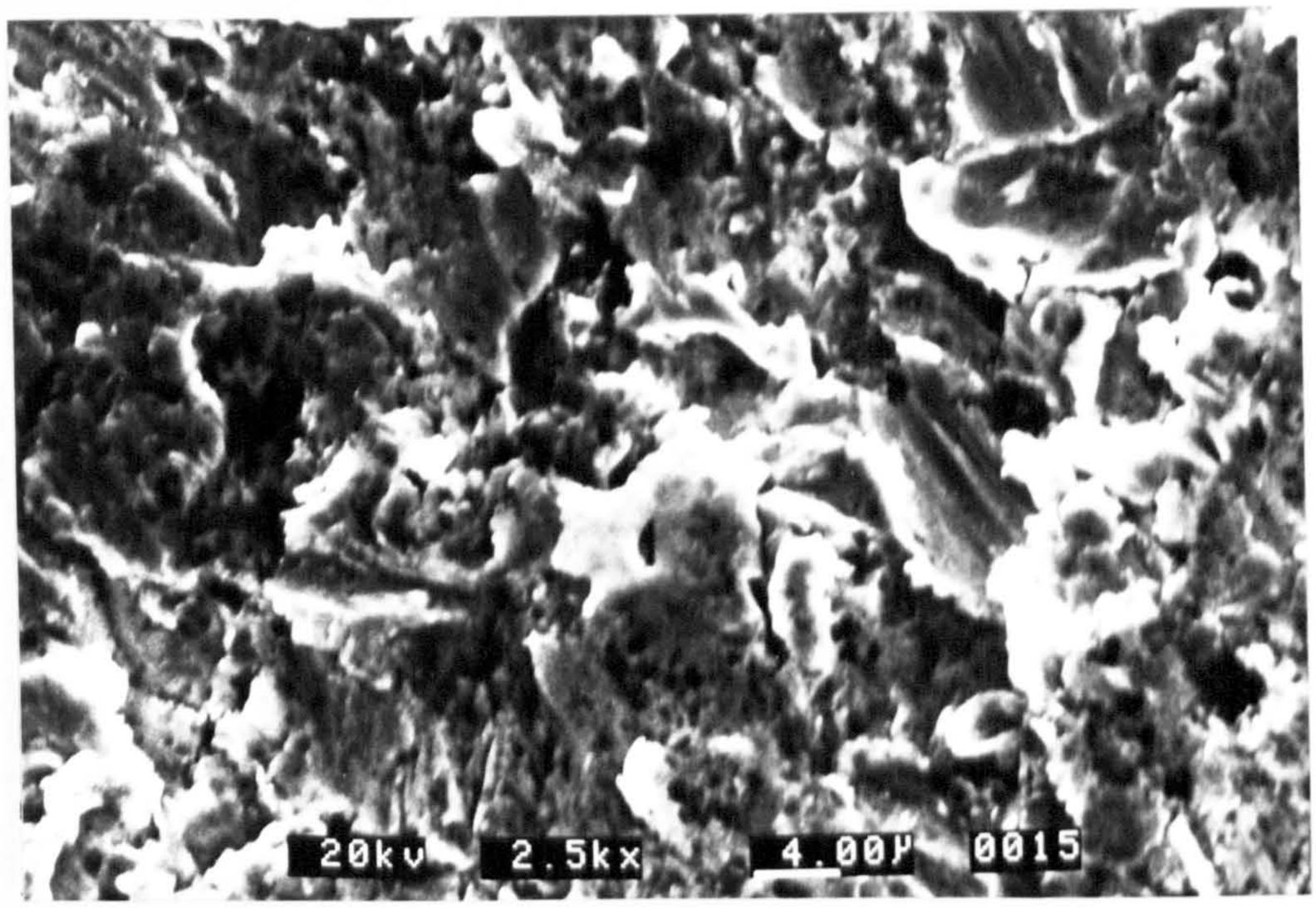

(c). 45° Impact angle.

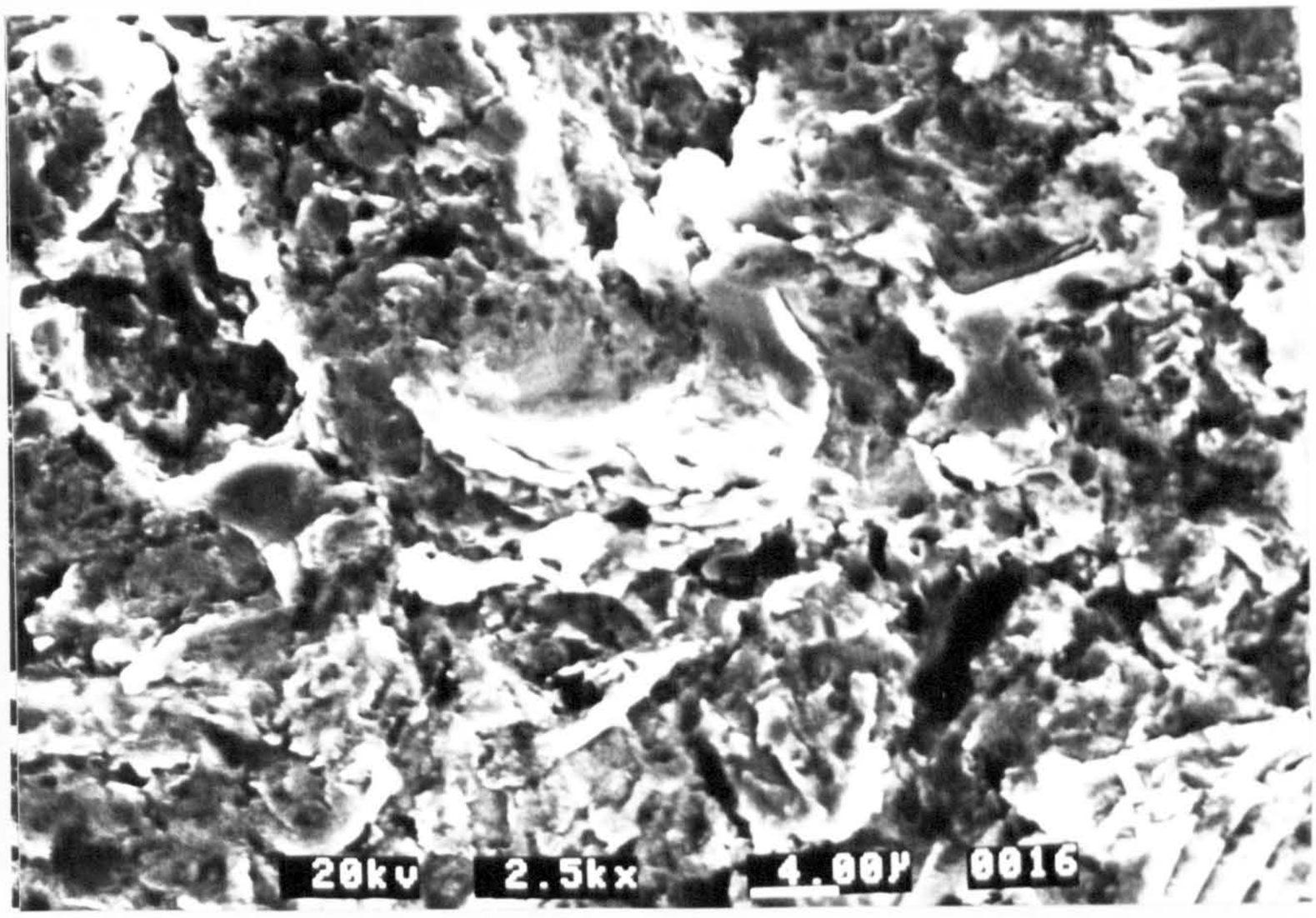

(d). 90° Impact angle.

Figure 39. Surface morphology of IN625 due to erosion by sand after 5h exposure.

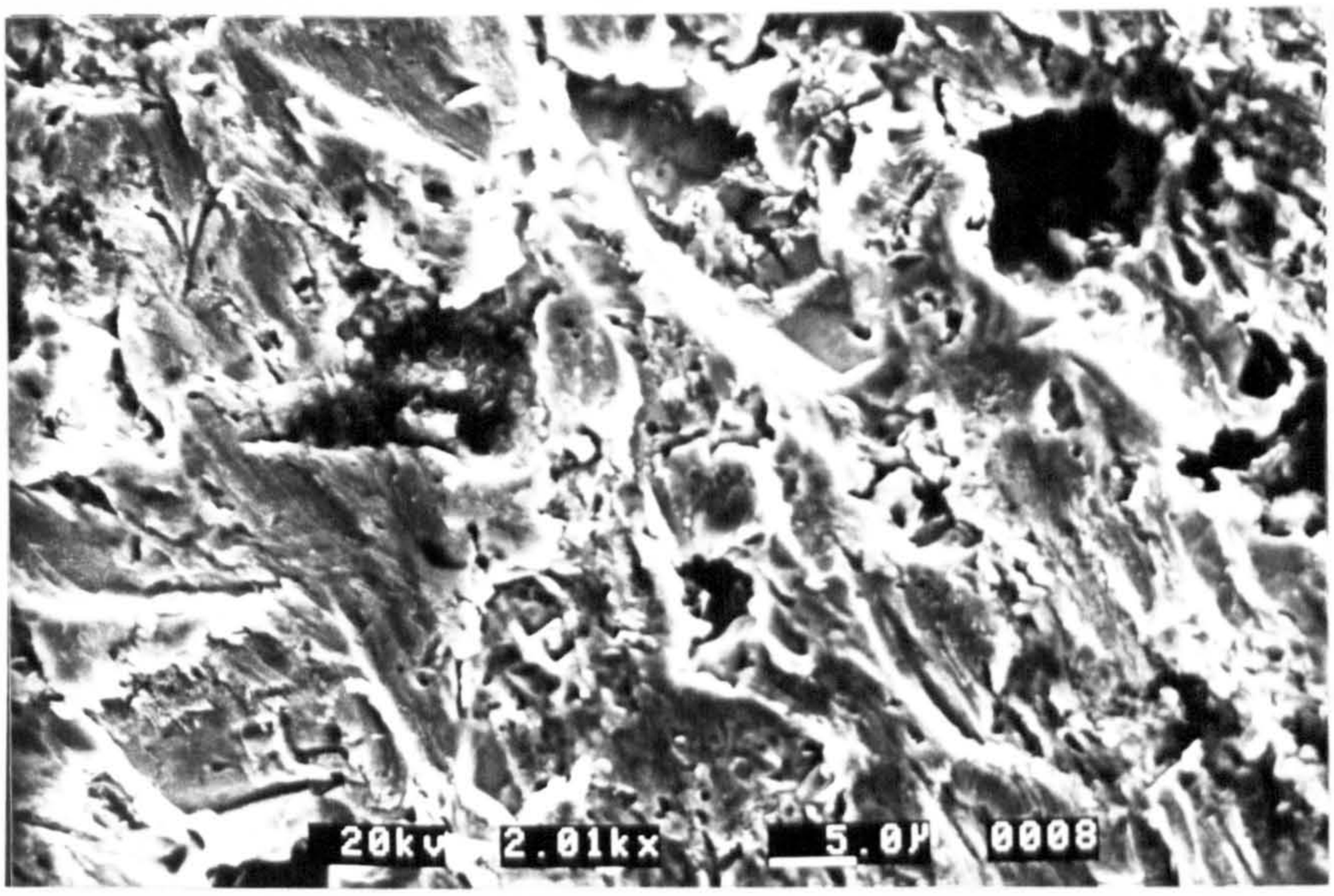

(a). 15° Impact angle.

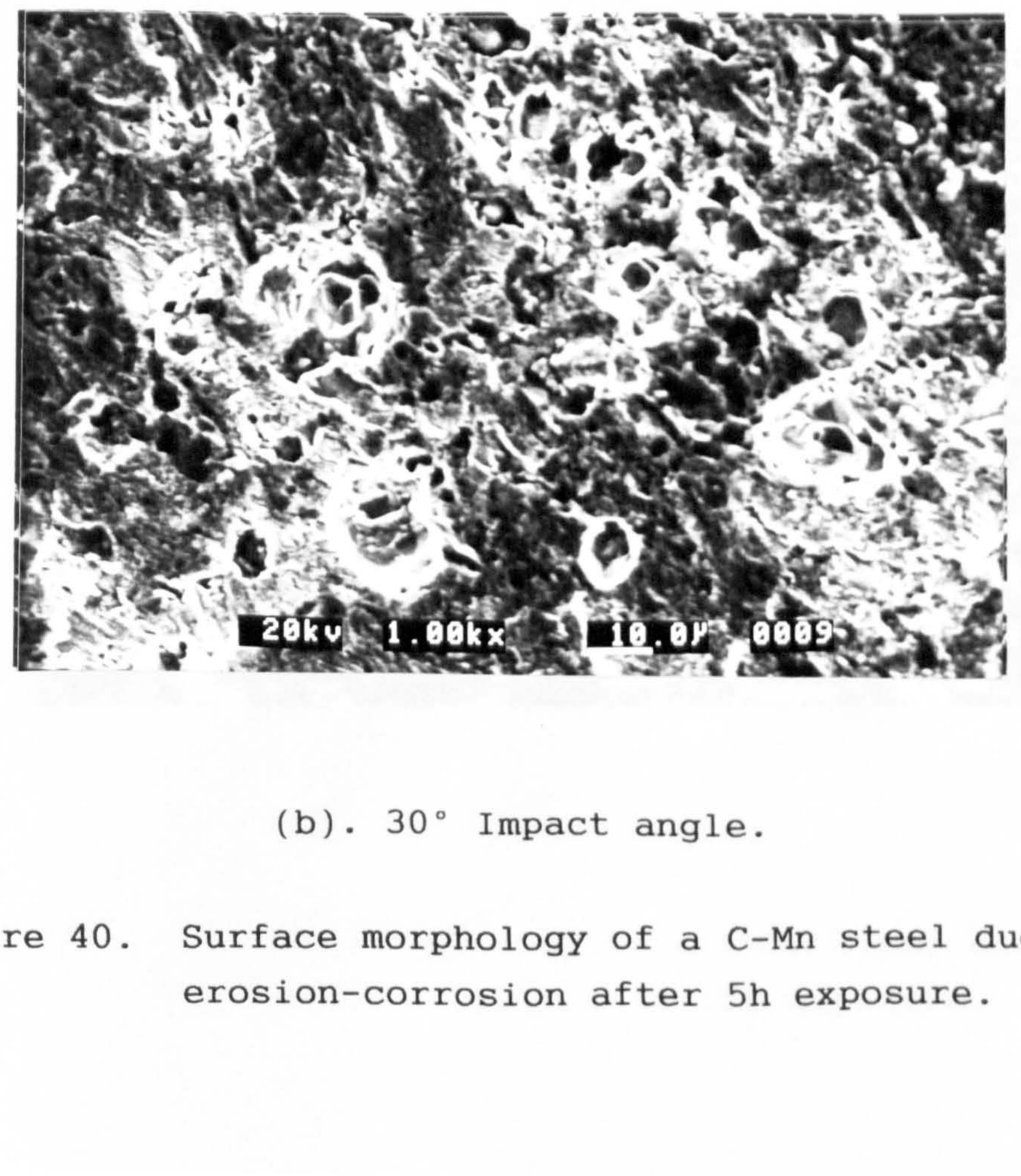

(b). 30° Impact angle.

Figure 40. Surface morphology of a C-Mn steel due to erosion-corrosion after 5h exposure.

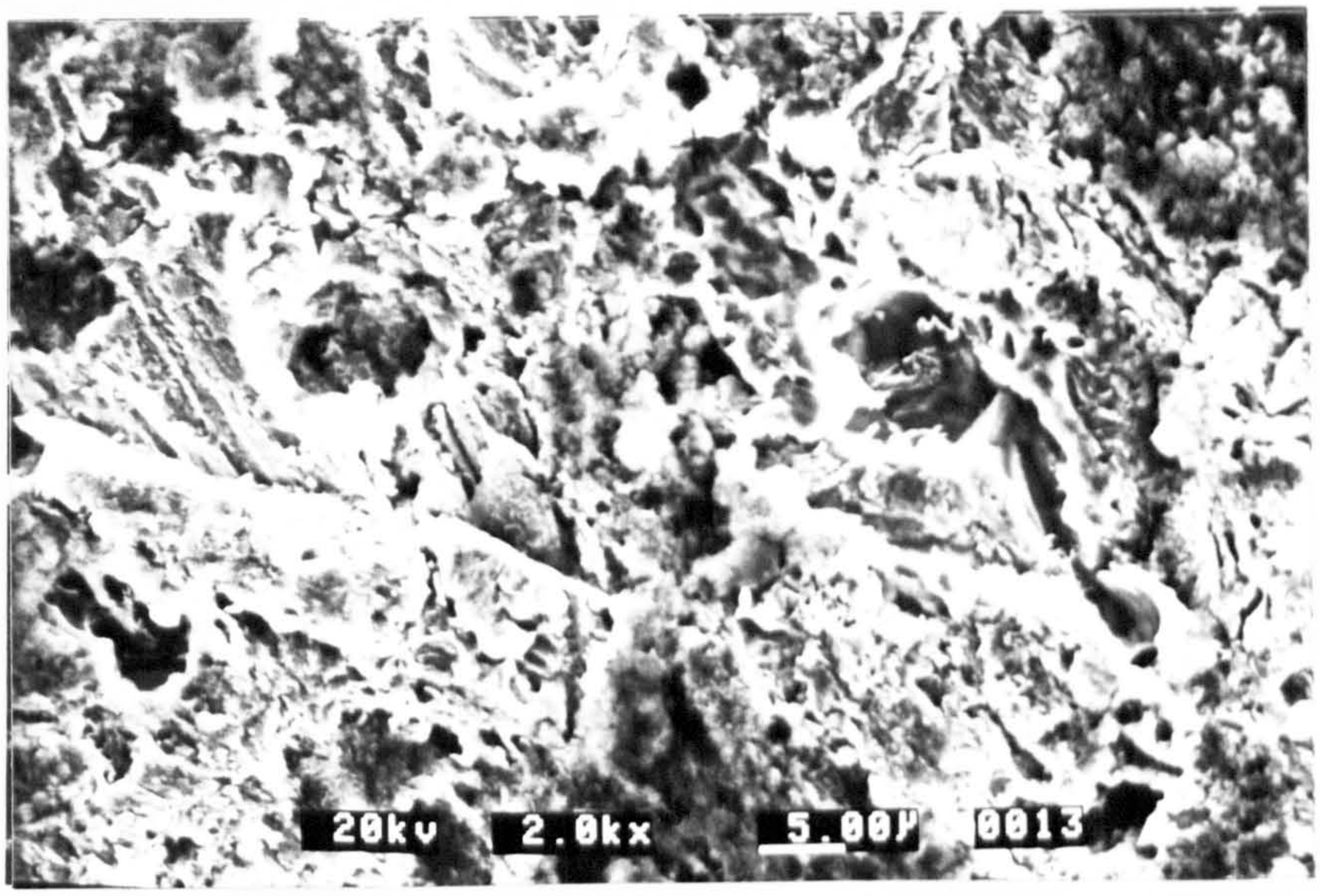

(c). 45° Impact angle.

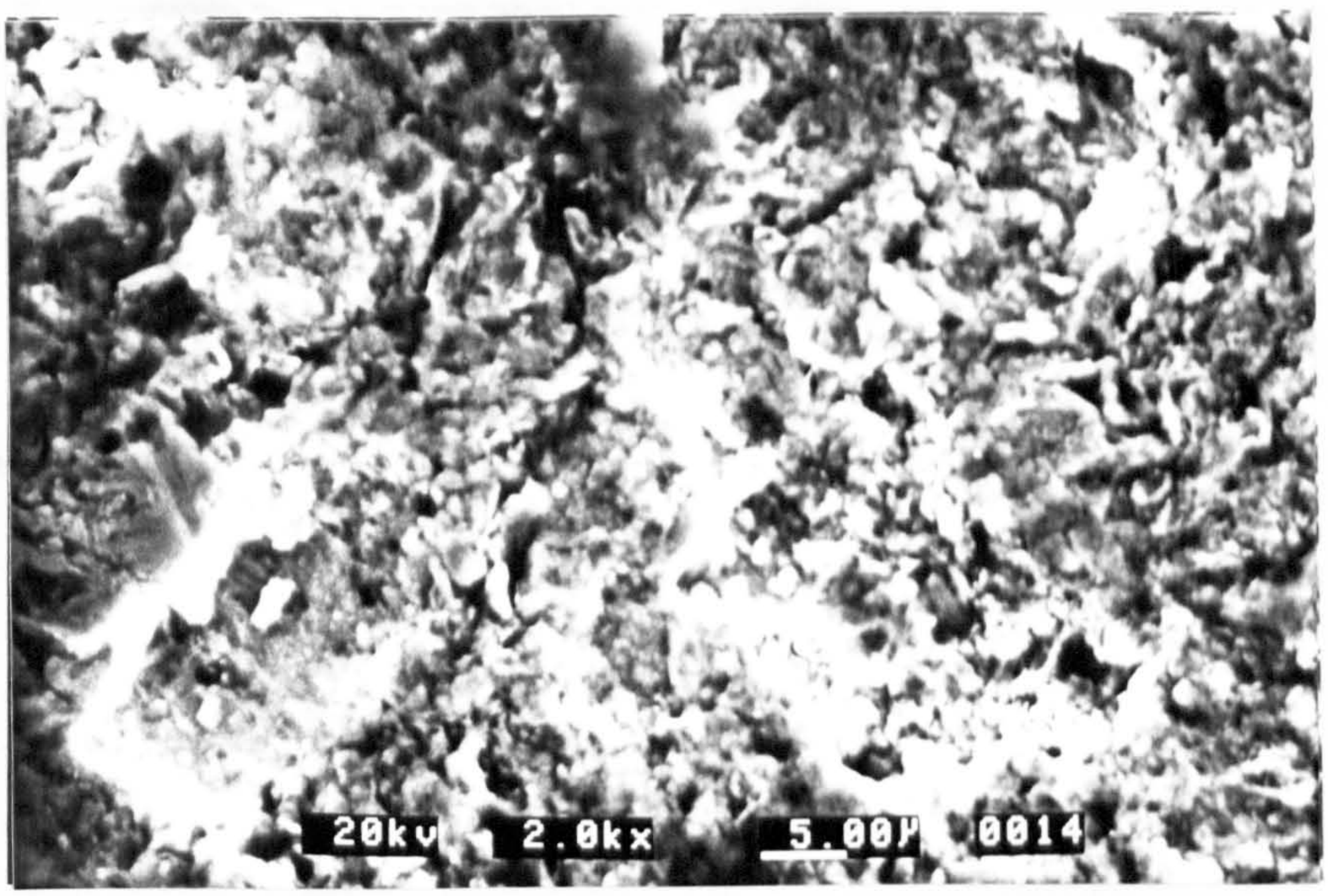

(d). 90° Impact angle.

Figure 40. Surface morphology of a C-Mn steel due to erosion-corrosion after 5h exposure.

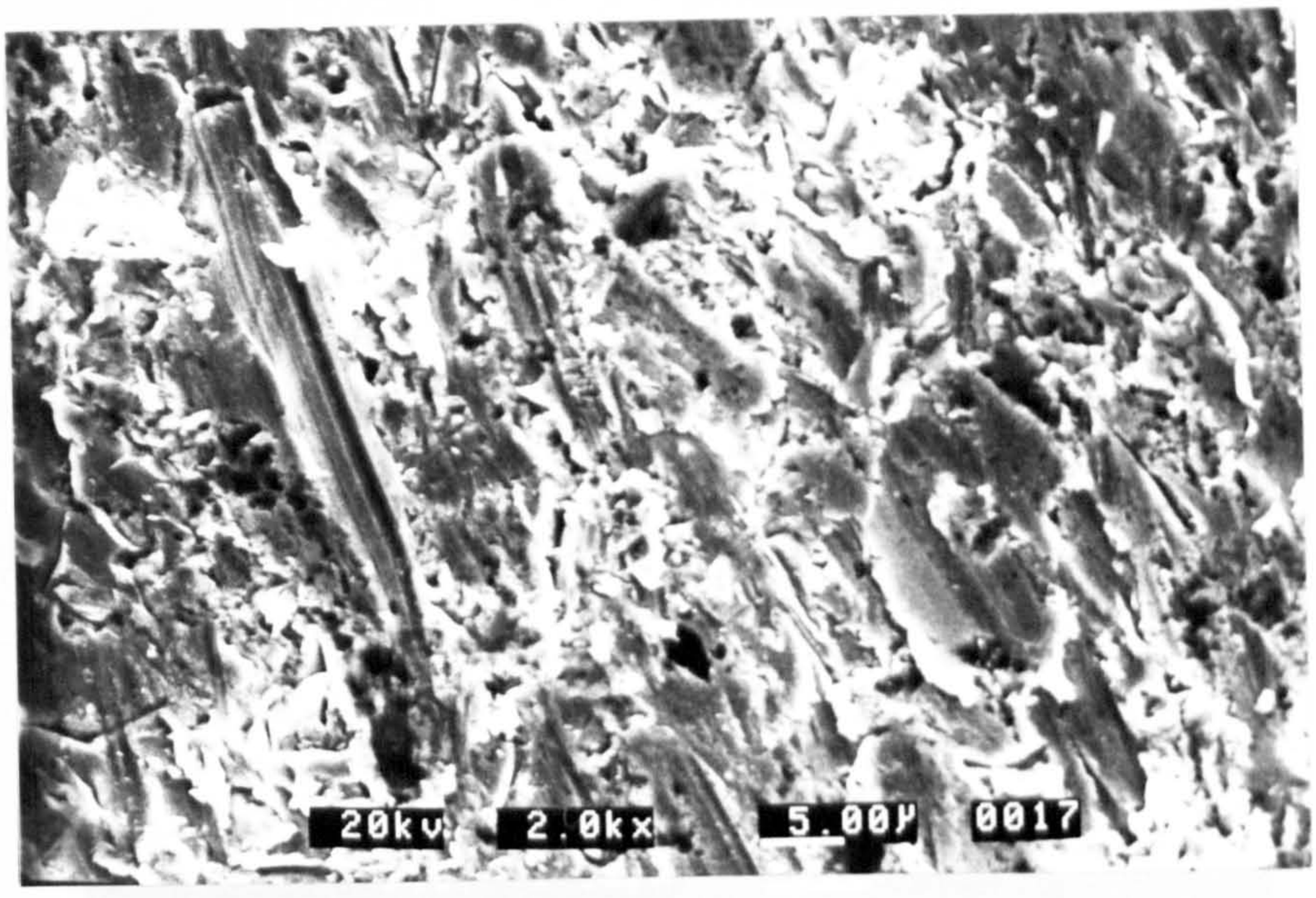

(a). 15° Impact angle.

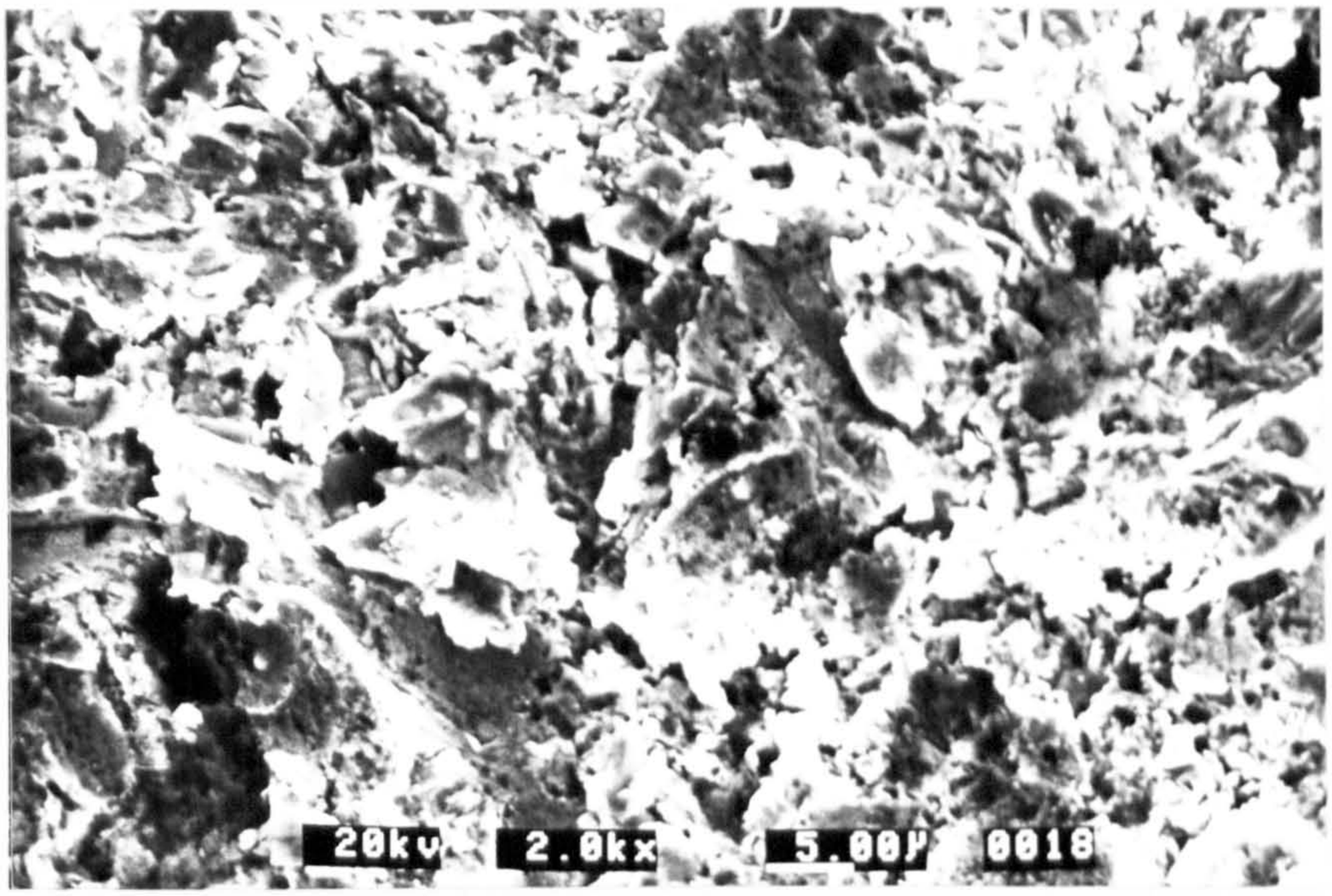

(b). 90° Impact angle.

Figure 41. Surface morphology of IN625 due to erosion-corrosion after 5h exposure.

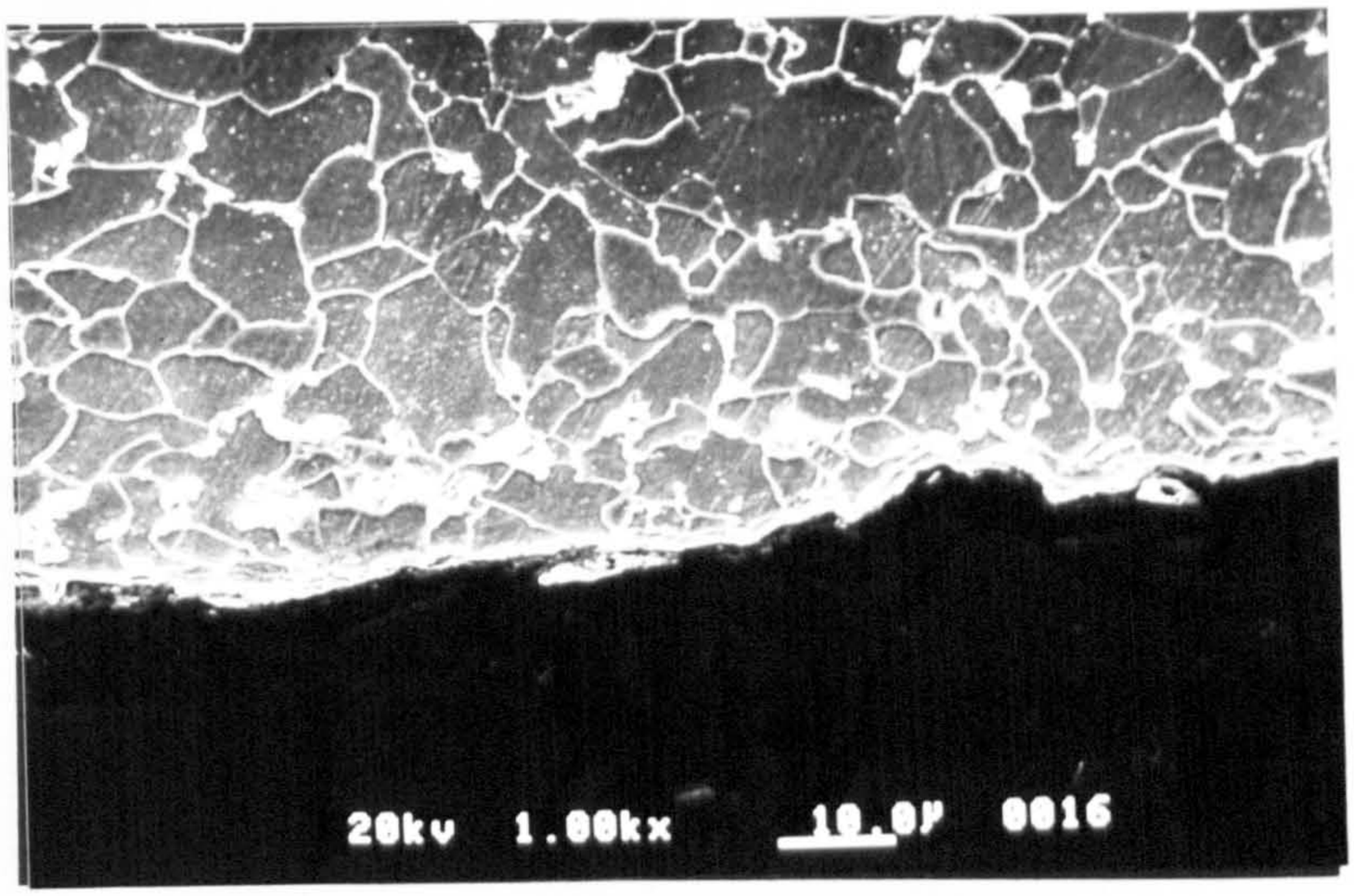

(a). X52 and 15° Impact angle.

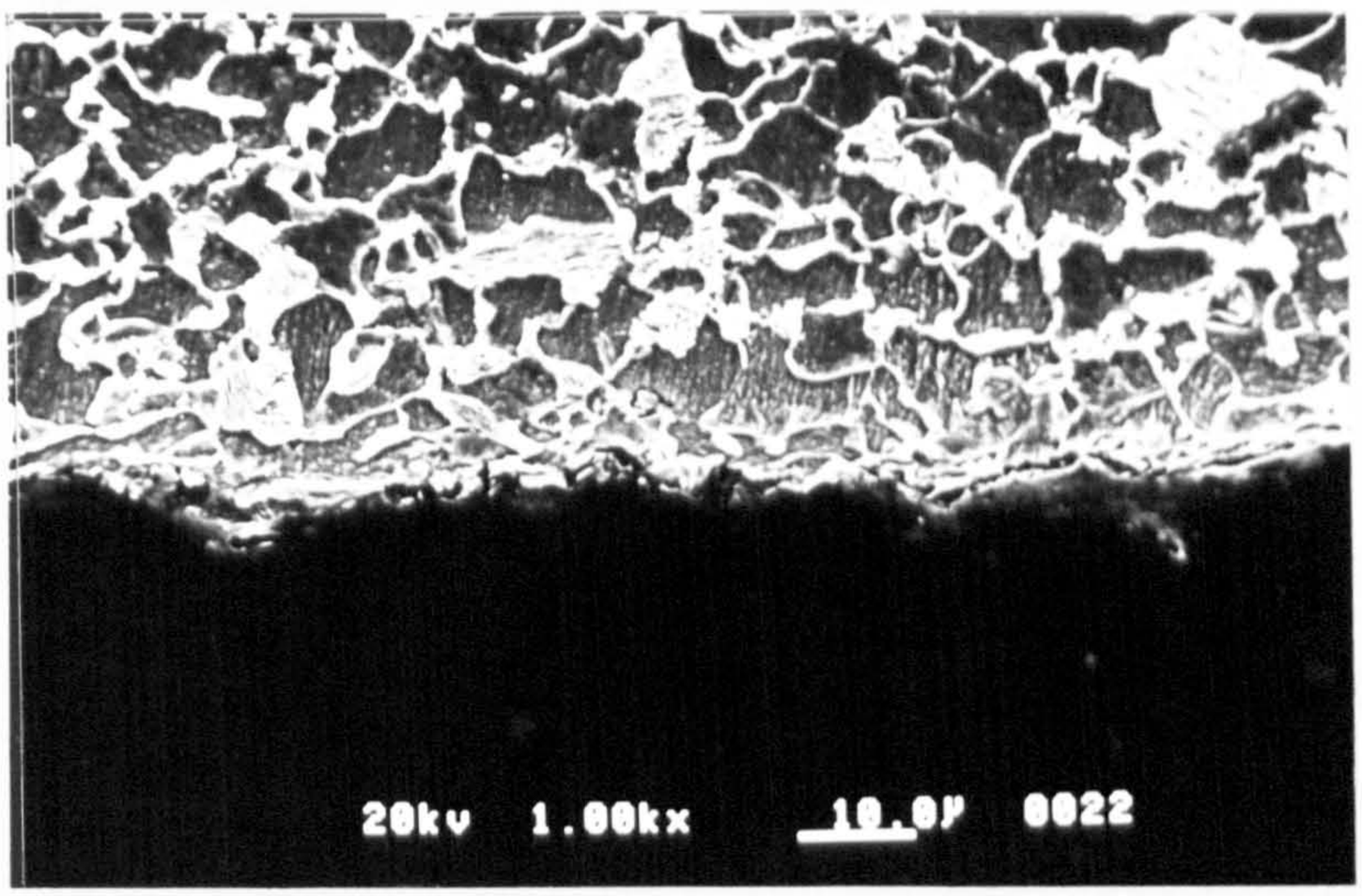

(b). X52 and 30° Impact angle.

Figure 42. Cross-sections of erosion-corrosion surfaces.

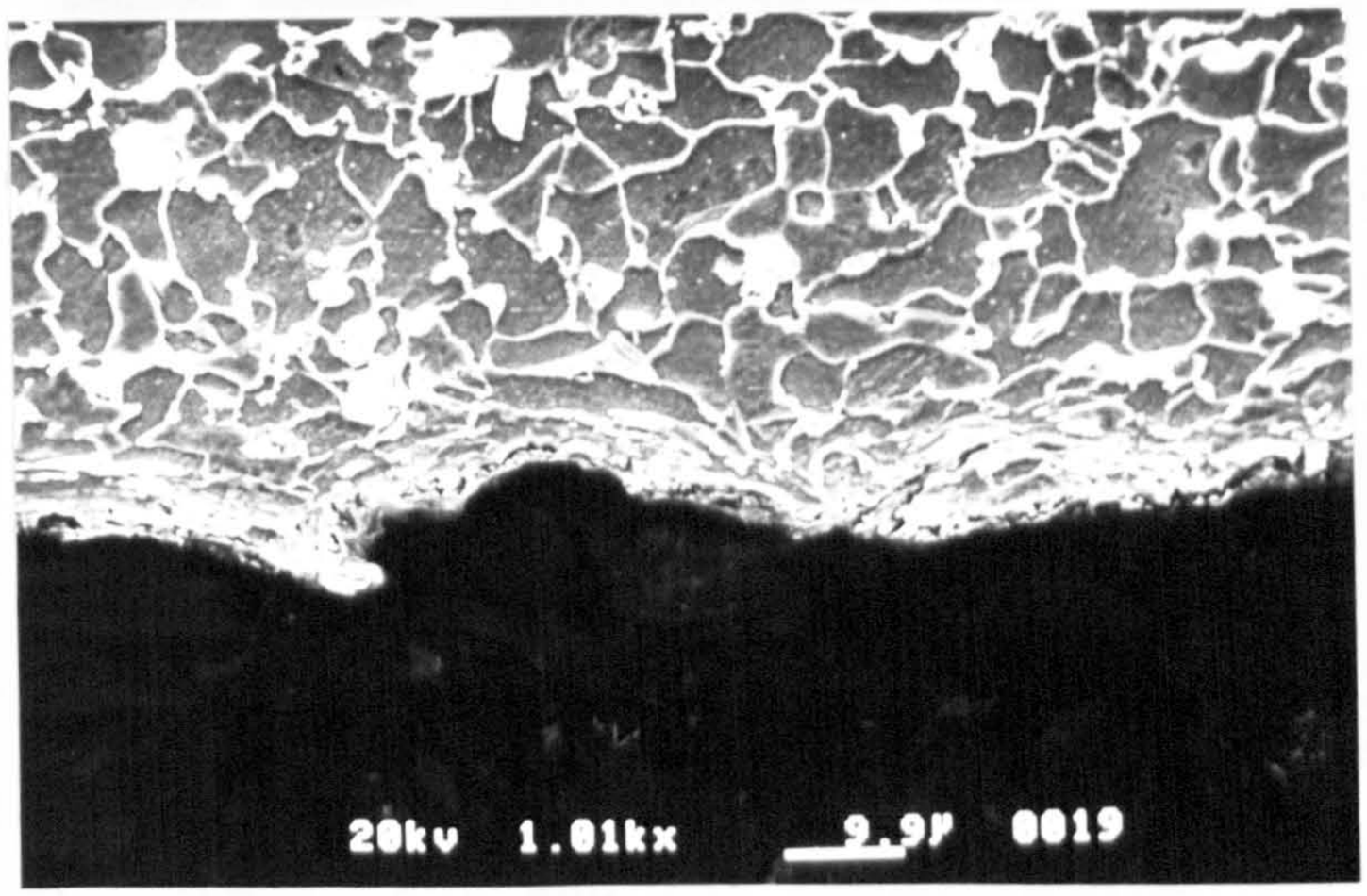

(c). X52 and 45° Impact angle.

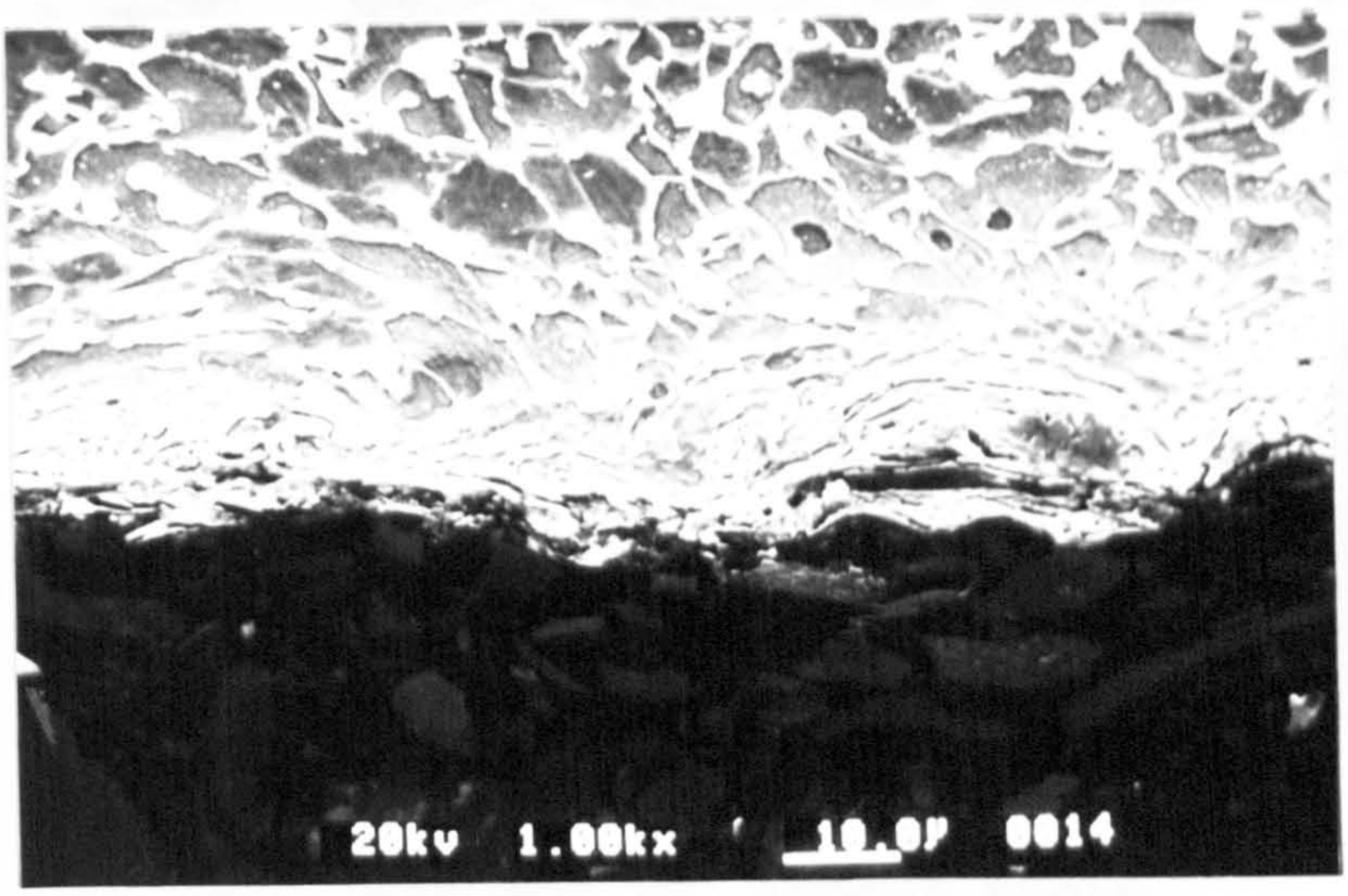

(d). X52 and 90° Impact angle.

Figure 42. Cross-sections of the erosion-corrosion surfaces.

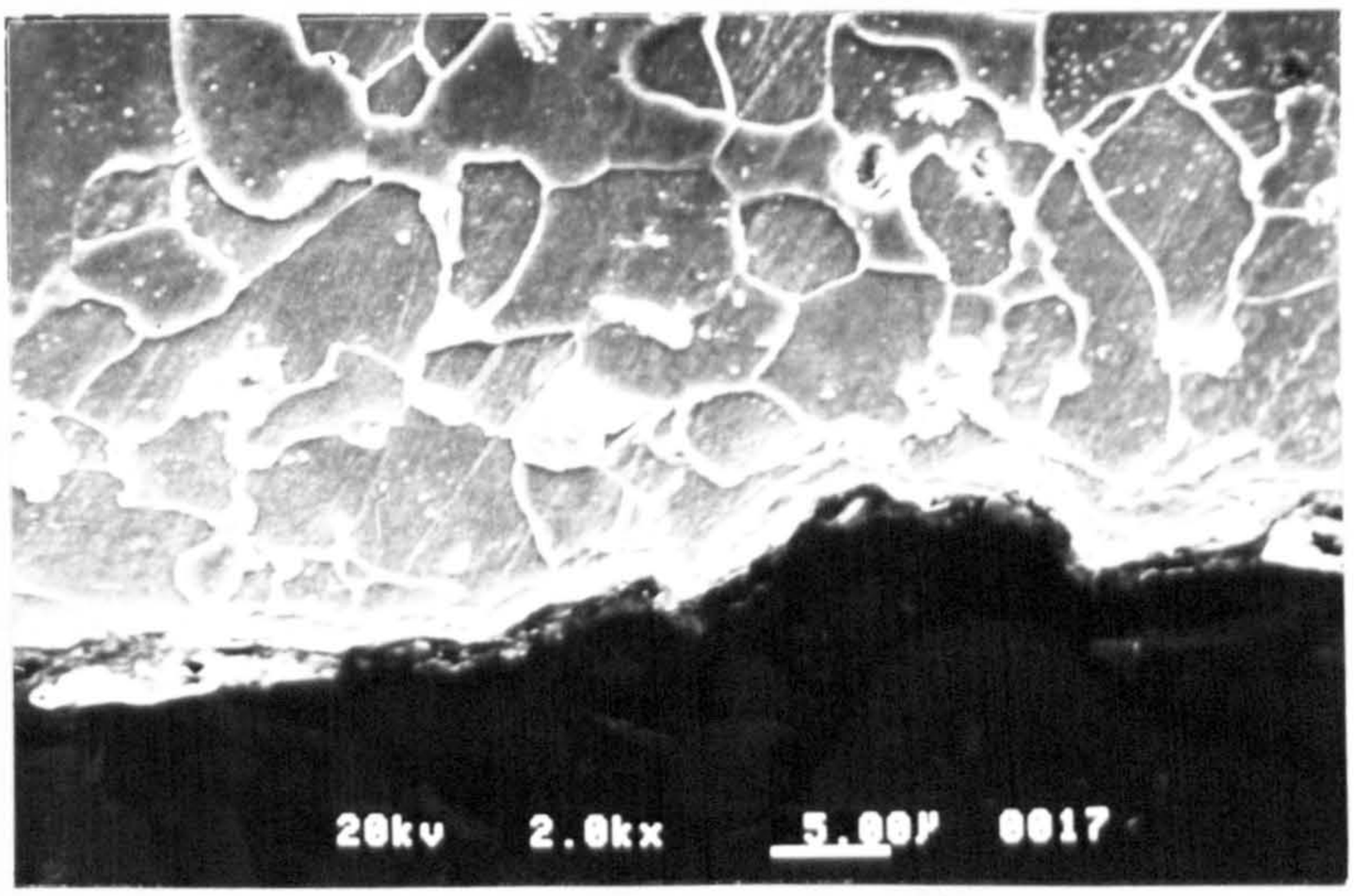

(a). X52 and 15° Impact angle,
Showing the cutting trough.

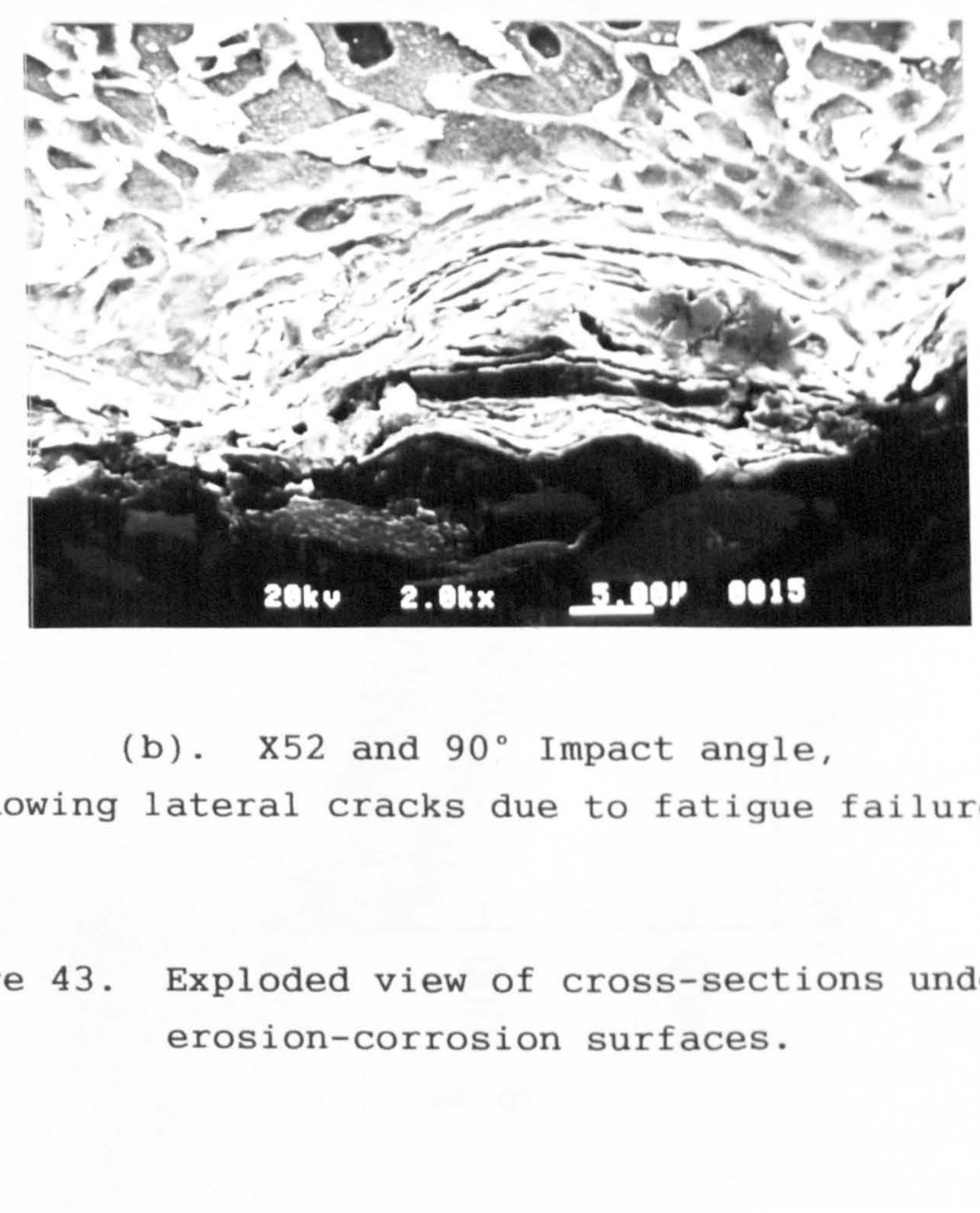

(b). X52 and 90° Impact angle,
Showing lateral cracks due to fatigue failure.

Figure 43. Exploded view of cross-sections under the erosion-corrosion surfaces.

Figure 44(a). XPS-Spectrum.

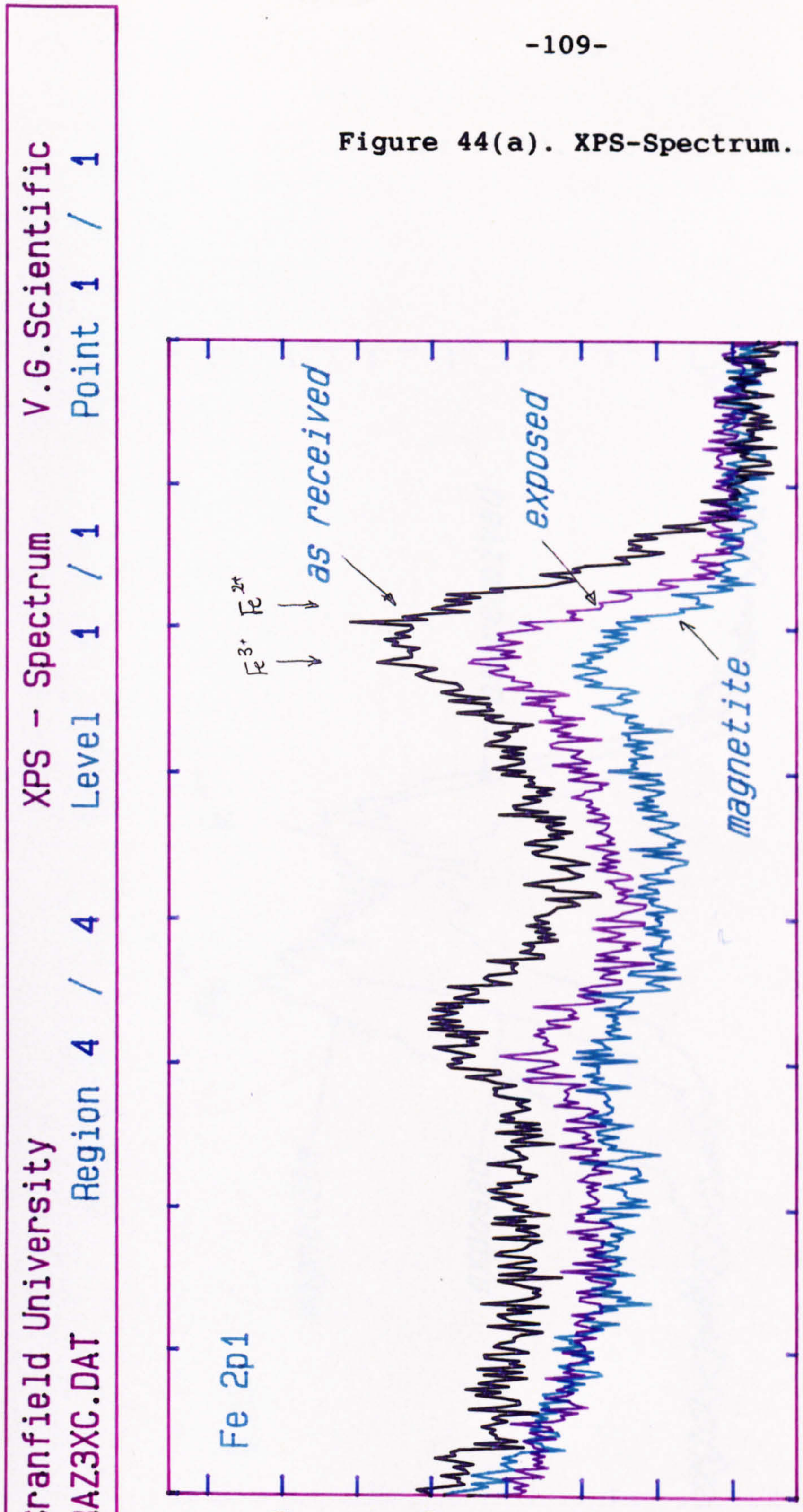

Figure 44(b). XPS-Spectrum.

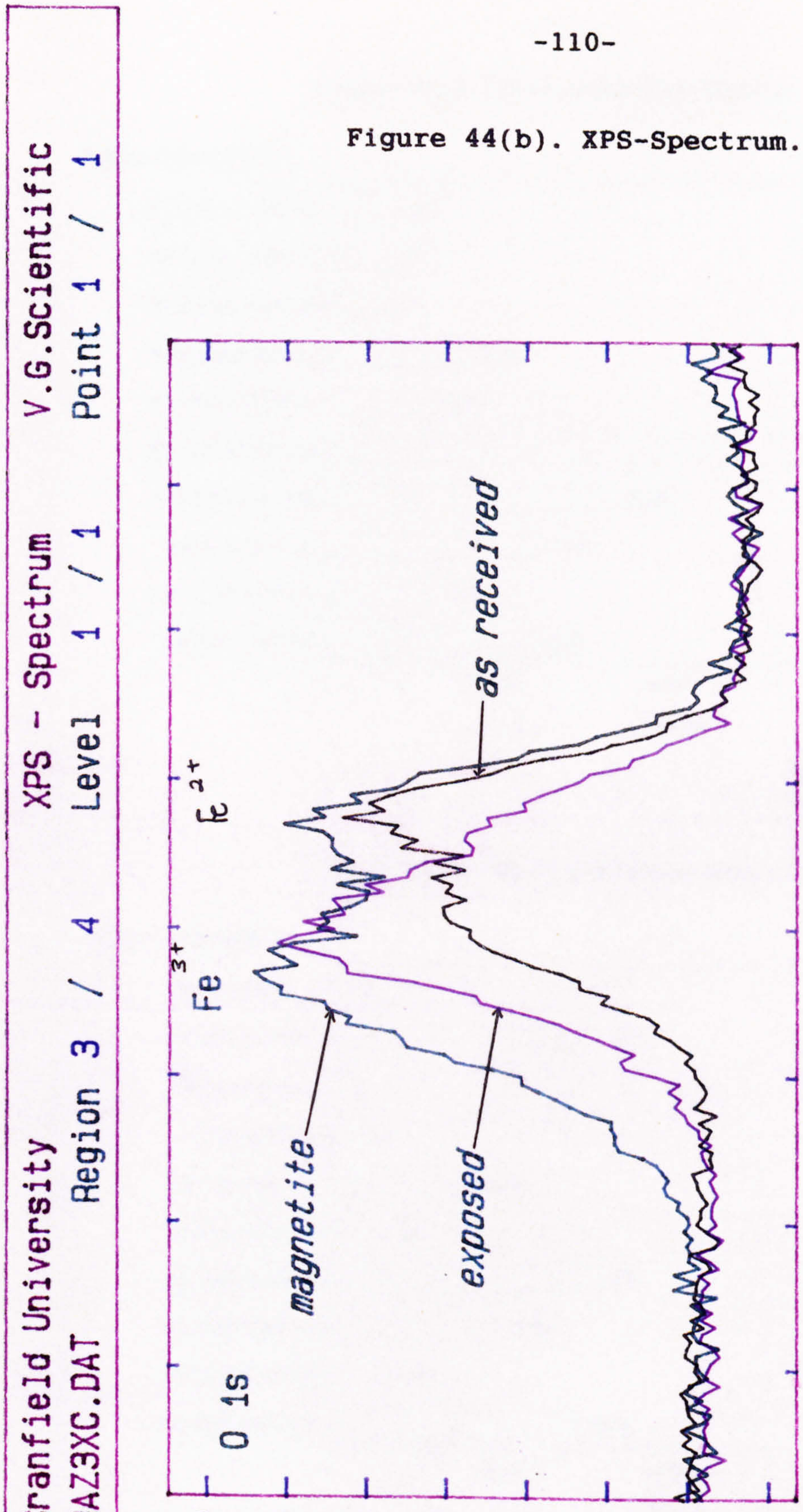

Figure 45(a). Sand production history.

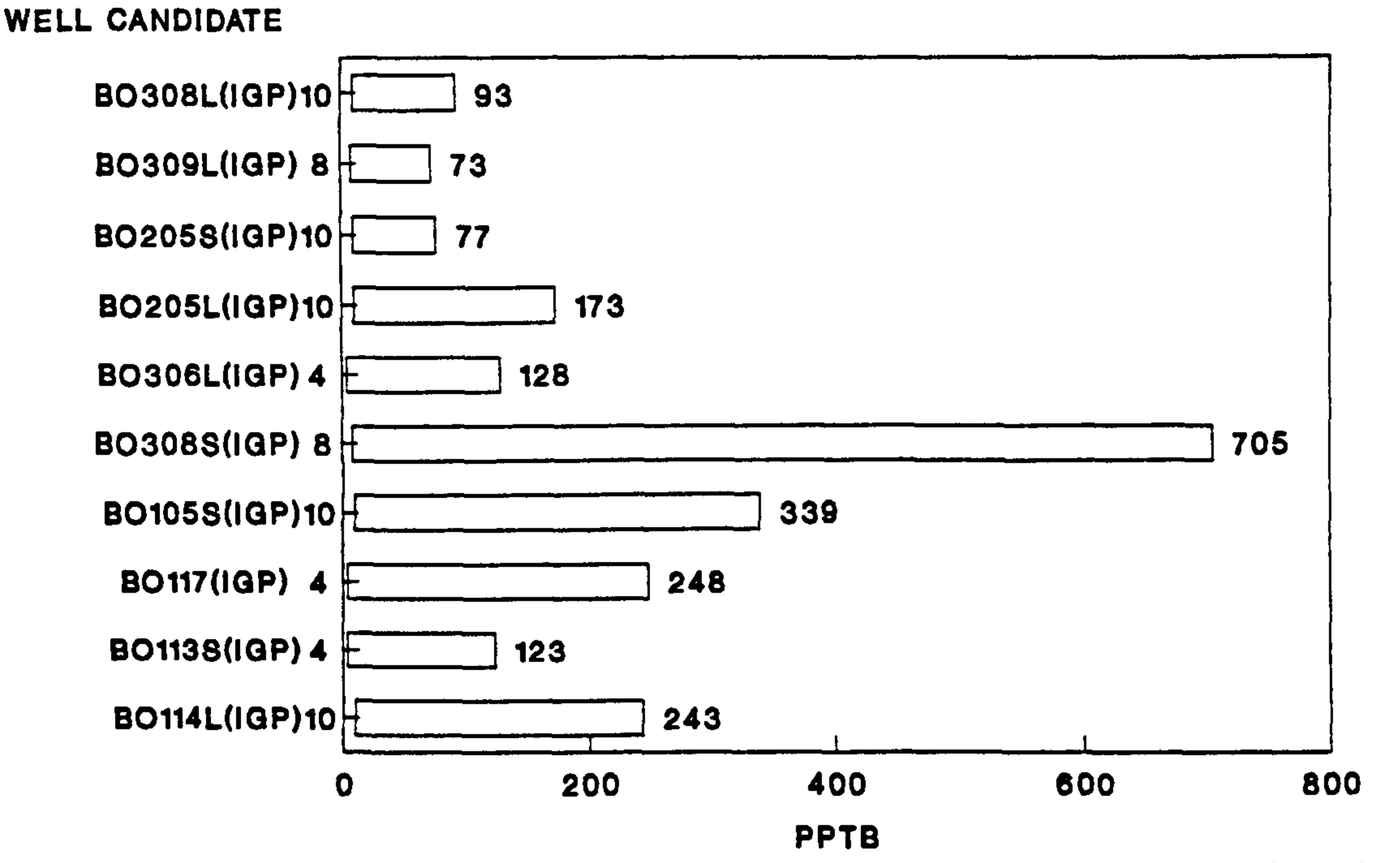

Low Values are Normal,
High Values are Maxima.
Bokor Field

Figure 45(b). Sand production history.

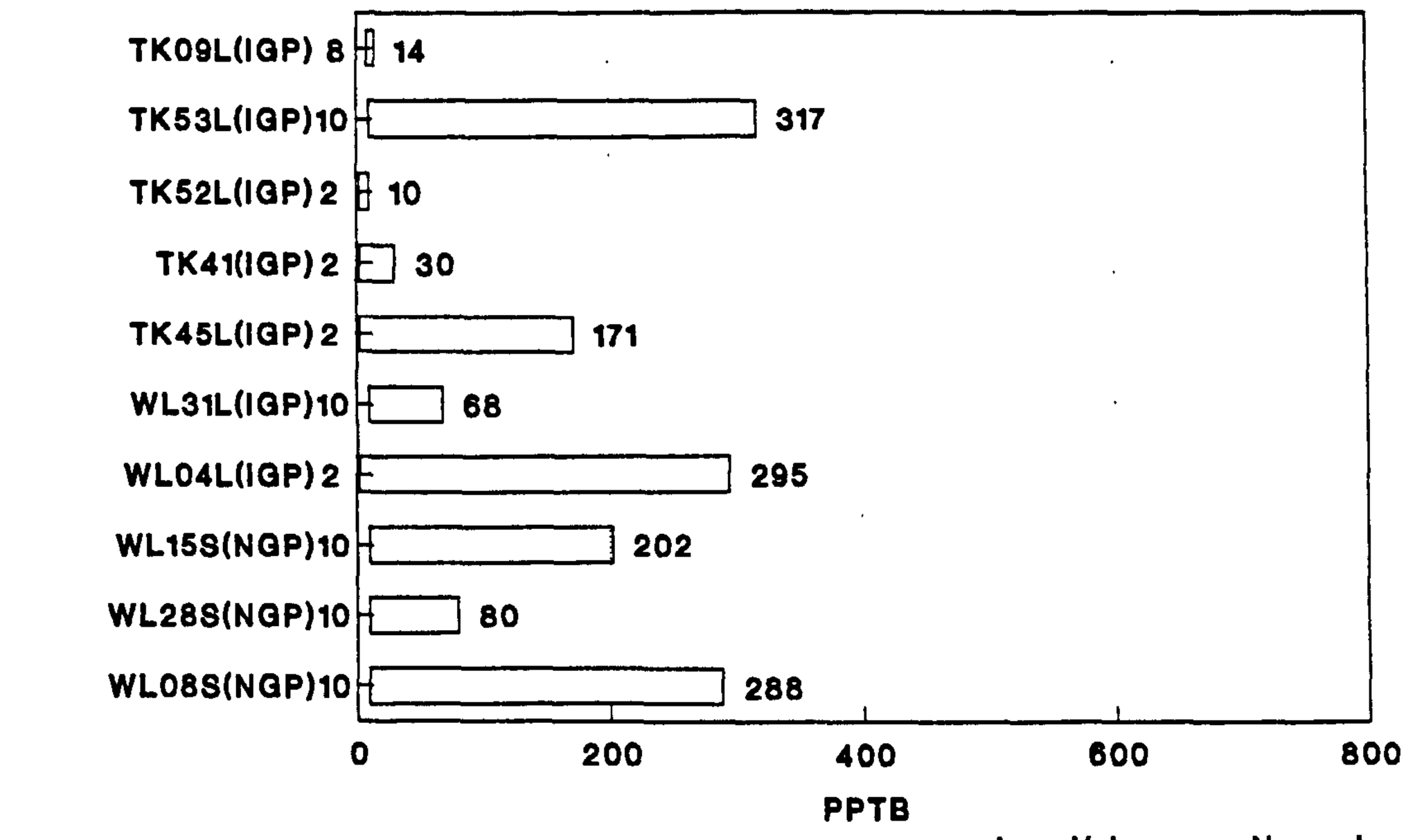

Low Values are Normal,
High Values are Maxima.
Tukau and W/Lutong Fields

Figure 45(c). Sand production history.

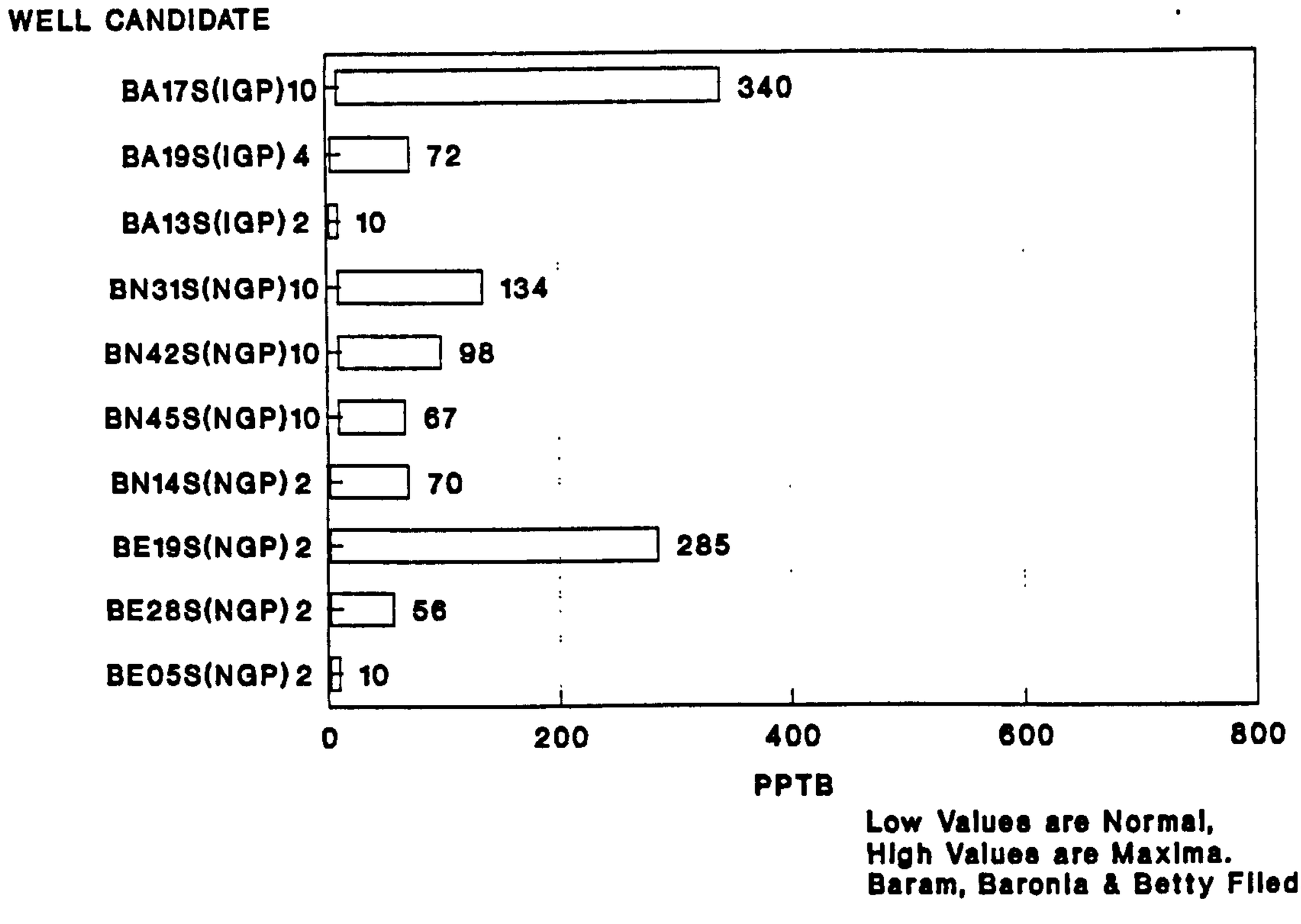

(a) 88 mm. L80-Tubing from WL-9.

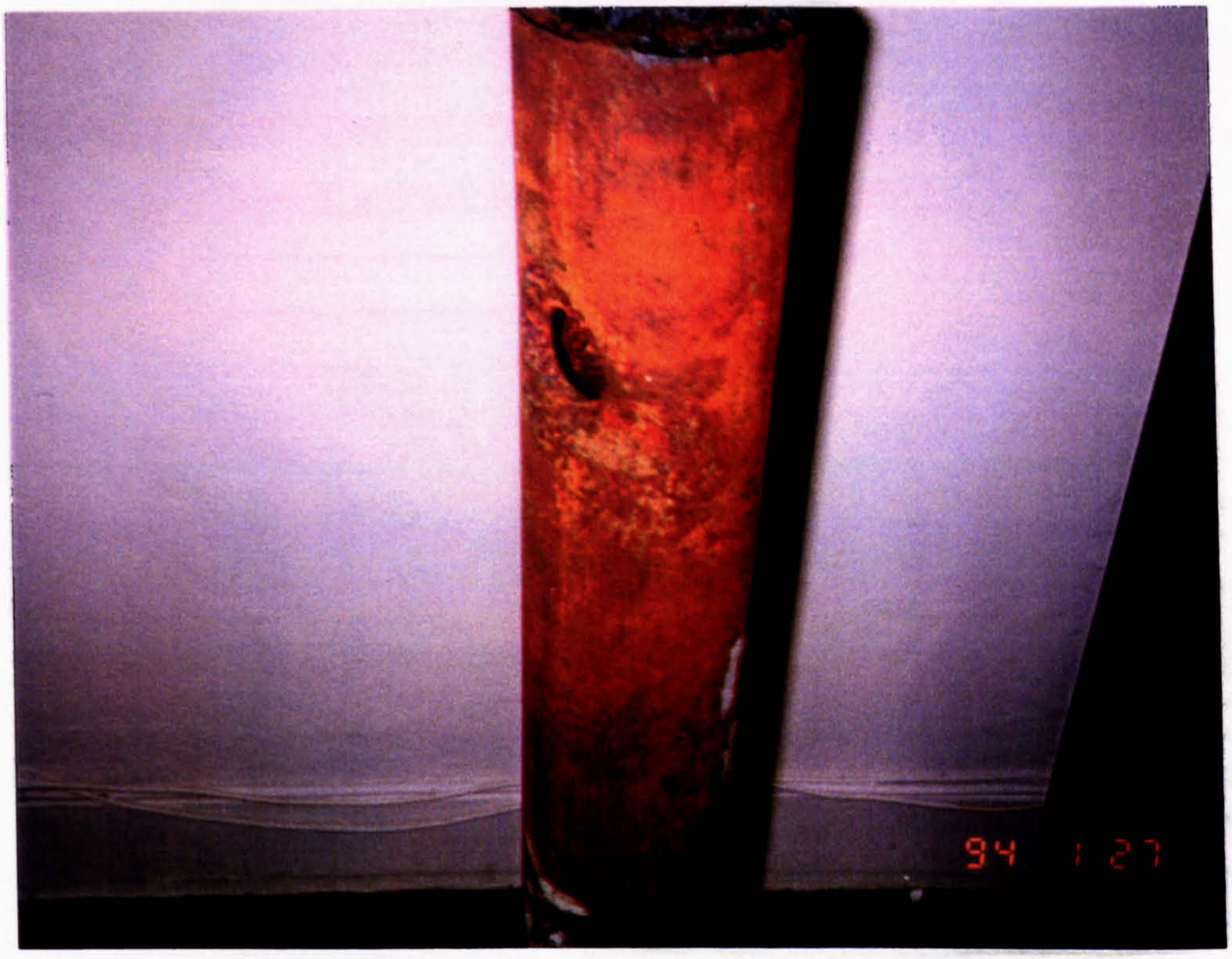

(b) 88 mm. L80-Tubing from WL27.

Figure 46. Erosion of downhole equipment by sand particles.

(c) 88 mm. N80-Tubing from BO105S.

(d) 24/64 Permanent choke severely eroded.

Figure 46. Erosion of downhole equipment by sand particles.

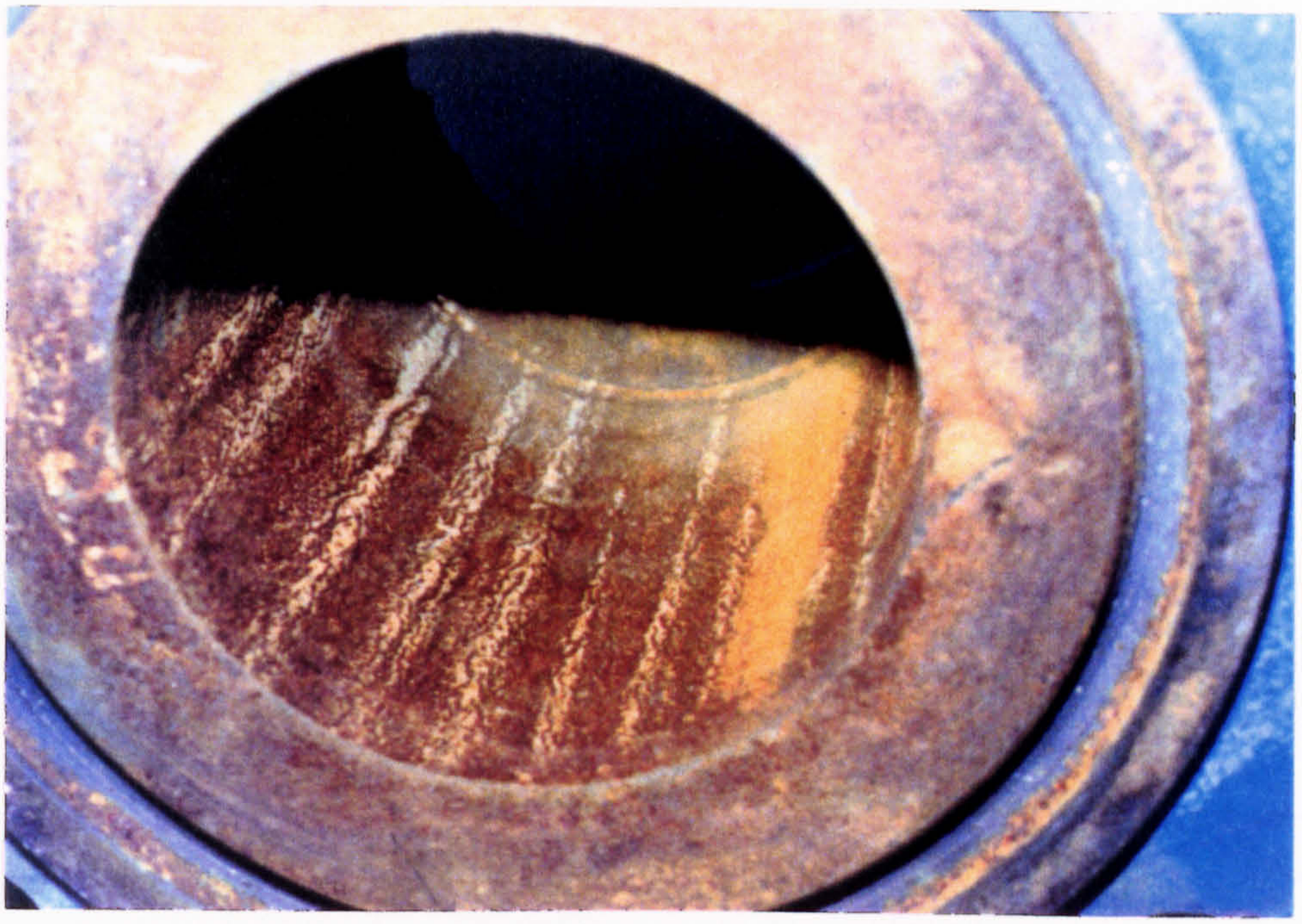

(a) Internals of a flange connection.

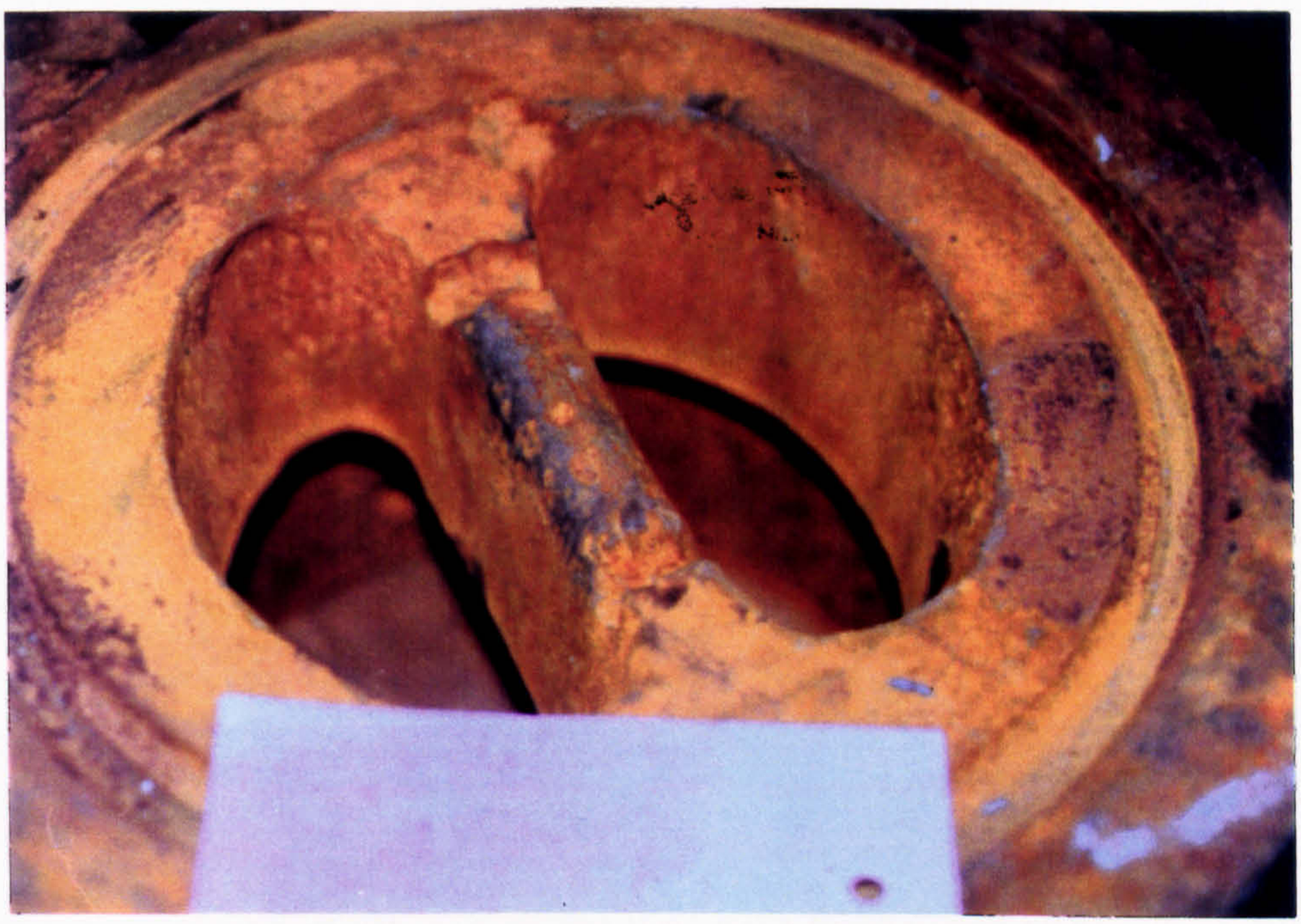

(b) Component of a wing valve.

Figure 47. Erosion of surface equipment by sand particles.

CHAPTER 6

Erosion-Corrosion Modelling

CHAPTER 6

6. EROSION-CORROSION (E/C) MODELLING.

The first serious attempt to generate a predictive erosion-corrosion computer simulation model was made by Nicholls et. al (45), in the late 80s and early 90s in the modelling of the erosion-corrosion processes in Energy Conversion Systems. Their efforts were particularly pertinent to coal gasification, fluidised bed coal combustion and combined cycle gas turbine systems, where critical plant components may be exposed to severe erosion/corrosion processes at high temperature and high velocity environments. Their model is therefore designed to simulate erosion-corrosion processes in which the surface scales form at high temperatures and provide a barrier, akin to having a layer of coating of superior but brittle material over the substrate material. The model is similar to that developed for erosion of materials with an overlay of erosion resistant coating.

To-date the simulation programme is written in Turbo-Pascal and can be run on a PC computer using MS-DOS Operating System. This model was used in this research programme to simulate the erosion-corrosion of materials used in petroleum production subjected to erosion by sand particles and corrosion in wet CO_2 gaseous environments. Necessary improvements and modifications were made to the routines originally put in the programme, to suit the processes taking place and the results obtained during the experimental modelling. Details of the modifications made to the programme are described in this chapter and Appendix H.

6.1 Monte Carlo Erosion-Corrosion Simulation.

The original computer simulation model that has been developed employs a 2-Dimensional Monte Carlo simulation technique which considers the erosion of a ductile material (substrate) at a given impact site on the target surface (53). More precisely, the erosion-corrosion model for the prediction of material removal at high temperature and high velocity was adopted from the model originally used in predicting erosion of composite materials consisting of a brittle monolayer coating on a ductile substrate (46). The model uses input parameters consisting of the mechanical properties and variables of the erodent (particles), the substrate (target material), the oxides (scale) and the environment. The input parameters are listed in Table 10.

The model is based on a particle by particle impact damage accumulation approach on a target material. The model assumes a log-normal distribution for the size of the particles. Each particle is selected at random, its size, mass and velocity (if not known, using the environmental data) are calculated before impact. The time increment between each impact is also determined on a random basis, depending on the particle size distribution and the assumed particle loading. Therefore, both the particle size distribution and the time between impact at a given site are assumed to be independent random variables following the same log-normal distribution.

In order to predict the rate of metal loss, the growth of surface scale thickness 'z' between each impact on a given site must be calculated. It is generally assumed that the scale growth follows a parabolic growth rate. When the particle impacts the scale, it indents the surface. The contact radius 'a' of the particle on the target surface is then determined and from these two values the 'z/a' ratio is

calculated. The 'z/a' ratio determines the material response to the impact. If z/a < 0.1, then the erosion is substrate dominated, if 0.1 < z/a < 1 then the erosion is scale modified and when z/a > 1 then the erosion is scale dominated. Each of these 3 processes are subject to separate models and the programme switches to one or another of these process models depending on the 'z/a' value predicted.

Substrate Dominated (z/a<0.1).

In the case of the substrate dominated model, the flow stress of the target surface can be calculated (53) and from this the critical velocity, $V_{crit.}$, i.e. the minimum velocity to initiate plastic damage in the surface layer is determined. From here, if the value of $V_{crit.}$ is greater than the impact velocity, V, then the collision is deemed to take place under elastic conditions and erosion is then insignificant (i.e. no material removal). However, if V is greater than $V_{crit.}$, the effective velocity ($V - V_{crit.}$) is used to calculate the incremental strain introduced into the target surface from which the total strain is computed on each subsequent impact. The total strain and the number of particles impacting are used to define failure criteria based on an accumulated strain or low cycle fatigue mechanisms depending on the total strain increment per particle impact. It is assumed that material removal is by the loss of extruded platelets whose volume is some fraction of the crater's volume. Their values are determined from single impact observations. The new strain level at the surface is estimated and the material removal process is repeated until the total exposure time is reached.

Scale Modified (0.1 > z/a > 1).

When the erosion model falls within the scale modified regime, the maximum tensile stress in the scale

resulting from the impacts is calculated. If the maximum tensile stress is estimated to be greater than the fracture stress of the scale, the amount of scale removed is then calculated. In this case the scale removed is assumed to be down to the oxide/substrate interface.

Scale Dominated (z/a > 1).

When the erosion model is within the scale dominated regime, the maximum tensile stress which develops in the scale during the impacts is also calculated. If this tensile stress is estimated to be greater than the fracture stress of the scale, the amount of scale removed is then calculated. In this case the amount of scale removed is equivalent to the volume of the crater formed, which is in turn related to the particle/scale contact radius.

The time elapsed between impacts allows the oxide to grow, and the process of removal and growth continues until the exposure time is reached. The total number of particles impacting the scale are calculated and the total erosion rate, through scale removal is determined. Finally, the resultant scale layer still remaining after the total exposure time is also calculated.

Figure 48 shows the general flow diagram of the erosion model. Figures 49(a-c) are the flow diagrams for (a) Scale Modified Regime, (b) Scale Dominated Regime and (c) Substrate Dominated Regime procedures.

Table 10. Input parameters for erosion-corrosion computer modelling (e.g. E/C modelling for X52 material).

1. Particles Properties	2. Substrate Properties
a). Name: Sand b). Mean Size: 200 (μm). c). Standard Deviation: 80 (μm). d). Velocity: 50 (m/s). e). Loading: 0.1 ($g/mm^2/h$). f). Density: 2.63 (g/c.c.). g). Modulus: 150 (GPa). h). Poisson's Ratio: 0.25 i). Shape Factor (0-1): 0.6	a). Name: X52 b). Density: 7.89 (g/c.c.). c). Modulus: 200 (GPa). d). Poisson's Ratio: 0.3 e). Yield Strength: 359 (MPa) (74). f). Strain to Failure: 20 % g). Maximum Work-Hardening Exponent:0.06
3. Oxides Properties	**4. Environmental Variables**
a). Name: $FeCO_3$ b). Density: 3.96 (g/c.c.) (69). c). Molecular Weight of Scale: 116 (g). d). Atomic Weight of Oxide-forming Cation: 55.8 (g). e). Parabolic Growth Rate Constant: $27x10^{-3}$ ($\mu m^2/h$). f). Elastic Modulus: 50 (GPa). g). Poisson's Ratio: 0.2 h). Fracture Stress: 10 (MPa).	a). Temperature: 20 (°C). b). Gas Velocity: 0 (m/s). c). Gas Drag Coefficient: 0 d). Gas Density: $1.80x10^{-3}$ (g/c.c.) (73). e). Particle's Acceleration Length: 0.134 (m). f). Total Exposure Time: 50 (h).

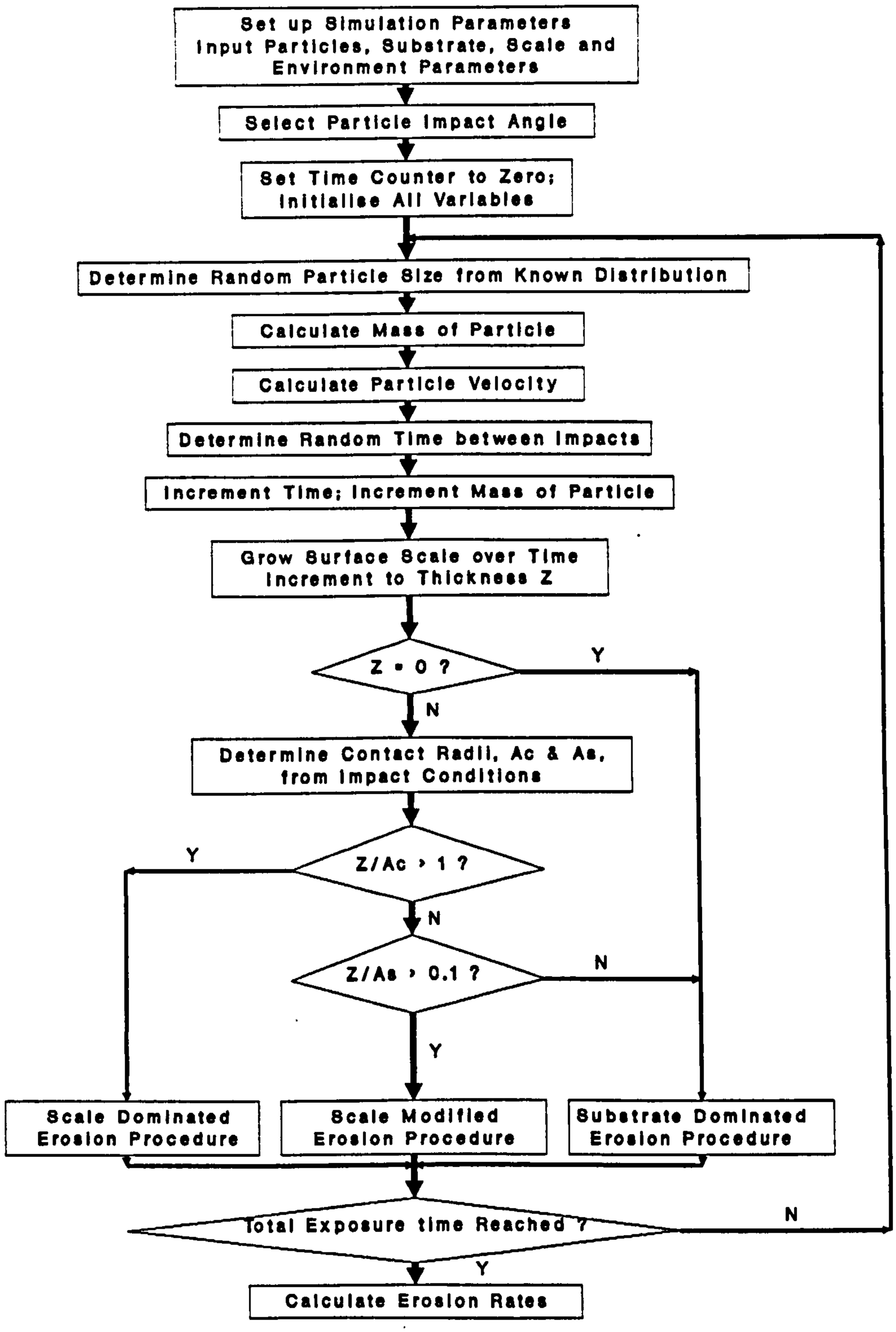

Figure 48. Flow diagram of erosion model.

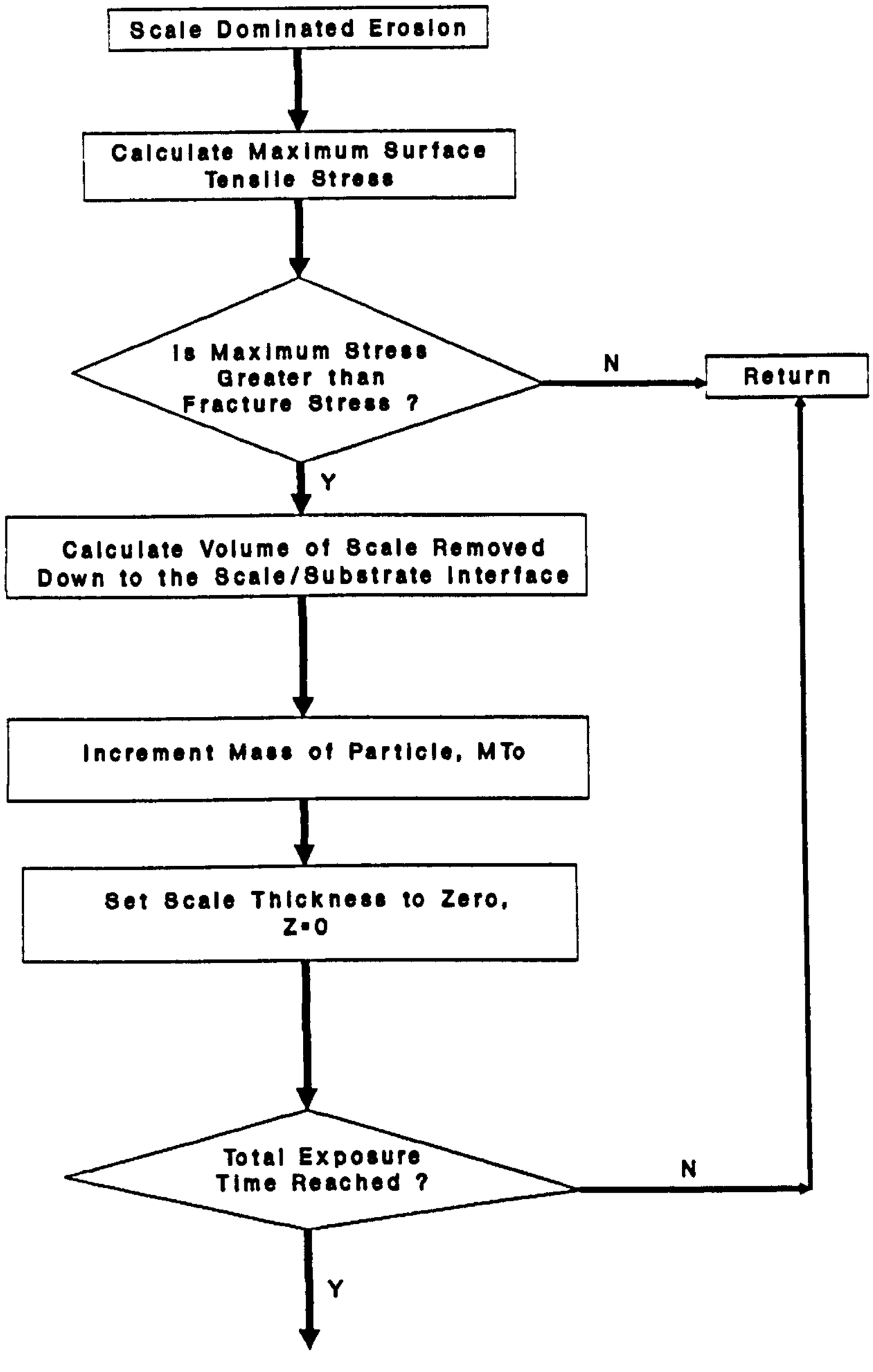

Figure 49(a). Scale modified erosion procedure.

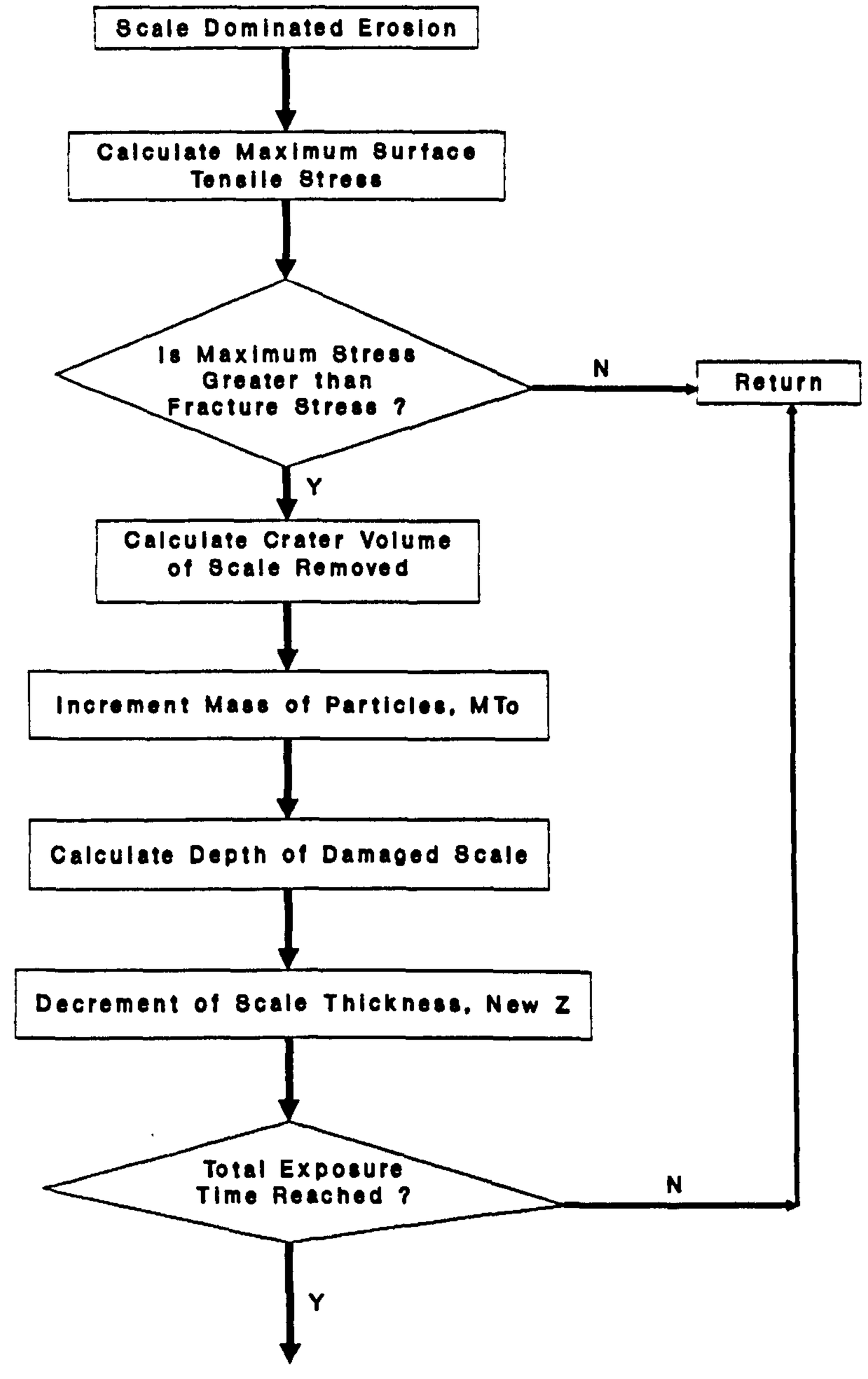

Figure 49(b). Scale dominated erosion procedure.

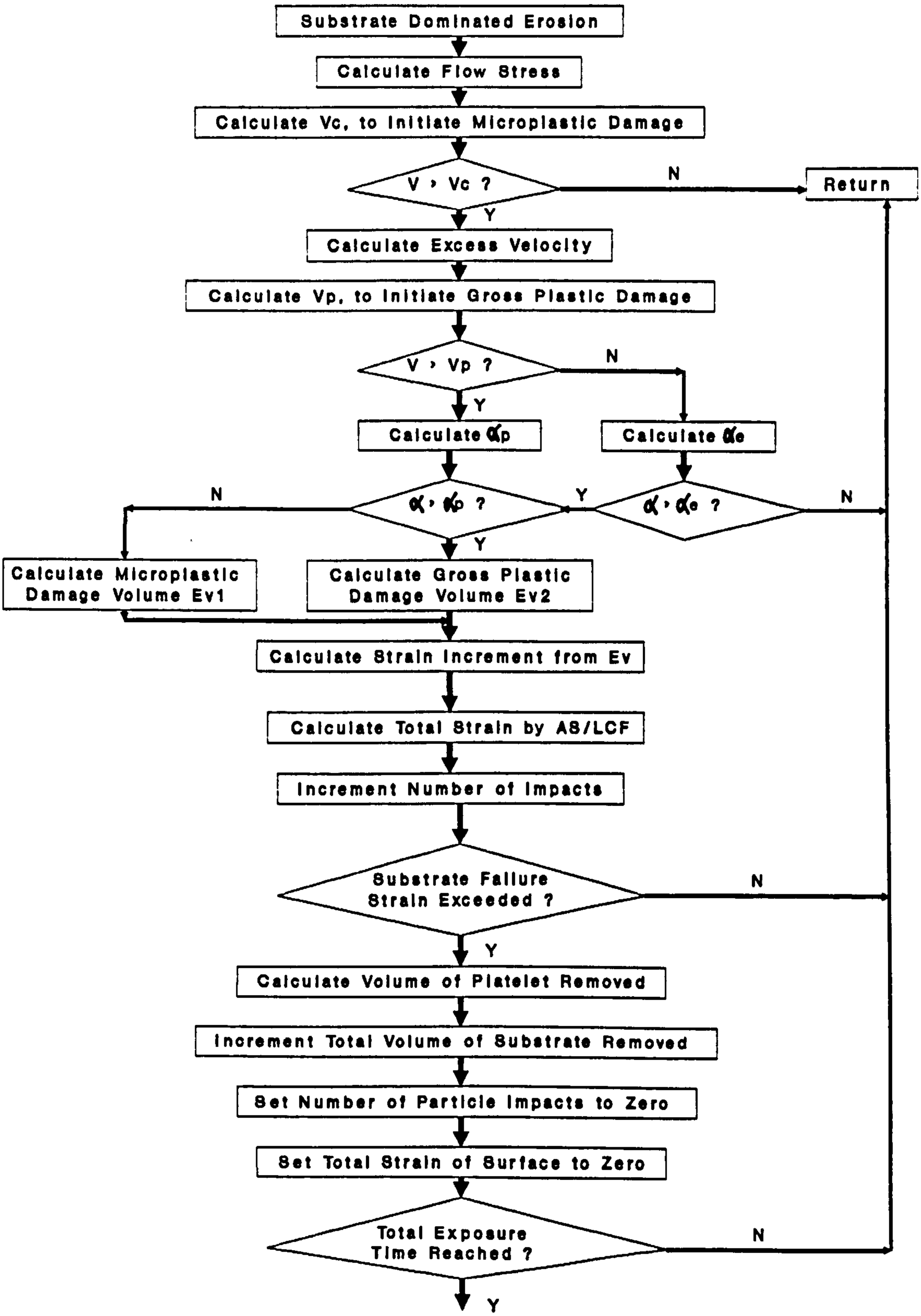

Figure 49(c). Substrate dominated erosion procedure.

6.2 Improvements to the Computer Modelling Programme.

The Monte Carlo erosion simulation programme was studied, tested and modified to suit the processes involved in the experimental modelling of erosion and erosion-corrosion of materials used in oil production. The modified computer simulation model has the following improvements incorporated.

(a). A new value for the β-factor of 0.30 was used to replace the previous value of 0.57. β is defined as the volume of metal loss per crater over the volume of crater. This value was obtained from the single and multiple impact experiments for X52 and IN625 materials. Appendix H, Item H1, shows an example of the calculation for β-factor.

(b). The following definitions were used for the mass of particles impacting a given site in consideration during the erosion-corrosion simulation process:

MT = Total mass of particles impacting,
MTs= Total mass of particles impacting, damaging and removing substrate, and
MTo= Total mass of particles impacting, damaging and removing corrosion scale.

Therefore, the following logic was followed and incorporated in the simulation programme.

Oxide Modified Regime.

$$Total\ Erosion\ Rate, (g/g) = \frac{Total\ mass\ of\ metal\ loss}{MT},$$

6.2 Improvements to the Computer Modelling Programme.

The Monte Carlo erosion simulation programme was studied, tested and modified to suite the processes involved in the experimental modelling of erosion and erosion-corrosion of materials used in oil production. The modified computer simulation model has the following improvements incorporated.

(a). A new value for the β-factor of 0.30 was used to replace the previous value of 0.57. β is defined as the volume of metal loss per crater over the volume of crater. This value was obtained from the single and multiple impact experiments for X52 and IN625 materials. Appendix H, Item H1, shows an example of the calculation for β-factor.

(b). The following definitions were used for the mass of particles impacting a given site in consideration during the erosion-corrosion simulation process:

MT = Total mass of particles impacting,
MTs= Total mass of particles impacting, damaging and removing substrate, and
MTo= Total mass of particles impacting, damaging and removing corrosion scale.

Therefore, the following logic was followed and incorporated in the simulation programme.

Oxide Modified Regime.

$$Total\ Erosion\ Rate, (g/g) = \frac{Total\ mass\ of\ metal\ loss}{MT},$$

$$\textit{Substrate Erosion Rate, } (g/g) = \frac{\textit{Total mass of Substrate Loss}}{MTs}$$

$$\textit{Scale Erosion Rate, } (g/g) = \frac{\textit{Total mass of Scale Loss}}{MTo},$$

and

$$MT = MTs + MTo.$$

Oxide Dominated Regime.

To cater for situation when there is no substrate loss by the impacting particles then the following conditions can be visualised:-

When the total mass of substrate loss = 0, then MTs = 0 and therefore Substrate Erosion Rate = 0. In this case MT = MTo and the Total Erosion Rate = Oxide Erosion Rate. An appropriate routine is then included in the 'procedure-for-calculating-erosion-rate' sub-routine in order to satisfy these conditions. This is shown in Appendix H, Item H2.

Substrate Dominated Regime.

In order to cater for the situation in which there is no scale and therefore there is no scale loss, i.e. a substrate erosion only scenario, then the following conditions can be expected to take place:-

MTo = 0, Total mass of scale loss = 0 and Scale erosion rate = 0. Then, Total Erosion Rate = Substrate Erosion Rate and MT = MTs. An appropriate routine is included in the programme as shown in Appendix H, Item H3.

The substrate and scale thickness erosion rate expressions were found to contain errors in the conversion process and therefore were corrected accordingly as outlined in Appendix H, Item H4.

Additional refinements were also included in the calculations of; (a) Total metal loss: modification of the total metal loss calculation to include the mass of metal growing into corrosion scale and (b) Total mass of particles: modification of the total mass of particles calculation to include the increment in the total mass of particle for each time increment. These refinements were included in their appropriate location subroutines of the programme as shown in Appendix H, Item H5.

In order to initialise the programme, the mass of particles was set to zero at time=0 (originally MTo:=1), zero metal loss by corrosion, and to avoid divide-by-zero problems, an appropriate routine has been included in the main procedure as shown in Appendix H, Item H6.

In the case of the Oxide Dominated regime in operation, the mass of particle eroding the oxide scale is assigned the value of the total mass of particles impacting, in the main procedure. When the Oxide Modified regime is in operation the routine, shown in Appendix H, Item H7, was inserted in the main procedure. This was used to cater for the transition between the Oxide Dominated and the Oxide Modified regimes, where for the latter there is also erosion of the substrate taking place.

The results printed on the screen were improved by including information on the Modulus ratio, the name of scale and the scale growth rate constant along with the other information already presented. This was found to be

necessary to ensure better tracking ability and understanding of the results generated during the simulation exercises. Typical results displayed on the screen are shown in Figure 50.

```
*---------------------- Predicted Erosion Rates ----------------------*

For Impact Angle [1] =  30.0 Degrees :
Substrate          : X52 ;            Es/Eo         :  4.00 ;
Erodent            : Sand1 ;           Oxide gK     :  2.7E-0002 µm2/h;
Particle size      :  200.0 µm ;       Oxide Scale  :  FeCO3 ;
Particle loading   :  0.10 g/mm2/h
Particle velocity  : 50.00 m/s
Gas velocity       :  0.00 m/s
Temperature        : 20.00 °C
Exposure time      : 50.00 hours

MTs =  1.705E-0003 Kg,  MTo =  5.418E-0003 Kg,  MT =  7.122E-0003 Kg.
Oxid_mass_loss  =  2.266E-0010 Kg, Metal_mass_loss =  6.928E-0004 Kg,
Subst_mass_loss =  2.287E-0007 Kg, Total_mass_loss =  2.289E-0007 Kg.

Erosion rate is         :  3.214E-0005 g/g  or  8.616E-0001 µm/h
Substrate loss rate is  :  1.342E-0004 g/g  or  8.611E-0001 µm/h
Oxide loss rate is      :  4.183E-0008 g/g  or  5.281E-0004 µm/h
Oxide thickness is      :  3.637E-0001 µm

*--------------------------------------------------------------------*
Do you wish another run ? (y/n)
Answer :
```

Figure 50. Typical display of results.

6.3 Erosion and Erosion-corrosion Modelling.

The improved erosion/corrosion computer simulation programme was tested using parameters for X52 and IN625 materials. Table 11 shows the list of parameters used in the simulation.

Table 11. Data for X52 and IN625 used in the simulation.

Substrate Name:	X52	IN625
Density, g/cc:	7.80	8.40
Elastic Modulus, GPa:	200	201
Poisson's Ratio:	0.3	0.306
Yield Strength, MPa:	359	490
Strain to Failure:	20	50
Max. Work-hardening Exponent:	0.06	0.1

Note: The other parameters for the particles, Scales/oxides (for X52 at 20°C) and the environment are listed in Table 9, on page 120.

X52 Material.

(a). For the erosion modelling, the programme was run using a flux rate of 0.05 g/mm^2/h, a temperature of 20°C at a range of velocities of 20 m/s, 50 m/s, 80 m/s and 150 m/s at five different impact angles of 15°, 30°, 45°, 60° and 90°. An average of the results generated from ten runs were made in order to establish each data point. The predicted results obtained were plotted on a graph versus the measured values obtained from the experiments, as shown in Figure 51(a). Error bars on the graph indicate the variation of data about the average of the values predicted by the model.

(b). Another set of ten runs was made for a constant velocity of 50 m/s using the flux rates; 0.01, 0.05, 0.1 and 0.5 g/mm^2/h. Again the average of the results from ten runs were generated in order to establish each data point and similarly results were plotted on the graph shown in Figure 51(b).

(c). Similar runs to those described in (a) and (b) above, were made for the erosion-corrosion modelling of the X52 material. In this modelling a scale growth constant of $K_p=27x10^{-3}$ $\mu m^2/h$ and data shown in Table 10 were used. The results obtained were plotted on graphs versus the measured values obtained from the experiments. They are shown in Figures 53(a) and 53(b), respectively.

IN625 Material.

(d). Only one set of runs was made for this material i.e. at a constant flux rate of 0.05 g/mm^2/h and for a range of velocities of 20 m/s, 50 m/s, 80 m/s and 150 m/s. The results obtained were plotted on a graph versus the measured values obtained from the experiments.

Summary of the results are shown in Appendix I. The data plotted graphically are shown in Figure 51(a) for the predicted versus measured erosion rates for X52 at a constant flux and different velocity, Figure 51(b) for the predicted versus measured erosion rates for X52 at a constant velocity and different flux, Figure 52 for the predicted versus measured erosion rates for IN625 at a constant flux and different velocity, Figure 53(a) for the predicted versus measured erosion-corrosion rates for X52 at a constant flux and different velocity, and Figure 53(b) for the predicted versus measured erosion-corrosion rates for X52 at a constant velocity and different flux.

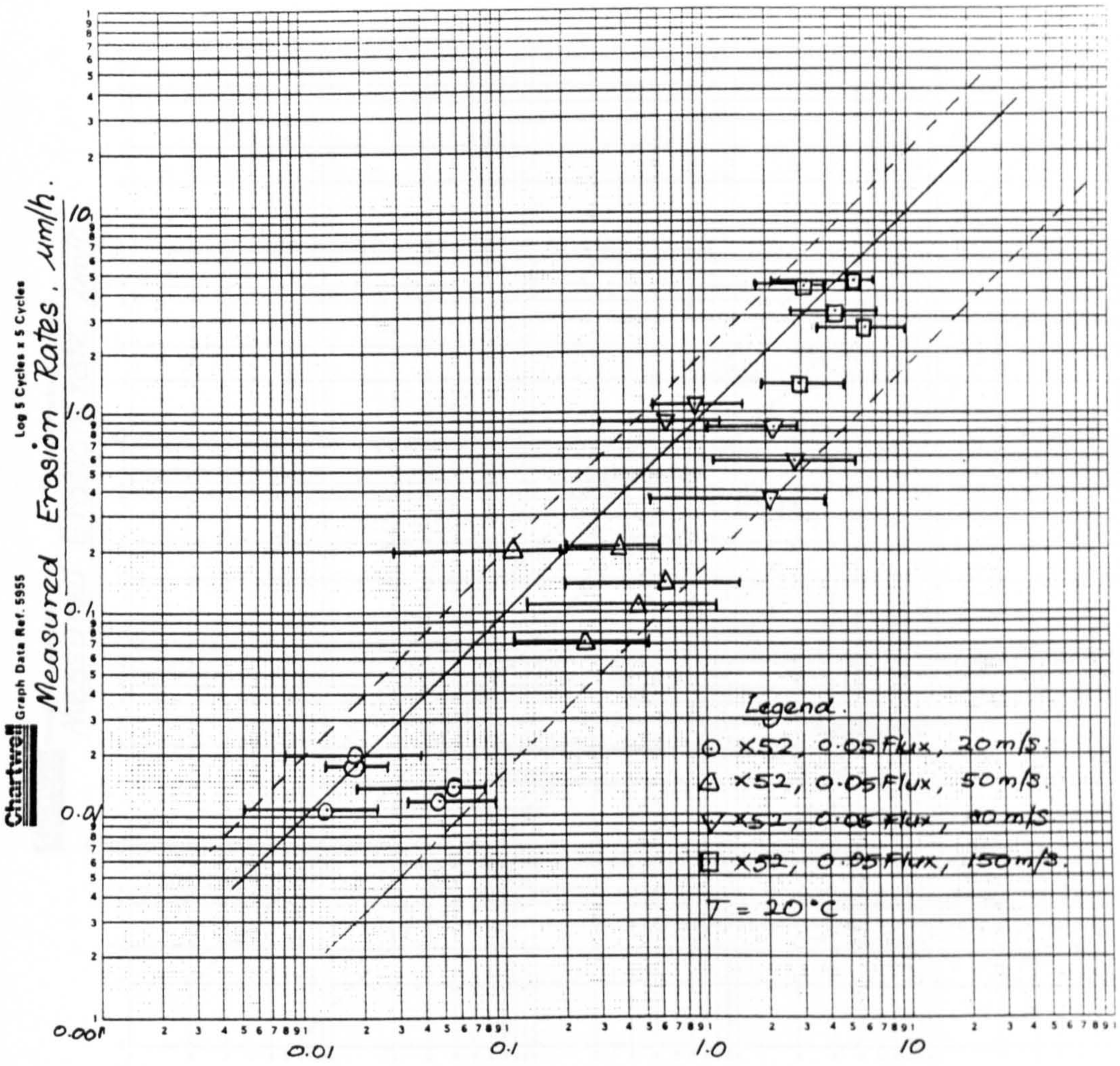

Figure 51(a). Predicted versus measured erosion rates for X52 at a constant flux and different velocity.

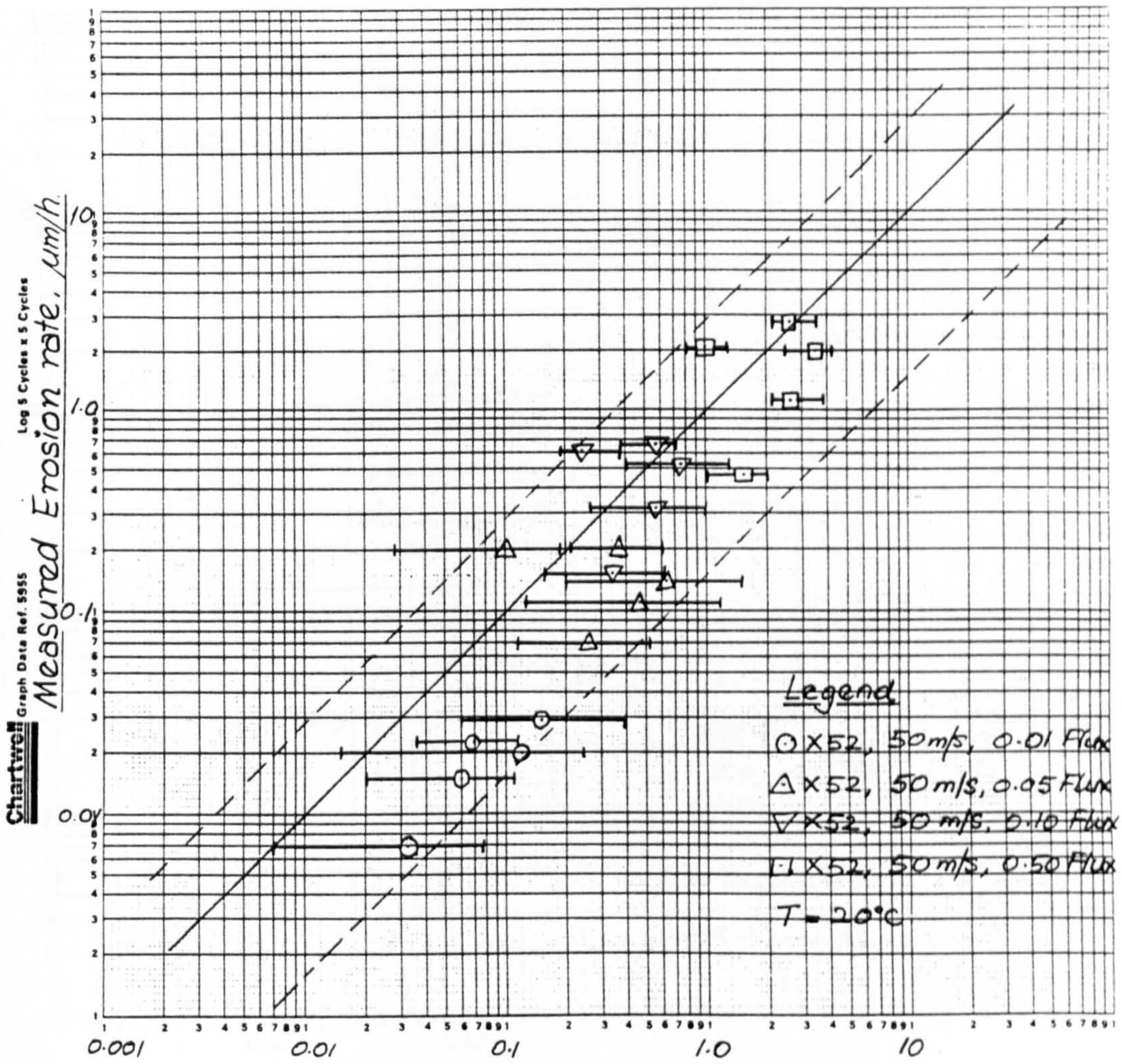

Figure 51(b). Predicted versus measured erosion rates for X52 at a constant velocity and different flux.

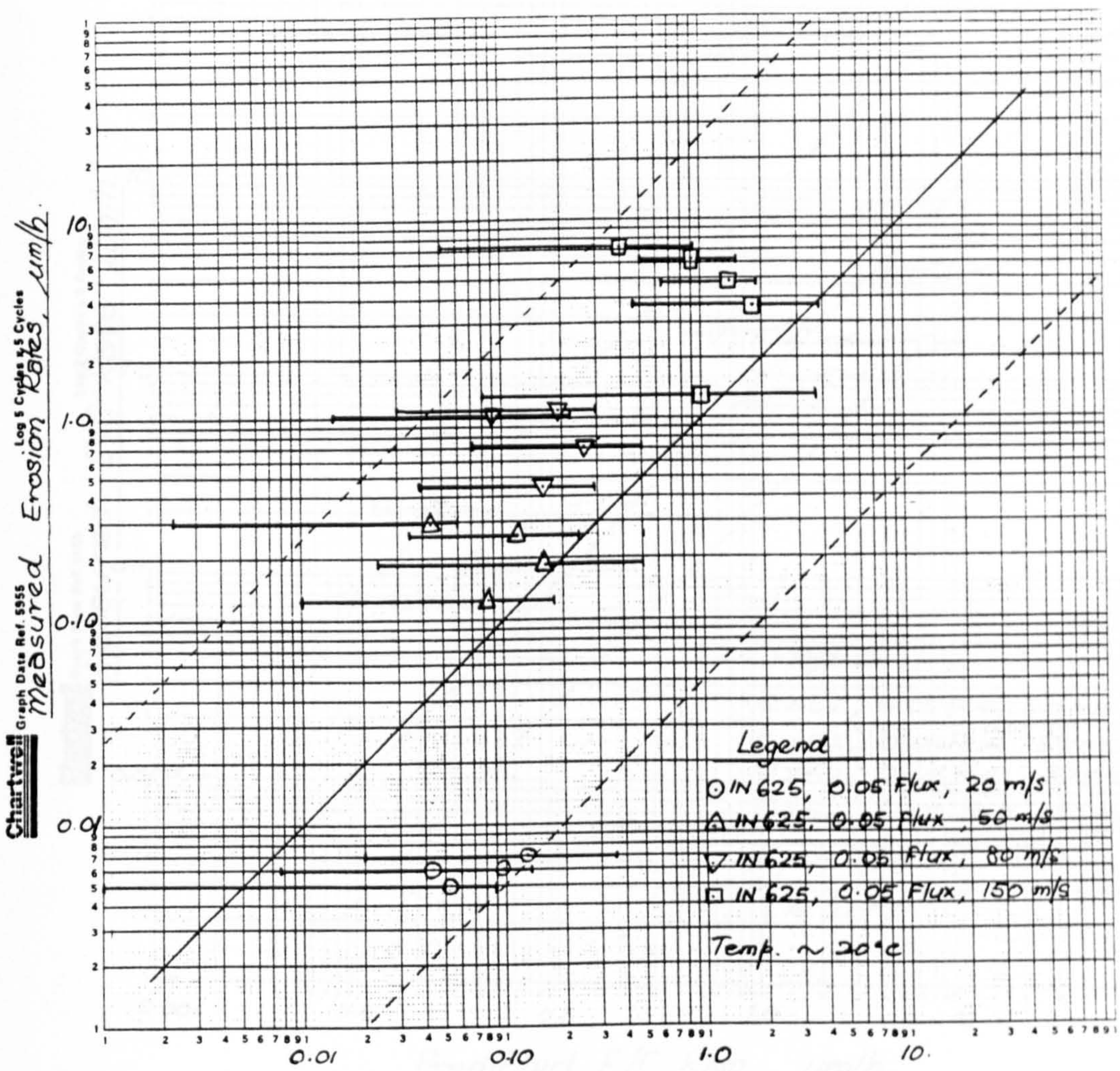

Figure 52. Predicted versus measured erosion rate for IN625 at a constant flux and different velocity.

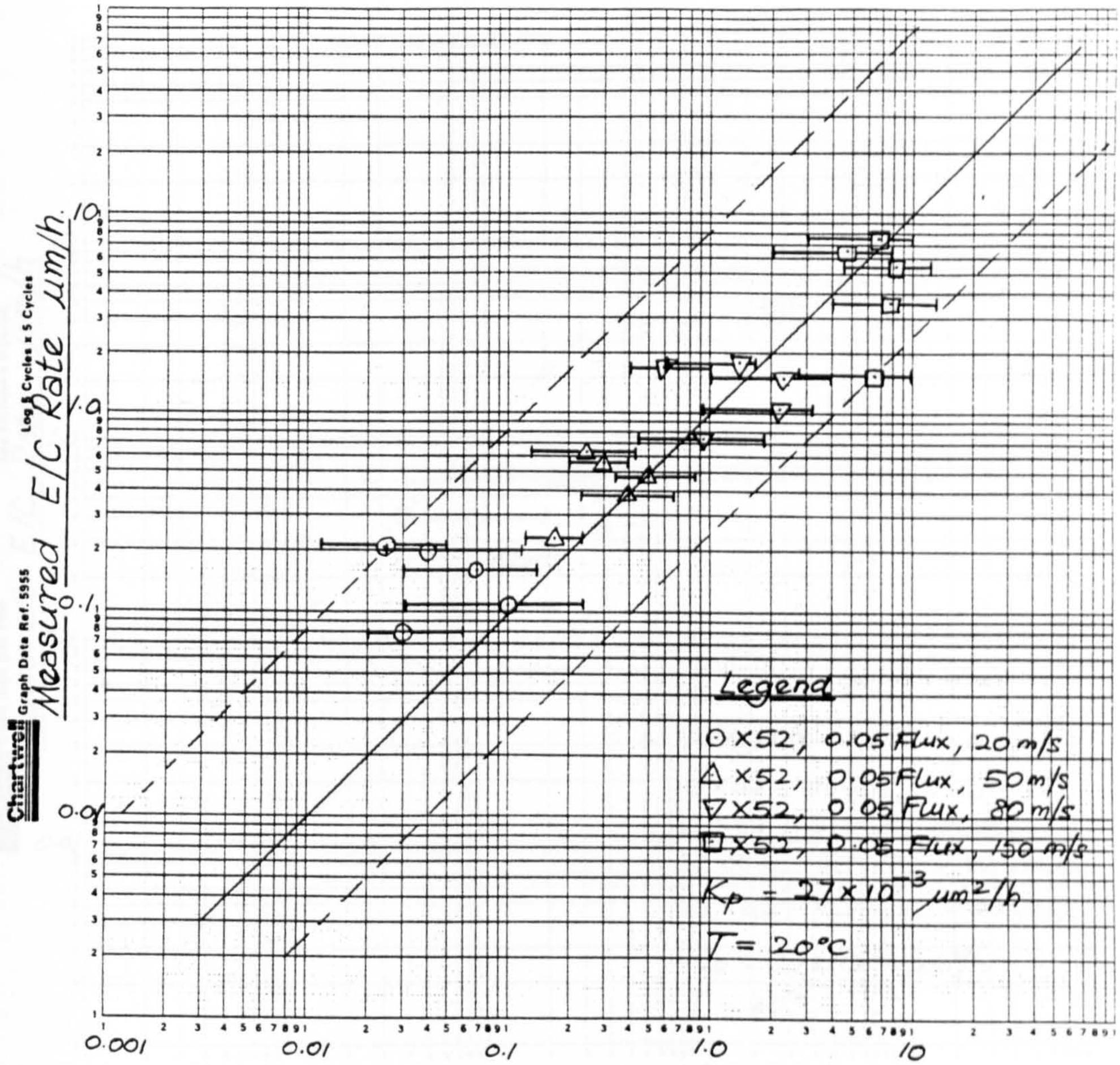

Figure 53(a). Predicted versus measured erosion-corrosion rates for X52 at a constant flux and different velocity.

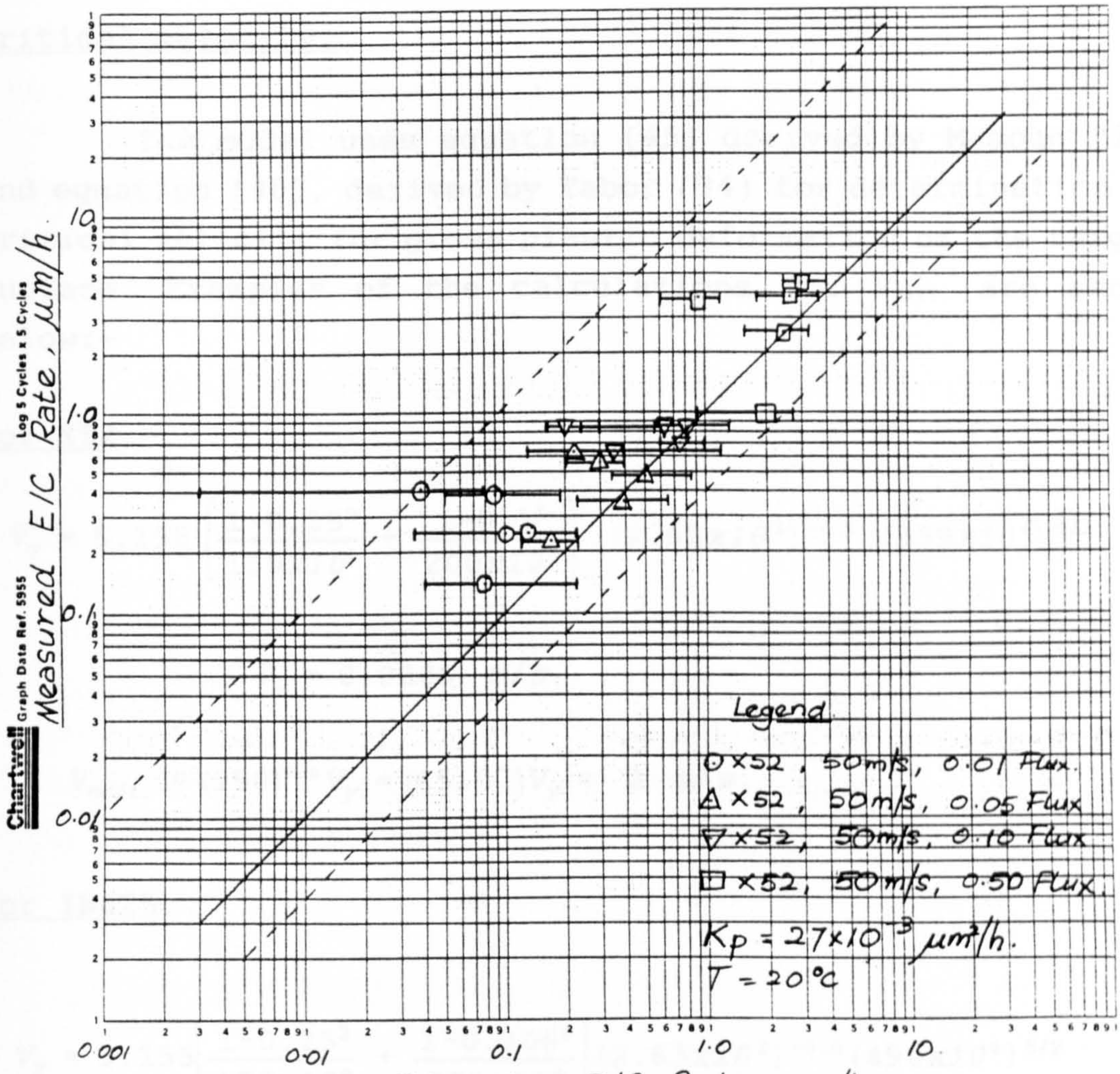

Figure 53(b). Predicted versus measured erosion-corrosion rates for X52 at a constant velocity and different flux.

6.4 Validation of the Model.

6.4.1 Single Impact Experiment versus Model.

Critical velocity.

The model uses equation (45) derived by Mamoun (39) and equation (46), derived by Tabor (34) for determination of critical velocity for gross plastic deformation of the target surface. Examples of the calculations for $V_{crit.}$ are shown below:-

For X52,

$$V_y = 5.155\left[\frac{1-0.25^2}{150x10^9} + \frac{1-0.3^2}{200x10^9}\right]^2 (2.63x10^3)^{-0.5} (359x10^6)^{5/2}$$

$$V_y = 0.0286 \ \ m/s.$$

$$V_{crit.} = (150)^{5/6} V_y = (65.07) V_y \approx \ \ 2 \ \ m/s.$$

For IN625,

$$V_y = 5.155\left[\frac{1-0.25^2}{150x10^9} + \frac{1-0.306^2}{201x10^9}\right](2.63x10^3)^{-0.5}(490x10^6)^{5/2}$$

$$V_y = 0.062 \ \ m/s.$$

$$V_{crit.} = (65.07)\ V_y \approx \ \ 4 \ m/s.$$

From Figures 19(b) and 19(d), the values of $V_{crit.}$ are estimated to be ≈ 3 m/s for X52 and ≈ 5 m/s for IN625. Their values are therefore found to be very close indeed.

Crater volume versus Particle size.

Figures 54(a) and 54(b) for X52 at 90° impact angle, show that the model predicts reasonably good values of crater volume compared with the values generated by the experiments. This is particularly so at velocities of 50 m/s, 80 m/s and 100 m/s. At a velocity of 150 m/s, the model predicted a slightly higher values of crater volume for any given particle size between 130-300 μm compared to that obtained from experiments.

Figures 55(a) and 55(b) for X52 at 30° impact angle, show that the model predicts a much higher value of crater volume compared to those generated by the experiments. The difference increases with increasing velocity. This is because the model assumes that the shear component of the impact velocity (hence energy) is efficiently transferred to the target material to do work. This may not be true for practical situations. At 30° impact angle, this value is extremely large compared to the deformation (normal) component, especially for a high velocity particle.

6.4.2 Erosion Experiment versus Model.

Figures 51(a) and 51(b) show the scatter plots of the predicted erosion values generated by the model versus the experimental values, for X52 material. In general, the model generates very good results when compared with those values generated by experiment. However, there is a tendency for the predicted values to be slightly greater than the experimental results. This can be seen clearly on the graph, that is, the scatter is found to be more on the right of the ideal line (solid line) than the left. Assuming that the boundary lines drawn (broken lines) as best-fit lines to contain the average value of scatter points and show the trends, one can deduce

that the model tends to over-predict by a factor of 7 than to under-predict by factor of 2.5 from both scatter diagrams generated for X52 material. The error bars represent the minimum and the maximum values predicted for the average value from ten runs. Putting these into consideration, then the model may predict values close to the ideal line.

Figure 52 shows the erosion rates scatter for IN625 material as predicted by the model versus experimental values. It gives an even wider scatter than that of X52 material. It also shows that the model tends to predict higher values at a low particle velocity below 50 m/s and lower values at a high particle velocity, equal to or greater than 50 m/s, compared with the values generated by experiment.

Velocity exponent.

Table 12 shows the velocity exponents of X52 generated by the model at different impact angles. It gives an average value of n=2.6 which is comparable to those values generated from experiments as shown in Table 8, which suggests that n=2.5-2.7.

Table 12. Velocity exponents derived by the Model on X52 material.

Impact angle	15°	30°	60°	90°
n	2.6	2.6	2.6	2.6

Therefore the model can generate a reasonably good prediction of the trend in erosion behaviour of materials used in petroleum production when exposed to sand erosion.

6.4.3 Erosion-corrosion Experiment versus Model.

Figures 53(a) and 53(b) show the scatter diagram of the predicted erosion-corrosion rates versus the corresponding measured values as obtained from experiments for X52 material. The predicted E/C rate values were found to be slightly lower when compared with those values obtained from experiments. The results seem to be the reverse of erosion only scenario scatter diagram, i.e. most of the scatter points are to the left of the ideal (solid) line. It also appears that the effect of corrosion was very negligible in the E/C rates generated by the model. However, at high velocity e.g. 150 m/s the points seem to stay very well near to the ideal line.

Erosion-corrosion rate factor.

Table 13 shows the E/C rate factor calculated from the results generated by the model for X52 material. It generally shows that similar E/C rate factors were generated by the model when compared with those calculated from experimental results as shown in Table 16, at medium and high sand fluxes. This highlights that there is some interaction between erosion and corrosion shown by the model. However, the E/C rate factors at a low sand flux of 0.01 g/mm^2/h, were very much the same as at other sand flux rates.

Table 13. Erosion-corrosion rate factor for X52 generated by the Model (V_p=50 m/s, T=20°C and K_p=27x10^{-3} $\mu m^2/h$).

Flux, g/mm^2/h	15°	45°	90°
0.01	2.3	0.9	0.6
0.05	0.7	0.8	2.2
0.10	1.9	1.1	1.1
0.50	1.3	0.8	0.9

It is concluded that the model gives a good prediction of erosion and erosion-corrosion rates comparable with the results produced by the experiments. The model can therefore be used for predicting erosion/corrosion rates for materials used in petroleum production.

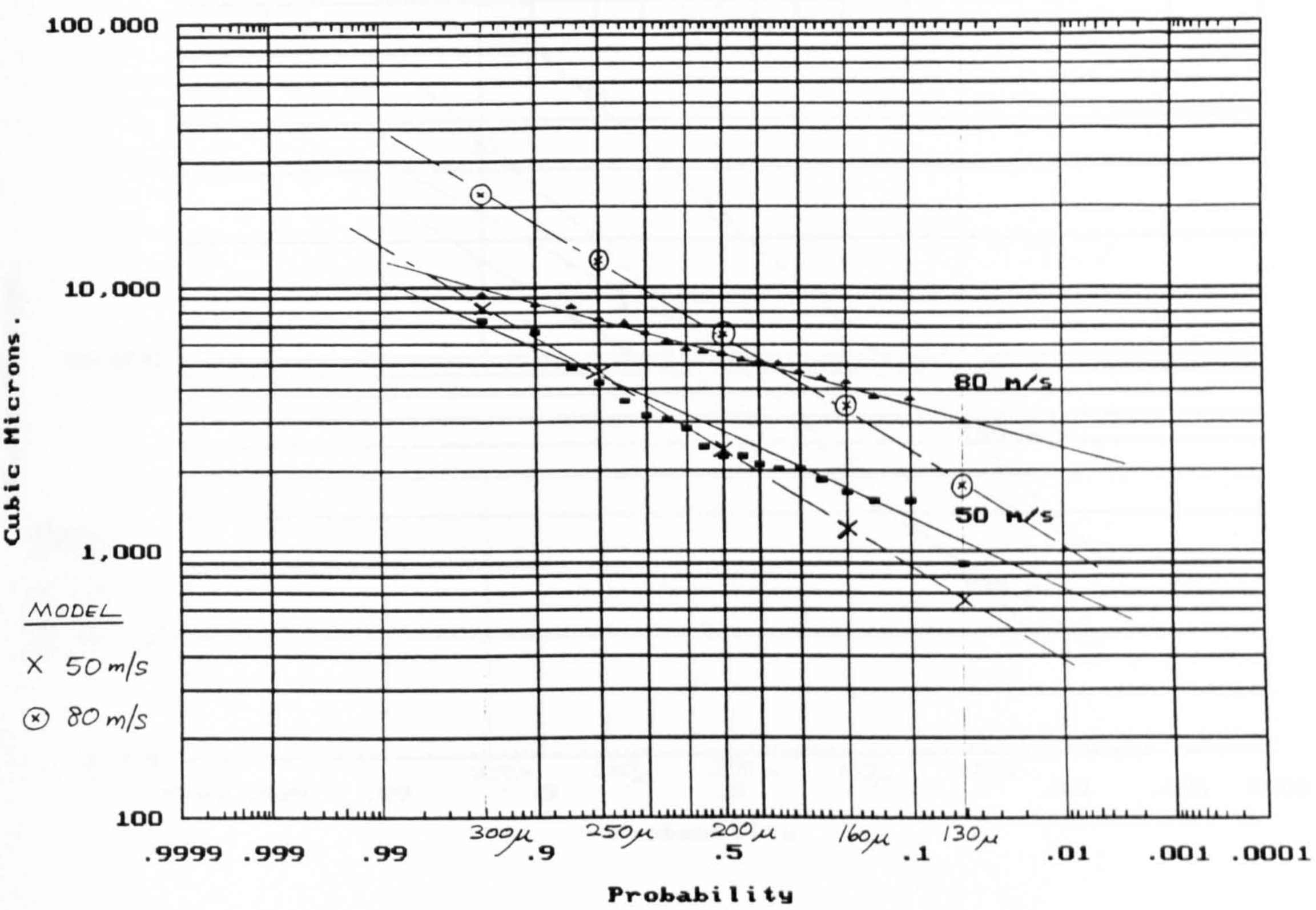

Figure 54(a). Predicted and measured crater volumes versus particle size, at 90° impact angle, V_p=50 m/s and V_p=80 m/s.

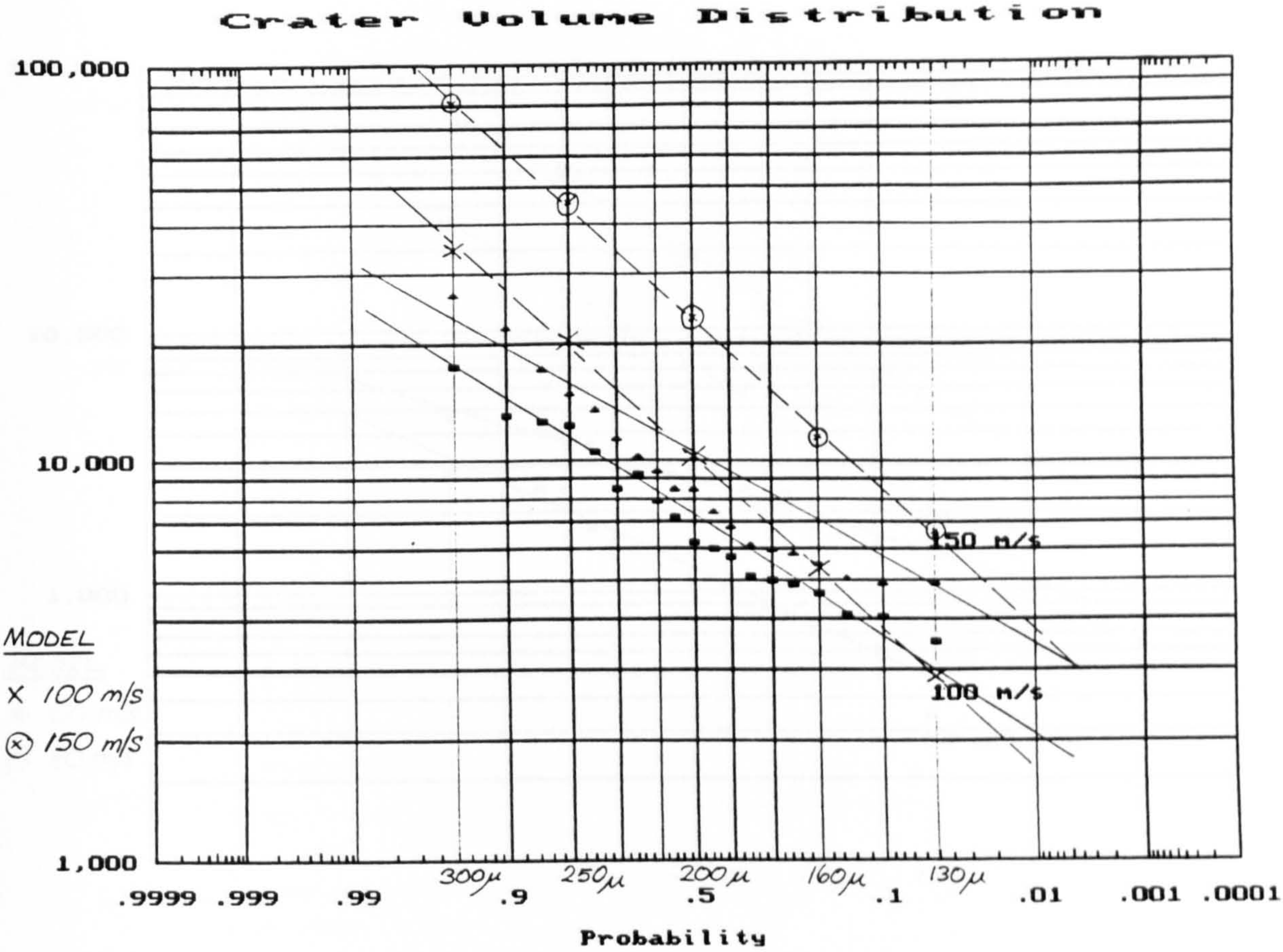

Figure 54(b). Predicted and measured crater volumes versus particle size, at 90° impact angle, V_p=100 m/s and V_p=150 m/s.

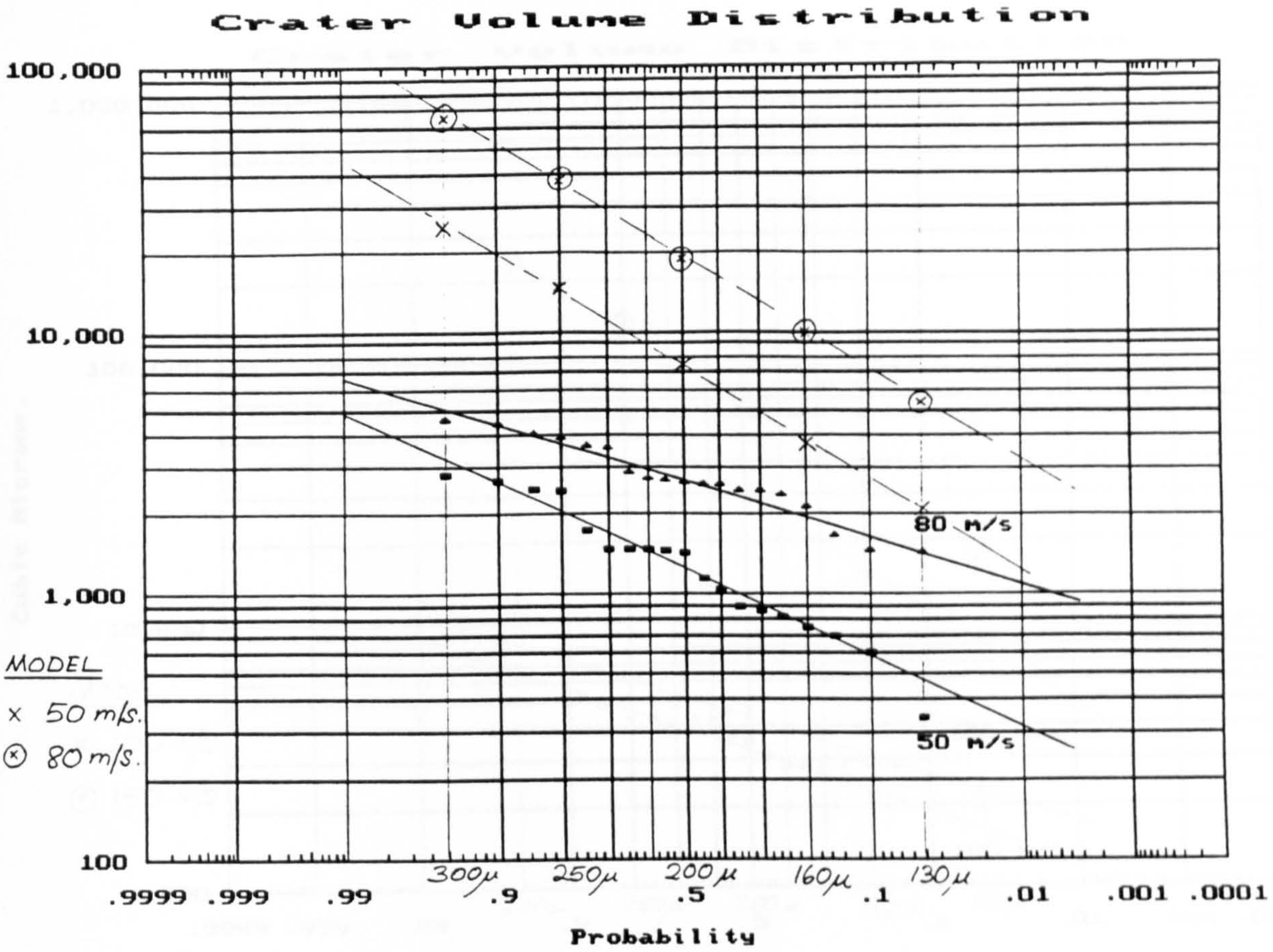

Figure 55(a). Predicted and measured crater volumes versus particle size, at 30° impact angle, V_p=50 m/s and V_p=80 m/s.

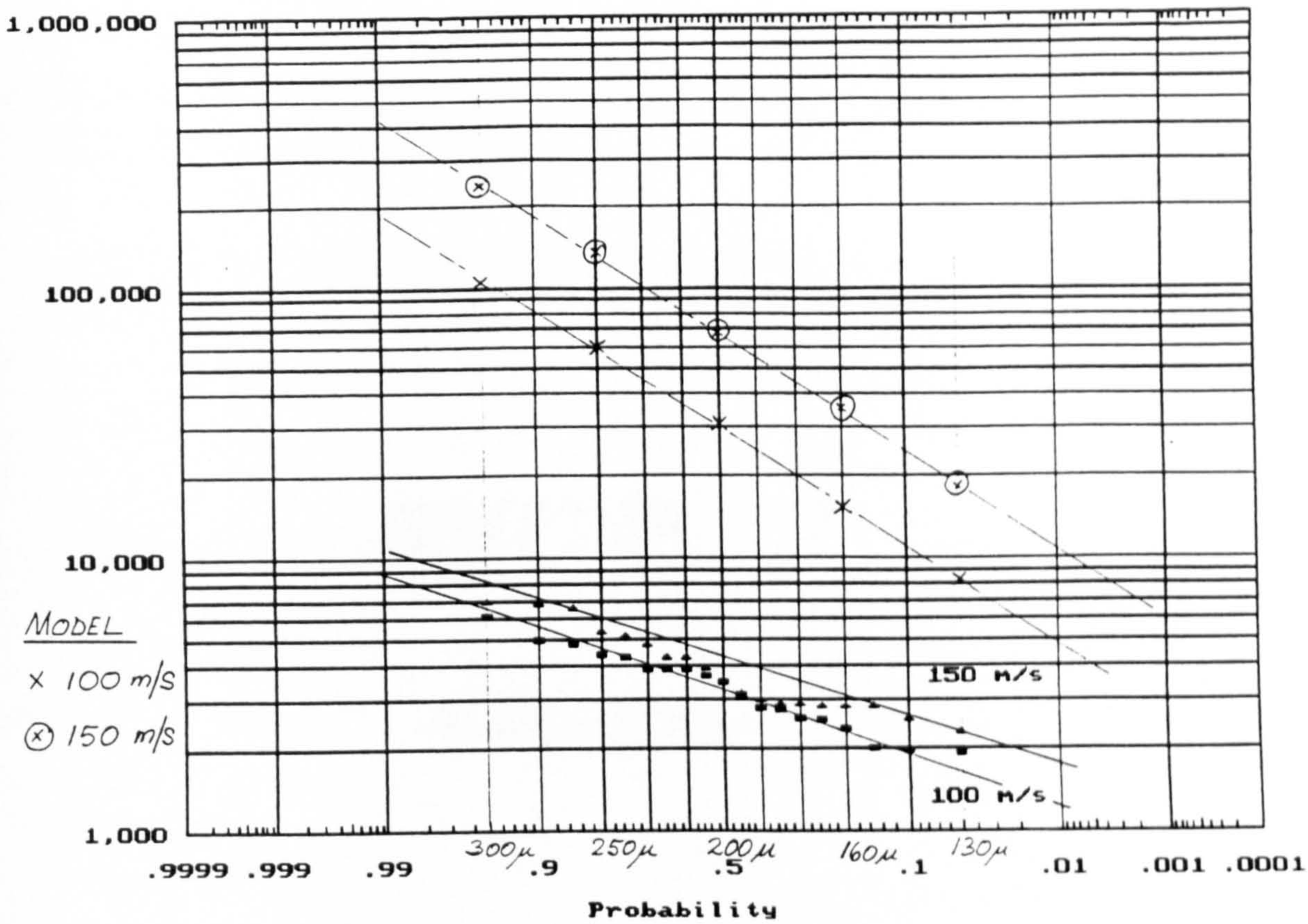

Figure 55(b). Predicted and measured crater volumes versus particle size, at 30° impact angle, V_p=100 m/s and V_p=150 m/s.

CHAPTER 7

Discussion

CHAPTER 7

7. DISCUSSION.

It is pertinent to mention initially the limits and bounds of the modelling experiments carried out in this work. They can be summarised as follows:-

a). The pressure in which the experiments were carried out was in the region of 1.5 bar(a). This is well below the system pressures of most oilfield equipment which may vary from a few bars in the surface facilities up to sometimes in excess of 100 bar at wellheads and downhole. However, the estimated partial pressures for CO_2 in the test chamber, at temperatures of 20°C and 80°C were about 1.4 bar(a) and 1.0 bar(a) (after making allowance for water vapour pressure (72)), respectively. These are sufficiently high levels of CO_2 partial pressures, for wet CO_2 gas to be considered corrosive.

b). The actual gas composition used for experimental work contains no hydrocarbon gas components which may have an influence on the corrosion process. For example, the presence of hydrocarbons may help to inhibit the corrosion reactions by providing a protective barrier on the surface of the specimens.

c). The duration of exposure for all tests on the specimens varied between 5 to 30 hours. This may not be representative of actual erosion-corrosion phenomena that take place in real field life. The duration of exposure is expected to influence the rate of erosion/corrosion especially when gas composition changes occur during the life of the reservoir.

d). The sand flux rates modelled in these experiments were designed to be as constant and uniform as possible and were constrained to behave in that manner throughout the experiments to facilitate analysis. Whereas in service, sand production behaviour is normally highly variable and non-uniform. Fluctuations do occur and sometimes sand production appears in batch production manner. However, in order to understand the material behaviour, it was important to study the erosion-corrosion behaviour under constant and uniform exposure of sand flux rates.

e). The test temperature was limited by the maximum operating temperature of the atomizer, i.e. 150°C. In order to achieve a temperature of 80°C in the region near the specimens in the erosion test rig, the furnace temperature had to be well above 300°C, depending on the ambient and the water supply temperatures. The glass wool and asbestos impregnated lagging materials used to shield the atomizer from the radiation heat generated by the furnace were not 100% efficient and damage would have been caused to the atomizer had the furnace temperature been set above 300°C to achieve a higher test temperature. In practice however, the atomizer was cooled down by the use of the mains water supply which was normally below 10°C during the performance of the tests. However, because of the above mentioned risks no attempt was made to run tests above 80°C in the corrosion, erosion and erosion-corrosion experiments. As the test pressure was rather low (≈0.5 bar(g)), the rig was unable to sustain wet CO_2 conditions when the temperature was raised above 100°C. This limits the application of results as in some field conditions, temperatures may be as high as 150°C, downhole for example, or in geothermal areas. Nevertheless, temperatures of 80°C and below are typical of many oil and gas process systems.

f). Low velocity experiments were limited to low sand flux rates below 0.1 g/mm^2/h. Higher sand flux rates were impossible to run, especially in wet conditions, without blocking the vertical particle feed tube with damp sand. The lowest velocity that was practicable to run was about 20 m/s with a sand flux rate of 0.05 g/mm^2/h or lower.

g). Throughout the experiments, dissolved oxygen in the mains water was not removed prior to feeding into the test chamber, as positive pressure is required inside the test chamber in order to exclude any atmospheric air from coming in. One simple way to drive away dissolved oxygen from the water is to bubble nitrogen gas through it, but, this will also remove the water pressure which is required to overcome the back pressure inside the chamber. However, when fine droplets are introduced in the test chamber containing ≈1 bar of CO_2 and zero partial pressure of O_2, the water very quickly equilibrates with the CO_2 atmosphere. This will result in a drastic fall in the concentration of O_2 in the water as it was introduced into the test chamber in this manner. Therefore, it was felt that the dissolved oxygen in the water mains had no major influence on the rate of corrosion, that is the corrosion was essentially wet CO_2 gas corrosion. This is supported by the following experimental observations.

Two sets of experiments were performed in wet atmospheric (oxygen rich) environment. These gave corrosion products which were brown in colour rather than greyish black as is normally the case for wet CO_2 gas corrosion products. As the wet CO_2 gas corrosion experiments produced grey/black scales it was believed that the effect of dissolved oxygen in the mains water used in this experimental work is insignificant.

Using the rig in wet conditions in this manner, experiments were carried out to investigate the behaviour of materials subjected to simultaneous wet CO_2 gas corrosion and erosion by sand particles. These are described in the following discussion.

7.1 Detail Discussion of the Results.

7.1.1 CO_2 Corrosion Experiments.

The results obtained from conventional wet CO_2 gas corrosion experiments suggest that even at 20°C, there are corrosion scales which form on the surface of the C-Mn steel specimens and that these are protective in nature so long as they remain undisturbed. Although the type of scale formed is soft and could easily be removed by wiping them with a soft piece of cloth, the scales remain intact under the low velocity gaseous environment and are protective giving low corrosion rates. As the size of the specimens used was also rather small, (average weight was around 3.5 g. only) it was difficult to detect any weight change due to wet CO_2 gas corrosion. This is clearly shown in Table 4.

The results show that the corrosion scales forming on the surface of the specimens were very thin, about 5 μm in thickness even after 500h exposure at a temperature of 80°C, the initial impression was that the rate of material loss was going to be minimal. However, the corrosion scales were found to grow with time and that their thickness varied proportionally with the square root of time (for X52, X65, L80 and N80 materials). Their scale growth kinetics, K_p, are therefore parabolic (64) and found to have values between $18x10^{-3}$ $\mu m^2/h$ and $50x10^{-3}$ $\mu m^2/h$ measured at a temperature of

80°C (Table 5 and Figure 11). Using the Arrhenius relationship (47,70,71), i.e. assuming K_p to be proportional to $e^{-E/RT}$, where E is the activation energy needed for scale growth, R is the gas constant and T is the temperature, the values for K_p at 20°C can be estimated. These were found to be approximately 8 $x10^{-3}$ $\mu m^2/h$ for X65, L80 and N80, and 27 $x10^{-3}$ $\mu m^2/h$ for X52.

The thickness of the scales was assessed by observing samples using an SEM. Samples were prepared by first mounting the specimen in bakelite, polishing to a 6μ surface finish and etching with 10 % nitric acid in alcohol for about 4 minutes. This helped to demarcate the boundary between the scales and the metal, as a deep crevice was preferentially etched out, thus forming a clear boundary between metal/scale contact (see Figures 12(c) and 12(d)).

It is believed that the corrosion scales formed were primarily iron bicarbonate (inner layer if any, being more soluble) and iron carbonate (the outside layer, being less soluble) (13,14,18). Magnetite was also present on the surface as a result of the specimens heating up at the end of the experiment to a temperature above 80°C when the water supply was switched off and the whole set up allowed to cool down. This normally took more than two hours before the specimen could be removed for examination. This seemed to be the case when comparing the results obtained from the X-ray diffraction as shown in Tables 9(a) with the standard characteristics of X-ray diffraction for magnetite as shown in Table 9(c) (66).

It is likely that the scales developed in these experiments were primarily iron bicarbonate/carbonate. The scales were soft, and grew slowly at a parabolic growth rate of between $8x10^{-3}$ $\mu m^2/h$ to $50x10^{-3}$ $\mu m^2/h$ depending on the materials as the temperature increased from 20°C to 80°C.

Based on wet CO_2 gas corrosion alone, assuming the scale is not disturbed, the predicted rates of scale growth and hence metal loss are negligibly small. This can be seen clearly in Table 14 below:-

Table 14. Scale thickness estimates versus time.

K_p, ($x10^{-3}$) $\mu m^2/h.$	Scale Thickness, µm.					
	1 year.	2 years.	3 years.	4 years.	5 years.	6 years.
8	8.4	11.8	14.5	16.7	18.7	20.5
18	12.6	17.8	21.8	25.1	28.1	30.8
27	15.4	21.7	26.6	30.8	34.4	37.7
50	20.9	29.6	36.3	41.9	46.8	51.3

This demonstrates that wet CO_2 gas corrosion rates are very low when samples are not totally immersed in liquid phase. Therefore, the De Waard-Milliams expression (2) cannot be used, for corrosion rates determination.

7.1.2 Single Impact Experiments.

The results from single impact experiments, as shown in Tables 7(a) and (b), indicate that no significant weight change occurred during the experiments, at impact angles of 30° and 90° for particle average velocity between 50 m/s to 150 m/s. Examination under the SEM, revealed that the type of craters formed at 30° impact angle are those of craters with lips as described by Hutchings (33). Although the metal was displaced in the direction of particle impact on the

plane of the surface, the displaced material remains attached. At 90° impact angle the craters formed are of the indentation damage type. Thus, for both cases, there is no material/weight loss. The photomicrographs in Figure 56 are examples of the type of craters formed at 30° and 90° impact angles.

Figures 17(a) and 17(b) and Figures 18(a) and 18(b) show that the crater volume distribution fits well to a log-normal distribution, and similar to the original particle size distribution. The trends show that, crater volume increases with the impact velocity of the particle. The same is also true with impact angles, i.e. larger craters are formed at 90° impact angle than those at 30° (see Figures 17 and 18). This is implying that the normal velocity component of the particle causes more damage to the metal surface than the horizontal component.

Referring to Figure 15(a), it is reasonable to assign an equivalent diameter of particle for a given probability value. For simplicity, the 5% probability can represent a 130 μm diameter particle, 20% probability for a 160 μm diameter particle, 50% probability for a 200 μm diameter particle, 80% probability for a 250 μm diameter particle and 95% probability for a 300 μm diameter particle or less than each of the given value. From the crater volume distribution plots, one can see that the crater volume increases with particle size/diameter. This is of course expected as the kinetic energy of each impacting particle is proportional to its mass which, in turn, is proportional to the cube of its equivalent diameter.

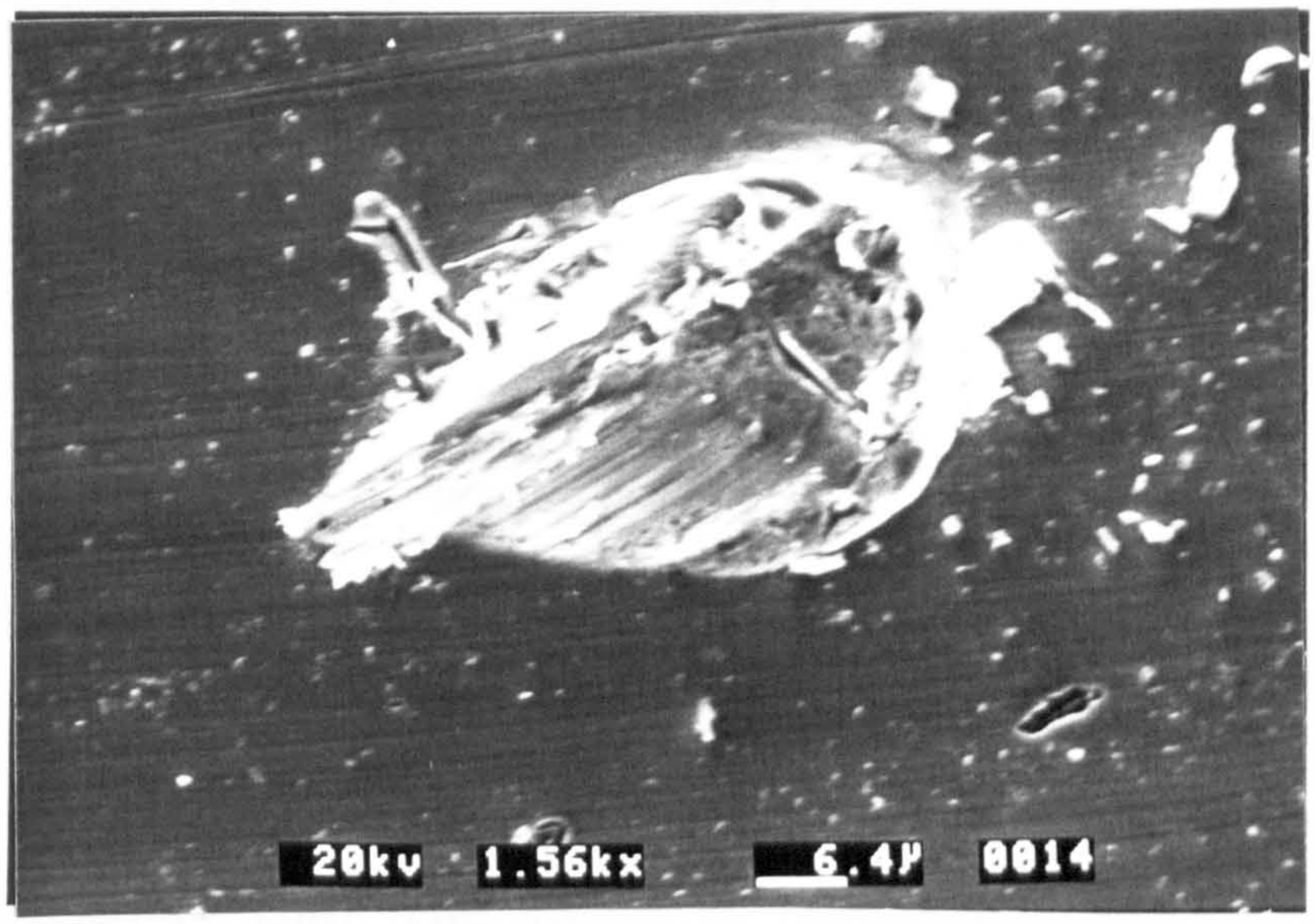

(a) 30° Impact angle.

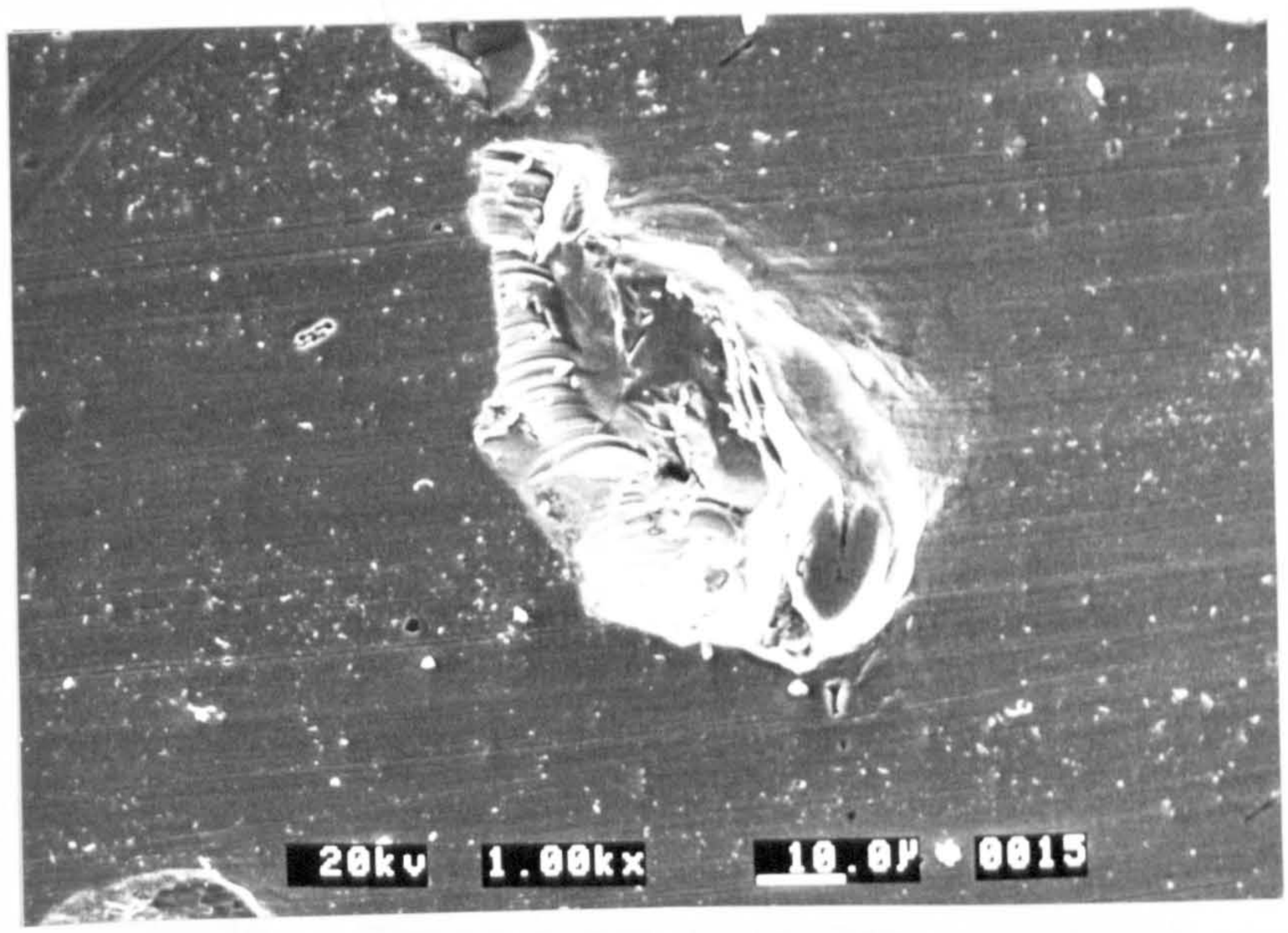

(b). 90° Impact angle.

Figure 56. Typical craters formed in single impact experiment.

These values of equivalent diameters could also be used in Figures 19(a)-(c). From these graphs, it can be seen that there is a critical impact velocity below which the particle impact will not cause any damage to the material. This critical impact velocity will depend on the combination of the properties of the particle, the target material and also the impact angle. The critical impact velocity for X52 is about 3 m/s at 90° impact angles ($V_{crit.}$ ≈ 3 m/s). The critical impact velocity for IN625 is about 5 m/s at 90° impact angles ($V_{crit.}$≈ 5 m/s). It is difficult to give a single value for the critical impact velocity at 30° impact angle because the lines do not converge at the same point on the abscissa as in the case of 90° angle. However, the trends indicates that the value of critical impact velocity for 30° angle is about twice that for 90° impact angle. Therefore the critical impact velocities for X52 and IN625 are approximately 6 m/s and 10 m/s, respectively. It can generally be said that the critical impact velocities are higher at 30° than at 90° impact angles for both of these materials. This again supports the assertion that it is the normal component of velocity which causes the damage to the metal surface when impacted by a particle. Since the critical impact velocity for IN625 is higher than that for X52, it suggests that ductile materials with high yield strength have better resistance to impact damage than those with a lower yield strength.

Using equations (45) and (46), the model developed by Mamoun (39), the predicted values of $V_{crit.}$ are 2 m/s for X52 and 4 m/s for IN625. These show that the measured values of $V_{crit.}$ are slightly higher than the theoretical values predicted by the model. This is probably because of the effect of high strain rate during impact which generates a higher dynamic yield stress of the surface material while the model considers a static yield stress in the erosion process. Working backward from equations (46) and (45), and inputting

the measured $V_{crit.}$ values, the corresponding dynamic yield stresses for X52 and IN625 are calculated and found to be 434 MPa and 534 MPa, as compared to original yield stresses of 359 MPa (74) and 490 MPa (75), respectively.

7.1.3 Erosion Experiments.

It is important to note that, the duplicate test results show that the erosion rig is capable of generating repeatable and reliable results for all of the materials as shown in Figure 20. Analysis of duplicate test results for four of the materials, as shown in Table 15 below, confirms the reliability of the erosion test system.

Table 15. Analysis of duplicate erosion test results.

	α°	E.R./1	E.R./2	δ % f.m.pa
X52,	15	0.616	0.494	12.3
	30	1.529	1.159	16.0
	45	1.922	1.976	1.4
	60	2.843	2.867	0.4
	90	1.970	2.117	3.6
IN625,	15	0.386	0.687	29.0
	30	1.034	1.321	12.2
	45	1.907	2.295	9.2
	60	2.555	2.701	2.8
	90	2.648	2.768	2.2

L80,	15	0.476	0.543	6.6
	30	1.135	1.135	0
	45	1.738	1.708	0.8
	60	1.098	2.605	10.8
	90	1.867	1.964	2.5
13Cr,	15	0.342	0.435	12.0
	30	1.107	1.107	0
	45	1.505	1.735	7.1
	60	2.096	2.133	0.9
	90	1.810	2.027	5.7

α° = impact angle, E.R./1 = Erosion rate from test No. 1, E.R./2 = Erosion rate from test No. 2, and δ% f.m.pa = Percentage deviation from mid-point average.

Figures 22 and 23 show that, for sand flux levels equal to or greater than 0.05 g/mm^2/h, the general trend is for the erosion rate to increase with increasing impact angle up to about 60° and then to remain at a constant level between 60° to 90°. This result indicates that at a certain threshold value of sand flux rate, when there are enough particles bombarding at the target surface per unit time to cause sufficiently high strain rate of the material surface, the material then exhibits more of the brittle form of failure. At the same time, the ductile property of the material was still present, but to a lesser extent, perhaps due to the adiabatic shear heating process as a result of high frequency of impacts by the particles (37). Therefore, over and above this threshold value of sand flux the brittle failure mechanism is more prevalent than the ductile failure mechanism. The mechanism is illustrated in Figure 57(a).

For low sand flux (0.01 g/mm^2/h), there appears to be a change in behaviour. Below a threshold value, the results show a trend in which the erosion rate increases to a maximum value at about 45°, decreasing thereafter. This indicates that at low flux rate the ductile property of the material is dominant throughout the erosion process. In this case the surface of the material will accumulate a lower level of strain due to low the frequency of impacts by the particles. This behaviour can be described schematically as in Figure 57(b).

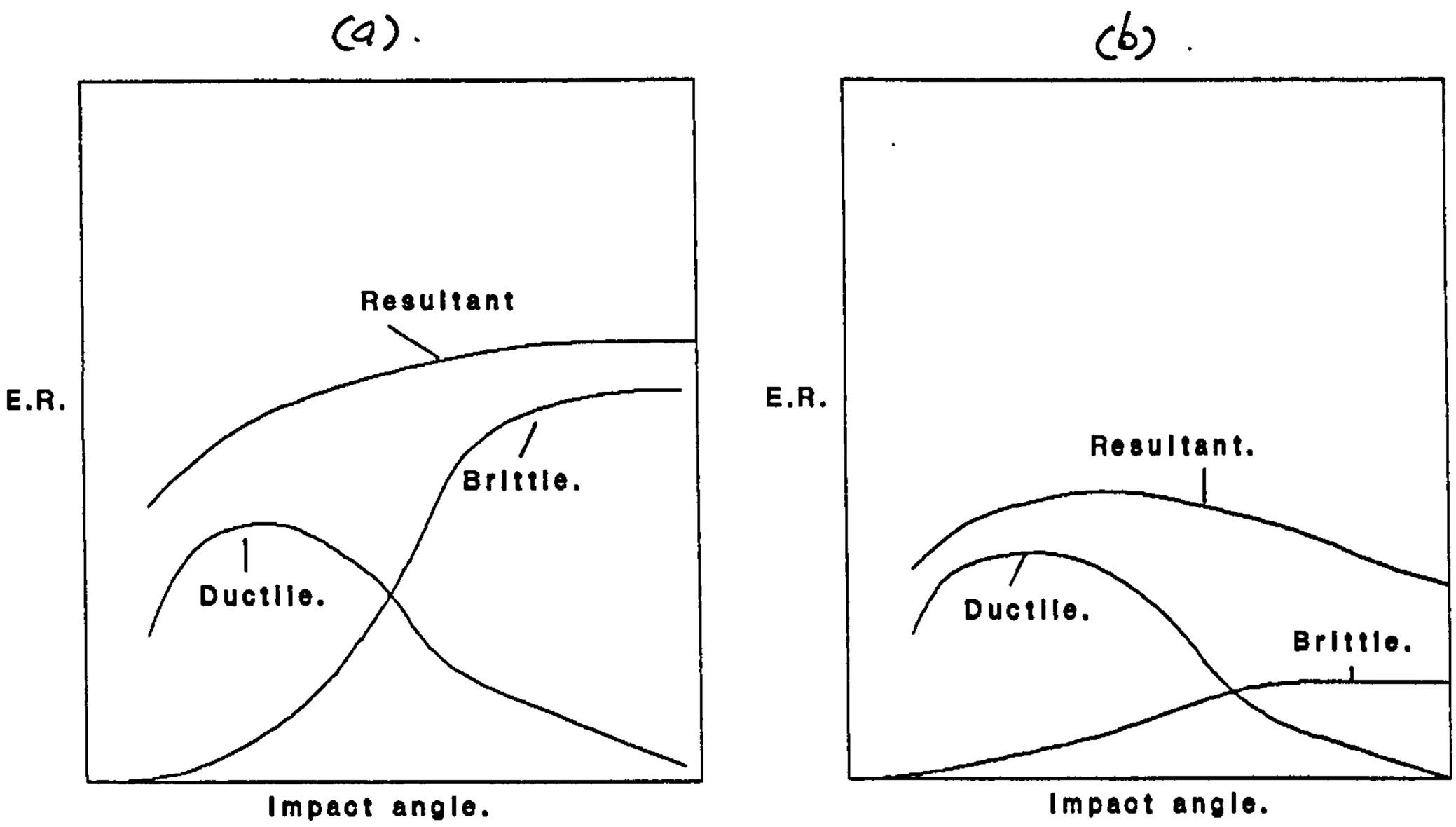

Flux › 0.05, Ductile failure is overshadowed by Brittle failure.
-High level of accumulated strain

Flux ‹ 0.05, Ductile failure is dominant.
-Low level of accumulated strain.

Figure 57. The influence of accumulated strain on ductile and brittle failures of ductile material.

It has been shown in Table 8, that erosion rate increases with particle (velocity)^n, and that the exponents n, lies within the range of 2.5 - 3.1 for four of the materials. Figures 24 and 25 show the effects of velocity exponents in graphical forms. These values of velocity exponents are comparable to some of the results obtained by previous workers (23,29,32,44).

From the plots of weight loss versus time as in Figures 26 and 27, we can see that at low impact angles such as 15°, the material appears to start losing weight immediately but at a very slow rate (by cutting process), and at higher angles it takes a while before high rate of weight loss to commence (by deformation fatigue process) (33,35,36). This is another implication of the significant contribution of the normal component of the particle impact velocity towards material removal. The time taken before the material starts to lose weight is called the incubation period. The incubation period appears to be increasing with impact angle, and at 90° impact angle the incubation period is approximately 2 hours for 0.1 g/mm^2/h sand flux. This indicates that the incubation period also has a direct relationship with the normal component of the particle velocity, hence the level of deformation wear. Earlier workers (28,29,30) found that the target material had actually experienced an increase in weight during the early stage of erosion, i.e. during the incubation period, due to particles imbedded into the surface. During the incubation period the material has not reached its steady state of erosion process. Using equation (44) as suggested by Hutchings (44), and putting e_c=0.2% proof strain, P=3Y=3x359 MPa for X52, A=1 for unit area, R= 100 μm, V=50 m/s and 0.0001 Kg/mm^2/h, the estimated incubation period is found to be 21.5 hours. This model predicts an incubation time more than ten times longer for X52 material than what was measured from the experiment. Therefore, more work is still required

to produce a reasonable model for the prediction of incubation time.

7.1.4 Erosion-Corrosion Experiments.

Figure 28 shows the synergy of the erosion/corrosion processes acting conjointly, whereas Figure 29 for IN625, shows corrosion was absent. In general, there was a considerable increase in the rate of metal loss when corrosion was present in an erosive environment or vice versa. In this case, the degree of increase is significant when the particle flux is low, in which the probability of impacts on a site is low allowing time for the corrosion scale to re-grow before the next impact takes place. As a result, the type of erosion-corrosion process consists of mainly the removal and regrowth of the corrosion scale which is equivalent to a scale modified type of erosion-corrosion regime (53). As the particle flux increases, the gap between the erosion and the erosion-corrosion rates narrows down. This indicates the transition of the process from the scale modified to substrate dominated erosion-corrosion regime. Until such a time when the frequency of particle impacts at a site is high enough, i.e. at a much higher flux, resulting in less time and chance for the corrosion scale to re-grow hence the particle has to erode the substrate instead. This is the substrate dominated regime (53). Having to erode the substrate which is harder, the result is a metal recession rate approaching the pure erosion which is lower than expected when combining the effect of corrosion/erosion together. If the comparative increase in the rate of metal loss due to erosion-corrosion is compared to pure erosion and defined as the Erosion-Corrosion Rate Factor, then Table 16 below shows the E/C Rate Factors for X52, X65, L80 and N80 at increasing particle flux calculated at different impact

angles for an average particle velocity of 50 m/s and a temperature of 20°C.

Table 16. The erosion-corrosion rate factors.

(a). X52.

Flux,g/mm²/h	15°	45°	90°
0.01	20	10	26
0.05	3.1	3.0	3.2
0.10	2.8	1.6	1.5
0.50	4.0	2.0	2.0

(b). X65.

Flux,g/mm²/h	15°	45°	90°
0.01	34	30	38
0.05	8.5	4.5	3.7
0.10	2.3	1.1	1.4
0.50	2.3	1.4	1.3

(c). L80.

Flux,g/mm²/h	15°	45°	90°
0.01	35	17	38
0.05	2.4	1.6	2.4
0.10	2.6	1.5	1.3
0.50	2.3	1.3	1.6

(d). N80.

Flux, g/mm²/h	15°	45°	90°
0.01	24	10	40
0.05	4.4	2.4	2.1
0.10	3.3	1.7	1.7
0.50	5.2	1.6	1.5

From the above values of erosion-corrosion rate factors it can be said that the substrate dominated regime started at a sand flux of about 0.05 g/mm²/h for V_p=50 m/s, at a temperature of 20°C. for those materials.

There are similarities in the behaviour of X65, L80 and N80 materials as in X52, where the erosion-corrosion rate factors are significantly higher at low sand flux (see also Figures 30, 32 and 33). These are indications of soft scale products forming on the metal surfaces and metal recession was dominated by corrosion scale removal processes whereas at higher flux, metal recession was dominated by substrate erosion.

Figure 35 shows that with an increase in temperature there was also an increase in erosion-corrosion rate. The increase in temperature will increase the corrosion scale growth kinetics. The erosion-corrosion rate was also found to have increased considerably with the increase in particle velocity. This is evident as in Figures 36 and 37. When the particle velocity is high, the kinetic energy of the particle before impact is also high which is proportional to the (velocity)^n , and n is normally found to be greater than 2.

7.1.5 Surface Morphology and Cross-Sections.

Erosion Surfaces.

Looking at the SEM photomicrographs taken for X52 and IN625 specimens as in Figures 38(a), (b), (c), (d) and Figures 39(a), (b), (c), (d), it is evident that the mechanism of surface damage and material removal is that of the micro-machining process (cutting damage) (22,35), taking place at low angle of 15° and gradually changes to micro-extrusion and forging process (cutting, plus deformation damage) (42) taking place at higher angle such as 30°. The cutting damage seen at 15° impact angle are longer and thinner with smaller lips formed at the point where the particle leaves the surface as compared to those seen at 30° impact angle which are shorter, wider and with thicker lips. These lips will form platelets after several impacts before being detached from the surface. The deformation damage becomes more evident at 45° and 90° impact angles. At high impact angles such as 90°, particles may break apart during impact and particle debris may embed into the damaged surface as shown in Figure 38(d). Cracks may develop after several impacts and platelets pile up before being detached from the surface.

From the calculation in Appendix H it is found that the average volume of platelet generated by an average particle size of 200 μm is generally bigger for IN625 material (1337 μm^3) than for X52 material (1201 μm^3). These are not so evident from the surface morphology photographs.

Erosion-corrosion Surfaces.

In Figures 40(a), (b), (c) and (d), we can see that corrosion pits are forming on the damaged surface and they probably help to increase the rate of metal recession. It must be stressed here that the mode of metal recession here is that of substrate dominated rather than scale dominated, as in this case, the flux was 0.5 g/mm^2/h and V_p=50 m/s. The extensive corrosion pits found on the surfaces could have been formed while the specimens being prepared for examination. However, those pits could form as evidence that pitting may be an important process that enhances the process of metal loss which is also a known process in wet CO_2 gas corrosion. The corrosion scale products cannot be seen on the surfaces as they are thin (and soft), and are continually being removed by the particle impacts.

Similar surface damage is also seen on the surfaces of IN625 specimens exposed to erosion/corrosion as previously experience in erosion only tests (see Figure 41). This confirms that IN625 is resistant to wet CO_2 gas corrosion, and in turn supports the similar erosion and erosion-corrosion rates obtained from the experiments.

Surface Cross-sections.

Figures 42(a), (b), (c) and (d) illustrate evidence of the development of work-hardened layers immediately below the impacted surfaces. At low impact angles, such as 15°, the work-hardened layer was almost none-existent. As the impact angle increases the work-hardened layer thickness increases until it reached a maximum thickness of approximately 20 μm at 90° impact angle. This confirms the fact that surface work-hardening is caused by the normal component of particle impact velocity, i.e. it thickness

increases as the impact angle, α, increases. This work-hardened layer is indicated by the thinning of layers of grains of the material immediately beneath the impacted surface.

Figure 43(a) and (b) illustrate the evidence of two mechanisms of material removal. The former shows a clean cut surface will result at low impact angles and the latter shows that the surface will deform until enough energy is absorbed and lateral cracks develop under the surface before material is removed due to the normal component of impact velocity by a delamination mechanism.

Figure 58 shows the Vickers microhardness distributions on the X52 specimens cross-sections and the impacted surfaces. These again confirm that the work-hardening and deformation damage are associated with the normal components of the particle impact velocities. However, the soft surface zone on the impacted surface as proposed by Levy (42), could not be detected in this examination, perhaps because the layer was very thin and the author was using a microhardness machine on 500g load. However, the soft surface zone as described by Levy (42) may be a dynamic one which involved the adiabatic shear heating which occur during the erosion processes only, as described by Winter et. al (37). Any smaller loads used in the detection was not successful because the roughness of the eroded surfaces made the identification and measurement of the indentations difficult and inaccurate.

Figure 58. Vickers microhardness number distributions.

(a). Specimens cross-sections.

(b). Specimens impacted surfaces.

15° Impact angle.

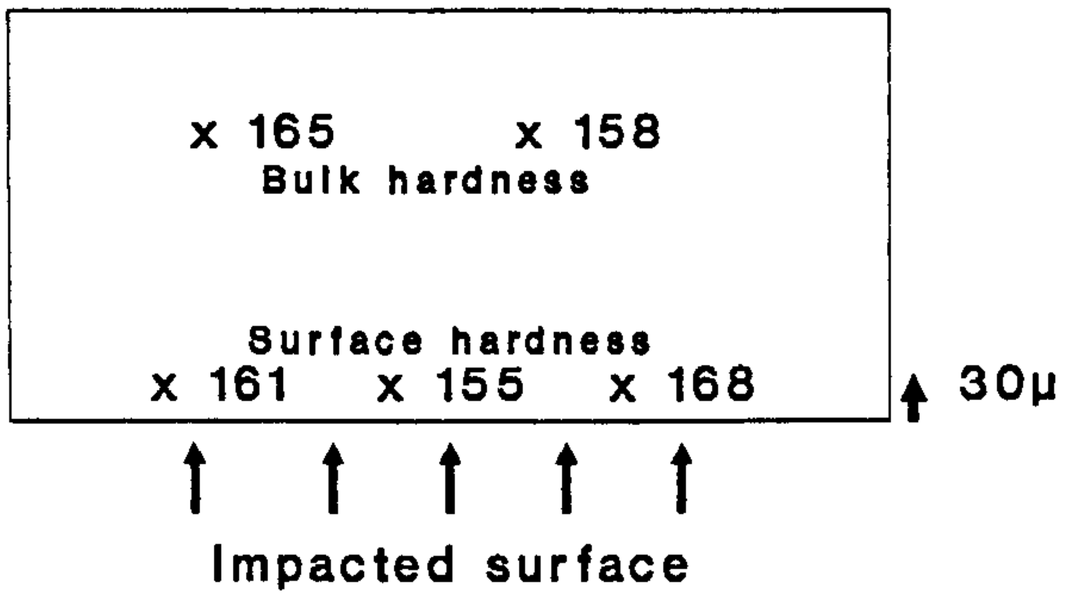

15° Impact angle.

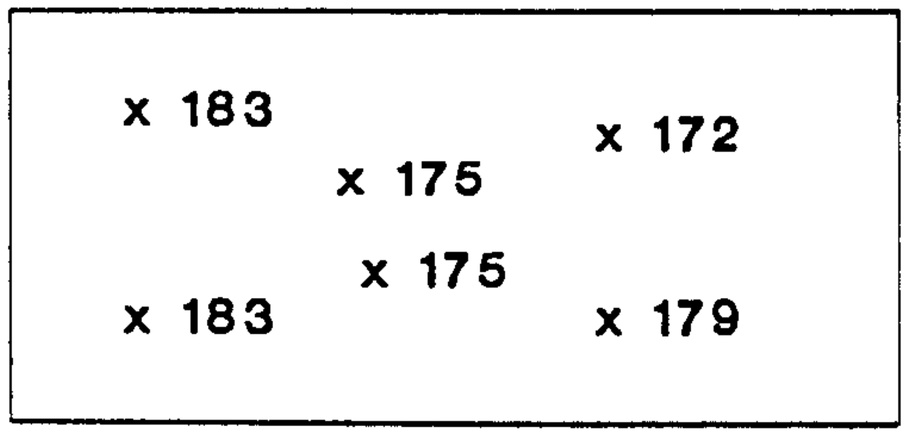

45° Impact angle.

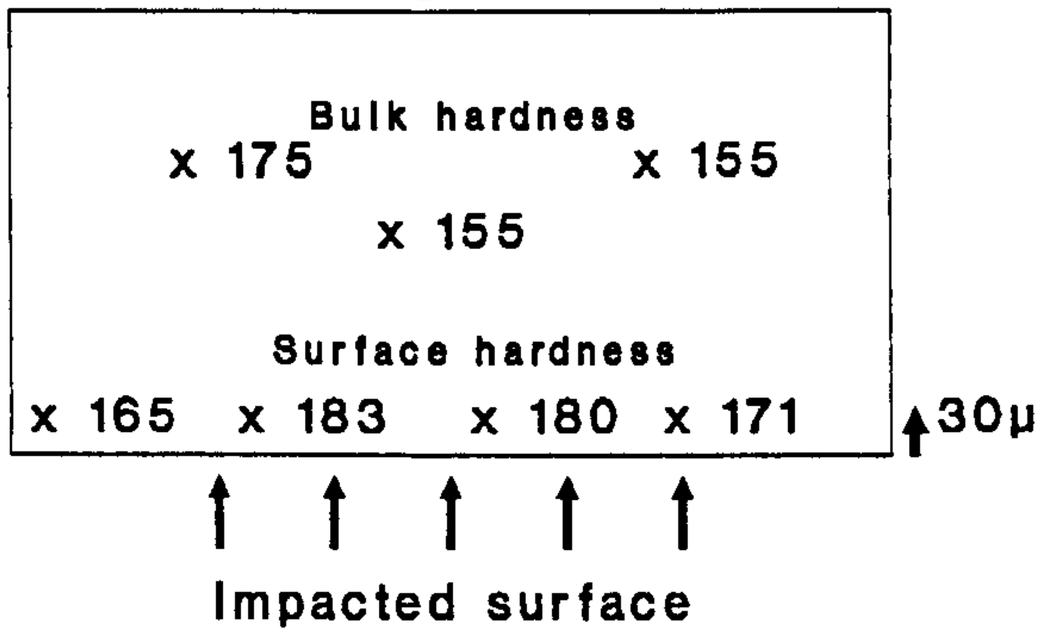

45° Impact angle.

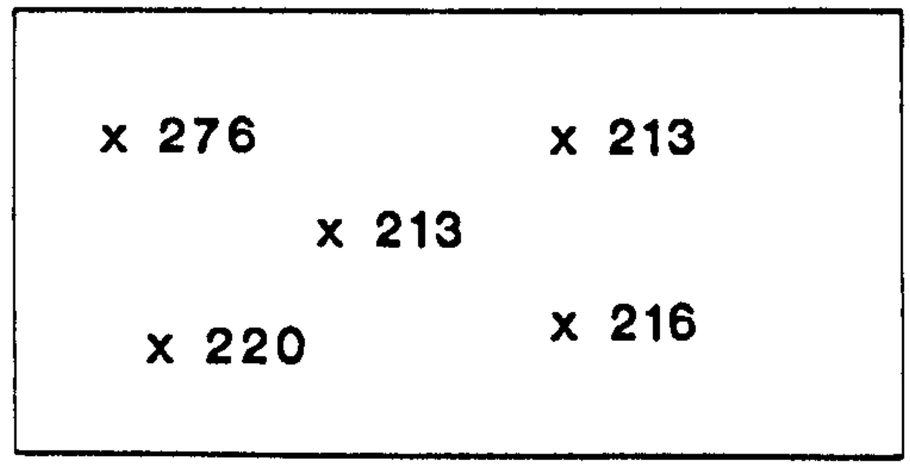

90° Impact angle.

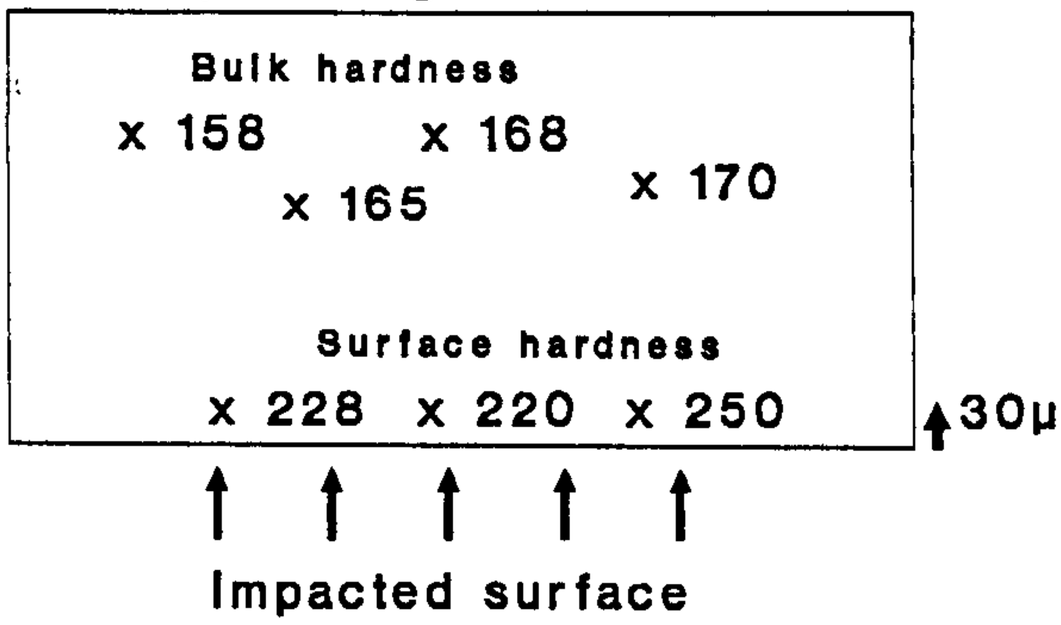

90° Impact angle.

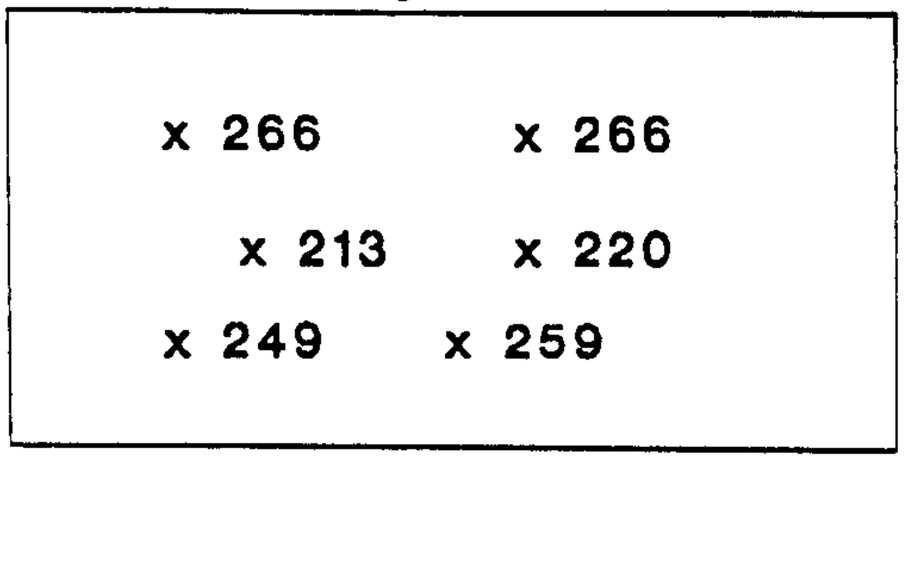

7.1.6 Computer Modelling.

The improved Monte-Carlo Computer Simulation programme, for the prediction of erosion-corrosion rate, was tested on the X52 and IN625 materials and the results generated were compared with those obtained from the experimental modelling. Figures 51(a), 51(b), 52, 53(a) and 53(b) are the scatter diagrams constructed from the arithmetic average results generated from ten runs with the error bars showing the minimum and maximum values. The erosion-corrosion rates were predicted and measured using a $K_p=27x10^{-3}$ $\mu m^2/h$. In general the scatter diagrams show a good comparison between the measured and the predicted values over the range of test environments considered.

The detailed comparison of the results generated by the computer model with those obtained from experiments had been dealt with in Section 6.4. Although, it has been generally concluded that the improved computer model could be used to predict the order of magnitude type of estimates of erosion and erosion-corrosion rates for situations encountered in petroleum production, the following analysis revealed some of the reasons as to why the results from the model tend to deviate from those obtained by experiments:

(a). Equation (59) is used in the model to calculate the volume of material removed/crater as a result of impact by a particle. The equation can be re-written in a slightly different form as,

$$Q_v = \frac{m\,(V \sin \alpha - V_y)^2}{2Y(3-2\cos\alpha)} + \frac{m\,(V\cos\alpha)^2}{2Y}$$

(A) (B)

If the normal impact component term is (A), and the horizontal impact component term is (B), one can generate separately the resultant crater volumes by each term. For ease of comparison with the single impact experimental results, one can chose α=30°, and the results generated for X52 material at V_p=50 m/s, 80 m/s, 100 m/s and 150 m/s are shown in Table 17, below. This table shows values of term (A), (B), Q_v in equation (59) and also considers the sensitivity of Q_v to changes in (A) in terms of ratio of $Q_v/(A)$. This ratio is seen to be reasonably constant.

Table 17. Crater volumes generated by each term of equation (59) at α=30°, for X52 material.

Particle Size	(A), μm^3	(B), μm^3	Q_v, μm^3	$Q_v/(A)$
50 m/s,				
130µm	347	1706	2053	5.9
160µm	647	3180	3828	5.9
200µm	1265	6215	7480	5.9
250µm	2470	12648	15000	6.1
300µm	4270	20972	25242	5.9
80 m/s,				
130µm	983	4362	5345	5.4
160µm	1832	8143	9975	5.4
200µm	3579	15910	19490	5.4
250µm	6989	31073	38062	5.4
300µm	12076	53689	65765	5.4
100 m/s,				
130µm	1586	6826	8412	5.3
160µm	2955	12723	15678	5.3
200µm	5775	24860	30635	5.3
250µm	11278	48552	59830	5.3
300µm	19486	83889	103375	5.3

150 m/s,				
130μm	3721	15359	19080	5.1
160μm	6935	28626	35361	5.1
200μm	13552	55937	69489	5.1
250μm	26466	109240	135706	5.1
300μm	45729	188750	234479	5.1

Plotting the values of (A) term only on the same probability plots for experimental values of the crater volume we can produce such a plot as shown in Figures 59(a) and 59(b). These results show that the horizontal velocity component, (B) has not played any role in creating the crater volume. We have to be cautious here that this may not mean that it did not contribute in metal recession process.

(b). Considering the predicted and measured erosion rate results tabulated in Appendix I, Item I.1, we can generate similar table(s), but for erosion of X52 material at 30° impact angle. This can be done by treating the erosion rate values at 90° as representing the erosion rate due to (A) term of the equation and the difference between the erosion rate values at 30° impact angle with those of 90° as the erosion rate due to the (B) term, for series of erosion rates obtained by the model. The only difference is that the erosion rates were derived by particle of size range between 50-300 μm. Further, additional analysis could also be done between the experimental and the predicted erosion rates at all those impact angles. Thus a set of data can be derived as shown in Tables 18 and 19.

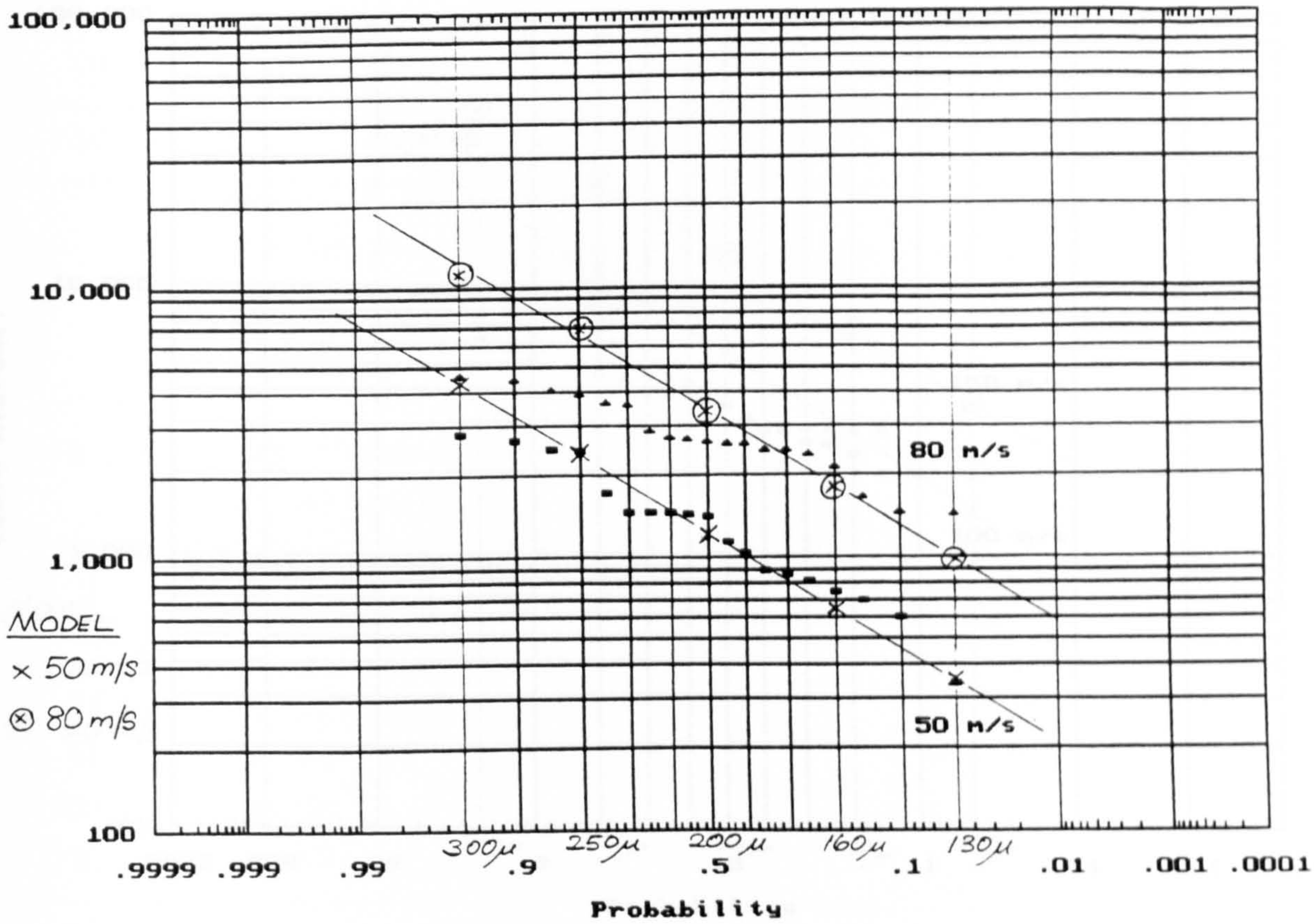

Figure 59(a). Predicted crater volumes by the normal component of equation (59) and the measured crater volumes plotted on the same probability chart for $\alpha=30°$, $V_p=50$ m/s and $V_p=80$ m/s.

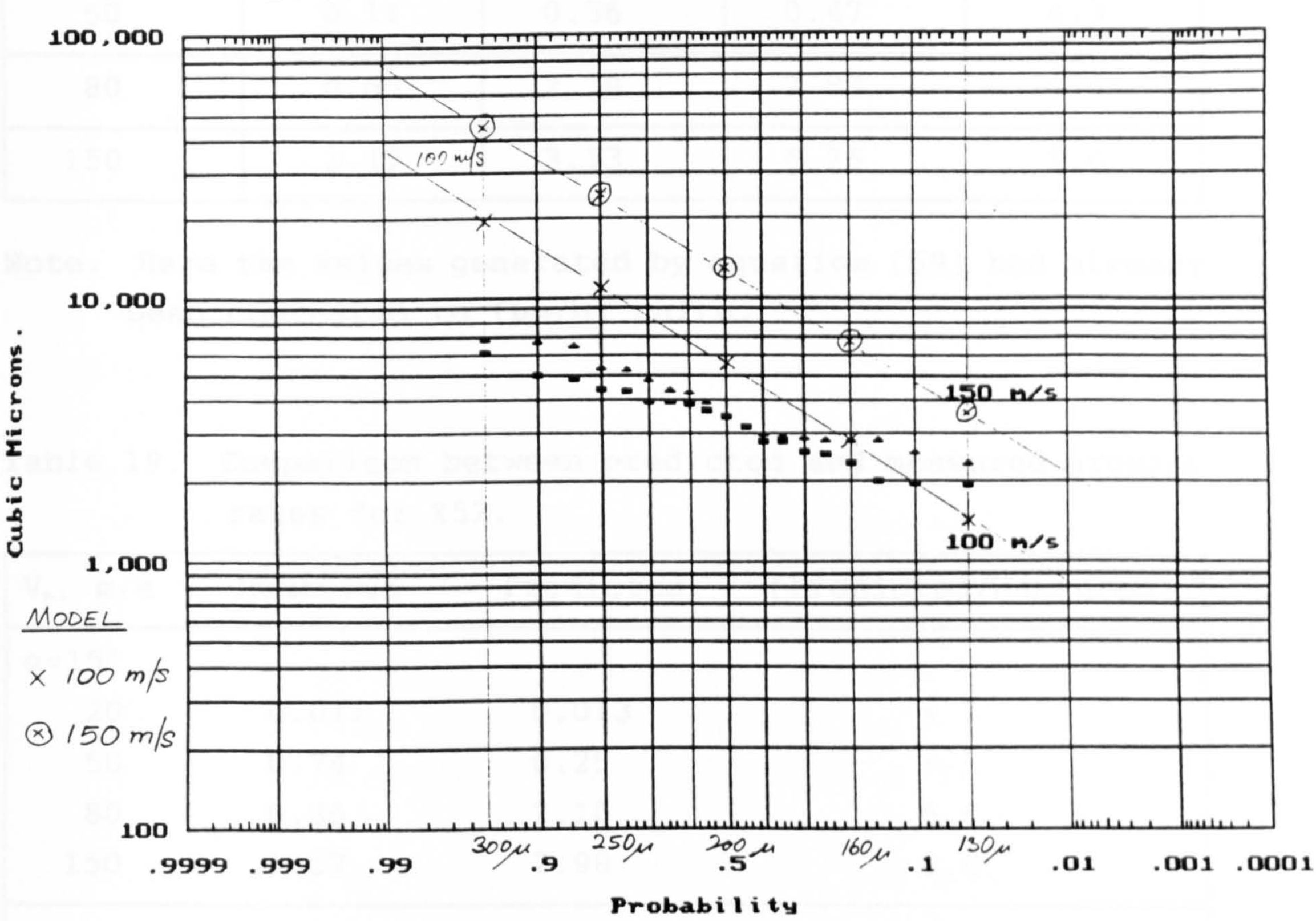

Figure 59(b). Predicted crater volumes by the normal component of equation (59) and the measured crater volumes plotted on the same probability chart for $\alpha=30°$, $V_p=100$ m/s and $V_p=150$ m/s.

Table 18. Erosion rates as predicted by each term of equation (59) at $\alpha=30°$, for X52 material.

V_p, m/s.	(A), μm/h	(B), μm/h	Q_v, μm/h	$Q_v/(A)$
20	0.02	0.027	0.047	2.4
50	0.11	0.36	0.47	4.3
80	0.65	2.18	2.83	4.4
150	3.12	3.13	6.25	2.0

Note. Here the values generated by equation (59) had already been converted to (μm/h) units.

Table 19. Comparison between predicted and measured erosion rates for X52.

V_p, m/s	Measured	Predicted	(Predicted/Measured)
$\alpha=15°$			
20	0.011	0.013	≈ 1
50	0.74	0.25	≈ 1
80	0.36	2.10	5.8
150	1.57	2.98	2.0
$\alpha=30°$			
20	0.012	0.047	3.9
50	0.11	0.47	4.3
80	0.58	2.83	4.9
150	2.73	6.25	2.3
$\alpha=45°$			
20	0.014	0.054	3.9
50	0.14	0.63	4.5
80	0.85	2.20	2.6
150	3.21	4.41	1.4

α=60°			
20	0.02	0.02	1
50	0.21	0.38	1.8
80	1.11	0.90	≈ 1
150	4.55	4.50	≈ 1

Comparing the numbers of the last column of Tables 18 and 19, we can see that they are identical, in the regions of impact angles of 30° and 45°. From Table 19, as the impact angle increases beyond 45°, say to 60° and perhaps higher, then the predicted and measured erosion rates are almost identical. This is because at high impact angles the (B) term of the equation diminishes and the (A) term becomes dominant; therefore confirming that the effect of using equation (59) has no significance in the model at high impact angles, i.e. the (B) term approaches zero.

Based on these experimental results, it can be concluded that using equation (59) as in the model will not give a good prediction of the erosion rates for a ductile material, whereas using equation (57) only will, be more appropriate, for all impact angles. From the same analysis, it can also be concluded that it is the normal component of the particle velocity that contribute to the erosion of substrate material.

7.1.7 Samples obtained from the Field.

In Figures 46 and 47 we can see typical examples of erosion and corrosion commonly taking place in the field of petroleum production. The first and most critical components directly exposed to the sand particles are the blast joints of the production tubing being located immediately in the perforated production casing. The examples show that the production tubing was in turn perforated by the sand produced from the formation, resulting in the production in that zone being mixed up with those of the production from the other zone below. This is definitely not accepted by the reservoir engineers as they cannot monitor the production from each individual zone effectively which will lead to poor reservoir management and monitoring.

The other well equipment often subjected to severe erosion are the choke valves. The function of the choke valve is to control the rate of hydrocarbon production. As it represents a point of restriction to the flow of hydrocarbon fluid, the velocity in that region is normally very high as compared to other areas of the well production equipment. If sand is present this will make the environment very erosive. The example in Figure 46(d) is one of the permanent choke that has been eroded apparently at and around the flange connection outside the bore of the choke. This may be due to the poor connection at the flange, resulting in sand laden fluid passing through the screw connection rather than through the choke bore and eroding the flange screw connection away. Normally a permanent choke such as this has its bore protected by a layer of tungsten carbide material.

Figure 47(a) and (b) are examples of the surface facilities components that have been subjected to erosion, if sand is present. These samples are obtained from one of the gas production platforms in Malaysian offshore operations.

The first sample is a flange connection opposite to the flow direction. This may be caused by the improper placement of the gasket that generates turbulence in the flow of the fluid causing a pattern of lines of erosion. The second sample is a component of a wing valve which helps to straighten up the flow down stream of the valve. As the velocity is normally high, downstream of such a valve, any sand carried by the fluid will make the environment very erosive.

It is therefore important to avoid situations that causes turbulence in the fluid flow. It has been mentioned earlier that it is the normal component of the particle velocity that contributes to the major erosion processes on the substrate material. When turbulence occurs we are basically introducing the normal component effect. Ideally, if the fluid flow is in a continuous streamline one can expect an erosion free situation.

There are many more examples in which erosion and corrosion could be of concern in petroleum production. The centrifugal pump impellers are often subject to erosion not only by sand but also by cavitation erosion (58). The gas turbine rotor blades used in power generation offshore may suffer severe erosion by the shedding of salt particles that deposit on the blades (52). The elbows and T-connections of production piping and pipelines are also known to have suffered failures from erosion either by sand or liquid. Therefore, there is an endless list of equipment related to petroleum production that could suffer from erosion-corrosion. If a predictive model could be constructed and reliably tested then it would be very beneficial for designers and manufacturers in their efforts to understand better the effect of erosion/corrosion and develop equipment to meet the requirement of the industry.

7.2 Description of the Erosion-Corrosion Mechanisms.

Wet CO_2 gas corrosion is generally regarded as film free corrosion at temperatures of about 40°C to 60°C. The corrosion products believed to form in wet CO_2 gas environment at temperatures between 20°C and 80°C are those of ferrous bicarbonate (soluble) and ferrous carbonate (less soluble) (13). At these temperatures they are soft in nature and loosely adherent to the surface.

It has been known that corrosion rates are greatly reduced by the presence of a scale as ferrous ion concentrations reach their saturation level beneath the carbonate layer (9,17,18,19) and effectively polarising the anodic dissolution process. However, when sand particles impact the surface, the slowly growing scale is removed locally, depolarising the anodic sites and accelerating the corrosion rate. This process is repeated for every particle impact on the surface. As for carbon manganese steels, at low sand flux (<0.05 g/mm^2/h) and low velocity (<50 m/s), the erosion-corrosion process is essentially dominated by scale formation and removal. However, as the velocity and/or sand flux increases, the erosion-corrosion process becomes dominated by substrate erosion.

It has also been known that wet CO_2 gas corrosion is characterised by pitting or localised surface corrosion. When corrosion is being superimposed with erosion the rate of corrosion attack on locally exposed surface is accelerated. It has been shown earlier in section 7.1. that with erosion the surface may also become heavily pitted.

7.3 Basis for Design in Erosion-Corrosion Environment.

It is clear that when sand is produced, erosion is going to take place if the particle velocity is at or above the critical impact velocity of the material. If corrosion is also present in an erosive environment, the rates of material loss will also be increased. If the corrosion product is soft and loosely adherent to the surface of the material, as in wet CO_2 gas corrosion, the critical impact velocity for erosion of the substrate is no longer the critical impact velocity for the metal recession process, but instead the critical impact velocity to fracture the scale has to become the deciding factor. For soft and loosely adherent scales, the critical velocity can become relatively low as compared to the critical velocity for metallic materials. The rate of material loss now becomes very high, which may be equal to the initial parabolic rate of corrosion as indicated by Evans (47).

From an erosion and erosion-corrosion point of view, it would be prudent for designers to consider the following guidelines in their design considerations:-

(a) Hardness Number: Generally the material with high hardness number is the first indication of resistance to indentation, and therefore is a good indication of material resistance to erosion by solid particles.

(b) Yield Strength: Equivalently it has been demonstrated that high yield strength materials will have good resistance to particle erosion. In fact hardness number has very close relationship with the yield stress of a material (Hv=3Y). This will also imply that materials with high yield strength will also be resistant to erosion by particles. Therefore, the use of high yield strength materials whenever they are available if erosion is likely to be of concern, is advisable.

(c) Eliminate the effect of Corrosion: When the environment is corrosive then the only alternative is to use corrosion resistant materials (alloys). This will eliminate the effect of corrosion on the rate of metal recession in erosive environment. Use of inhibitors may not help if the inhibitor film is removable by the particle impact as in the removal of the protective corrosion scales. The instantaneous exposure of bare metal to the corrosive environment may aggravate the localised metal recession.

(d) Control of Particles Flux: As the erosion rates depend very heavily on the probability of damage by particle impacts, then to reduce the particle flux rate is definitely a good measure in order to reduce erosion of material. In petroleum production using sand production control techniques may be helpful. However, experience shows that sand may still be produced despite installing gravel-packing for sand control. Sand rate at 5 PPTB may still be erosive in erosion-corrosion environment in petroleum production.

(e) Particle Impact Velocity: Rate of metal loss is a function of (Velocity)^n, where n may have values from 2 - 3, or even higher, then reducing the particle impact velocity will help considerably in reducing the rate of metal loss by erosion. This can be done by the proper sizing of equipment.

(f) Avoidance of turbulence and sharp bends: It has been shown that it is the normal component of the particle velocity that contributes to the effective material removal. By inciting turbulence or introducing sharp bends in a fluid flow we are effectively introducing a normal velocity component of the particle relative to the metal surface. Thus, with better design where turbulence and sharp bends are avoided, severe erosion may not take place in sand bearing fluid flow conditions.

It is therefore, important to know the environment in which the equipment would be operating as accurately as possible at the design stage.

It is always difficult for the designers and manufacturers to ensure that equipment being designed and manufactured will be suitable for everybody's need. However, knowing the exact environment that equipment is being exposed to is an important but a difficult function as well. First of all, when equipment is initially specified, the information on which the specification is based, is usually very limited. This is because when a new area is discovered which has not been fully appraised, the design is started too early when the fluid compositions may be based on very limited production test results or the fluid compositions could be changing over the life of the field because of various reservoir treatments for enhanced hydrocarbon recovery. Unforeseeable co-mingling of production streams because of economic and operational reasons, at a later stage of production may totally change the stream compositions and rates, hence making the original equipment specifications no longer suitable.

To have a predictive model that enables designers to make reliable estimates of the rates of metal removal under various erosion-corrosion environments is therefore most welcome by the oil industry. To date, designs have been based on the experience of the individual companies in their effort to solve the erosion-corrosion problems. In deciding the value of constant C, as in API RP14E, in the empirical equation for the calculation of the erosional velocity, has raised a lot of unresolved arguments amongst the engineers.

7.4 Suggestions for V_e, the Erosion Velocity for Sand Producing Systems.

The subject of erosion velocity has long been dealt with by engineers in the design of petroleum production systems. Empirical formulae have been introduced in guidelines and practices for easy reference by the engineers. There has been concerns with regard to the validity of values of constants used in the empirical formulae (58,59). To date, all of these formulae can be treated as well as any other until proven otherwise. It is therefore pertinent in these erosion and corrosion studies to make an attempt to deal with this problem with the hope that new knowledge could be put to useful practice.

From the experimental data generated in this work on common materials such as X52, the following Table 20 and Table 21 could be generated for easy reference by field engineers working in petroleum production. They may be used as a guide to determine the effect of erosion and corrosion on the material loss rate when the two processes are conjointly active.

Table 20. Sand erosion rates on X52 material, (mm/y).

FLUX in PPTB		FLUX in $g/mm^2/h$	Vp=20 m/s		Vp=50 m/s		Vp=80 m/s		Vp=150 m/s	
2"Dia	3"Dia		30°	90°	30°	90°	30°	90°	30°	90°
1	2.5	0.01	N.A.	N.A.	0.2	0.13	N.A.	N.A.	N.A.	N.A.
5	12	0.05	0.10	0.16	1.0	1.8	5.0	7.8	23.5	35.7
10	25	0.10	N.A.	N.A.	2.7	5.5	N.A.	N.A.	N.A.	N.A.
53	130	0.50	N.A.	N.A.	10.0	18.3	N.A.	N.A.	N.A.	N.A.

N.A.= Data not available.

Table 21. Erosion-corrosion rates on X52 material, (mm/y) at $P_{(CO2)}$=1 bar, T=20°C.

FLUX in FPTB.		FLUX in $g/mm^2/h$	Vp=20 m/s.		Vp=50 m/s.		Vp=80 m/s.		Vp=150 m/s.	
2°Dia.	3°Dia.		30°	90°	30°	90°	30°	90°	30°	90°
1	2.5	0.01	N.A.	N.A.	2.1	3.5	N.A.	N.A.	N.A.	N.A.
5	12	0.05	1.0	1.8	3.2	5.4	9.0	14.8	31.1	57.6
10	25	0.10	N.A.	N.A.	6.1	7.6	N.A.	N.A.	N.A.	N.A.
53	130	0.50	N.A.	N.A.	22.4	32.6	N.A.	N.A.	N.A.	N.A.

N.A.= Data not available.

As more data become available the matrix could be filled in accordingly or extended. This type of reference table could be very useful for designers as well as for the field engineers.

It is obvious that with the presence of erosion and corrosion the rate of metal recession, in this case X52, is tremendously high. It would be very difficult to consolidate these phenomena in a simple empirical equation as indicated in API RP14E etc.. In these examples of reference tables, for a piping of X52 material to sustain a pure erosion condition where the maximum allowable metal loss is, say 0.254 mm/y, then V_e could be said to be ≈20 m/s for a flux of 0.05 $g/mm^2/h$. or equivalent. When wet CO_2 gas is present with a partial pressure of 1 bar, then V_e has to be much lower than 20 m/s for the same design conditions, otherwise one must expect early replacement of elbows and T-connections etc. If we can assume that the erosion-corrosion rate is proportional to fluid velocity to the power of 'n' where n is a velocity exponent (this relationship has NOT been established in this work, only an approximation) then using measured values in Table 21, the design V_e, for an allowance of 0.254 mm/y erosion-corrosion rate is found to be less than

1 mm/s. This is an extremely low velocity situation. The obvious choice is to eliminate the effect of corrosion, eg. by using corrosion resistant alloys or introducing corrosion inhibition. The use of corrosion resistant alloys has been an accepted practice in petroleum production activities where the benefit of being able to sustain longer life in erosion-corrosion environment outweighs the high initial costs of materials (4).

CHAPTER 8

Conclusions

CHAPTER 8

8. CONCLUSIONS.

The following conclusions could be drawn up from the modelling work carried out in this thesis:-

(1). Wet CO_2 gas corrosion is generally regarded as film free at low temperatures of about 40°- 60°C. However, the erosion results indicate that the corrosion products do form even at 20°C. The corrosion products believed to form in wet CO_2 gas environment, between 20° and 80°C are those of ferrous bicarbonate and ferrous carbonate (13). At these temperatures, they are soft in nature and loosely adherent to the surface.

(2). The corrosion rate kinetics are found to be parabolic and have values between $8x10^{-3}$ $\mu m^2/h$ to $50x10^{-3}$ $\mu m^2/h$ depending on the material and temperature. Corrosion rates were greatly reduced by the presence of a scale as ferrous ions concentrations reach their saturation level beneath the bicarbonate or carbonate layer, effectively polarising the anodic dissolution process. However, when sand particles impact the surface, the growing scale was removed locally depolarising the anodic sites and accelerating the corrosion rate. This process was repeated for every particle impact on the surface.

(3). It is found that the difference between the wet and dry erosion rates (E/C versus Erosion only) for C-Mn steels such as X52, L80, X65 and N80 greatly exceed the rate of corrosion by CO_2 as measured by conventional corrosion tests, indicating that there is a strong interaction between the erosion and corrosion processes. The process of metal

recession consists of the removal and regrowth of soft corrosion scale at low flux and low particle velocity, and removal of substrate at high flux and high particle velocity. The E/C rate factor may vary between 2-30 times depending on the sand flux, particle velocity and temperature.

(4). The rates of corrosion itself was accelerated beyond that expected for the process fluid conditions as fresh metal surface is continually exposed to the corrosive environment due to repeated impact by sand particles. As an example, at 1 bar CO_2 partial pressure and temperature of 20°C, under worst case scenario the rate of metal loss (corrosion rate) is 0.8 mm/y (9); but with a sand flux of 0.5 g/mm^2/h and a V_p=50 m/s the rate of metal loss becomes 32 mm/y.

(5). The results from single and multiple impact experiments show that it is the normal component of the particle velocity that causes damage to the metal surface and resulting material removal. The horizontal velocity component has little or no cause to material removal. However, only when the surface is roughened by the repeated particle impacts then the horizontal component may contribute to material removal from the target surface as well.

(6). Ductile material with high yield stress shows a better resistance to erosion and this is also indicated by equation (45) as used in the model.

(7). High flux rates help to induce high levels of accumulated strain in the metal surface, and cause material failure which has been successfully modelled in terms of a fatigue mechanism. If the accumulated strain is high enough, depending on the sand flux, 'brittle' erosion behaviour will predominate as reflected by the change in the metal recession rate with impact angle.

(8). The use of equation (57) should be sufficient to cover most of the impact angles encountered in the field and to be more representative compared to the results obtained by experiments.

(9). Metal recession rate by erosion-corrosion process could be mitigated by the (a) abatement of corrosion, (b) reduction of particle velocity, (c) reduction in particle flux, (d) avoidance of turbulence and sharp bends, and (e) use of high strength alloys.

(10). Using the model and experimental results, a standard reference table could be generated for easy reference by engineers in the field.

SUGGESTION FOR FUTURE WORK.

The work performed in this programme was still very limited for it to cover the total scenarios applicable to oil/gas production. There are more studies that could be carried out in this area which would help to understand further the total effects of erosion/corrosion in petroleum production. The following suggestions are laid down for future work considerations:-

(a). It has been the intent of the work in this thesis that the corrosion environment be purely wet carbon dioxide gas. Although as explained in this work that the effect of dissolved oxygen from the water mains was negligible, it would still be better if the water be made oxygen-free before feeding into the test chamber through the atomizer. This probably could be done by simply bubbling the water with nitrogen and feeding it through the atomizer into the chamber with the aid of a pump, in order to overcome the back pressure.

(b). In the single impact experiments, tests had been performed for impact angles of 30° and 90° only. It would be very useful if experimental results could be generated and analyzed for other impact angles, such as 15° and 45°. This additional information would be very useful to compare with the results generated by the model and the erosion results.

(c). The effect of temperature had not been fully appraised in this work because of the limitation of the operating temperature of the atomizer. If a method of heating the chamber and lagging of the atomiser to prevent it from getting heated beyond 150°C could be done effectively, then experiments at higher temperatures could be performed

safely. It would be interesting to see erosion/corrosion results at higher temperatures, say at 150°C and 200°C. It is also important to note that the erosion rig should be made sustainable to operate at higher water vapour pressure, at those temperatures to maintain a wet atmosphere.

(d). In practice, there may be liquid droplets impinging on the scales as well as the metal surface because of vapour condensation when warmer gas comes in contact with colder tubing/piping at the dew point temperature. Additional erosion, by the impinging liquid droplets, of the soft scales may also take place in this condition, depending on the velocity and mass of the droplets. Experiments could be performed using the current erosion rig, with some modifications required to enable to feed sand and water together at controlled rates. Both experiments on the effects of liquid droplets and liquid droplets+sand entrained in the production processes could be studied.

References

REFERENCES.

1. Thompson, M.J.: Corrosion Due to Carbon Dioxide in the Hawkins Oil Field - A Systematic Evaluation, Material Performance, July 1990, pp. 58-61.

2. Ari Sumarno, Said Djabar & Hugh H. Fuller: 'The time is right' for Natuna gas development. Asian Oil & Gas, June 92, pp. 14 - 22.

3. NACE Standard MR-01-75, 1980 Revision.

4. Newton, L.E. & Hausler, R.H. : CO_2 Corrosion in Oil and Gas Production, NACE Publication 1984.

5. Tuttle, R.N. & Kane, R.D. : H_2S Corrosion in Oil and Gas Production, NACE Publication 1981.

6. SSB/SSPC Sand Control Report, 1990.

7. Heng, H.B., Sarawak Shell Berhad: An Overview of Gravel-Packed Completions, SPE Production Engineering, May 1987,pp.81- 88.

8. Rosli Boni, Petronas Carigali Sdn. Bhd./Baram Delta Operations: Report on the SIPM Progress Meeting on Sand Control and Perforating, The Hague, June 28-30, 1993.

9. De Waard, C. and Milliams, D.E.: Prediction of Carbonic Acid Corrosion in Natural Gas Pipelines, Paper F1 from First International Conference on Internal and External Protection of Pipes, University of Durham, 1975.

10. De Waard, C. and Milliams, D.E.: Carbonic Acid Corrosion of Steel, Corrosion-NACE, Vol.31, No.5, May 1975, pp.177-181.

11. Bockris, J.O'M., Drazic,D. & Despic,A.R.: The Electrode Kinetics of the Deposition and Dissolution of Iron, Electochemica Acta, 1961, Vol.4, pp.325-361.

12. Bockris, J.O'M. and Drazic,D: The Kinetics of Deposition and Dissolution of Iron: Effect of Alloying Impurities, Electrochimica Acta, 1962,Vol.7,pp.293-313.

13. Rogers, W.F. and Rowe, J.A.: Corrosion Effects of Hydrogen Sulfide and Carbon Dioxide in Oil Production, Proc. of 4th. World Petroleum Congress, Texas, 1955, Paper No.3, pp.479-499.

14. Xia, Z., Chou, K.C. and Szklarska-Smialowska, Z.: Pitting Corrosion of Carbon Steel in CO_2-Containing NaCl Brine, Corrosion, Vol. 45, No.8, August 1989, pp. 636-642.

15. Kowaka, M. and Nagata, S.: Stress Corrosion Cracking of Mild and Low Alloy Steels in CO-CO_2-H_2O Environments, Corrosion-NACE, Vol.32, No.10, October 1976, pp.395-401.

16. Ikeda, A., Mukai, S. and Ueda, M.: Corrosion Behaviour of 9 to 25% Cr Steels in Wet CO_2 Environments, Corrosion-NACE, Vol.41, No.4, April 1985, pp.185-192.

17. Vindem,K. and Dugstad, A.: Corrosion of Carbon Steel in an Aqueous Carbon Dioxide Environment, Part 1: Solution Effects, Material Performance, March 1989, pp. 63-67.

18. Vindem, K. and Dugstad, A.: Corrosion of Carbon Steel in an Aqueous Carbon Dioxide Environment, Part 2: Film Formation, Material Performance, April 1989, pp. 46-50.

19. Davies, D.H. and Burstein, T.: The Effects of Bicarbonate on the Corrosion and Passivation of Iron, Corrosion-NACE, Vol.36, No.8, August 1980, pp. 416-422.

20. McIntire, G., Lippert, J. and Yudelson, J.: The Effect of Dissolved CO_2 and O_2 on the Corrosion of Iron, Corrosion, Vol. 46, No.2, February 1990, pp. 91-95.

21. Jasinski, R.:Corrosion of N80-Type Steel by CO_2/Water Mixtures, Corrosion-NACE,Vol.43,No.4,April 1987, pp. 214-218.

22. Finnie, I.: Erosion of Surfaces by Solid Particles, Wear, Vol.3, 1960, pp.87-103.

23. Finnie, I., Wolak, J. and Kabil, Y.: Erosion of Metals by Solid Particles, Journal of Materials, Vol.2, No.3, Sept. 1967, pp.682-700.

24. Finnie, I.: Some Observations on the Erosion of Ductile Metals, Wear, Vol.19, 1972, pp.81-90.

25. Finnie, I., Levy, A. and McFadden, D.H.: Fundamental Mechanisms of the Erosive Wear of Ductile Metals by Solid Particles, Erosion: Prevention and Useful Applications, ASTM STP 664, W.F. Adler, ASTM 1979, pp.36-58.

26. Bitter, J.G.A.: A Study of Erosion Phenomena, Part 1, Wear, Vol.6, 1963, pp.5-21.

27. Bitter, J.G.A.: A Study of Erosion Phenomena, Part 2, Wear, Vol.6, 1963, pp.169-190.

28. Neilson, J.H. and Gilchrist, A.: Erosion by a Stream of Solid Particles, Wear, 11, 1968, pp.111-122.

29. Tilly, G.P.: Sand Erosion of Metals and Plastics: A Brief Review, Wear, 14, 1969, pp.241-248.

30. Tilly, G.P. and Sage W.: The Interaction of Particle and Material Behaviour in Erosion Processes, Wear, 16, 1970, pp.447-465.

31. Tilly, G.P.: A Two Stage Mechanism of Ductile Erosion, Wear, 23, 1973, pp.87-96.

32. Tilly, G.P.: Erosion Caused by Impact of Solid Particles, Treatise on Material Science and Technology, Vol.13, 1979.

33. Hutchings, I.M.: Mechanism of the Erosion of Metals by Solid Particles, Erosion and Useful Applications, ASTM, STP 664, 1979, pp. 59-76.

34. Tabor, D.: The Hardness of Metals, Oxford Press, 1951.

35. Hutchings, I.M.: Deformation of Metal Surfaces by the Oblique Impact of Square Plates, Int. Journal Mech. Sc. Vol.19, 1977, pp.45-52.

36. Hutchings,I.M., Winter,R.E. and Field, J.E.: Solid Particle Erosion of Metals: the Removal of Surface Material by Spherical Projectiles, Proc. R. Soc. London A348, 1976, pp.379-392.

37. Winter, R.E. and Hutchings, I.M.: The Role of Adiabatic Shear in Solid Particle Erosion, Wear, 34, 1975, pp.141-148.

38. Hutchings, I.M. and Winter, R.E.: Particle Erosion of Ductile Metals: A Mechanism of Material Removal, Wear, 27, 1974, pp.121-128.

39. Mamoun, M.M.: Analytical models for the Erosive-Corrosive Wear Process, Report ANL-75-xx-2, Appendix 1, 1975, Argonne National Laboratory.

40. Brainard, W.A. and Salik, J.: Scanning-Electron-Microscope Study of Normal-Impingement Erosion of Ductile Metals, NASA Technical Paper 1609, 1980.

41. Salik, J. and Buckley, D.H.: Effects of Erodent Particle Shape and Various Heat Treatments on Erosion Resistance of Plain Carbon Steel, NASA Technical Paper 1755, 1981.

42. Levy, A.V.: The Platelet Mechanism of Erosion of Ductile Metals, Wear, 108, 1986, pp.1-21.

43. Sheldon, G.L. and Kanhere, A.: An Investigation of Impingement Erosion using Single Particles, Wear, 21, 1972, pp.195-209.

44. Hutchings, I.M.: A Model for the Erosion of Metals by Spherical Particles at Normal Incidence, Wear, 70, 1981, pp.269-281.

45. Nicholls, J.R., Stephenson, D.J., Polden,M., Norton, J.F., Grandrey, M., Stott,F.H., Prescott, R., Stack,M., Wouters, G., Engelen,W., Debruyn, W. and Casteels,F.: Modelling of Erosion-corrosion Processes in Energy Conversion Systems, Contract No. EN3F-0027-B, 1991.

46. Salesses, I.: Modelling the Erosion of Compressor Materials and Coatings, MPhil Thesis 1992, Cranfield Institute of Technology.

47. Evans, U.R.: The Corrosion and Oxidation of Metal: Scientific Principles and Practical Applications, Edward Arnold Ltd. 1977.

48. Brijes Vyas: Erosion-Corrosion, Treatise on Materials Science and Technology, Vol.16, 1979.

49. Stephenson, D.J., Nicholls, J.R. and Hancock, P.: The Interaction between Corrosion and Erosion during Sea Salt Compressor Shedding in Marine Gas Turbine, Corrosion Science, Vol.26,No.10, 1986, pp.757-767.

50. Restall, J.E. and Stephenson, D.J.: High Temperature Erosion of Coated Superalloys for Gas Turbines, J. Mat. Sc. and Engineering, Vol.88, 1987, pp.273.

51. Ninham, A.J., Hutchings, I.M. and Little, J.A.: Erosion/Oxidation of Austenitic and Ferritic Alloys, Corrosion, Vol.46, N0.4, April 1990, pp.296-301.

52. Stephenson, D.J., Nicholls, J.R. and Hancock, P.: The Erosion of Gas Turbine Blade Materials by Solid Sea Salt, Corrosion Science, Vol.25, No.12, 1985, pp. 1181-1192.

53. Stephenson, D.J. and Nicholls, J.R.: Modelling Erosive Wear, Corrosion Science, 1993.

54. Stack. M.M. and Newman, R.C.: Identification of Transitions in Erosion-Corrosion Regimes in Aqueous Environments, 8th. International Conference on Erosion by Liquid and Solid Impact, Cambridge England, Paper No.92B, Sept. 1994.

55. Song-Roehrle, Q., Stack, M.M., Stott, F.H. and Wood, G.C.: Modelling the Transitions between Erosion-Corrosion Regimes at Elevated Temperatures using Computer Graphics, 8th. International Conference on Erosion by Liquid and Solid Impact, Cambridge England, Paper No. 92A, Sept.1994.

56. API RP14E, API Recommended Practice for Installation of Offshore Production Platform Piping Systems, 4th. Edn. April 15, 1984.

57. BS 8010, Code of Practice for Pipelines, Part 3: Pipelines subsea design, construction and installation, 1993.

58. Salama, M.M. and Venkatesh, E.S.: Evaluation of API RP 14E Erosional Velocity Limitation for Offshore Gas Wells, Offshore Technology Conference, OTC 4485, 1983.

59. Oudeman, P.: A survey of Erosional Velocity and Sand Production Limits, Paper No.4/13, Production Technology Conference, SIPM, 1984.

60. Short, D.A.E.: Sand Erosion in Flowlines, Paper No. 3/13, Production Technology Conference, SIPM, 1986.

61. Walters, N.S. and Verboom, B.: Erosional Velocity in Shell Expro Wells - Field Experience and Design, Paper No. 3/17, Production Technology Conference, SIPM, 1986.

62. Breckels, I.M.: Research into Erosion/Corrosion in Gas Wells, Paper No. 3/18, Production Technology Conference, SIPM, 1986.

63. Robinowicz, E.: The Wear Equation for Erosion of Metals by Abrasive Particles, Proc. Fifth Int. Conf. on Erosion by Liquid and Solid Impact, Cambridge, 1979.

64. Pieraggi, B.: Calculations of Parabolic Reaction Rate Constants, Oxidation of Metals, Vol.27, Nos.3/4, 1987, pp.177-185.

65. Kubaschewski and Hopkins: Oxidation of Metals and Alloys, Butterworth, 1953.

66. Powder Diffraction File by Joint Committee on Powder Diffraction Standards, 1963(Index) and 1967 Set(6-10) pp.314 and Set(11-15) pp.159.

67. German, R.N.: Powder Metallurgy Science, Published by Metal Powder Industries Federation, Princeton, New Jersey, 1984.

68. Ashby, M.F. and Jones, D.R.H.: Engineering Materials 1: An Introduction to their Properties and Applications, Pergamon Press, 1991.

69. Lide, D.R.: CRC Handbook of Chemistry and Physics, 72nd. Edn.1991-1992.

70. Smith, I.W.M.: Kinetics and Dynamics of Elementary Gas Reactions, Butterworth, 1980.

71. Glasstone, S.: Textbook of Physical Chemistry, D. Van Nostrand Co., 1947.

72. Treseder, R.S.: NACE Corrosion Engineer's Reference Book, Nace Publication, 1980.

73. Munday, A.J. and Farrar, R.A.: An Engineering Data Book, 1979.

74. Specification for Line Pipe, API Spec. 5L, American Petroleum Institute, 1991.

75. Metal Handbook, 9th. Edition, American Society for Metals, Volume 1-Properties and Selection, Irons and Steels.

76. Kalpakjian,S.: Manufacturing processes for Engineering Materials, Addison-Wesley Pub. Co., 1984.

Appendices

APPENDIX A

Procedure for Establishing Particle Velocity Curves.

In the single impact tests, the particle velocity, V m/s, is related to the gas velocity, U m/s, according to the following equation:

$$L = \frac{1}{K}\left[\left(\frac{V}{U - V}\right) - \ln\left(1 + \frac{V}{U - V}\right)\right] \qquad \ldots\ldots\ldots(A1)$$

where L is the acceleration length and K is a constant dependent on the properties of the accelerating gas and particles. K is defined by:

$$\frac{1}{K} = \frac{4 d_p D}{3 C_d d_G} \qquad \ldots\ldots\ldots\ldots\ldots\ldots\ldots(A2)$$

where, d_p and d_G are the densities of the particle and the accelerating gas respectively, D is the particle's diameter and the drag coefficient C_d is given by:

$$C_d = \frac{24}{R_{e,D}}\left(1 + 0.15\, R_{e,D}^{0.687}\right) \qquad \ldots\ldots\ldots\ldots\ldots(A3)$$

and the Reynold's number can be calculated by:

$$R_{e,D} = \frac{d_G . D\ (U - V)}{\eta_G} \qquad \ldots\ldots\ldots\ldots\ldots\ldots(A4)$$

where η_G is the viscosity of the propellant gas.

In the iteration process, to determine the corresponding value of a particle velocity, V, for a particular propellant gas velocity, U, equation (A1) is rewritten in the form:

$$K\,L + 1 = \left(\frac{U}{U - V}\right) - \ln\left(\frac{U}{U - V}\right) \qquad \ldots\ldots\ldots\ldots (A5)$$

The variable C = (K L + 1), being dependent on the value of Renoyld's number which in turn is a function of (U - V) only. For a set of known values of d_p, d_G, D, L and U; the iteration process can easily be performed by assuming an initial value of particle velocity, V, until a final value V_f is found such that at V = V_f. They satisfy the expression:

$$\left(\frac{U}{U - V_f}\right) - \ln\left(\frac{U}{U - V_f}\right) \equiv C \qquad \ldots\ldots\ldots\ldots (A6)$$

i.e. their values converge. For a particular gas velocity U, equation (A5) indicates that the value of particle velocity is dependent on its diameter, D.

In the single impact experiment, the gas velocity could be estimated by the following equation:

$$U = \sqrt{\frac{2 . d_{Hg} . g . h}{d_G}} \qquad \ldots\ldots\ldots\ldots\ldots\ldots (A7)$$

where density of mercury d_{Hg}=13,600 kg/m^3, the gravitational constant g=9.81 m/s^2, nitrogen gas density d_G=1.16 kg/m^3 and 'h' is the height of the mercury manometer measured through a Pitot tube.

The characteristic curves can be used for rapid estimation of the particle's velocity as shown in Figure A1. The plots for the gas (Nitrogen) Drag Coefficient at the end of the gun barrel on various sand particle's sizes against gas velocity is shown in Figure A2.

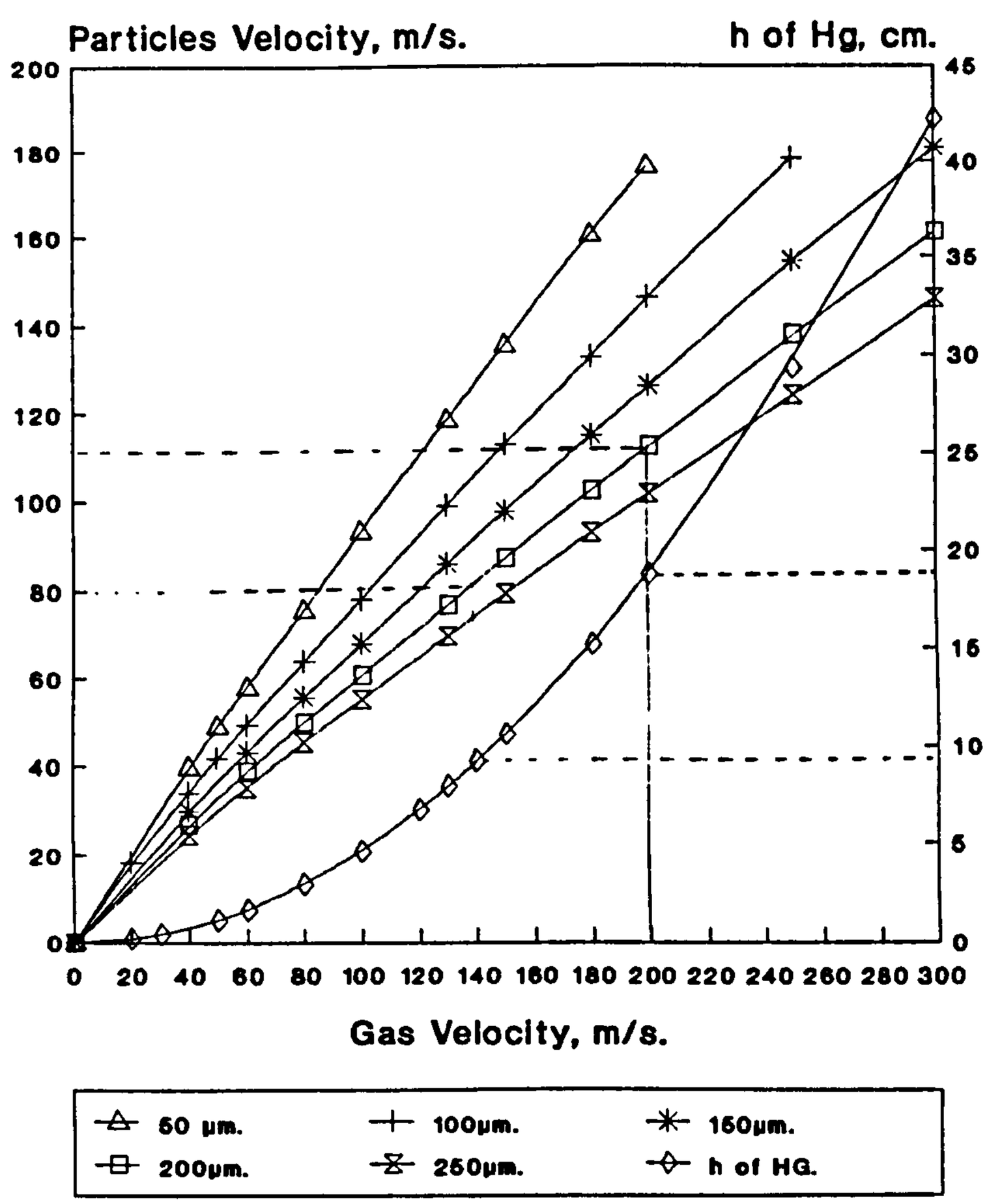

Figure A1. Particle Velocity v.s. Gas Velocity.

Drag Coefficient

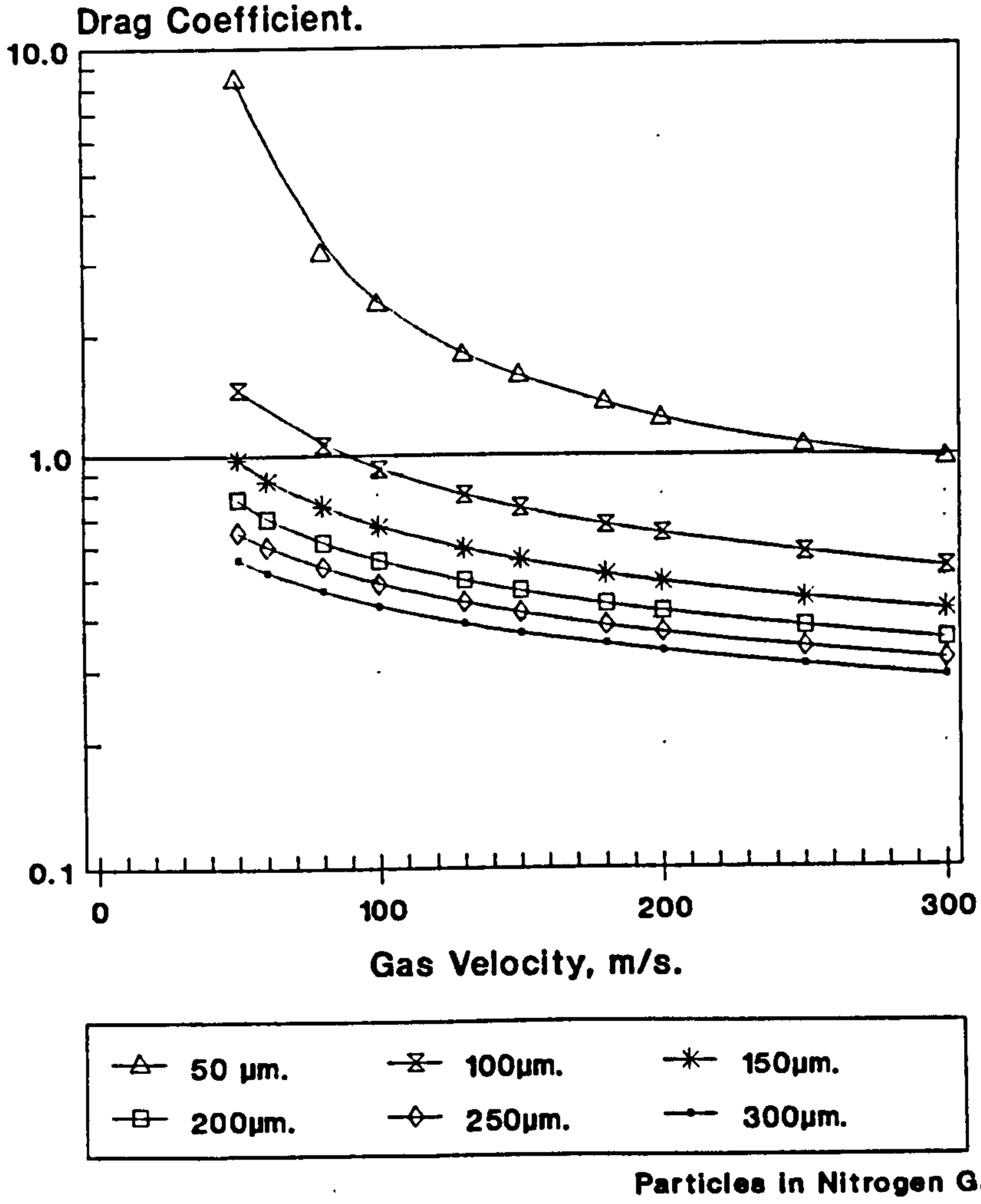

Figure A2. Particle Drag Coefficient at the End of Acceleration Tube.

APPENDIX B

Procedure for Estimating Crater Volumes.

The Joyce Loeble's Particles Image Analyzer was used to determine the basic dimensions of craters formed as a result of the single impact experiment. Some 24 craters were chosen at random and there were many ways of selecting the craters. The method used in this experiment was simply to choose all craters appearing within the field of view of the microscope at a standard magnification of 40 times. Normally up to 4 to 5 locations were needed, chosen at random, in order to gather a total of 24 craters.

After a crater was chosen, the cross sectional area was determined of the surface of the crater. A 40x objective lens was used in this examination which gave a reasonable resolution of the size of craters formed on the type of material used in the tests. First of all the object of using the analyzer was to determine the depths of the craters then the cross-sectional areas. The original surface of the specimen was first put into focus as a reference for the measurement of z-axis displacements. Then the microscope was brought to focus to the bottom of the crater and the distance traversed was recorded in a log book. Each unit traversed indicated on the screen represented 0.1 μm. The image of the crater was put back into focus and the perimeter of the image formed on the screen was traced by using the mouse. This was done by bringing the curser on one edge of the craters image and clicking the left button of the mouse and tracing could then start. Once tracing was completed and by clicking the left key of the mouse again the programme automatically calculated the area of the image traced and stored the value in the file just created. It was important to record the depth values in proper order throughout the process such that

one could be certain which depth corresponded to which crater area, so that the values of the area stored in the file when printed would be in order.

Typical values of depths measured are shown in Table B1 and those of the cross-sectional areas in Table B2. The crater volume was then calculated by multiplying the cross-sectional area by its depth and a factor 2/3. That is.

$$Crater's\ Volume = \frac{2}{3} \times Cross\text{-}sectional\ Area \times Depth \quad ..(B1)$$

Typical crater volumes calculated using equation (B1), crater depths values shown in Table B1 and cross-sectional areas as shown in Table B2 are summarised respectively in Table B3.

Table B1. Depths of Craters for X52 obtained at V_p=50 m/s and 30° Impact angle, (μm).

1. 5.4	7. 4.0	13. 4.6	19. 3.0
2. 4.6	8. 2.9	14. 5.3	20. 2.5
3. 3.8	9. 3.1	15. 3.5	21. 3.2
4. 2.7	10. 2.6	16. 4.0	22. 2.5
5. 3.9	11. 4.5	17. 5.1	23. 3.3
6. 3.5	12. 2.8	18. 2.3	24. 2.9

Table B2. Cross-sectional Areas of Craters for X52 obtained at V_p=50 m/s and 30° Impact angle, (μm^2).

1. 1690.0	7. 1053.4	13. 473.2	19. 165.8
2. 1931.6	8. 724.9	14. 756.5	20. 52.9
3. 972.4	9. 708.0	15. 297.6	21. 279.3
4. 950.8	10. 340.7	16. 336.1	22. 486.9
5. 931.0	11. 473.5	17. 425.9	23. 398.0
6. 482.4	12. 184.7	18. 177.2	24. 531.9

Table B3. Volume of Craters for X52 obtained at V_p=50 m/s and 30° Impact angle, (μm^3).

1.	6084	7.	2809	13.	1451	19.	331
2.	5923	8.	1401	14.	2672	20.	88
3.	2463	9.	1463	15.	694	21.	595
4.	1711	10.	752	16.	896	22.	811
5.	2420	11.	1420	17.	1448	23.	856
6.	1125	12.	345	18.	271	24.	1028

The distribution of the crater volumes can then be plotted on a probability graph, and such a plot is shown in Figure B1, below:

Figure B1. Crater volumes plotted on a probability graph.

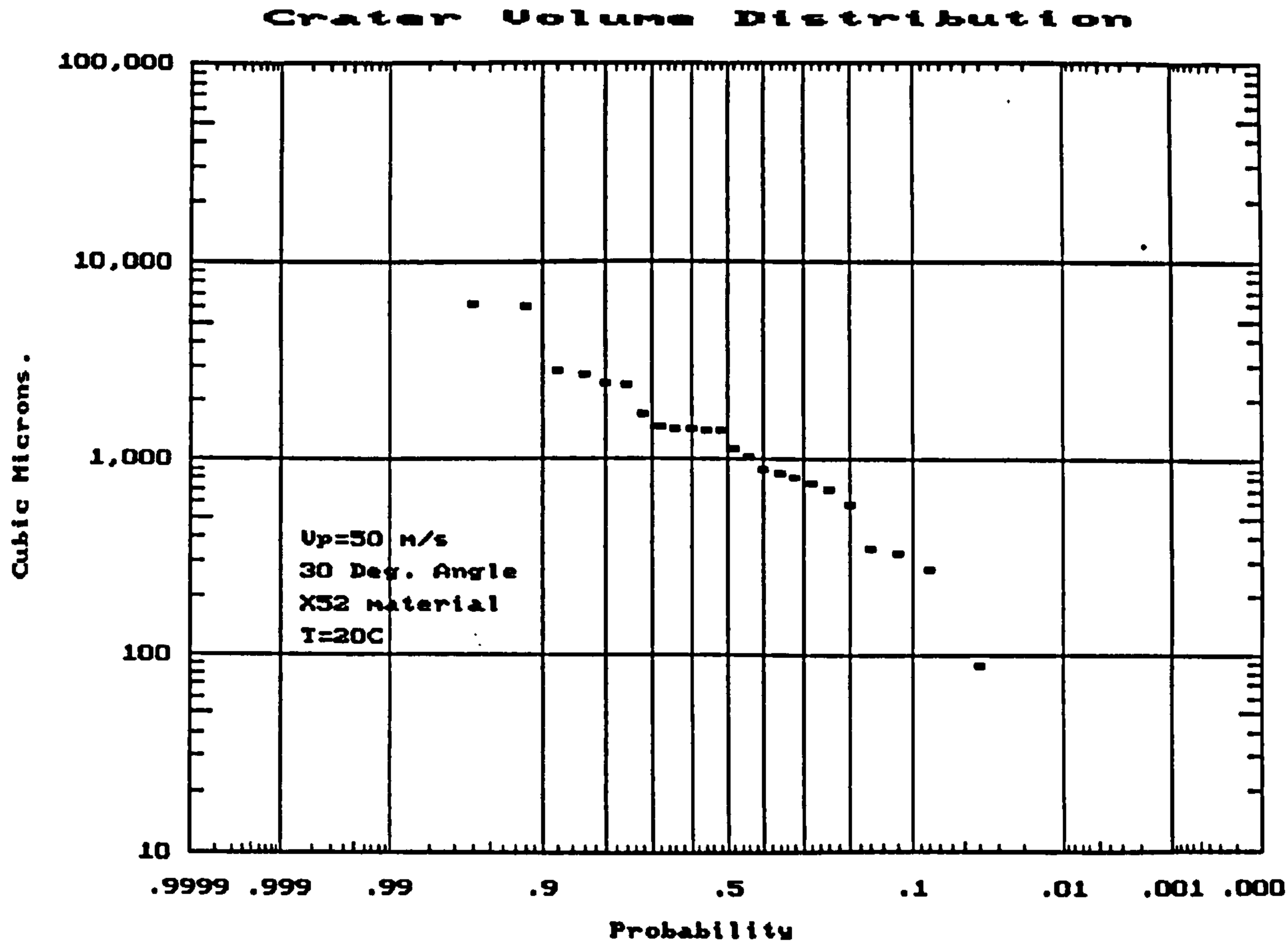

APPENDIX C

Procedure for Sand Hopper Feed Rate Calibration.

This procedure was adapted from the Calibration Procedure prepared by Accurate Inc. for the Dry Material Feeders included in the Instruction Manual.

The feed rate is determined by the speed and size of the helix in the feeder. There were two helix sizes, namely 6 mm. and 12 mm. outside diameters, used in this work to cover the range of sand flux needed for the tests.

Calibration of the feeder must be done with the actual material that will be used. The following outlines the step by step calibration process:

1. Run the feeder empty approximately five minutes prior to calibration to allow the DC motor to warm up.
2. Weigh an empty sample container.
3. Turn on the feeder and run until the discharge nozzle is full of material.
4. Set the feed rate potentiometer at the 100 setting (10% of maximum speed).
5. Collect 10 one-minute samples. Weigh and record each sample on the form provided in Figure C1. Determine the net weight of each sample by subtracting the weight of the empty sample container.
6. Obtain the average weight of these samples by adding the weights of 10 recorded samples and divided by 10.
7. To show the feed rate in g/h., multiply the average weight of the one-minute samples by 60.
8. Repeat this procedure (steps 2 - 7) at the 900 setting on the feed rate potentiometer(90% of maximum).

9. Figure C2., is a calibration graph on which the average feed rate obtained in steps 2 through 8 can be plotted.
10. At the bottom of this calibration graph are 10 boxes numbered 1 through 10. Place the averaged weight arrived at step 8 in the box numbered 10 (at 900 setting).
11. Divide the weight in box No. 10 and place the value in box No. 1. This value will help to set the scale on the graph.
12. Determine the value for each remaining box by multiplying the value in box No. 1 by the number of the box to be determined a value for and place the value in each respective box. The scale of the feed rate (X-axis) has now been determined.
13. To establish a calibration line:
    A. On the 100 feed rate pot setting line, place a point directly above the value on the feed rate per unit time value (X-axis) which matches the net weight value calculated in step 5.
    B. On the 900 feed rate pot setting line, place a point directly above the value on the feed rate per unit time value (X-axis) which matches the net weight value calculated in step 8.
    C. Draw a line between the points drawn above. This line represents the calibration line.

The feed rate at any one setting may now be determined from the graph or from actual testing. Steps 2 - 5 may now be repeated at a 500 setting (50% of speed) to make sure the 50% feed rate falls on the calibration line.

Figure C1. Calibration Data for 6 mm. Feed Helix Diameter.

Speed Pot Setting 100	One-Minute Sample No.	Sample Wt.	Container Wt.	Net Wt.
	1.	3.8913	3.2122	0.6791
	2.	3.8943	,,	0.6821
	3.	3.9035	,,	0.6913
	4.	3.9000	,,	0.6878
	5.	3.8996	,,	0.6874
	6.	3.8960	,,	0.6838
	7.	3.8888	,,	0.6766
	8.	3.8904	,,	0.6782
	9.	3.8940	,,	0.6818
	10.	3.8900	,,	0.6778
			TOTAL Wt.=	6.8259 g.
			AVERAGE Wt.=	0.68259 g.
			x 60 =	40.96 g/h.
Speed Pot Setting 900	1.	18.6527	3.2122	15.4405
	2.	18.7358	,,	15.5236
	3.	18.4400	,,	15.2278
	4.	18.6739	,,	15.4617
	5.	18.5574	,,	15.3452
	6.	18.8208	,,	15.6086
	7.	18.1537	,,	15.9415
	8.	19.0250	,,	15.8128
	9.	19.2035	,,	15.9913
	10.	19.3205	,,	16.1083
			TOTAL Wt.=	156.4613 g.
			AVERAGE Wt.=	15.6461 g.
			x 60 =	938.77 g/h.
Speed Pot Setting 500(Optional)	1.	11.7480	3.2122	8.5358
	2.	11.6760	,,	8.4638
	3.	11.6512	,,	8.4390
	4.	11.6713	,,	8.4591
	5.	11.6799	,,	8.4677
	6.	11.6928	,,	8.4806
	7.	11.6842	,,	8.4720
	8.	11.6972	,,	8.4850
	9.	11.7023	,,	8.4901
	10.	11.6968	,,	8.4846
			TOTAL Wt.=	84.7777 g.
			AVERAGE Wt.=	8.4777 g.
			x 60 =	508.67 g/h.

Figure C2. The Calibration Graph.

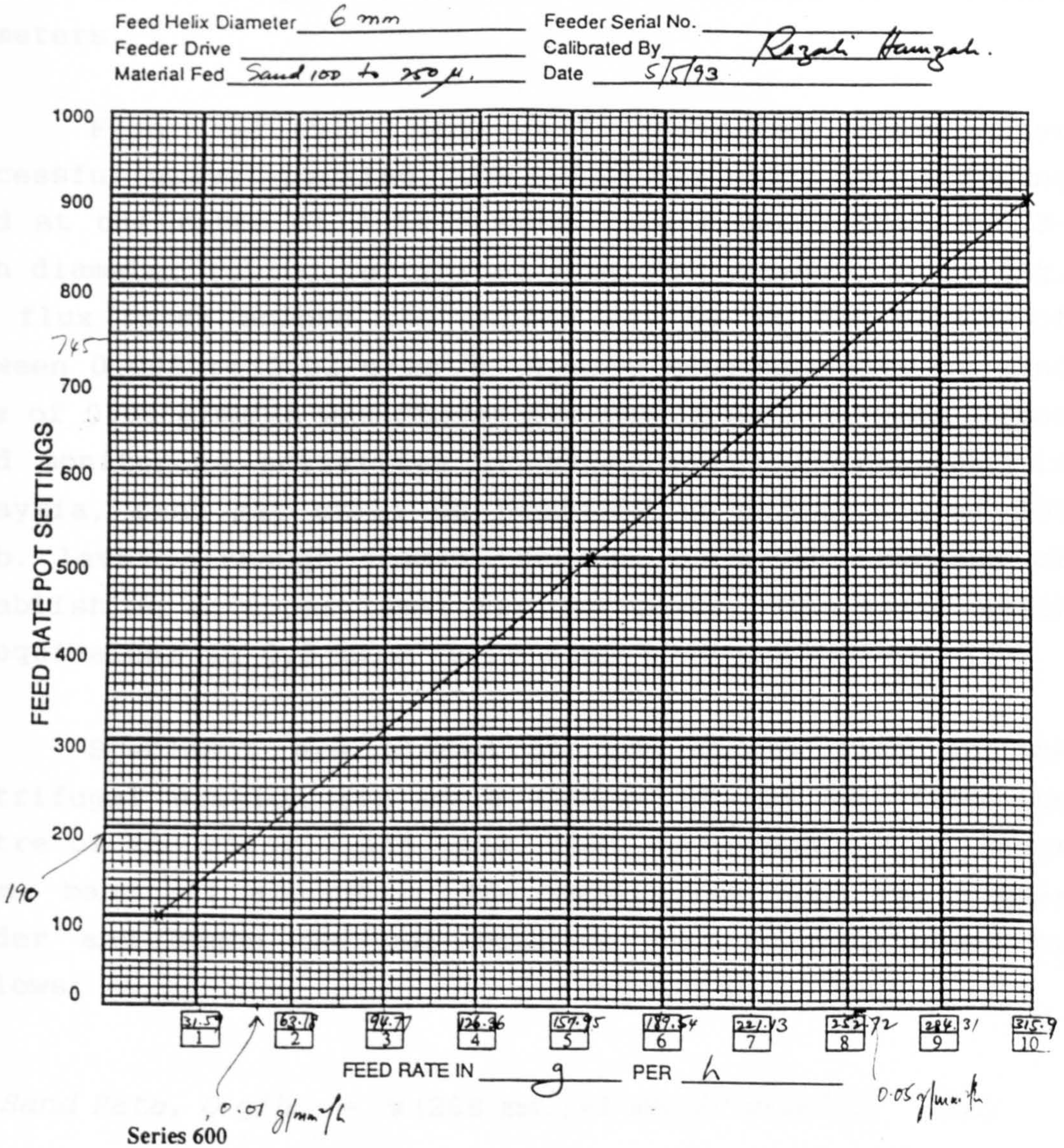

APPENDIX D

Procedure for Determining the Sand Flux Rates.

Figure D1 shows the conversion graph for the sand flux from lb/1000 barrel(pptb) to g/mm^2/h. The graphs were plotted for tubing nominal sizes from 1 inch to 4 inches diameters.

From ref.(5), Heng had indicated that after successful gravel-packing, the wells may still be producing sand at the rates of 2 to 5 pptb. This means that for 3-inch diameter tubing, a typical size for production string, the flux rates across the tubing may be in the region of between 0.008 to 0.02 g/mm^2/h, thus a minimum value of sand flux of 0.01 g/mm^2/h was chosen for the tests. However, from sand monitoring activities in Baram Delta Operations, in Malaysia, sand may still be produced in practice over 100 pptb. level although intermittently. For the purpose of establishing an upper limit for the tests, this value which is equivalent to 0.5 g/mm^2/h of sand flux was chosen.

Specimens are placed on the holder ring in the centrifugal erosion rig at a radius of 134 mm. from the centre of the rotor, and the sand is thrown out within a 6 mm. band all around. The sand rates from the hopper feeder and hence the pot setting, can be determined as follows:

$$\textit{Sand Rate, } Q \textit{ g/h, } = \pi(268 \textit{ mm.}) \times 6 \textit{ mm.} \times F \textit{ g/mm}^2\textit{/h} \qquad (D1)$$

Knowing the sand rate Q g/h, the pot setting can then be read from the graph in Figure C2 of Appendix C.

Figure D1. Sand Flux Rates

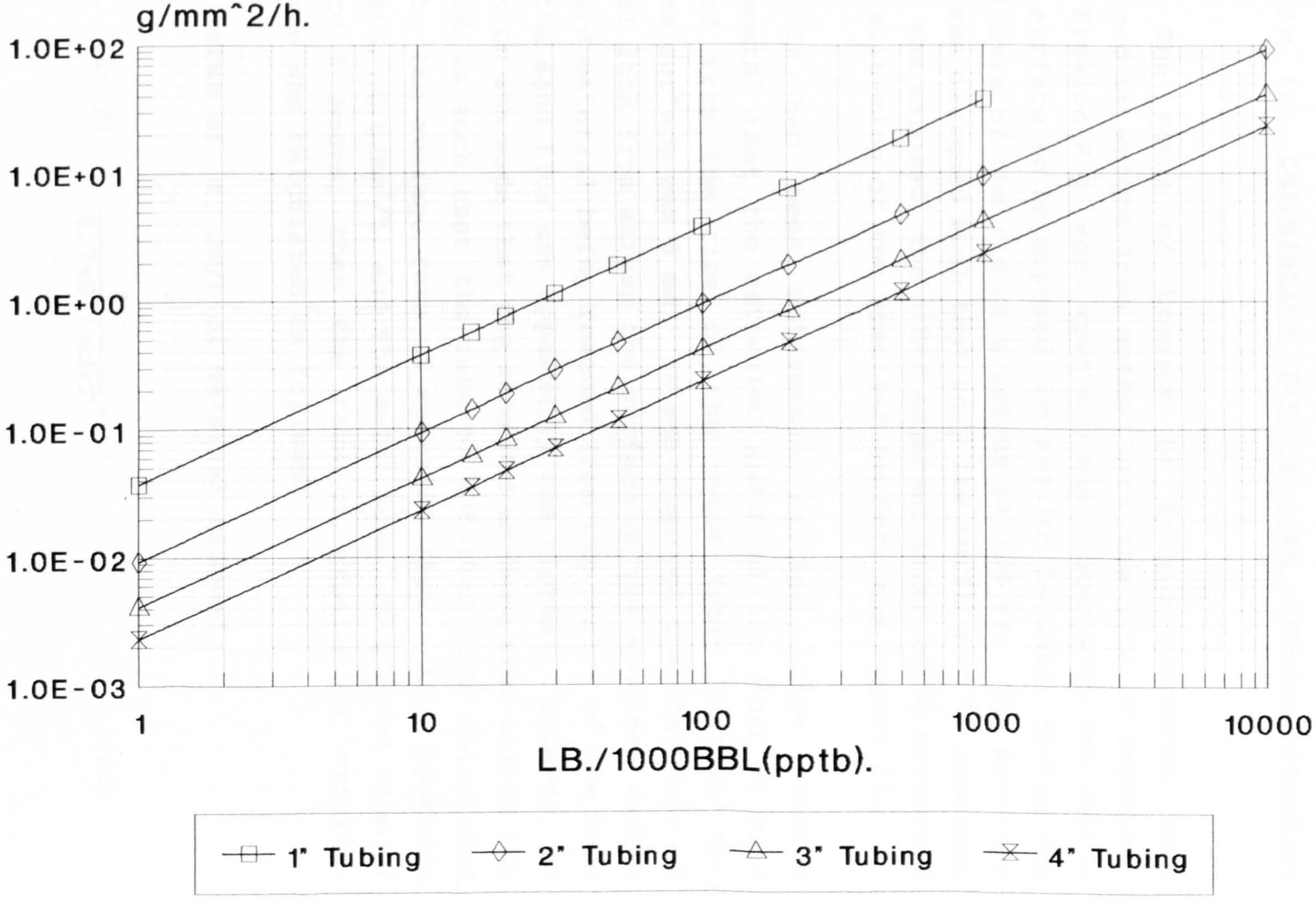

APPENDIX E

Procedure for Calculating Erosion and Erosion-Corrosion Rates.

The rates of Erosion or Erosion-Corrosion were determined by weight loss method over the time of exposure. In the Erosion Rig, each specimen was placed with the centre of its surface to be exposed for erosion by sand, facing the central axis of the rig at a radius of 134 mm. The specimen holder was designed such that only the surface to be impacted by sand was exposed, the other adjacent sides being protected by the slip-ring of the specimen holder, see Figure E1.

It had been determined earlier (from erosion experiments) that the estimated width of the band of sand imparted from the tips of the rotor tubes hitting the specimen surface was 6 mm. It was observed that the rate of material loss from across the surface of the specimen varied with more material being removed from the centre of the band where the sand flux was apparently the highest. However, an assumption was made that the sand had uniform flux across the band and as such that the rate of material loss calculated would be the average rate of material loss. At a specific flux rate, Q g/mm^2/h, and the metal loss, δW g, over time of exposure T hours; then the rate of erosion or erosion-corrosion was calculated as follows:

(a) In terms of r, µm/h of material removed,

$$r, \quad (\mu m/h) \quad = \quad \frac{\delta W}{0.7 \times 0.6 \times d \times T} \times 10^4 \qquad \ldots\ldots\ldots\ldots (E1)$$

OR

(b) In terms of r, (g of metal loss/ g of sand impacting),

$$r, \ (g/g) = \frac{100\ \delta W}{Q \times T \times 0.7 \times 0.6 \times \sin \alpha} \qquad \ldots\ldots\ldots\ldots (E2)$$

Where, 0.7 = width of surface of specimen, in cm.,
0.6 = width of band of sand flux hitting the specimen surface, hence depth of surface of material removed, in cm.,
d = density of material, in g/cm^3., and
α = angle of impact of sand particles.

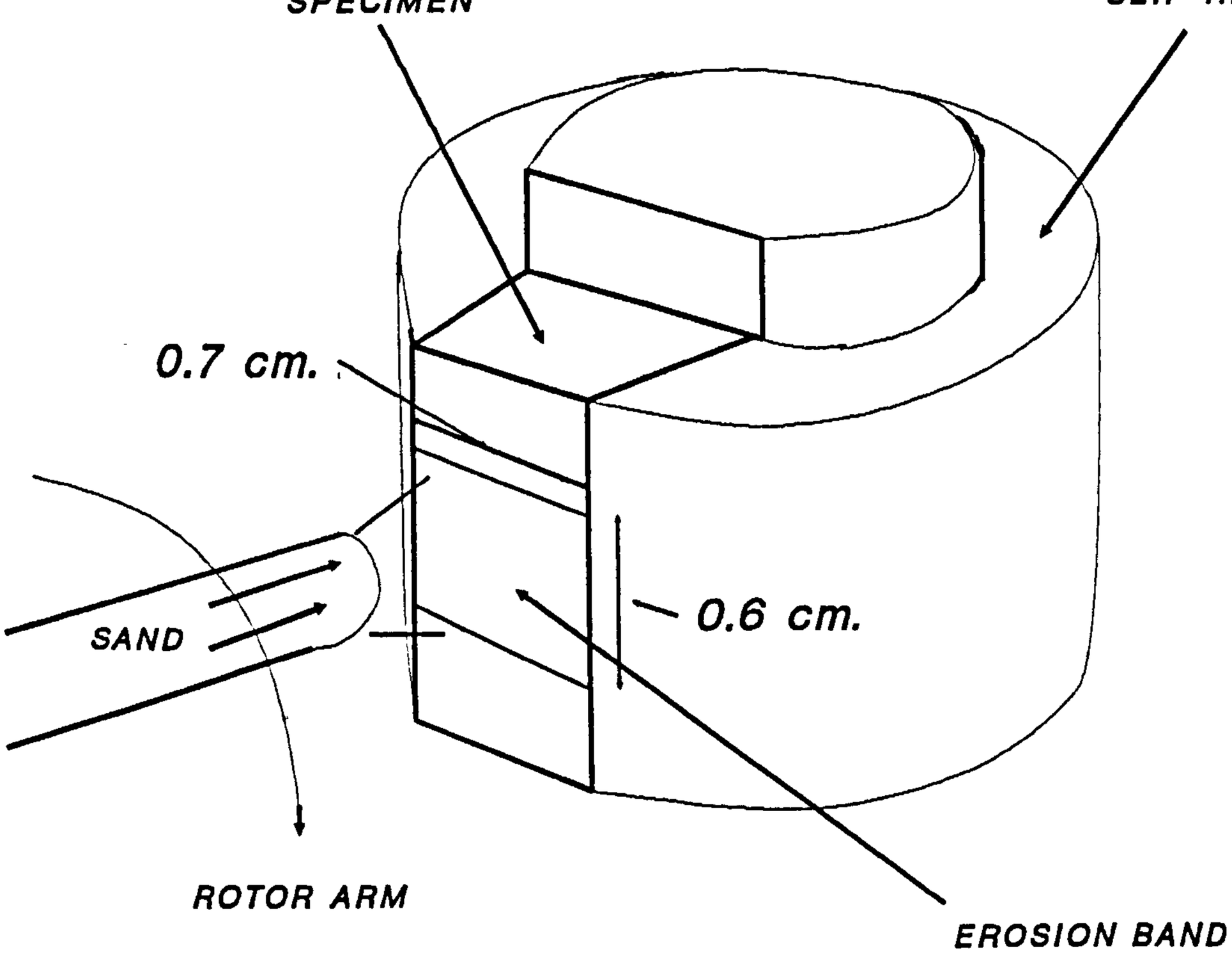

Figure E1. Schematic of a Specimen Impacted by Sand.

APPENDIX F

Summary of the Erosion and Erosion-Corrosion Tests Results, (μm/h).

CONDITIONS	α	X52	IN625	L80	13Cr	N80	X65	Fer255
Flux = 0.5	15°	0.494	0.386	0.476	0.342	0.227	0.494	0.363
Vp = 50 m/s	30°	1.159	1.034	1.135	1.107	1.318	1.177	0.985
Temp = 20°C	45°	1.976	1.908	1.739	1.505	1.827	1.757	1.737
Dry Atmos.	60°	2.867	2.555	2.098	2.096	2.256	2.190	2.310
	90°	2.117	2.648	1.867	1.810	1.870	1.995	2.292
Flux = 0.5	15°	0.474	0.555	0.708	0.415	N.A.	N.A.	N.A.
Vp = 50 m/s	30°	1.335	1.304	1.695	1.368	N.A.	N.A.	N.A.
Temp = 20°C	45°	2.088	1.756	2.051	1.801	N.A.	N.A.	N.A.
Dry CO_2	60°	2.760	2.512	2.041	2.115	N.A.	N.A.	N.A.
	90°	2.556	2.860	2.051	2.094	N.A.	N.A.	N.A.
Flux = 0.5	15°	1.403	0.452	1.979	0.650	N.A.	N.A.	N.A.
Vp = 50 m/s	30°	2.265	0.786	2.993	1.509	N.A.	N.A.	N.A.
Temp = 20°C	45°	3.743	1.911	3.254	2.238	N.A.	N.A.	N.A.
Wet Atmos.	60°	4.000	2.586	4.468	2.819	N.A.	N.A.	N.A.
	90°	3.654	2.238	3.695	2.280	N.A.	N.A.	N.A.
Flux = 0.5	15°	1.907	0.684	1.625	0.746	1.179	1.144	0.323
Vp = 50 m/s	30°	2.594	1.226	2.266	1.081	2.206	1.740	1.217
Temp = 20°C	45°	3.861	1.826	2.693	1.680	2.865	2.373	1.647
Wet CO_2	60°	4.662	2.285	3.777	2.365	2.627	3.052	3.372
	90°	3.777	2.544	3.258	2.606	2.757	2.647	2.818
Flux = 0.5	15°	2.386	0.763	1.417	0.359	N.A.	N.A.	N.A.
Vp = 50 m/s	30°	3.497	1.289	2.787	1.088	N.A.	N.A.	N.A.
Temp = 80°C	45°	4.288	2.875	4.766	1.656	N.A.	N.A.	N.A.
Wet CO_2	60°	5.468	2.742	4.800	2.268	N.A.	N.A.	N.A.
	90°	4.454	2.957	4.522	1.897	N.A.	N.A.	N.A.
Flux = 0.5	15°	0.339	0.446	0.759	0.394	N.A.	N.A.	N.A.
Vp = 50 m/s	30°	1.146	0.941	1.098	1.085	N.A.	N.A.	N.A.
Temp = 80°C	45°	1.756	1.934	1.729	1.661	N.A.	N.A.	N.A.
Dry CO_2	60°	1.702	2.245	1.810	1.562	N.A.	N.A.	N.A.
	90°	1.715	2.282	1.695	1.848	N.A.	N.A.	N.A.
Flux = 0.1	15°	0.146	0.084	0.182	0.131	0.146	0.217	0.092
Vp = 50 m/s	30°	0.317	0.209	0.329	0.255	0.254	0.294	0.213
Temp = 20°C	45°	0.523	0.337	0.525	0.334	0.395	0.523	0.334
Dry Atmos.	60°	0.662	0.531	0.720	0.454	0.526	0.619	0.440
	90°	0.636	0.593	0.587	0.339	0.446	0.483	0.433
Flux = 0.1	15°	0.357	0.085	0.468	0.130	0.489	0.508	0.098
Vp = 50 m/s	30°	0.704	0.184	0.738	0.264	0.582	0.564	0.180
Temp = 20°C	45°	0.851	0.327	0.792	0.373	0.671	0.575	0.258
Wet CO_2	60°	0.841	0.490	0.764	0.518	0.771	0.726	0.351
	90°	0.883	0.459	0.757	0.324	0.777	0.696	0.304
Flux = 0.1	15°	0.415	0.065	0.506	0.131	N.A.	N.A.	N.A.
Vp = 50 m/s	30°	0.655	0.203	0.828	0.324	N.A.	N.A.	N.A.
Temp = 80°C	45°	0.968	0.294	0.907	0.324	N.A.	N.A.	N.A.
Wet CO_2	60°	1.063	0.499	0.987	0.442	N.A.	N.A.	N.A.
	90°	0.986	0.496	0.860	0.464	N.A.	N.A.	N.A.

Summary of the Erosion and Erosion-Corrosion Tests Results, (µm/h).

CONDITIONS	α	X52	IN625	L80	13Cr	N80	X65	Fer255
Flux = 0.05	15°	0.011	0.003	0.005	0.002	N.A.	N.A.	N.A.
Vp = 20 m/s	30°	0.012	0.008	0.007	0.004	N.A.	N.A.	N.A.
Temp = 20°C	45°	0.014	0.007	0.009	0.007	N.A.	N.A.	N.A.
Dry Atmos.	60°	0.020	0.005	0.008	0.005	N.A.	N.A.	N.A.
	90°	0.018	0.005	0.004	0.005	N.A.	N.A.	N.A.
Flux = 0.05	15°	0.084	0.003	0.079	0.001	N.A.	N.A.	N.A.
Vp = 20 m/s	30°	0.115	0.005	0.154	0.003	N.A.	N.A.	N.A.
Temp = 20°C	45°	0.157	0.007	0.179	0.004	N.A.	N.A.	N.A.
Wet CO_2	60°	0.225	0.006	0.233	0.006	N.A.	N.A.	N.A.
	90°	0.213	0.006	0.204	0.004	N.A.	N.A.	N.A.
Flux = 0.05	15°	0.074	0.061	0.077	0.072	0.081	0.055	0.064
Vp = 50 m/s	30°	0.114	0.134	0.164	0.140	0.161	0.104	0.120
Temp = 20°C	45°	0.144	0.292	0.287	0.210	0.179	0.144	0.286
Dry Atmos.	60°	0.207	0.384	0.322	0.245	0.229	0.194	0.342
	90°	0.203	0.390	0.300	0.152	0.264	0.183	0.286
Flux = 0.05	15°	0.231	0.042	0.186	0.113	0.359	0.470	0.052
Vp = 50 m/s	30°	0.368	0.123	0.421	0.149	0.369	0.531	0.129
Temp = 20°C	45°	0.480	0.188	0.462	0.224	0.435	0.653	0.206
Wet CO_2	60°	0.555	0.263	0.612	0.330	0.521	0.825	0.257
	90°	0.629	0.295	0.714	0.328	0.559	0.673	0.302
Flux = 0.05	15°	0.495	0.049	0.375	0.045	N.A.	N.A.	N.A.
Vp = 50 m/s	30°	0.537	0.156	0.475	0.130	N.A.	N.A.	N.A.
Temp = 80°C	45°	0.645	0.174	0.760	0.225	N.A.	N.A.	N.A.
Wet CO_2	60°	0.779	0.217	1.006	0.256	N.A.	N.A.	N.A.
	90°	0.761	0.295	1.040	0.288	N.A.	N.A.	N.A.
Flux = 0.05	15°	0.365	0.284	0.244	0.266	N.A.	N.A.	N.A.
Vp = 80 m/s	30°	0.584	0.626	0.413	0.415	N.A.	N.A.	N.A.
Temp = 20°	45°	0.851	1.107	0.638	0.726	N.A.	N.A.	N.A.
Dry Atmos.	60°	1.107	1.311	0.921	0.711	N.A.	N.A.	N.A.
	90°	0.904	1.239	0.780	0.631	N.A.	N.A.	N.A.
Flux = 0.05	15°	0.719	0.155	0.733	0.377	N.A.	N.A.	N.A.
Vp = 80 m/s	30°	1.034	0.444	0.965	0.622	N.A.	N.A.	N.A.
Temp = 20°C	45°	1.475	0.720	1.322	0.867	N.A.	N.A.	N.A.
Wet CO_2	60°	1.767	1.081	1.955	1.072	N.A.	N.A.	N.A.
	90°	1.708	1.049	2.238	1.107	N.A.	N.A.	N.A.
Flux = 0.05	15°	1.565	1.621	1.160	1.438	N.A.	N.A.	N.A.
Vp = 150 m/s	30°	2.725	3.570	2.645	2.572	N.A.	N.A.	N.A.
Temp = 20°C	45°	3.265	6.974	4.291	3.416	N.A.	N.A.	N.A.
Dry Atmos.	60°	4.549	7.170	4.413	4.482	N.A.	N.A.	N.A.
	90°	4.134	7.222	4.264	3.917	N.A.	N.A.	N.A.
Flux = 0.05	15°	1.451	1.391	1.385	1.222	N.A.	N.A.	N.A.
Vp = 150 m/s	30°	3.603	3.673	3.124	2.439	N.A.	N.A.	N.A.
Temp = 20°	45°	5.298	4.912	4.365	4.171	N.A.	N.A.	N.A.
Wet CO_2	60°	7.625	6.450	5.115	5.140	N.A.	N.A.	N.A.
	90°	6.662	7.241	5.450	4.638	N.A.	N.A.	N.A.

Summary of the Erosion and Erosion-Corrosion Tests Results, (µm/h).

CONDITIONS	α	X52	IN625	L80	13Cr	N80	X65	Per255
Flux = 0.01	15°	0.007	0.007	0.007	0.004	0.007	0.012	0.005
Vp = 50 m/s	30°	0.023	0.020	0.012	0.019	0.012	0.015	0.011
Temp = 20°C	45°	0.029	0.026	0.022	0.022	0.041	0.021	0.015
Dry Atmos.	60°	0.022	0.022	0.014	0.017	0.018	0.027	0.022
	90°	0.015	0.012	0.008	0.008	0.008	0.020	0.003
Flux = 0.01	15°	0.024	0.018	0.027	0.018	N.A.	N.A.	N.A.
Vp = 50 m/s	30°	0.042	0.035	0.061	0.031	N.A.	N.A.	N.A.
Temp = 80°C	45°	0.058	0.049	0.074	0.054	N.A.	N.A.	N.A.
Dry Atmos.	60°	0.075	0.085	0.095	0.065	N.A.	N.A.	N.A.
	90°	0.078	0.079	0.077	0.055	N.A.	N.A.	N.A.
Flux = 0.01	15°	0.135	0.008	0.248	0.008	0.168	0.408	0.023
Vp = 50 m/s	30°	0.238	0.026	0.302	0.026	0.208	0.497	0.033
Temp = 20°C	45°	0.240	0.045	0.366	0.022	0.392	0.592	0.049
Wet CO_2	60°	0.392	0.047	0.417	0.016	0.320	0.696	0.046
	90°	0.410	0.067	0.302	0.010	0.322	0.772	0.042
Flux = 0.01	15°	0.318	0.011	0.389	0.005	N.A.	N.A.	N.A.
Vp = 50 m/s	30°	0.963	0.014	0.425	0.027	N.A.	N.A.	N.A.
Temp = 80°C	45°	1.702	0.047	0.443	0.040	N.A.	N.A.	N.A.
Wet CO_2	60°	1.365	0.042	0.457	0.077	N.A.	N.A.	N.A.
	90°	0.634	0.050	0.478	0.068	N.A.	N.A.	N.A.

APPENDIX G

Additional Results.

G1. Thickness Measurements from the Corrosion Tests, mm.

(a) For X52 Specimens (No.13* is the average thickness).

EXPOSURE	20 HOURS		100 HOURS		500 HOURS	
No.	BEFORE	AFTER	BEFORE	AFTER	BEFORE	AFTER
1.	5.957	5.955	5.946	5.958	5.956	5.949
2.	5.938	5.948	5.948	5.971	5.963	5.952
3.	5.951	5.941	5.949	5.955	5.957	5.958
4.	5.949	5.957	5.948	5.972	5.946	5.955
5.	5.945	5.944	5.941	5.960	5.952	5.957
6.	5.941	5.941	5.949	5.969	5.959	5.963
7.	5.942	5.959	5.943	5.956	5.951	5.959
8.	5.951	5.954	5.951	5.948	5.957	5.951
9.	5.950	5.944	5.945	5.950	5.948	5.961
10.	5.940	5.956	5.943	5.973	5.953	5.953
11.	5.942	5.949	5.947	5.966	5.952	5.956
12.	5.940	5.953	5.946	5.997	5.948	5.957
13.*	5.946	5.950	5.946	5.993	5.954	5.958

(b). For IN625 Specimens (No.13* is the average thickness).

EXPOSURE	20 HOURS		100 HOURS		500 HOURS	
No.	BEFORE	AFTER	BEFORE	AFTER	BEFORE	AFTER
1.	5.992	5.963	5.951	5.928	5.932	5.946
2.	5.962	5.992	5.938	5.920	5.942	5.941
3.	5.979	5.981	5.936	5.933	5.945	5.951
4.	5.953	5.978	5.930	5.952	5.932	5.958
5.	5.972	5.975	5.913	5.933	5.942	5.953
6.	5.956	5.989	5.929	5.928	5.939	5.950
7.	5.941	5.969	5.918	5.929	5.934	5.955
8.	5.943	5.980	5.918	5.916	5.923	5.960
9.	5.949	5.995	5.928	5.927	5.929	5.963
10.	5.950	5.978	5.920	5.926	5.935	5.965
11.	5.959	5.970	5.942	5.941	5.929	5.936
12.	5.961	5.971	5.932	5.935	5.936	5.953
13.*	5.960	5.978	5.930	5.939	5.935	5.964

G2. Determination of the Shape Factor of Sand Particles.

The Shape Factor is defined as the ratio of the inner circle diameter to the outer embracing circle diameter as shown in Figure G2. For a perfect sphere the Shape Factor is unity. It is the reciprocal value of the Aspect Ratio as defined in reference (54). The measurements of the respective particle diameters were made by using a mm-scale rule, on a random basis, from the particles photomicrograph. An arithmetic average value is obtained from between 15 to 25 readings. A sample of the calculation is shown in Table G2. The average value of the Particle Shape Factor in this case was found to be 0.64.

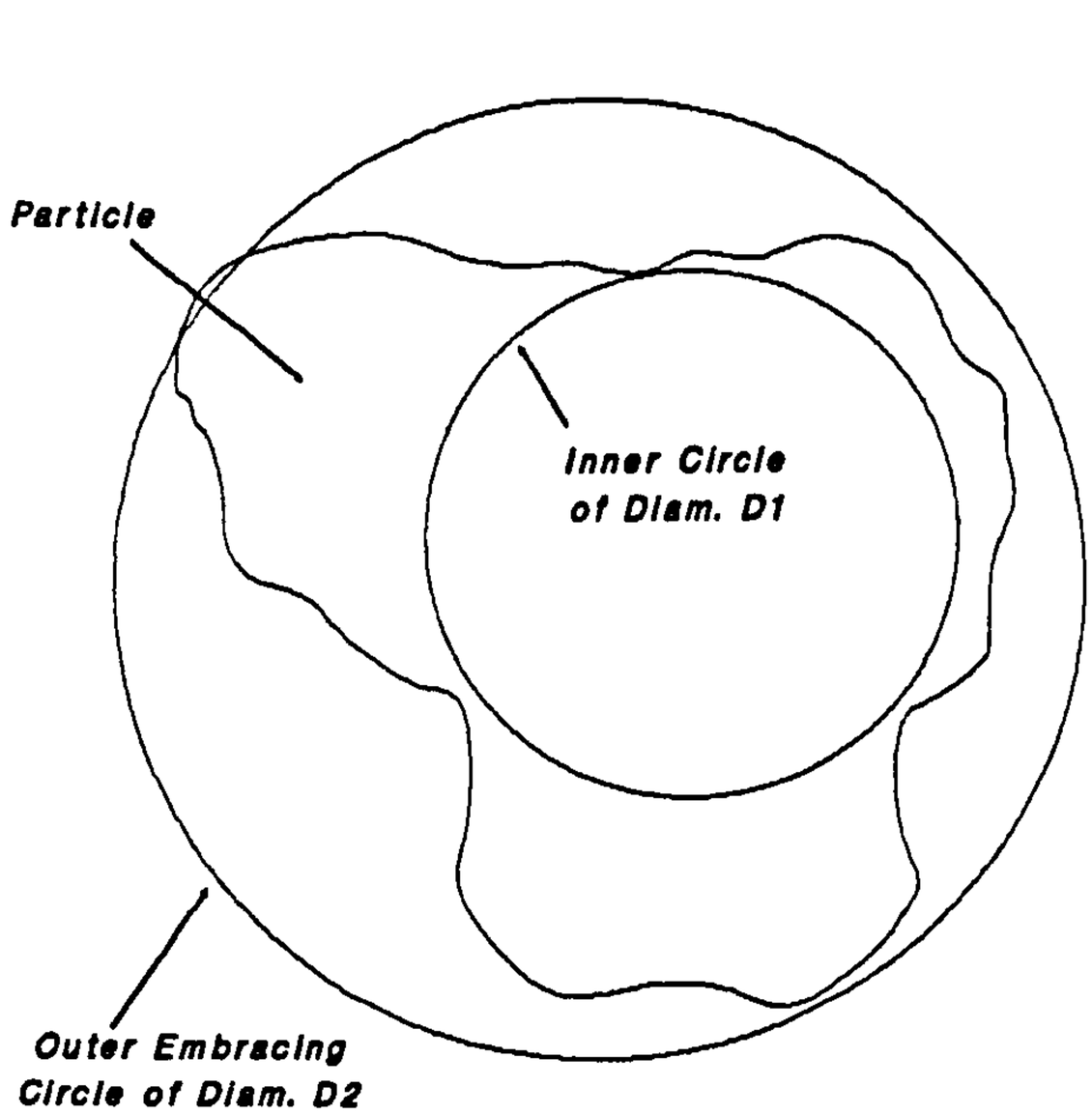

Figure G2. Definition of Particle Shape Factor.

Table G2. Sample of calculations for Particle Shape Factor.

OUTER CIRCLE DIAMETER	INNER CIRCLE DIAMETER	ASPECT RATIO	SHAPE FACTOR
25	15	1.67	0.60
17	8	2.13	0.47
16	12	1.33	0.75
19	12	1.63	0.63
18	12	1.50	0.67
15	11	1.36	0.73
22	14	1.57	0.64
14	9	1.56	0.64
16	12	1.33	0.75
17	12	1.42	0.71
17	10	1.70	0.59
18	15	1.20	0.83
18	11	1.64	0.60
22	12	1.83	0.54
13	8	1.63	0.62
13	9	1.44	0.69
14	9	1.56	0.64
17	11	1.55	0.65
15	10	1.50	0.67
18	9	2.00	0.50
18	9	2.00	0.50
15	12	1.25	0.80
21	12	1.75	0.57
15	9	1.67	0.60
16	10	1.60	0.62

G3. Records of Single Impact Experiments for X65, N80, L80, L80/13Cr and Ferrulium 255.

(a) X65.

Vp, m/s	Wp, mg.	Impact Angles, °	Wt. B/Impact (g)	Wt. A/Impact (g)
50	7.7	30	3.4502	3.4501
80	8.1	30	3.4693	3.4693
100	8.3	30	3.4538	3.4536
150	7.1	30	3.4518	3.4518
Vp, m/s	Wp, mg.	Impact Angles, °	Wt. B./Impact (g)	Wt. A/Impact (g)
50	5.7	90	3.4695	3.4695
80	9.7	90	3.4681	3.4681
100	6.0	90	3.4643	3.4642
150	7.2	90	3.4728	3.4727

(b) N80.

Vp, m/s.	Wp, mg.	Impact Angles, °	Wt. B/Impact (g)	Wt. A/Impact (g)
50	5.4	30	3.4550	3.4550
80	9.9	30	3.4523	3.4523
100	7.0	30	3.4394	3.4396
150	5.1	30	3.3757	3.3756
Vp, m/s.	Wp, mg.	Impact Angles, °	Wt. B/Impact (g)	Wt. A/Impact (g)
50	8.6	90	3.3620	3.3620
80	9.4	90	3.4147	3.4150
100	8.0	90	3.4659	3.4664
150	9.7	90	3.4434	3.4434

(c). L80.

Vp, m/s.	Wp, mg.	Impact Angles, °	Wt. B/Impact (g)	Wt. A/Impact (g)
50	4.0	30	3.4563	3.4562
80	8.9	30	3.4417	3.4417
100	6.1	30	3.4047	3.4050
150	9.8	30	3.4271	3.4268
Vp, m/s.	Wp, mg.	Impact Angles, °	Wt. B/Impact (g)	Wt. A/Impact (g)
50	6.4	90	3.3930	3.3928
80	7.4	90	3.4109	3.4107
100	9.9	90	3.4950	3.4949
150	7.8	90	3.4973	3.4973

(d). L80/13Cr.

Vp, m/s.	Wp, mg.	Impact Angles, °	Wt. B/Impact (g)	Wt. A/Impact (g)
50	6.2	30	3.3972	3.3972
80	8.3	30	3.3869	3.3868
100	6.1	30	3.3730	3.3729
150	8.3	30	3.4118	3.4118
Vp, m/s.	Wp, mg.	Impact Angles, °	Wt. B/Impact (g)	Wt. A/Impact (g)
50	7.8	90	3.4200	3.4202
80	7.6	90	3.4005	3.4001
100	10.0	90	3.3899	3.3900
150	9.3	90	3.4024	3.4025

(e). Ferrulium 255.

Vp, m/s.	Wp, mg.	Impact Angles, °	Wt. B/Impact (g)	Wt. A/Impact (g)
50	6.3	30	3.4510	3.4510
80	7.9	30	3.4398	3.4398
100	7.3	30	3.4385	3.4385
150	7.7	30	3.4709	3.4708
Vp, m/s.	Wp, mg.	Impact Angles, °	Wt. B/Impact (g)	Wt. A/Impact (g)
50	9.7	90	3.4478	3.4478
80	7.2	90	3.4638	3.4639
100	10.0	90	3.4725	3.4725
150	7.4	90	3.4648	3.4645

G4. Crater Volume Distribution for X65, N80, L80, L80/13Cr and Ferrulium 255.

(a.1). X65, V_p=50 m/s and 80 m/s, at 30°.

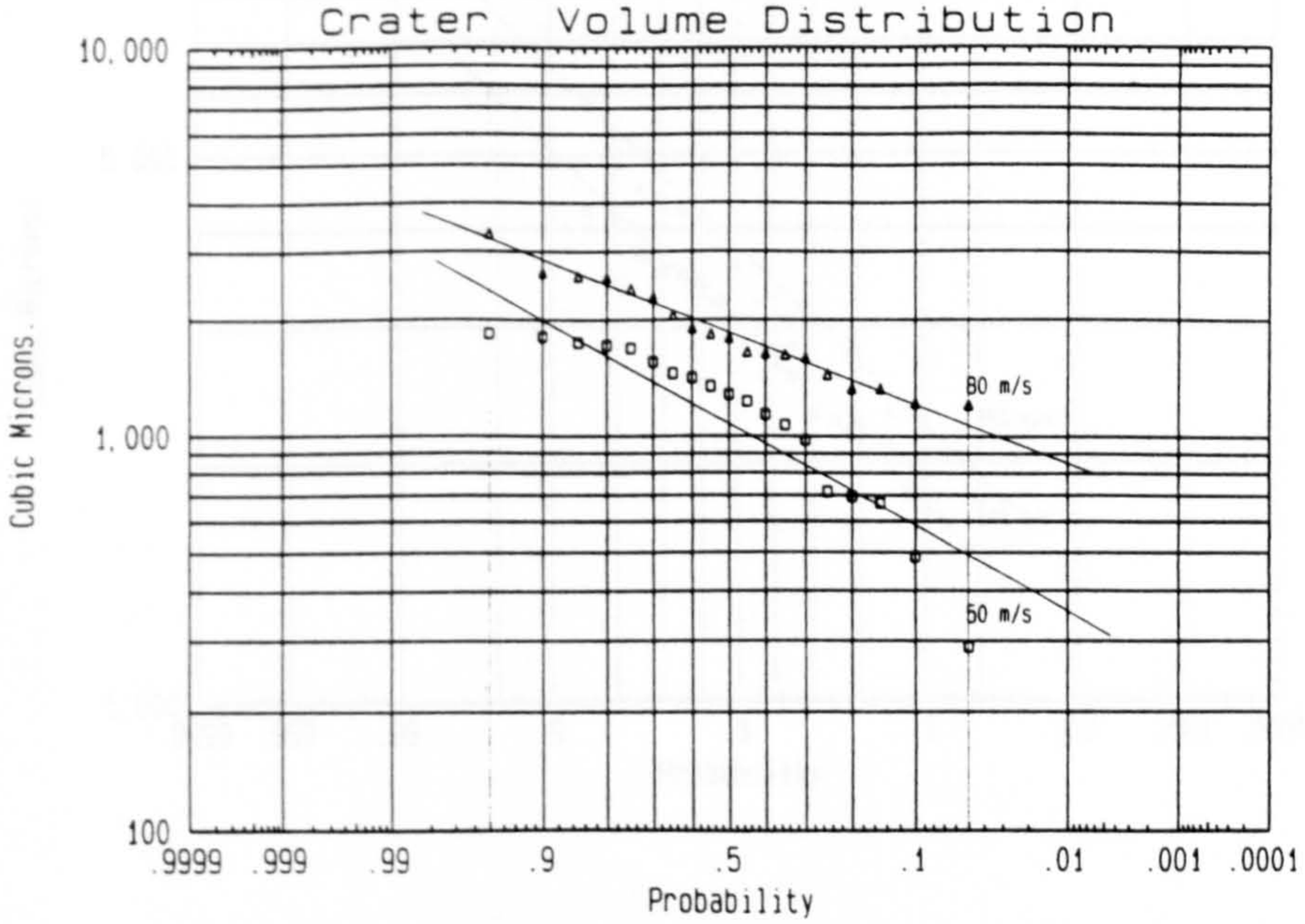

(a.2). X65, V_p= 50 m/s and 80 m/s, at 90°.

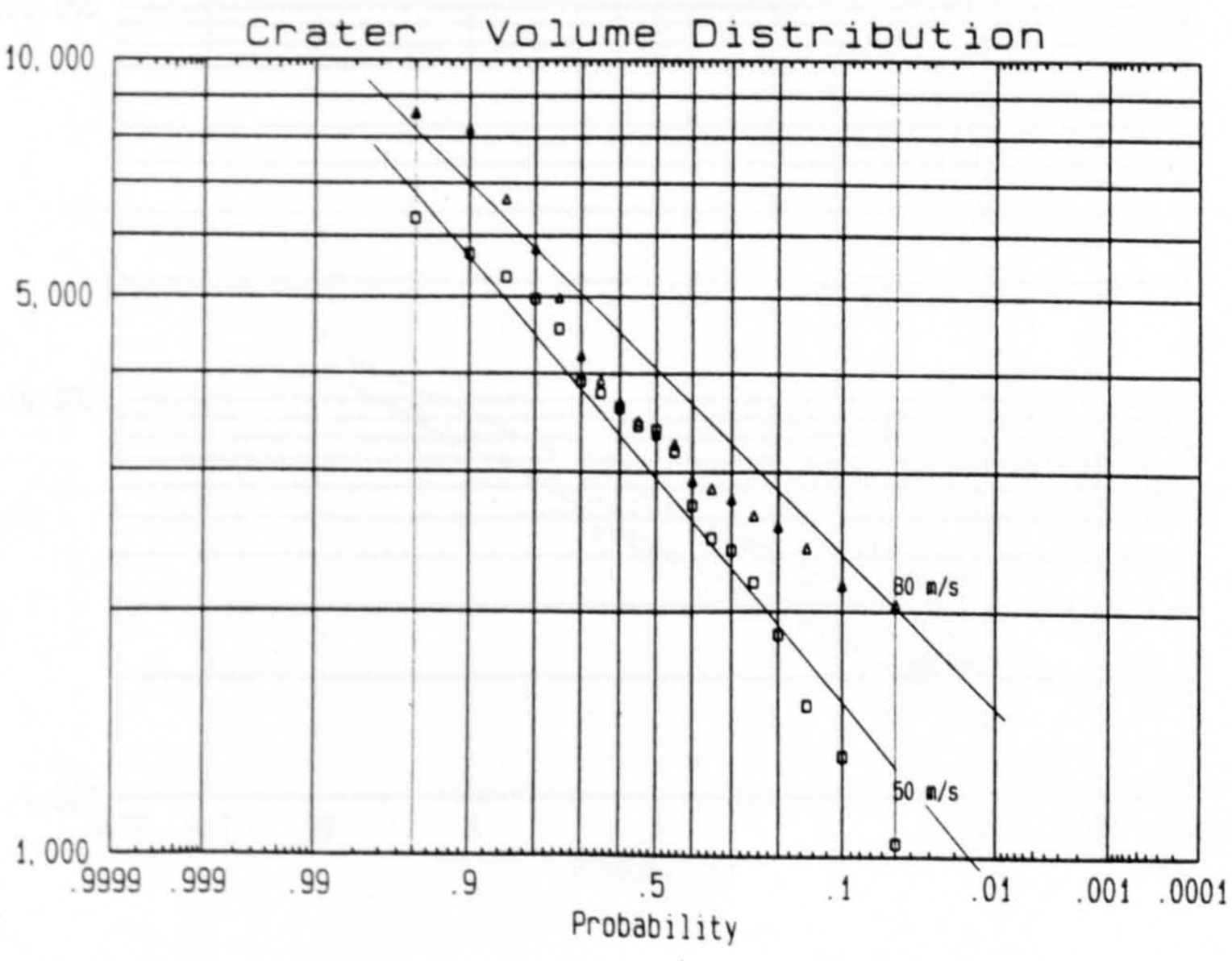

(a.3). X65, V_p=100 m/s and 150 m/s, at 30°.

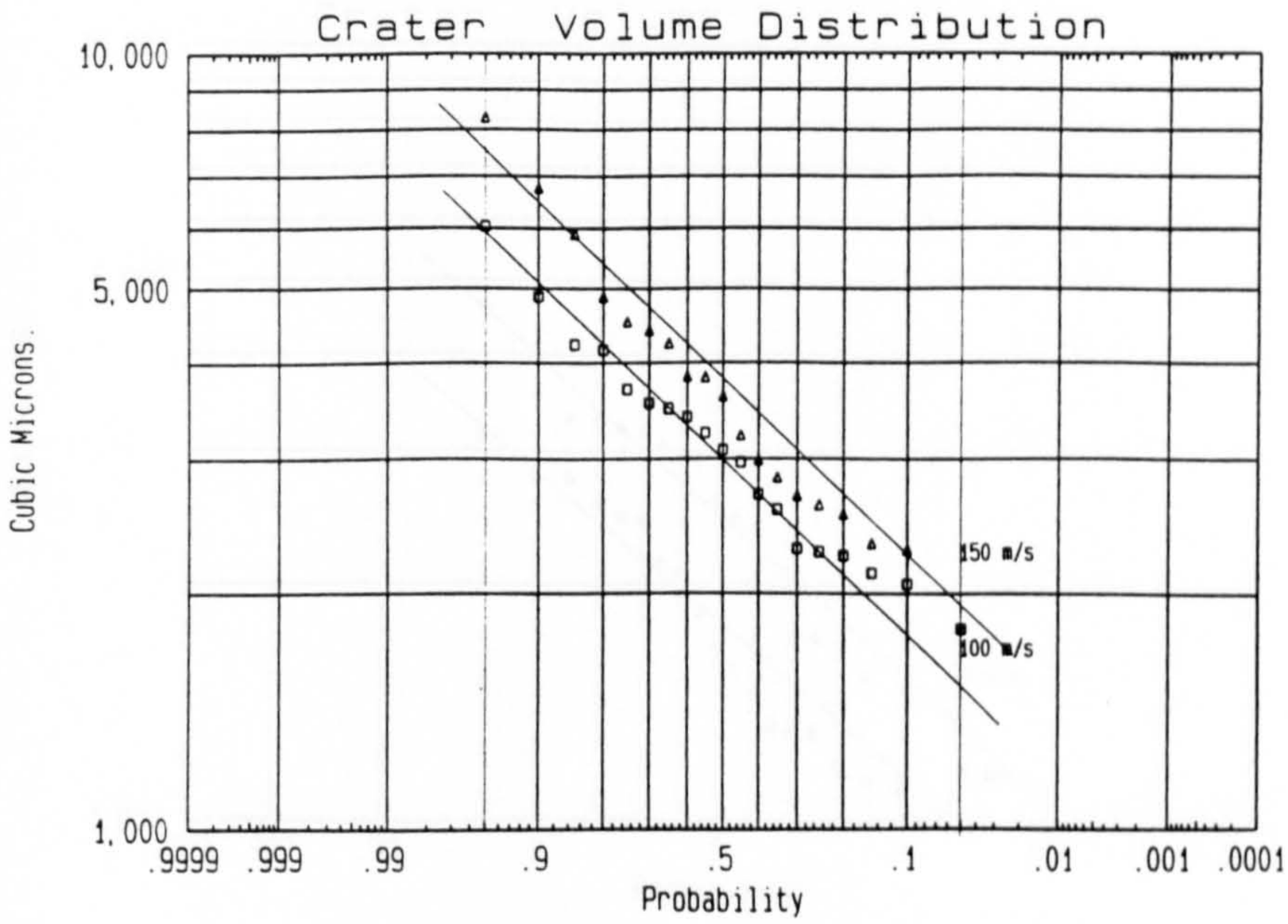

(a.4). X65, V_p=100 m/s and 150 m/s, at 90°.

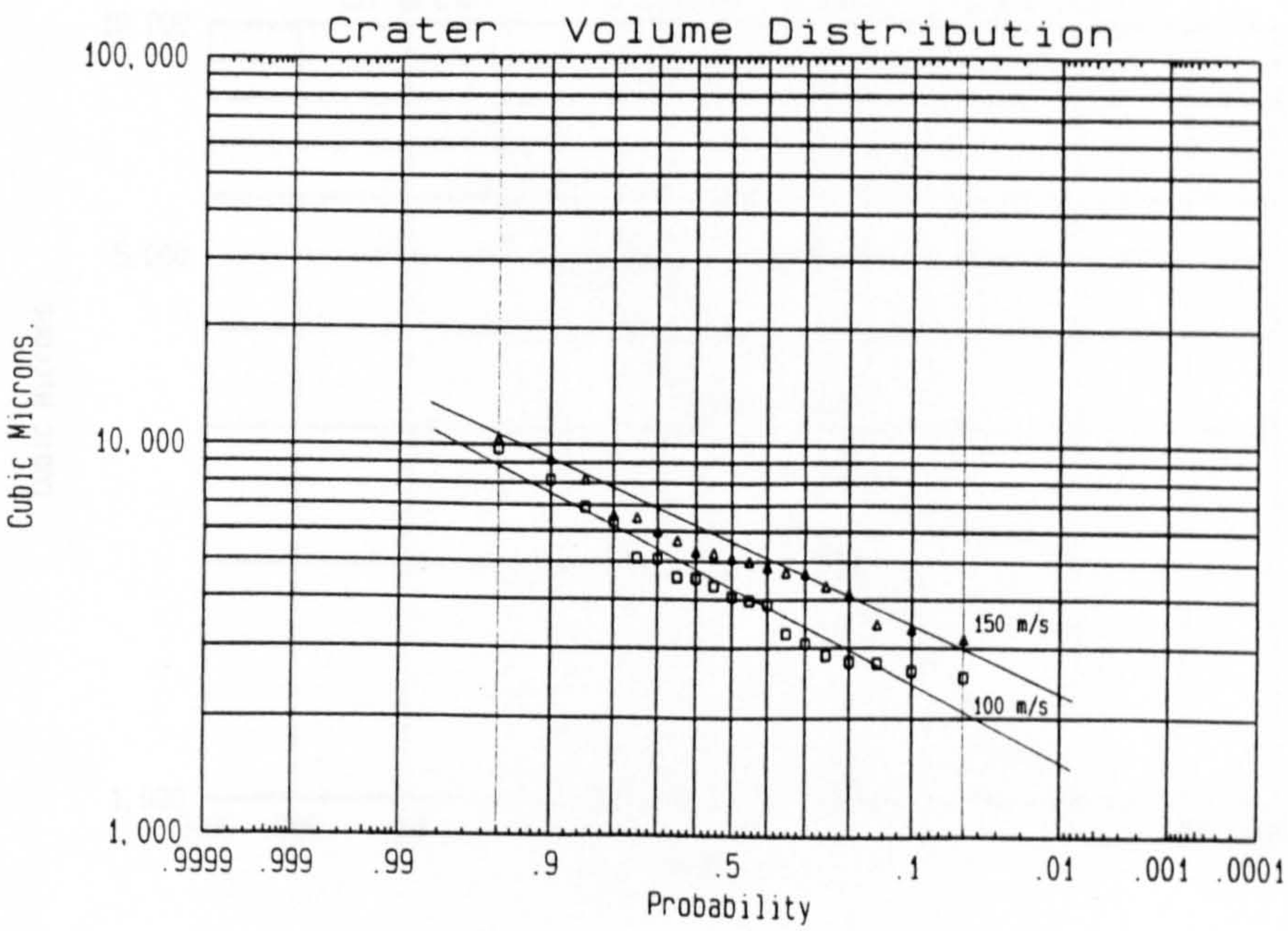

(b.1). N80, V_p=50 m/s and 80 m/s, at 30°.

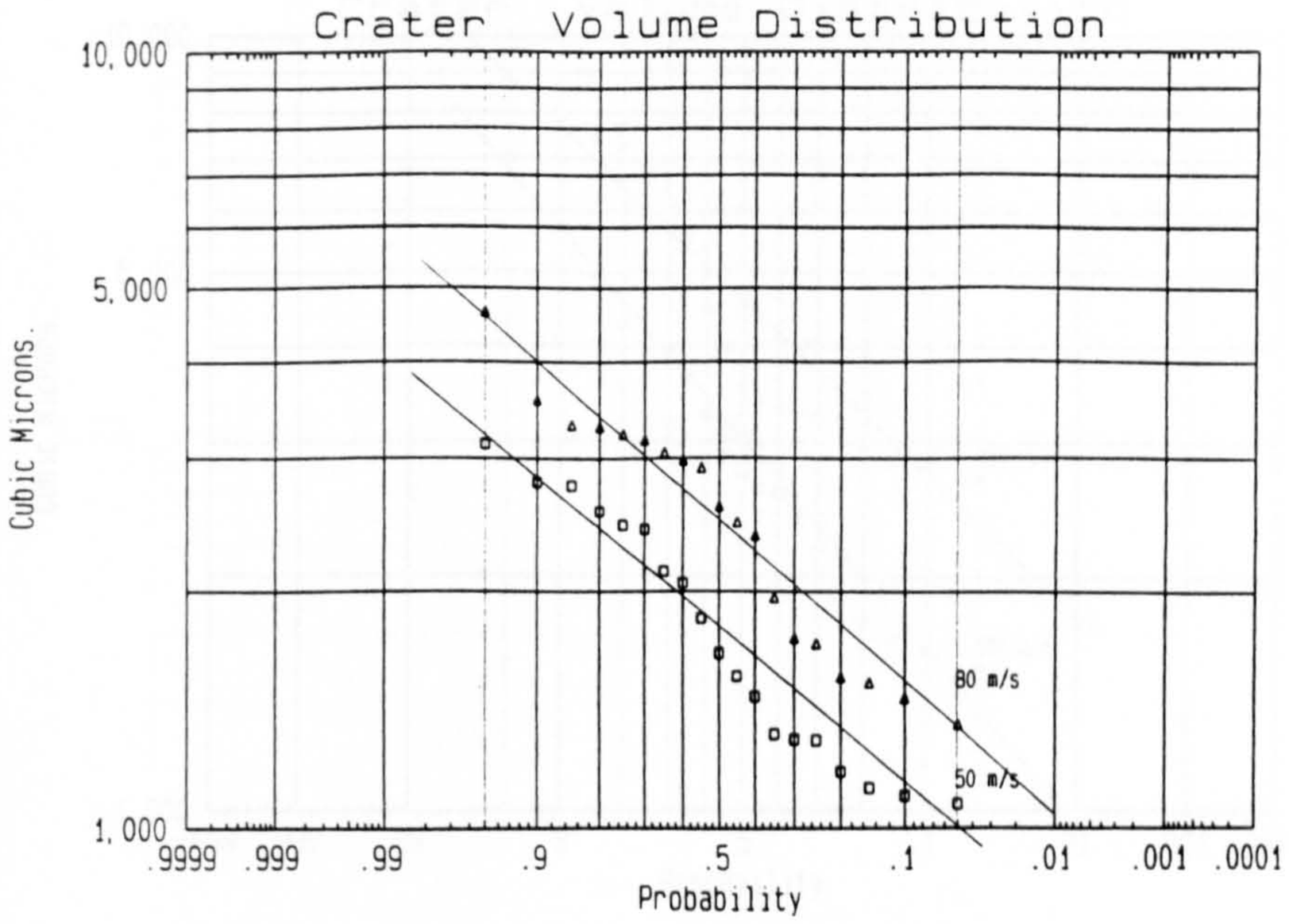

(b.2). N80, V_p=50 m/s and 80 m/s, at 90°.

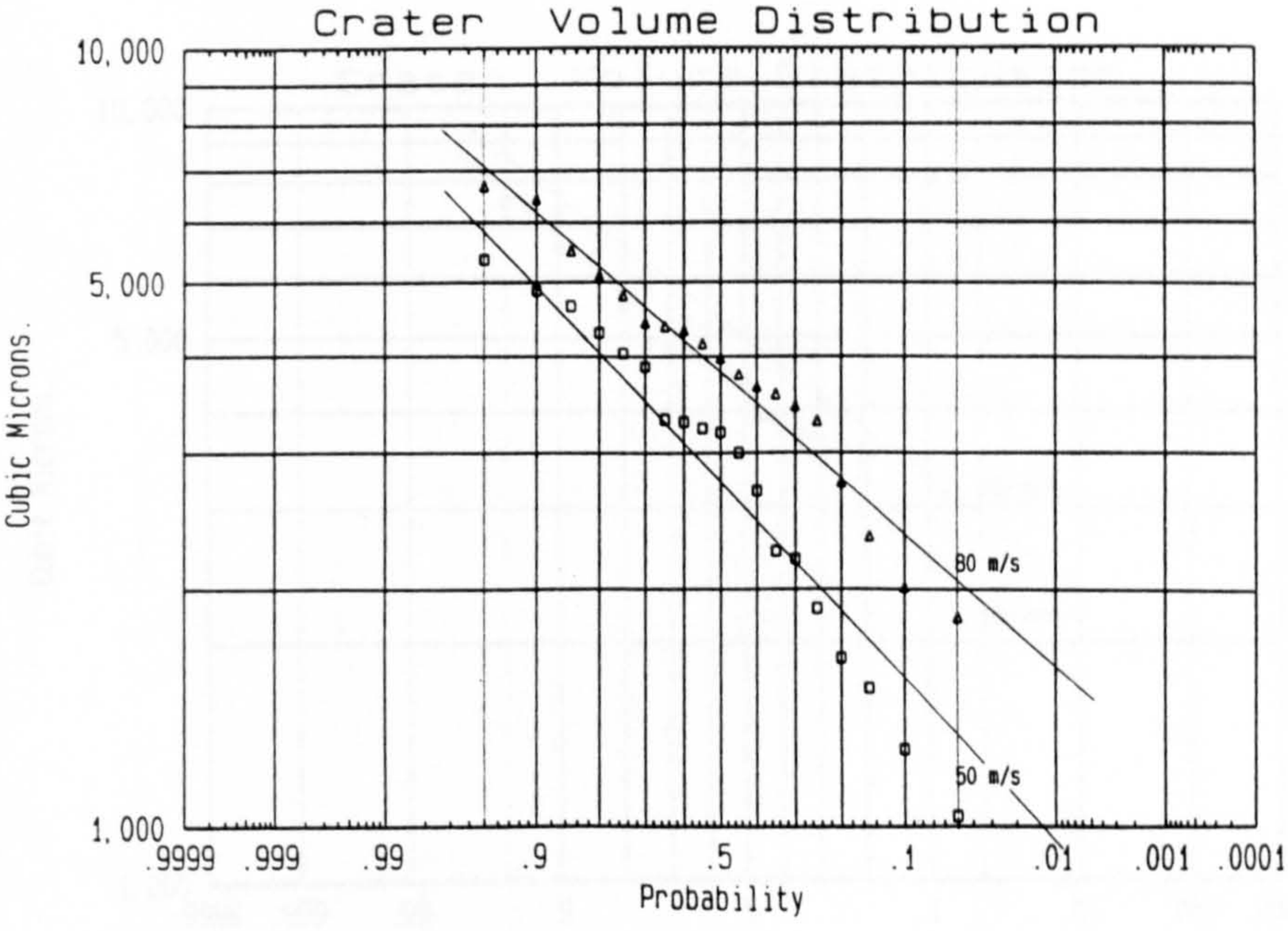

(b.3). N80, V_p=100 m/s and 150 m/s, at 30°.

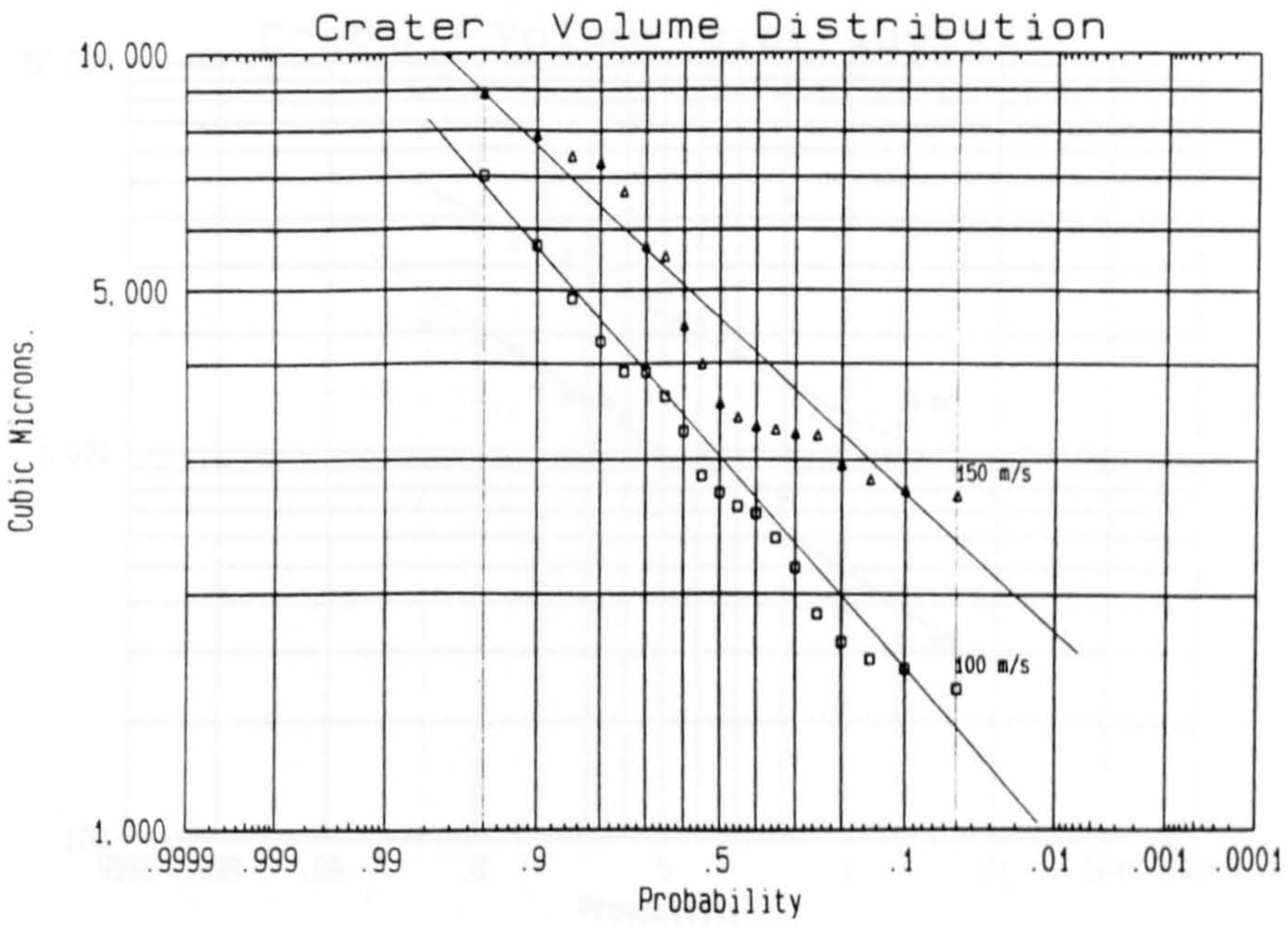

(b.4). N80, V_p=100 m/s and 150 m/s, at 90°.

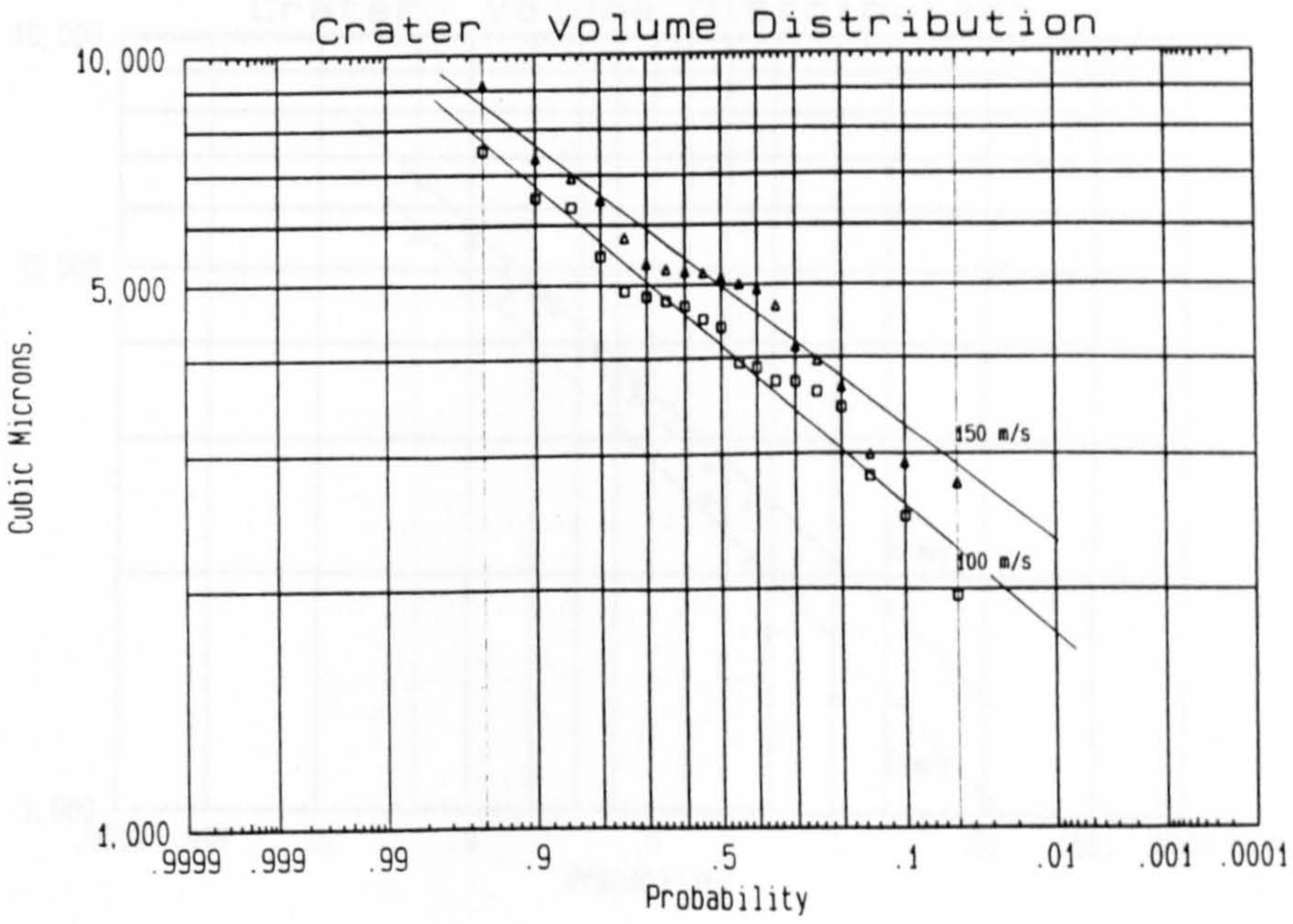

(c.1). L80, V_p=50 m/s and 80 m/s, at 30°.

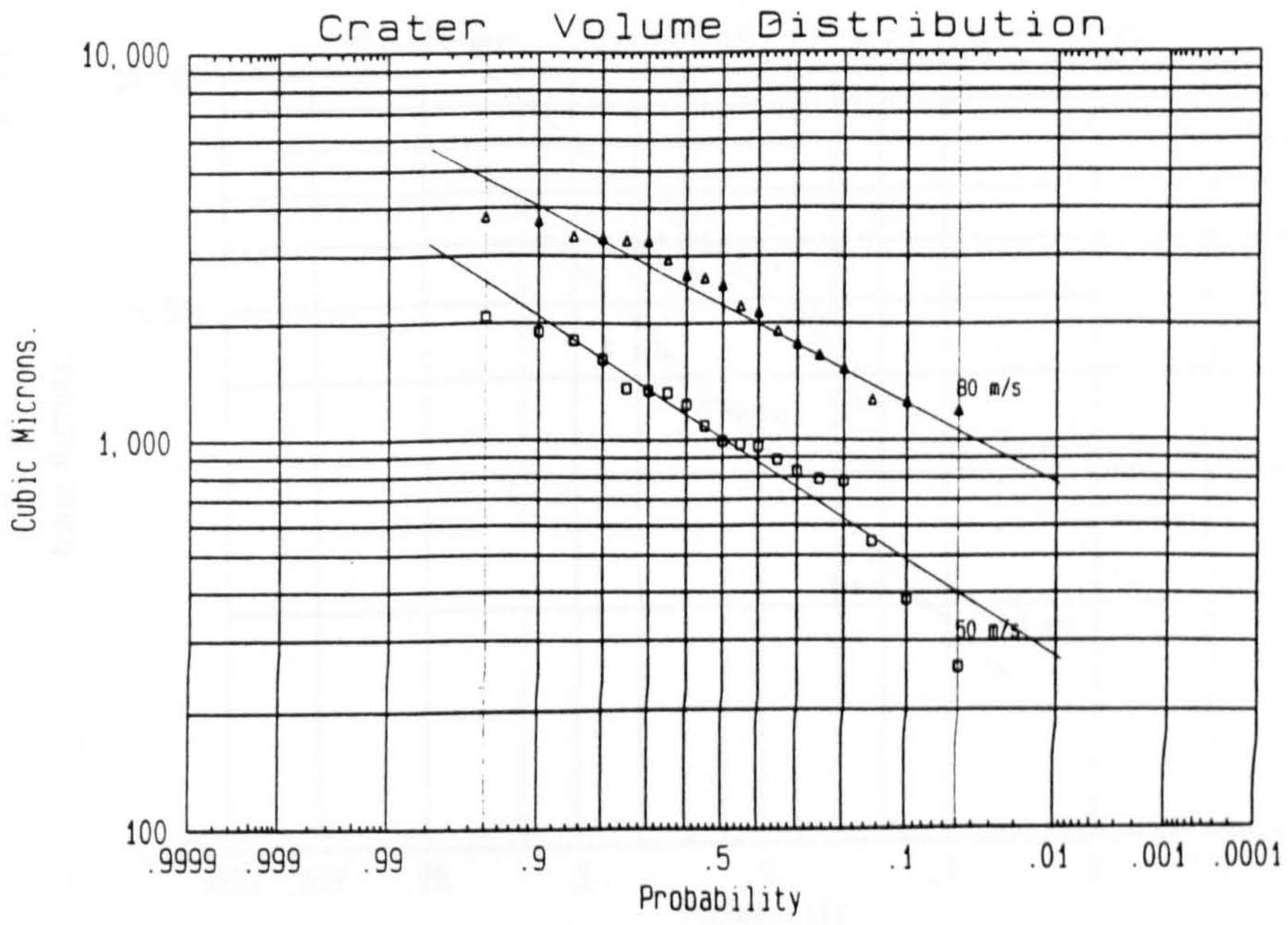

(c.2). L80, V_p=50 m/s and 80 m/s, at 90°.

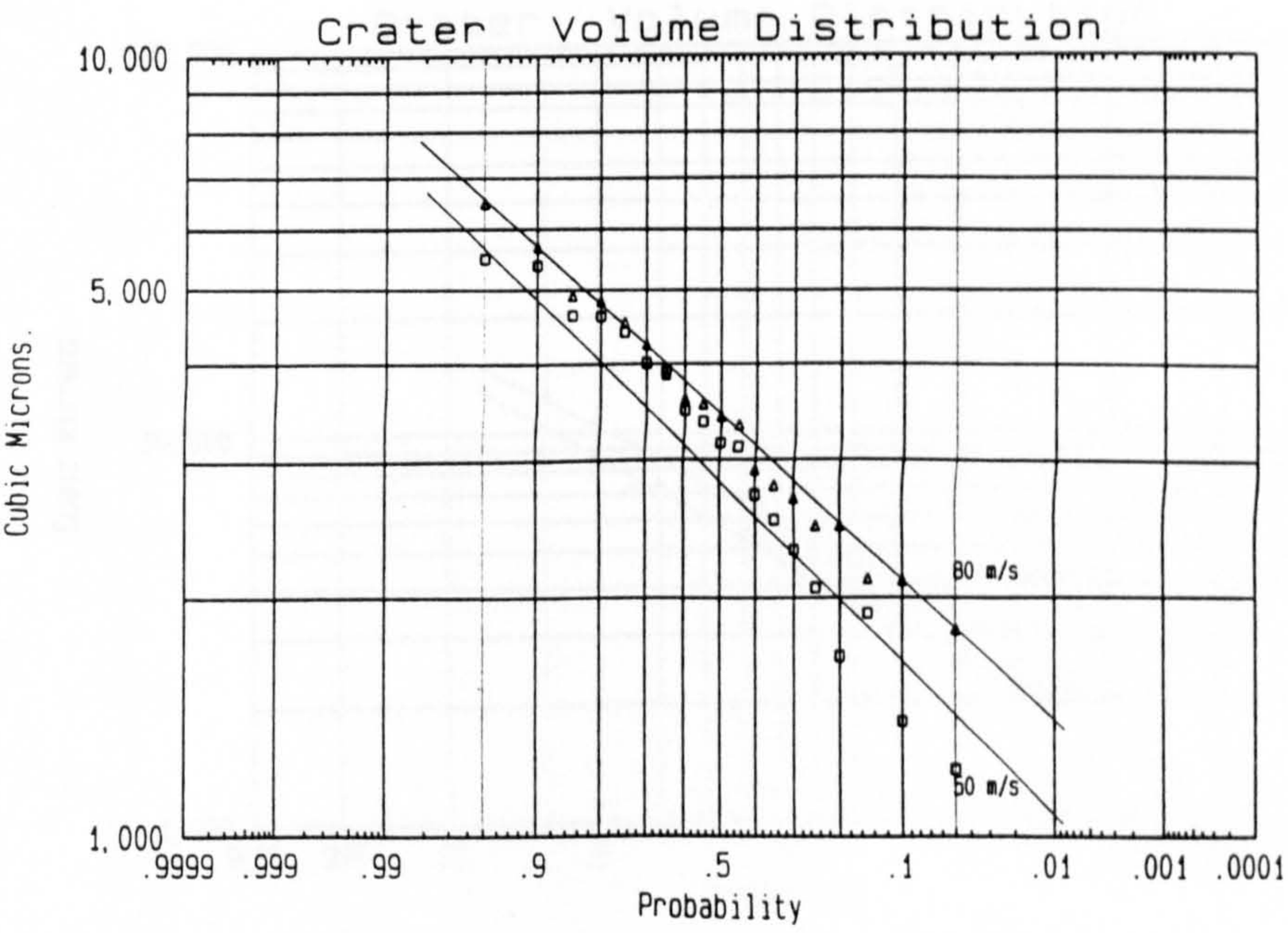

(c.3). L80, V_p=100 m/s and 150 m/s, at 30°.

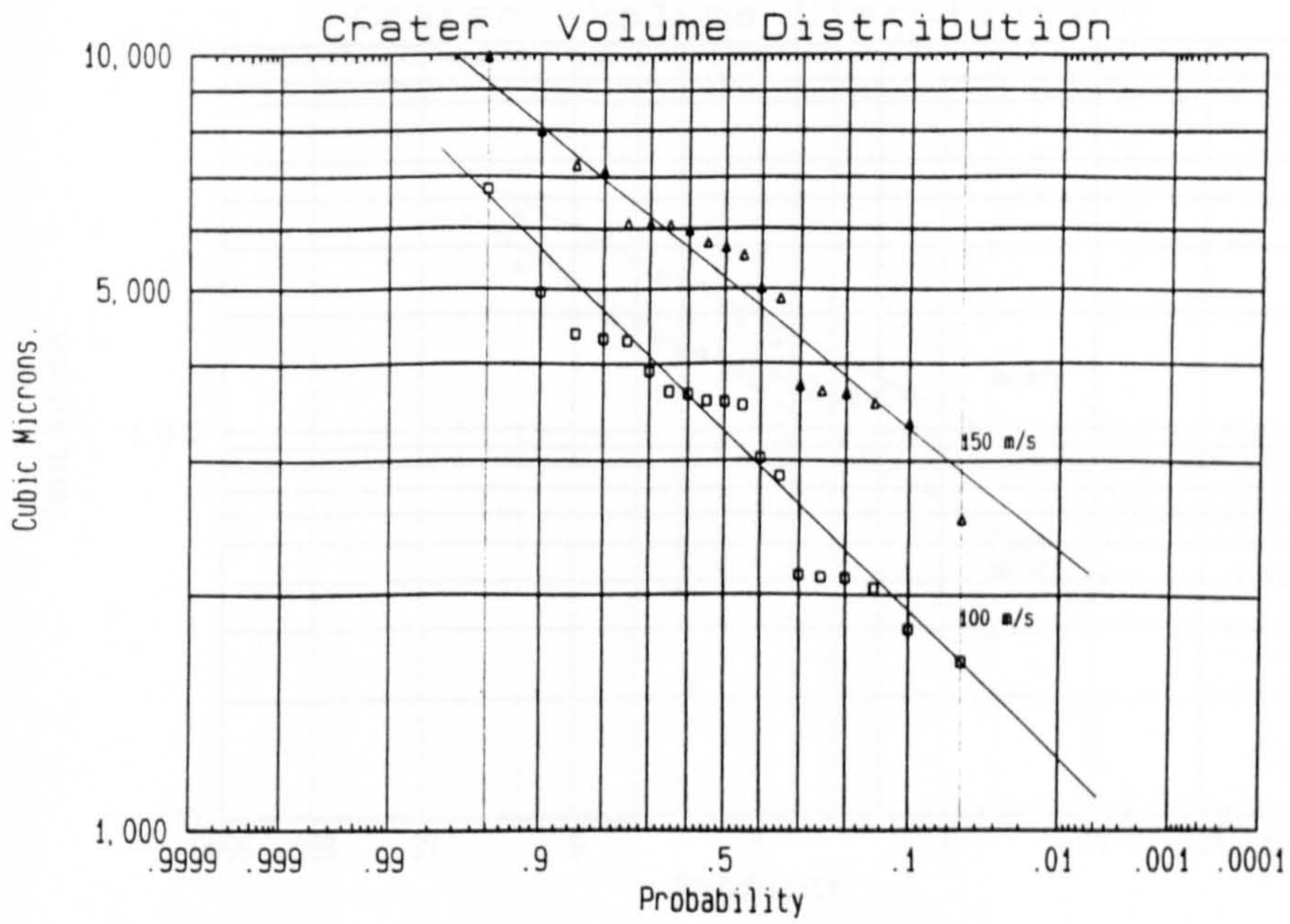

(c.4). L80, V_p=100 m/s and 150 m/s, at 90°.

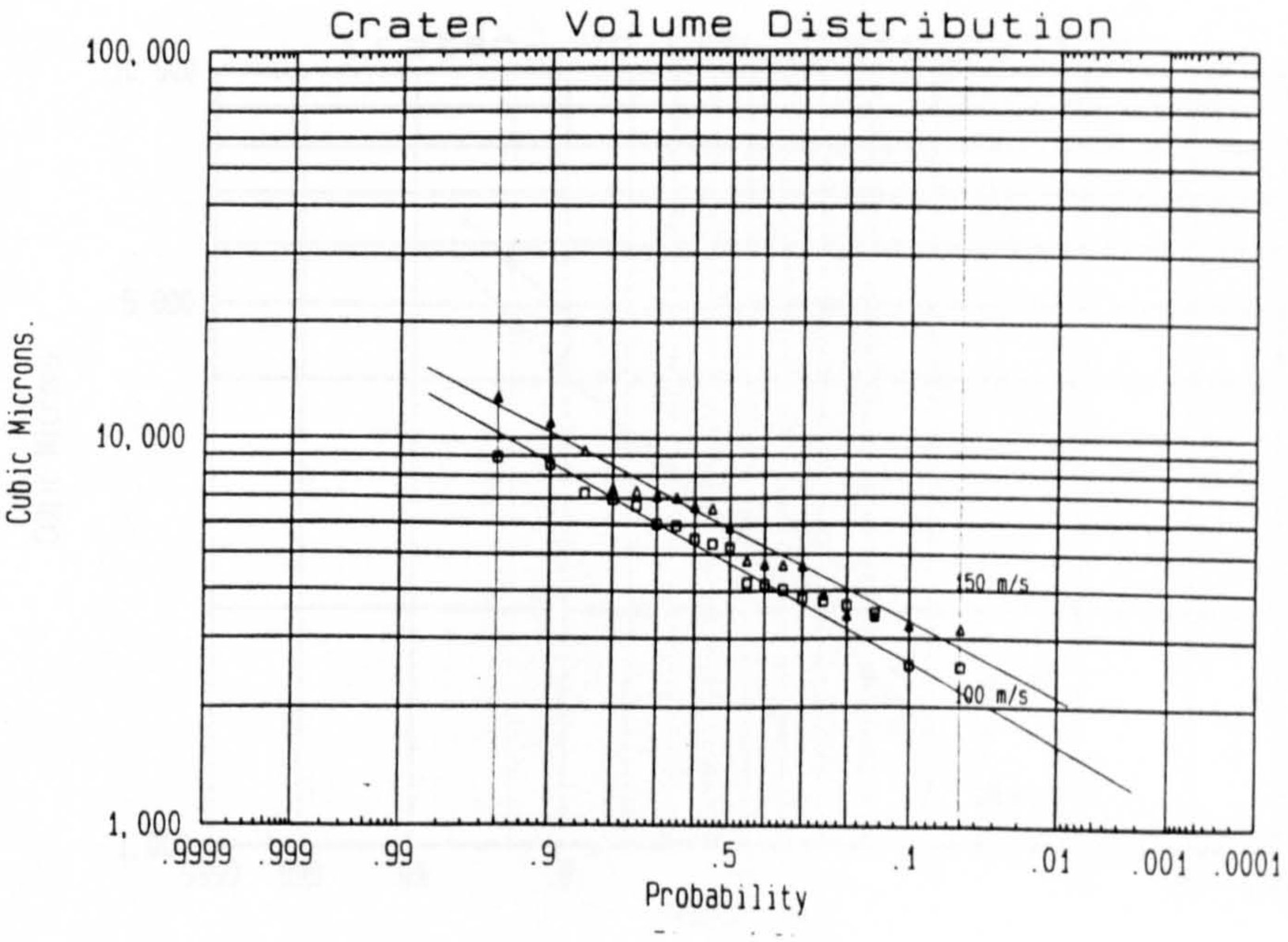

(d.1). L80/13Cr, V_p=50 m/s and 80 m/s, at 30°.

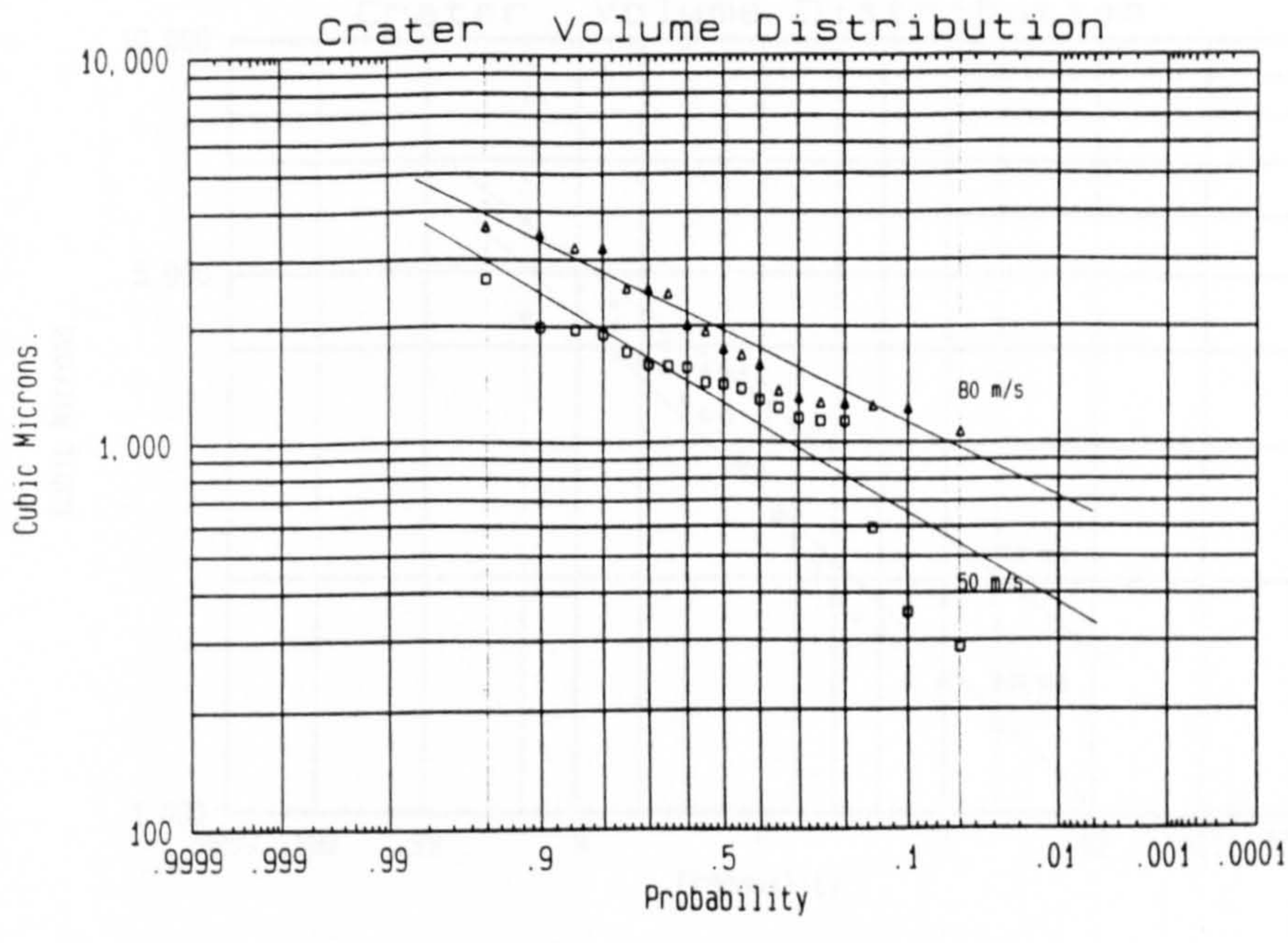

(d.2). L80/13Cr, V_p=50 m/s and 80 m/s, at 90°.

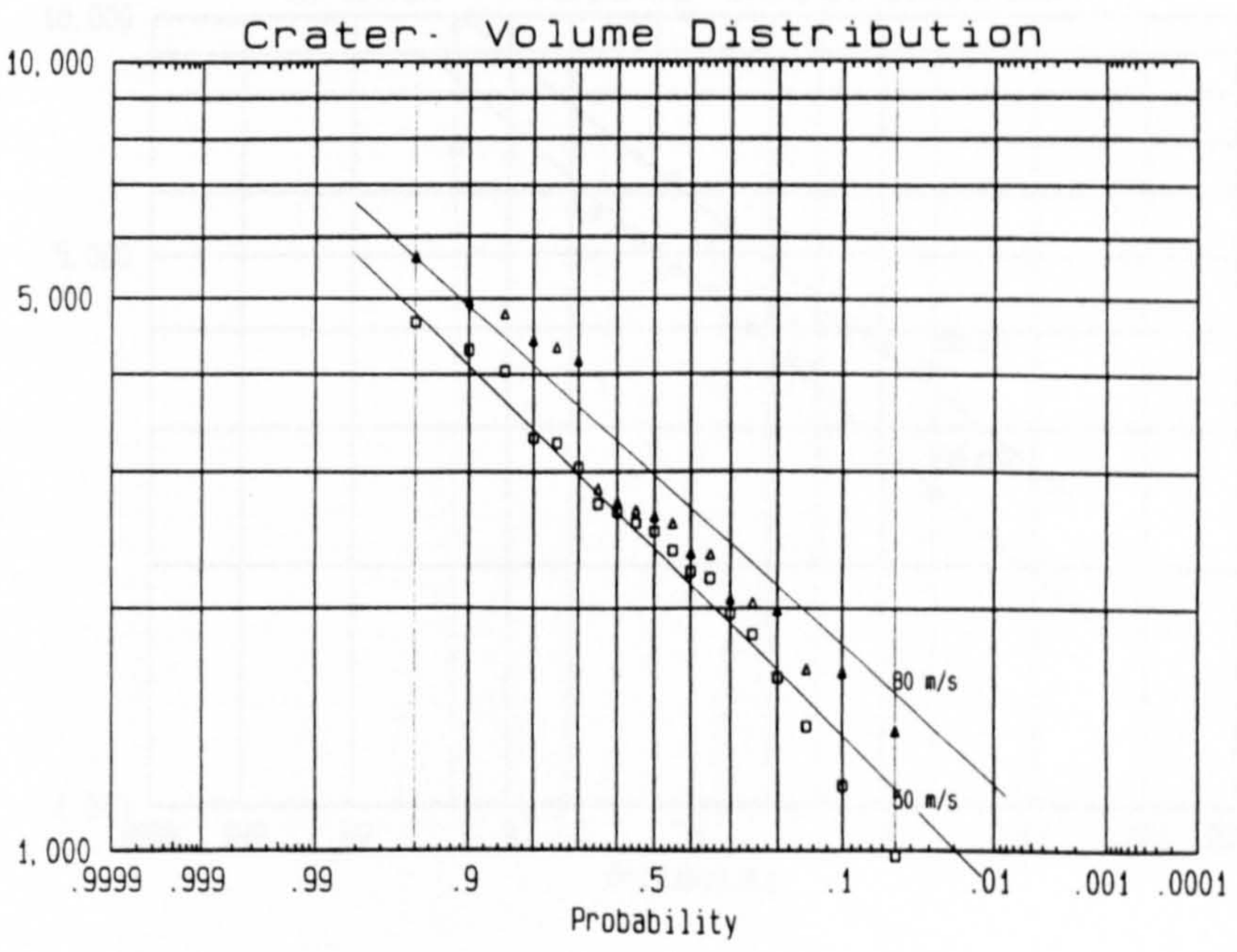

(d.3). L80/13Cr, V_p=100 m/s and 150 m/s, at 30°.

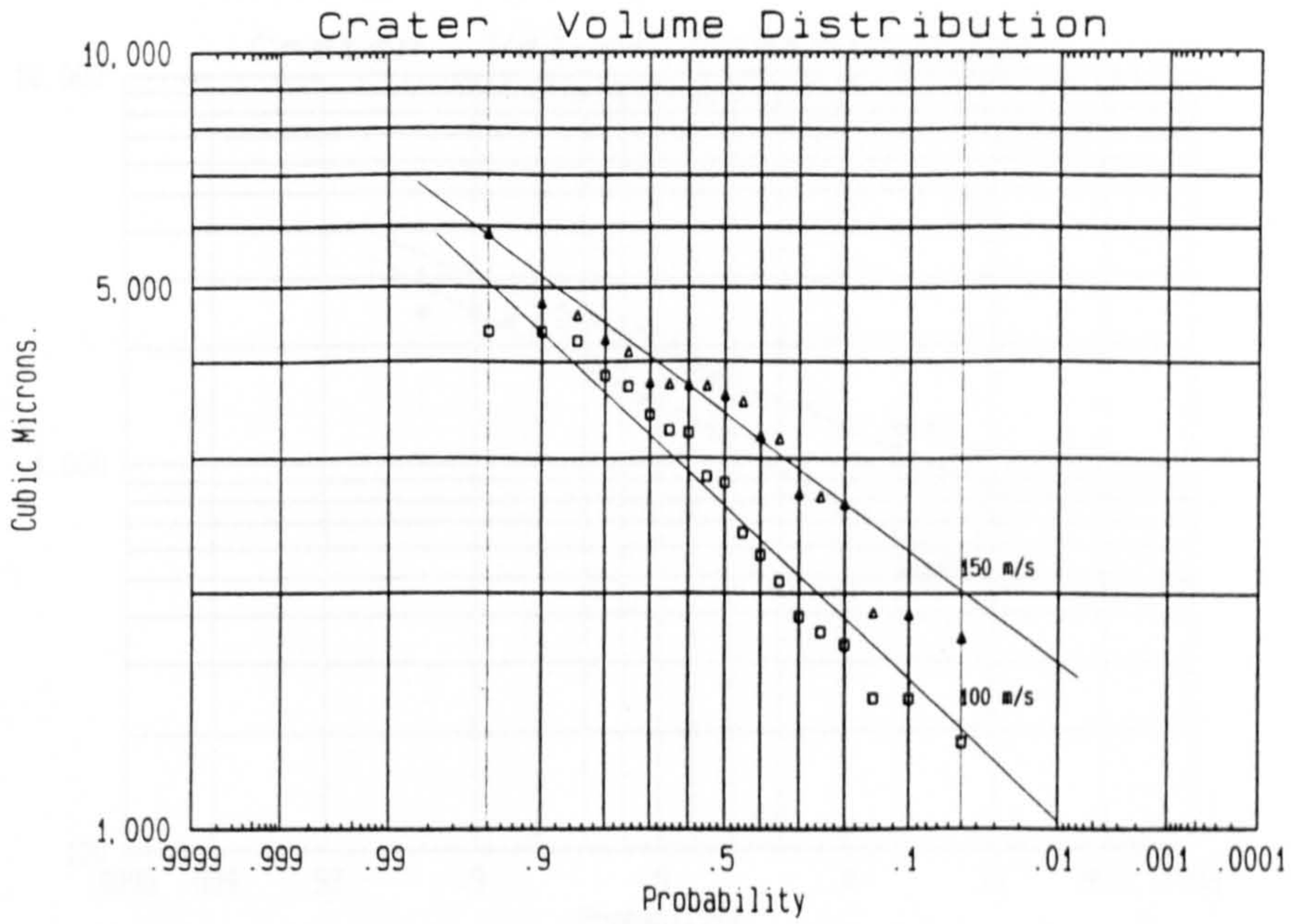

(d.4). L80/13Cr, V_p=100 m/s and 150 m/s, at 90°.

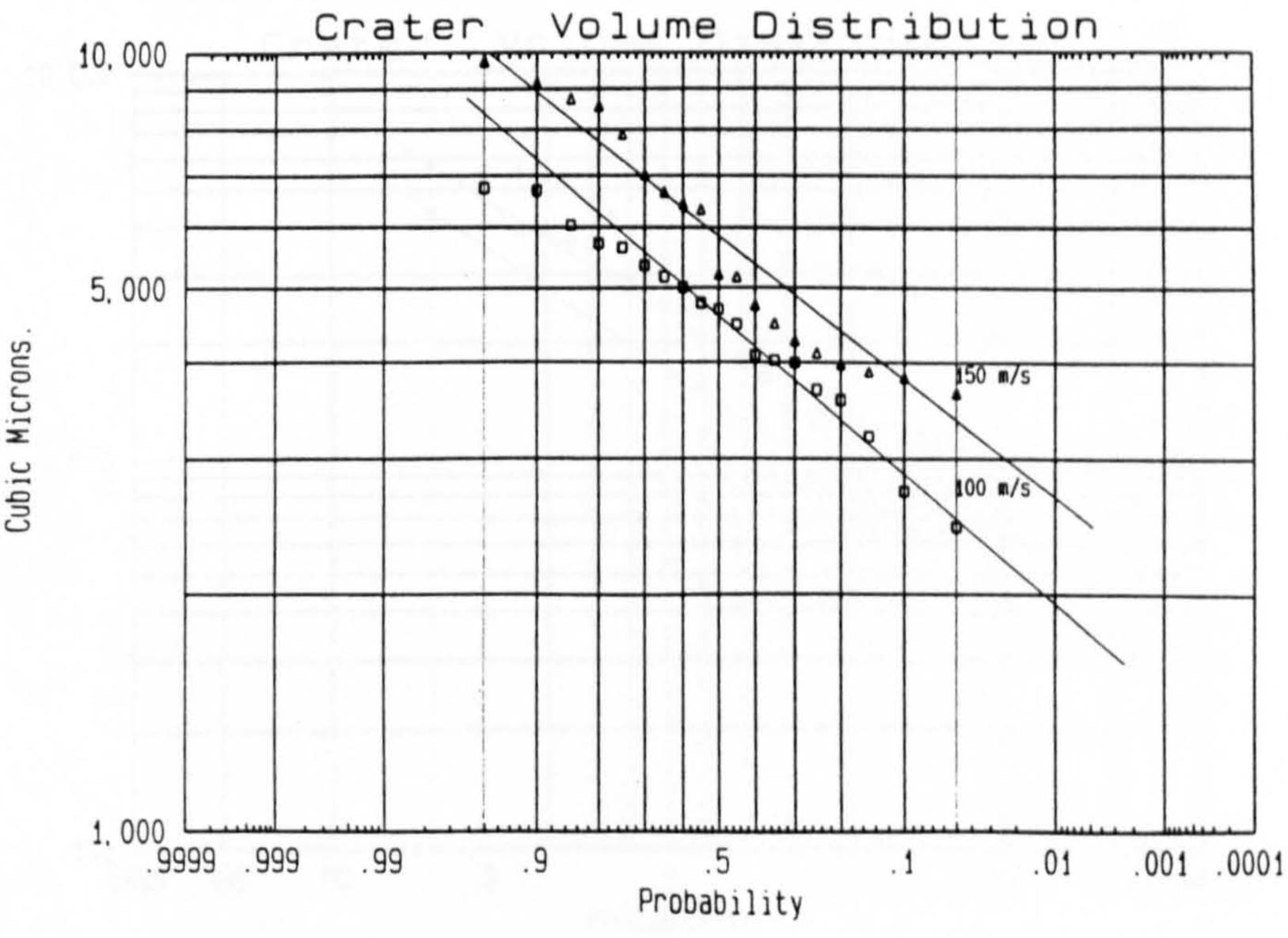

(e.1). Ferrulium 255, V_p=50 m/s and 80 m/s, at 30°.

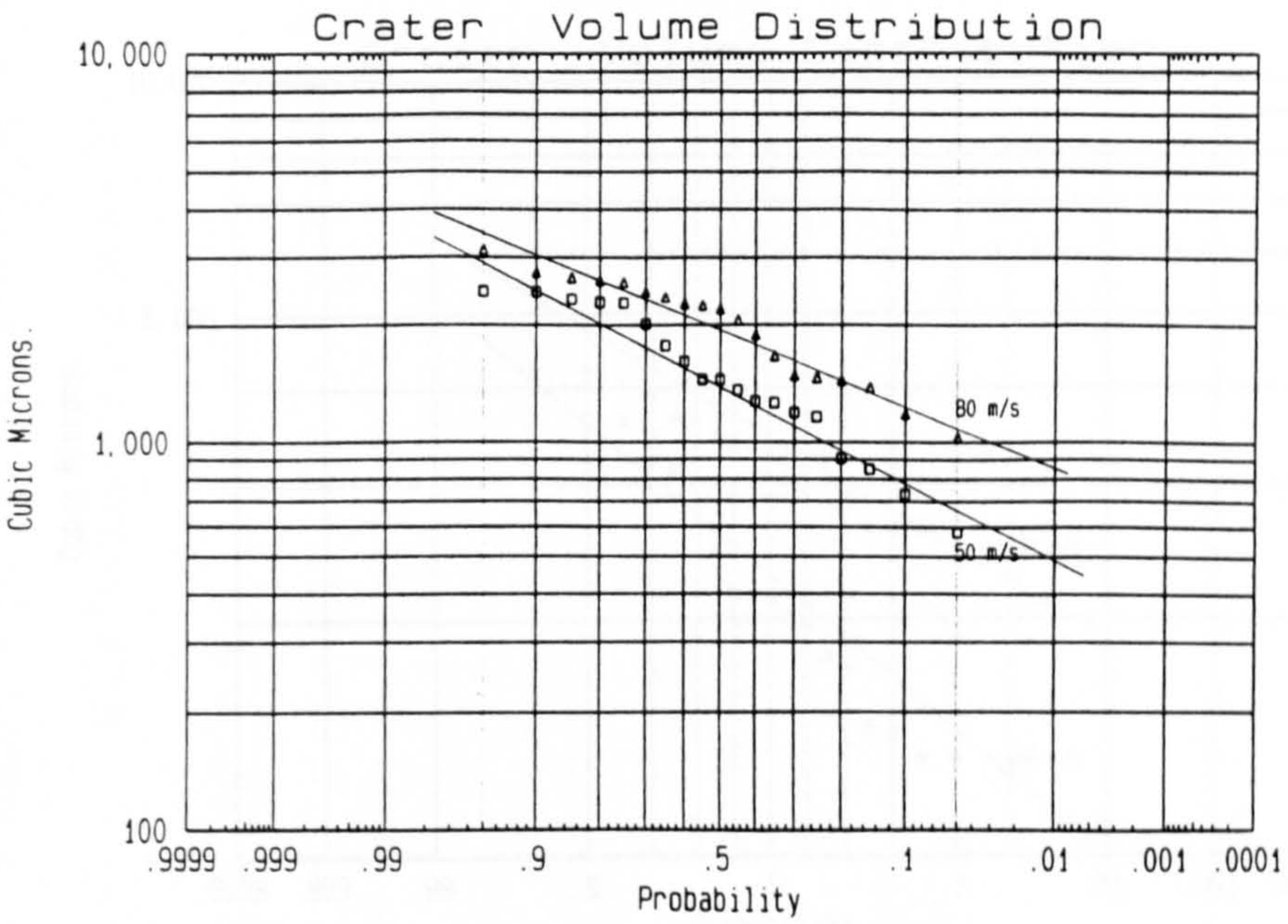

(e.2). Ferrulium 255, V_p=50 m/s and 80 m/s, at 90°.

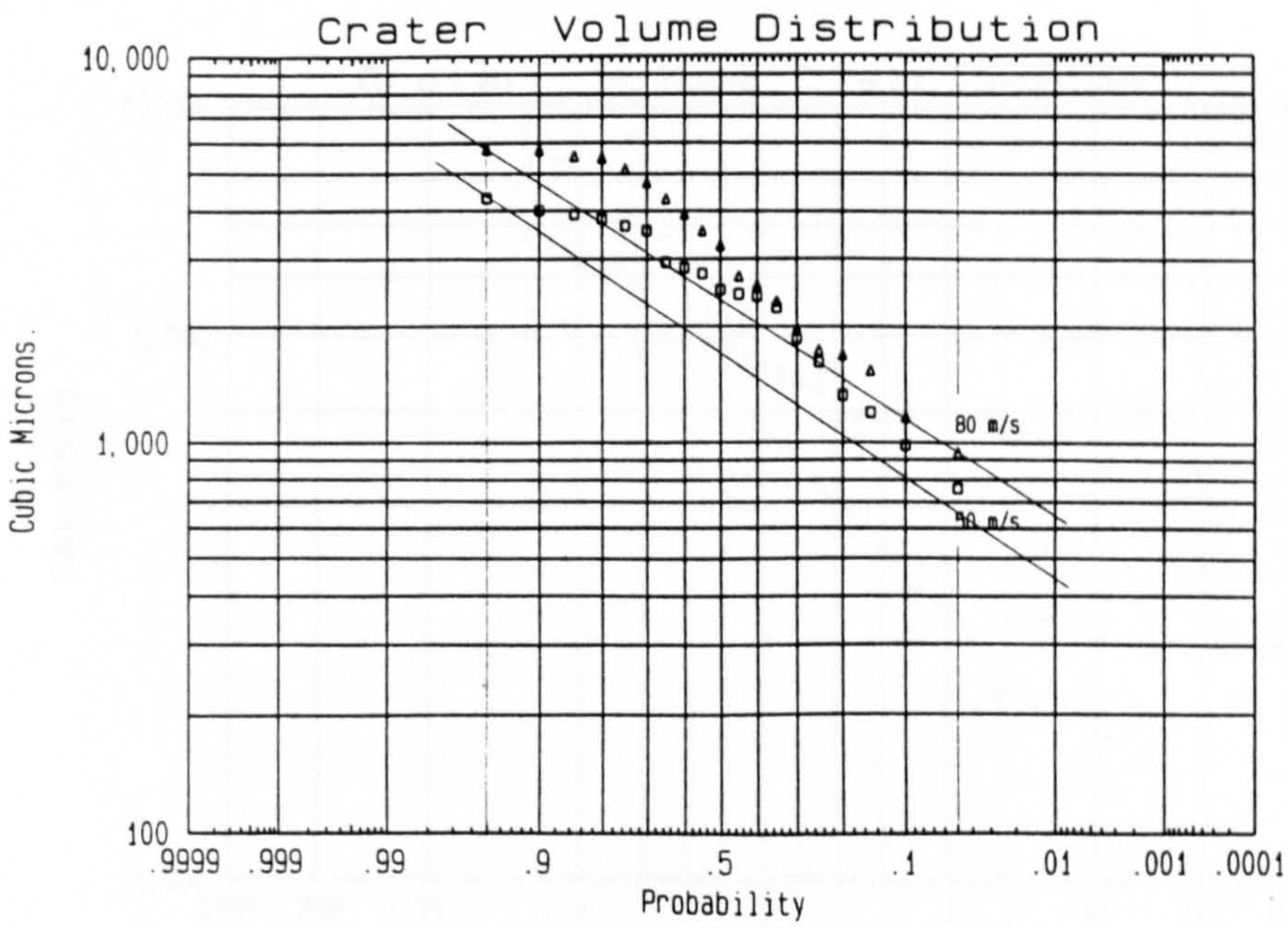

(e.3). Ferrulium 255, V_p=100 m/s and 150 m/s, at 30°.

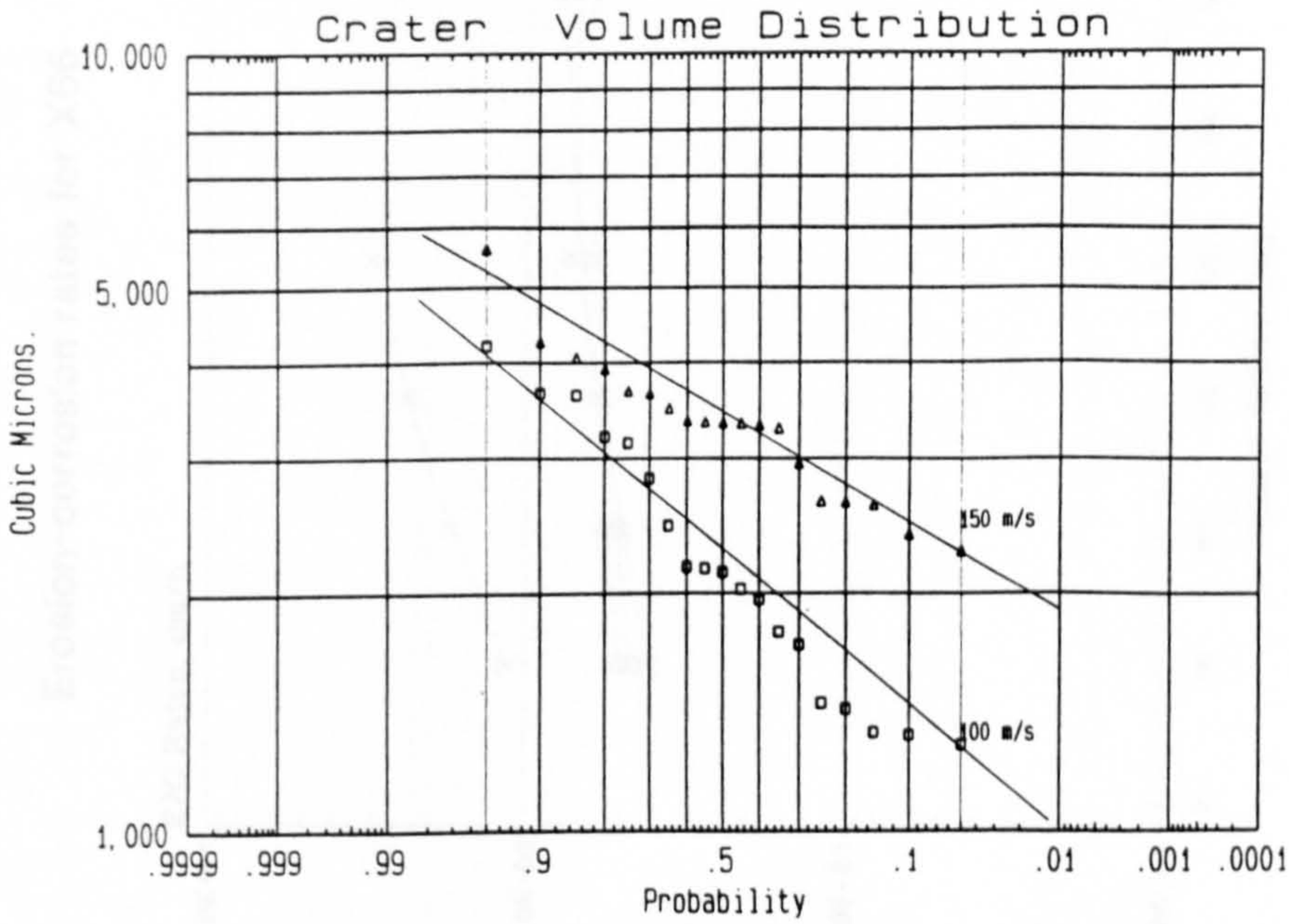

(e.4). Ferrulium 255, V_p=100 m/s and 150 m/s, at 90°.

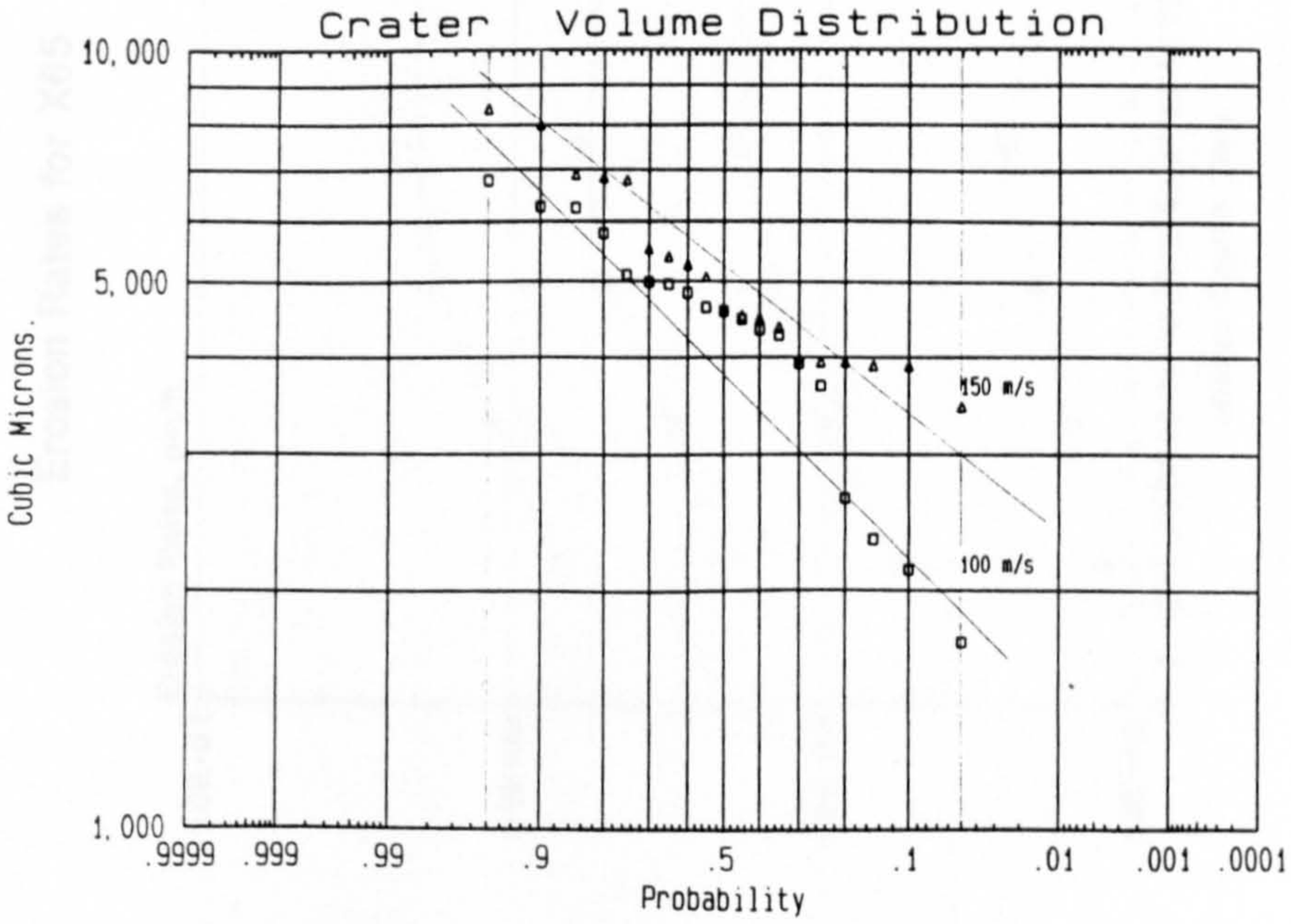

G5. Other erosion and erosion-corrosion rate graphs.

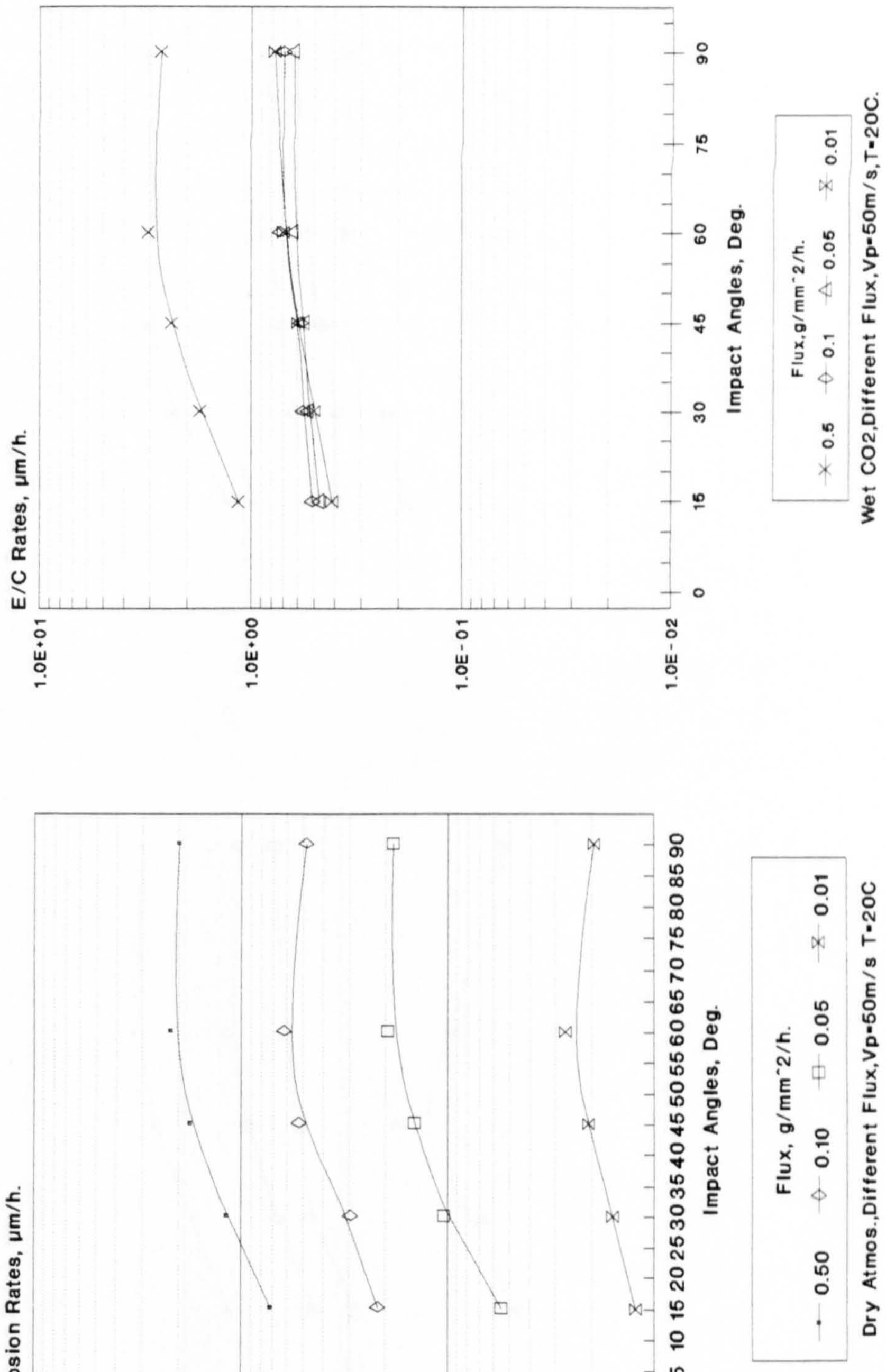

Erosion Rates for N80

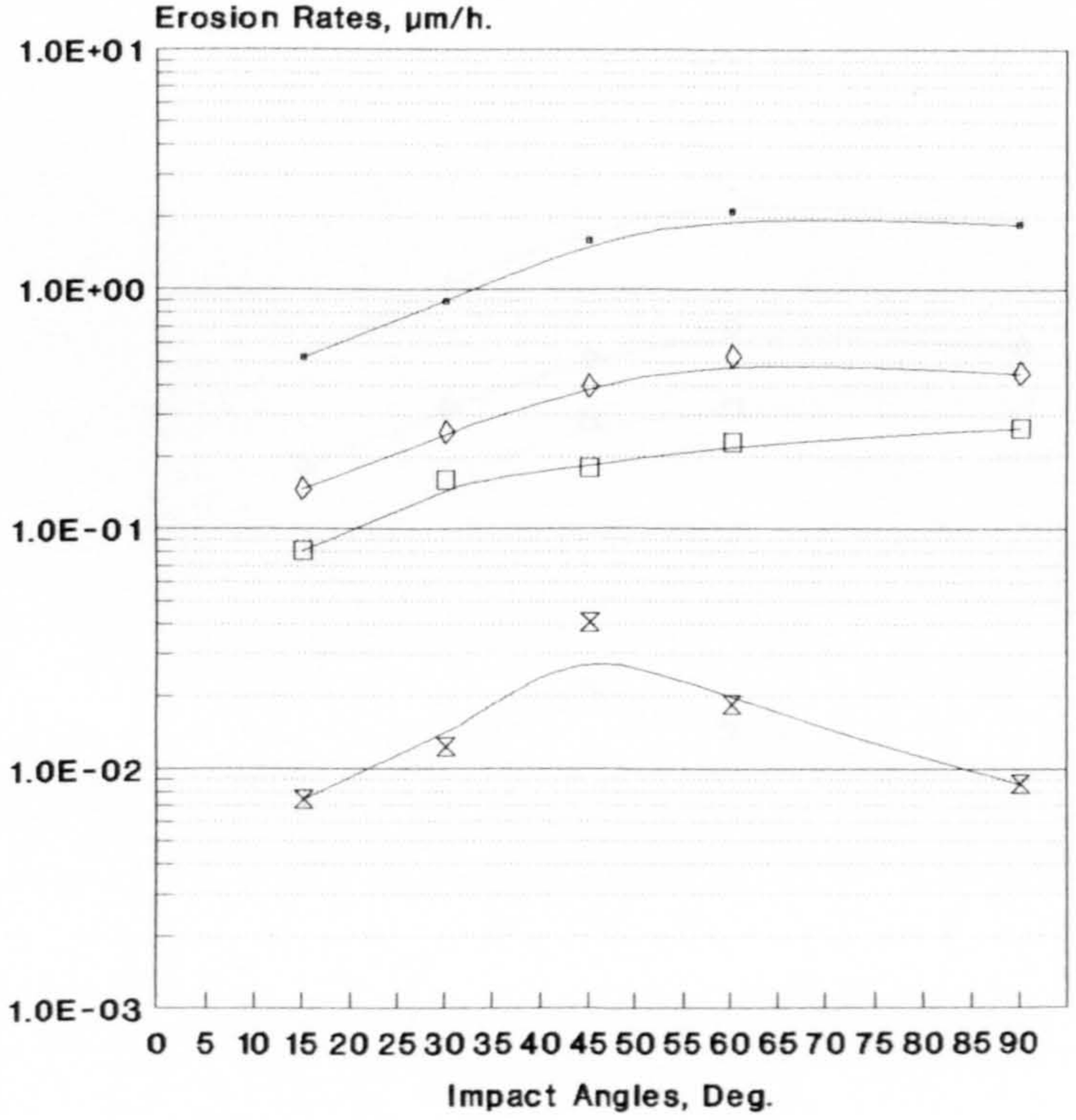

Dry Atmos.,Different Flux,Vp=50m/s,T=20C

Erosion-corrosion rates for N80

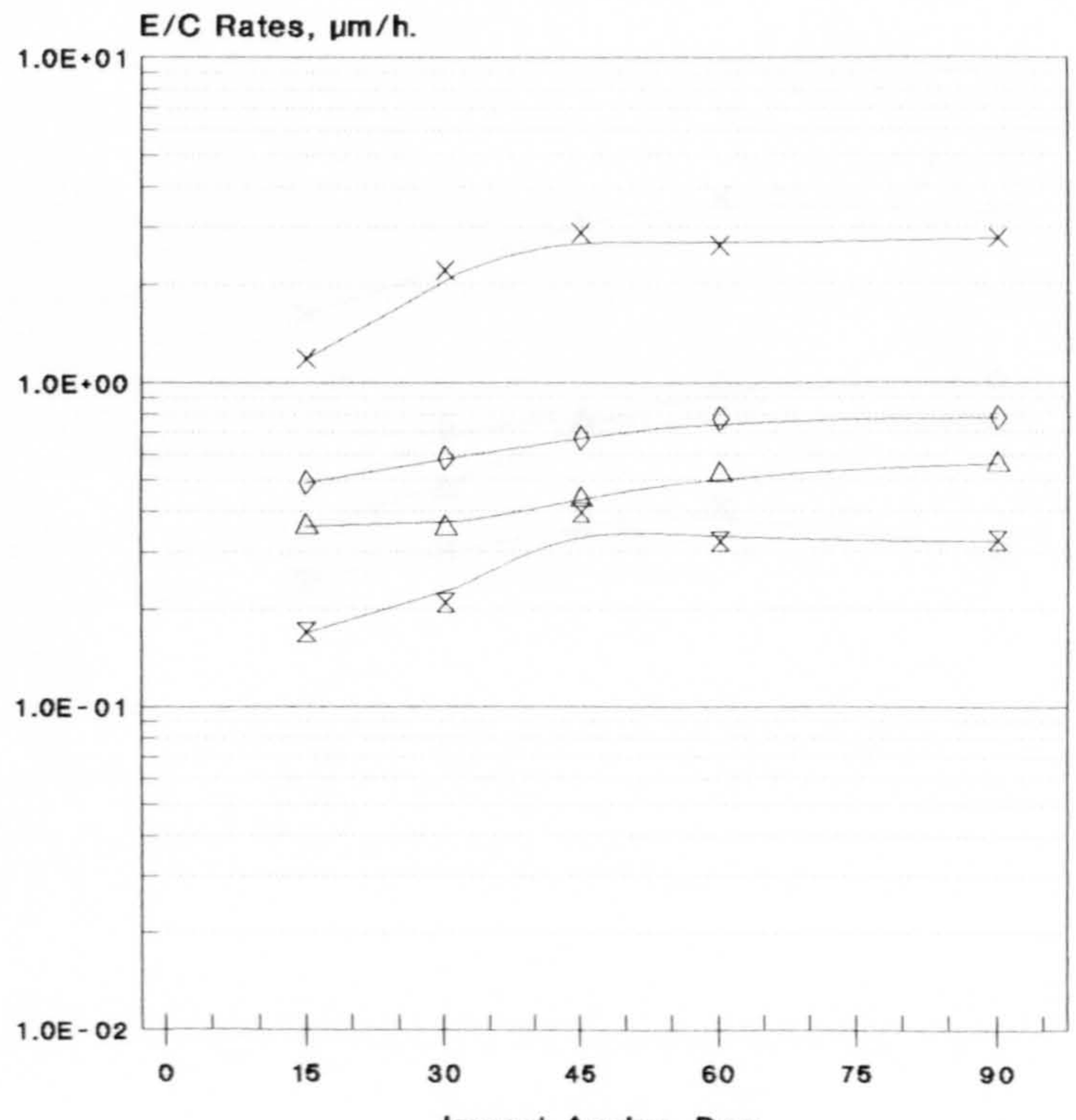

Wet CO2,Different Flux,Vp=50m/s,T=20C

Erosion Rates for L80

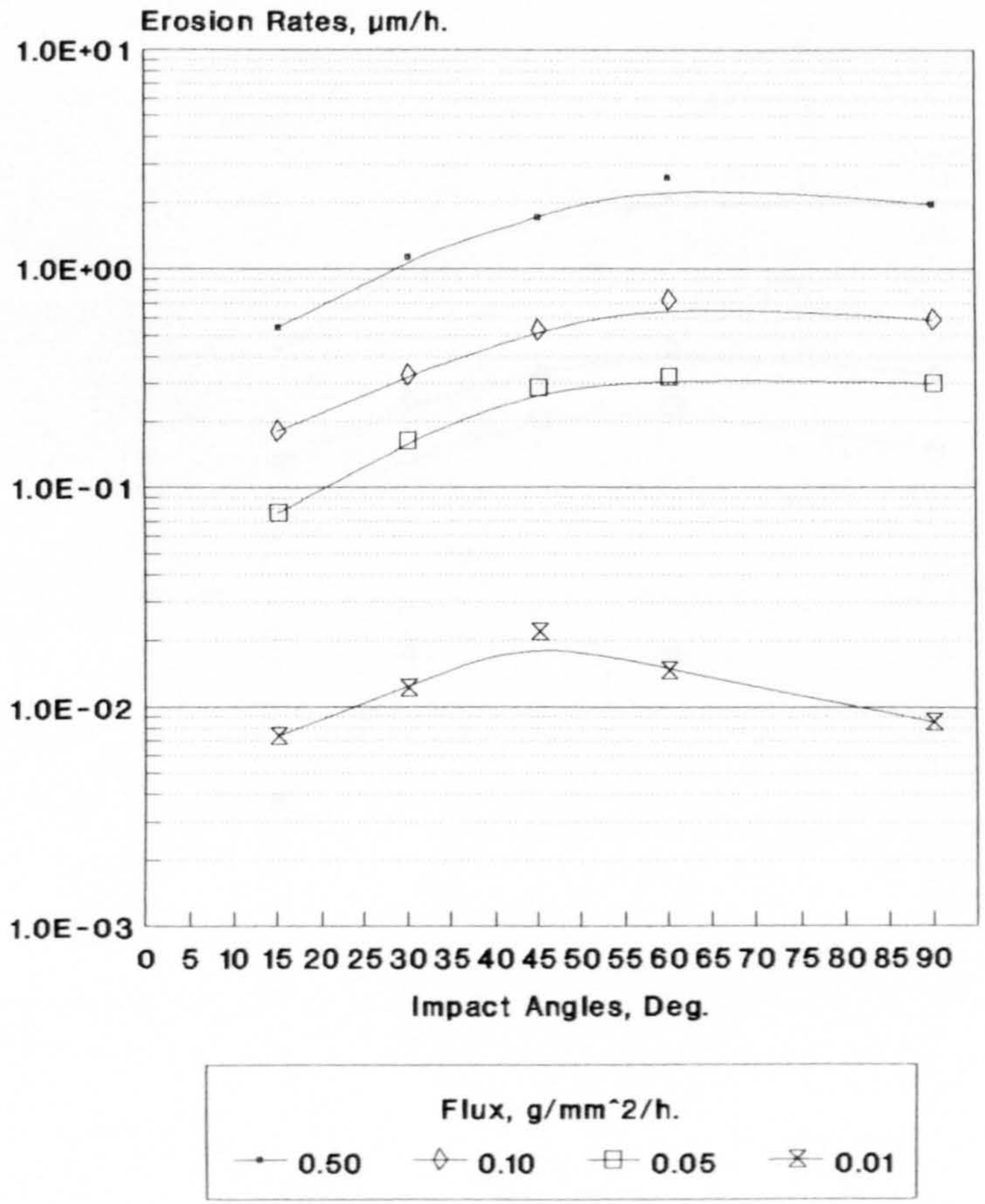

Dry Atmos.,Different Flux,Vp=50m/s T=20C

Erosion-corrosion rates for L80

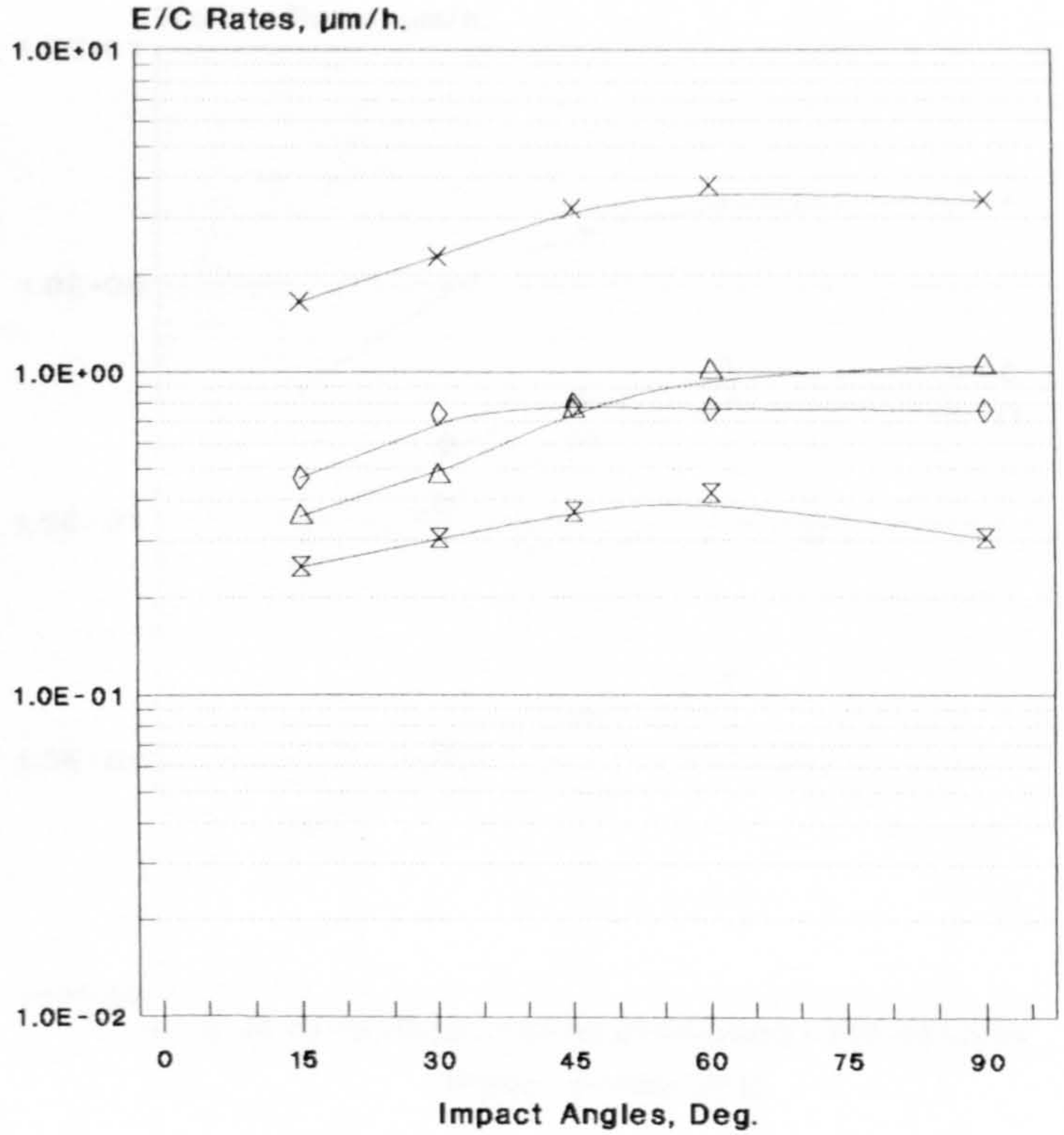

Wet CO2, Different Flux, Vp=50m/s.,T=20C

Erosion Rates for L80/13Cr

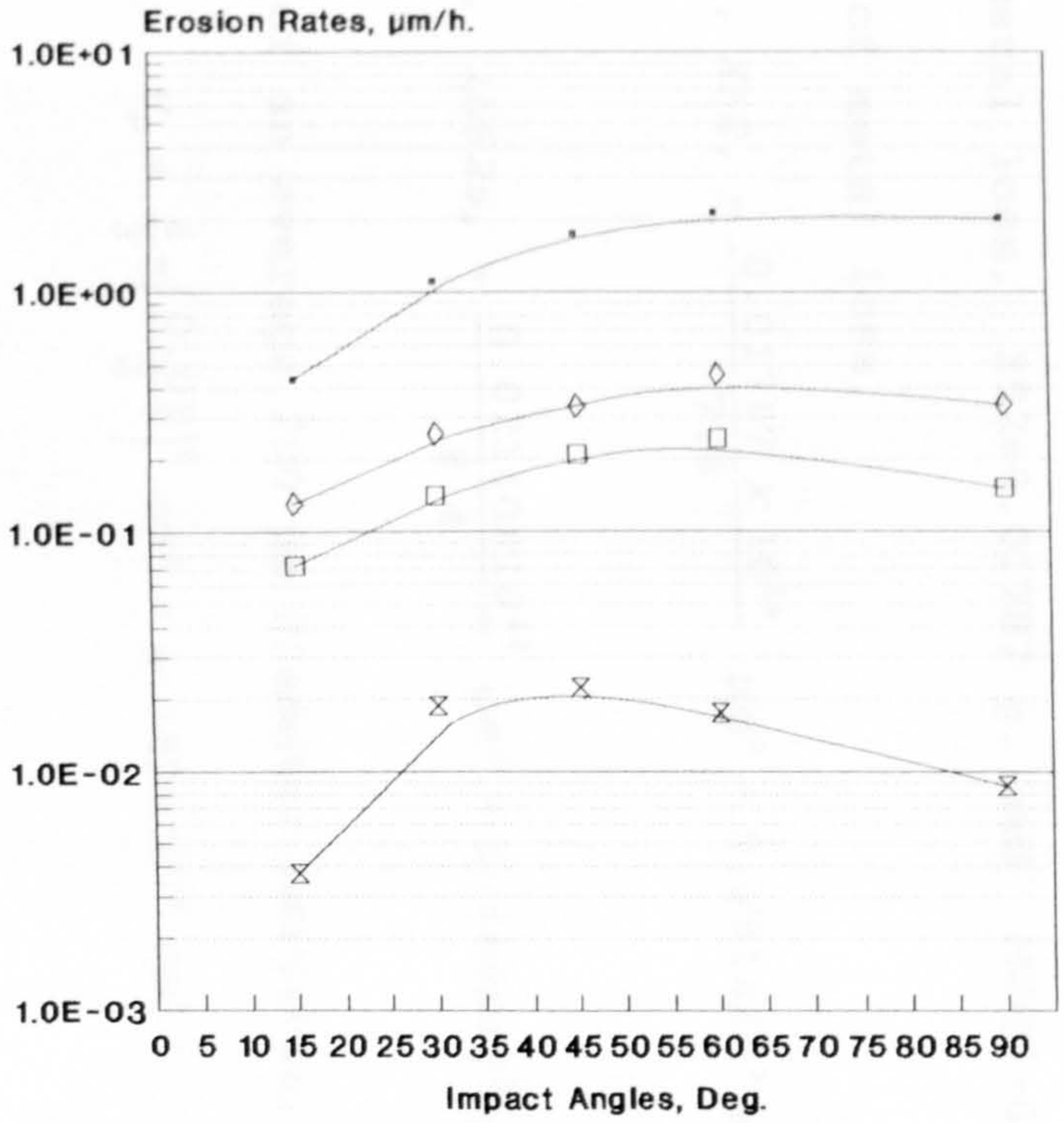

Dry Atmos.,Different Flux,Vp=50m/s T=20C

Erosion Rates for Ferrulium 255

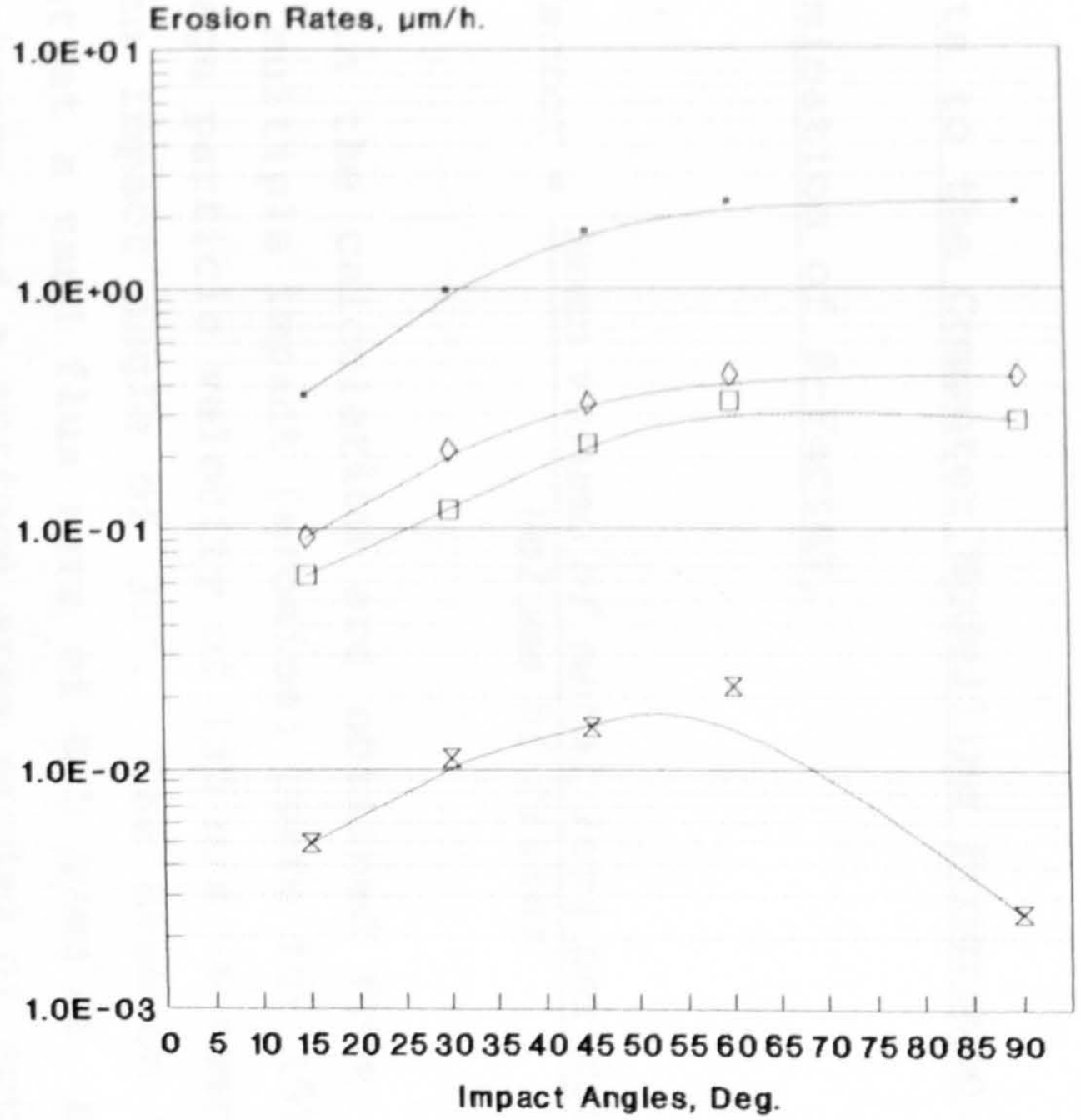

Dry Atmos.,Different Flux,Vp=50m/s T=20C

APPENDIX H

Improvements to the Computer Modelling Programme.

H1. Determination of β-Factor.

Definition,

$$\beta\text{-}Factor = \frac{Mean\ volume\ of\ metal\ loss\ per\ crater}{Volume\ of\ crater}$$

Data used in the calculation are obtained from the single impact and multiple impact (erosion) tests for X52 and IN625 at an average particle velocity of 150 m/s, a temperature of 20°C and an impact angle of 30°. The erosion tests were carried out at a sand flux rate of 0.5 g/mm²/h, an exposure time of 20 hours and a surface area eroded of approximately 42 mm².

1. Total metal loss, X52=0.01787 g. and IN625=0.02140 g.

2. Volume of metal loss,

$$For,\ X52,\ = \frac{0.01787 \times 10^{12}}{7.8}\ \mu m^3 = 2.291 x 10^9\ \mu m^3.$$

and

$$For,\ IN625,\ = \frac{0.02140 x 10^{12}}{8.4}\ \mu m^3 = 2.548 x 10^9\ \mu m^3.$$

3. Volume of an average 200 μm diameter particle,

$$V_p = \frac{4}{3}\pi\left(\frac{0.02}{2}\right)^3\ cm^3 = 4.189 x 10^{-6}\ cm^3.$$

4. Mass of a 200 μm diameter particle,

$$M_p = 2.63 \frac{g}{cm^3} \; x \; 4.189x10^{-6} \; cm^3 = 11.02x10^{-6} \; g.$$

5. Number of 200 μm particles impacting over 20 hours exposure,

$$Number\ of\ Particles, = \frac{0.05 \; x \; 42 \; x \; 20}{11.02 \; x \; 10^{-6}} = 3.812x10^6.$$

6. If it is assumed that on average it takes two particles to detach a platelet from the target surface, i.e. the first particle strikes the surface, creating a crater and lip, and when the second particle strikes the surface, it simply detaches the lip from the surface. Therefore,

(a) $Volume\ of\ a\ platelet\ for\ X52 = \frac{2.291x10^9}{(1/2)\ 3.812x10^6} = 1201 \mu m^3.$

and

(b) $Volume\ of\ a\ platelet\ for\ IN625 = \frac{2.548x10^9}{(1/2)\ 3.812x10^6} = 1337 \mu m^3$

7. Average volume of a crater obtained at a V_p=150 m/s, for X52 ≈ 4000 μm^3 and IN625 ≈ 4500 μm^3.

8. Therefore,

(a). $\beta\text{-}Factor,\ For\ X52 = \frac{1201}{4000} = 0.30$

and

(b). $\beta\text{-}Factor,\ For\ IN625 = \frac{1337}{4500} = 0.30$

H2. Routine Modification for Scale Dominated Regime.

```
If    Subst_mass_loss = 0  then
      Begin
           Eros_rate:=Oxid_mass_loss/MTo;
           If  MTs=0  then
               Subst_rate:= 0
           Else
               Oxid_rate:= Oxid_mass_loss/MTo;
      End
Else
      Subst_rate:=Subst_mass_loss/MTs;
```

H3. Routine Modification for Substrate Dominated Regime.

```
If  Oxid mass loss = 0  then
      Begin
           Eros_rate:=Subst_mass_loss/MTs;
           If MTo=0  then
              Oxid_rate:= 0
           Else
              Subst_rate:=Subst_mass_loss/MTs;
      End
Else
      Oxid_rate:=Oxid_mass_loss/MTo;
```

H4. Corrections for Thickness Erosion Rate Conversions.

```
Subst_thick_rate:=(Subst_rate*Ptle_Loading/Subst^.Density)
                       *3.6E9;
Oxid_thick_rate:=(Oxid_rate*Ptle_Loading/Oxid^.Density)
                       *3.6E9;
```

H5. Modifications to Total Metal Loss and Total Mass of Particles Calculations.

```
Metal_mass_loss:=(Z*Oxid^.Density+Oxid_mass_loss)*
                 (Oxid^.At_weight_cat/Oxid^.Mol_weight);
and,

Total_mass_of_ptle:=Total_mass_of_ptle+
                    ((MI*Time_Inc*3600)/TM);
```

H6. Routine for all Variables Set to Zero at t=0.

```
If gK<=1E-1000   then
     Begin
          If  MTo=0  then
              MTs:=Total_mass_of_ptle
          Else
              MTs:=Total_mass_of_ptle - MTo;
      End
Else
    MTo:=Total_mass_of_ptle - MTs;
```

H7. Modifications in the Main Procedure.

```
If  MTo=Total_mass_of_ptle  then
    Subst_rate:=0
Else
    MTs:=Total_mass_of_ptle - MTo;
```

APPENDIX I

Summary of results obtained from Erosion and E/C Modelling.

I.1. Predicted and measured erosion rates for X52 at 0.05 flux and T=20°C.

V_p, m/s		15°	30°	45°	60°	90°
20	M	0.011	0.012	0.014	0.02	0.02
	P	0.013	0.047	0.054	0.018	0.02
50	M	0.074	0.11	0.14	0.21	0.20
	P	0.25	0.47	0.63	0.38	0.11
80	M	0.36	0.58	0.85	1.11	0.904
	P	2.10	2.83	2.20	0.90	0.65
150	M	1.57	2.73	3.27	4.55	4.13
	P	2.98	6.25	4.41	4.50	3.12

I.2. Predicted and measured erosion rates for X52 at V_p=50 m/s and T=20°C.

Flux		15°	30°	45°	60°	90°
0.01	M	0.01	0.023	0.03	0.022	0.02
	P	0.03	0.07	0.15	0.12	0.06
0.05	M	0.07	0.11	0.14	0.21	0.20
	P	0.25	0.47	0.63	0.38	0.12
0.10	M	0.15	0.32	0.52	0.66	0.63
	P	0.34	0.58	0.75	0.56	0.24
0.50	M	0.49	1.16	1.98	2.86	2.12
	P	1.54	2.67	3.55	2.76	1.03

M = Measured values, P = Predicted values.

I.3. Predicted and measured erosion rates for IN625 at 0.05 flux and T=20°C.

V_p, m/s		15°	30°	45°	60°	90°
20	M	0.003	0.005	0.007	0.006	0.006
	P	0	0.054	0.13	0.098	0.044
50	M	0.042	0.12	0.19	0.26	0.30
	P	0	0.085	0.16	0.12	0.044
80	M	0.16	0.44	0.72	1.08	1.02
	P	0	0.17	0.26	0.19	0.09
150	M	1.39	3.7	4.9	6.45	7.2
	P	1.0	1.8	1.4	0.89	0.4

I.4. Predicted and measured E/C rates for X52 at 0.05 flux, $K_p=27x10^{-3}$ $\mu m^2/h$ and T=20°C.

V_p, m/s		15°	30°	45°	60°	90°
20	M	0.084	0.12	0.16	0.23	0.21
	P	0.029	0.096	0.07	0.044	0.025
50	M	0.23	0.37	0.48	0.55	0.63
	P	0.17	0.40	0.50	0.29	0.24
80	M	0.72	1.03	1.475	1.77	1.71
	P	0.92	2.21	2.372	1.40	0.61
150	M	1.45	3.60	5.30	7.63	6.66
	P	5.28	7.87	8.18	6.80	4.92

M = Measured values, P = Predicted values.

I.5. Predicted and measured E/C rates for X52 at V_p=50 m/s, K_p=27x10^{-3} μm^2/h and T=20°C.

Flux		15°	30°	45°	60°	90°
0.01	M	0.14	0.24	0.24	0.39	0.41
	P	0.08	0.10	0.13	0.10	0.04
0.05	M	0.23	0.37	0.48	0.56	0.63
	P	0.17	0.40	0.50	0.29	0.24
0.10	M	0.36	0.70	0.85	0.84	0.88
	P	0.65	0.76	0.82	0.62	0.26
0.50	M	1.91	2.59	3.86	4.66	3.7
	P	1.93	2.43	2.67	3.01	0.92

M = Measured values, P = Predicted values.